The Journal of Gemmology

Volume 38 / No. 1 / 2022

Colombian Emerald Oddities

Pink-Orange Euclase from Brazil

Inclusions in Demantoid from Madagascar

Photochromism Part 2

SSEF
SCHWEIZERISCHES GEMMOLOGISCHES INSTITUT
SWISS GEMMOLOGICAL INSTITUTE
INSTITUT SUISSE DE GEMMOLOGIE

Gem-A
THE GEMMOLOGICAL ASSOCIATION OF GREAT BRITAIN

SSEF

SCHWEIZERISCHES GEMMOLOGISCHES INSTITUT
SWISS GEMMOLOGICAL INSTITUTE
INSTITUT SUISSE DE GEMMOLOGIE

ORIGIN DETERMINATION · TREATMENT DETECTION

DIAMOND GRADING · PEARL TESTING

EDUCATION · RESEARCH

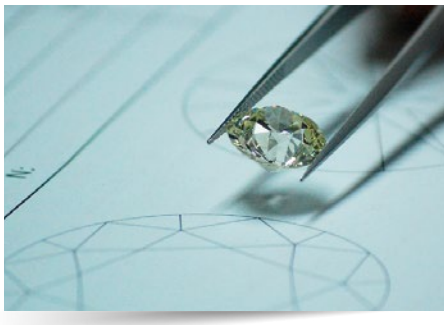

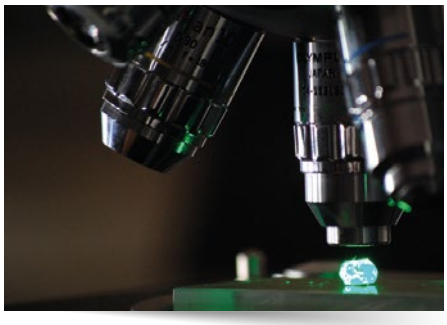

THE SCIENCE OF GEMSTONE TESTING™

Aeschengraben 26, 4051 Basel, Switzerland Tel. +41 61 262 06 40 Fax + 41 61 262 06 41 admin@ssef.ch www.ssef.ch

The Journal of Gemmology

Volume 38 / No. 1 / 2022

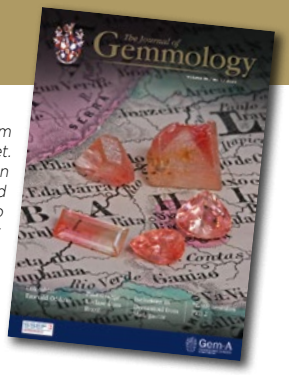

Cover photo: *Small quantities of pink-orange euclase from Bahia, Brazil, recently entered the international market. This material displays an attractive colour not seen previously in euclase, and also occurs in well-formed crystals and hosts interesting inclusions. From left to right, the cut stones weigh 0.92 ct (bicoloured), 0.72 ct and 1.30 ct, and the crystals are 0.45 and 1.47 g. Specimens courtesy of The Gem Trader (Cave Creek, Arizona, USA); photo by Brad Payne.*

COLUMNS

Photo by J. Štubňa

ARTICLES

Photo courtesy of G. Martayan

Composite photo courtesy of Thomas Hainschwang

The Journal is published by Gem-A in collaboration with SSEF and with the support of AGL.

Gem-A THE GEMMOLOGICAL ASSOCIATION OF GREAT BRITAIN

SSEF SCHWEIZERISCHES GEMMOLOGISCHES INSTITUT SWISS GEMMOLOGICAL INSTITUTE INSTITUT SUISSE DE GEMMOLOGIE

AGL AMERICAN GEMOLOGICAL LABORATORIES

The Journal of Gemmology

COVERED BY THE FOLLOWING ABSTRACTING AND INDEXING SERVICES:

Clarivate Analytics' (formerly Thomson Reuters/ISI) Science Citation Index Expanded (in the Web of Science), *Journal Citation Reports (Science Edition)* and *Current Contents (Physical, Chemical and Earth Sciences)*; Elsevier's Scopus; Australian Research Council's Excellence in Research for Australia (ERA) Journal List; China National Knowledge Infrastructure (CNKI Scholar); EBSCO's Academic Search Ultimate; ProQuest (Cambridge Scientific Abstracts); GeoRef; CrossRef; Chemical Abstracts (CA Plus); Mineralogical Abstracts; Index Copernicus ICI Journals Master List; Gale Academic OneFile; British Library Document Supply Service; and Copyright Clearance Center's RightFind application.

Science Citation Index Expanded
Web of Science Clarivate Analytics

CONTENT SUBMISSION

The Editor-in-Chief is glad to consider original articles, news items, conference reports, announcements and calendar entries on subjects of gemmological interest for publication in *The Journal of Gemmology*. A guide to the various sections and the preparation of manuscripts is given at https://gem-a.com/membership/journal-of-gemmology/submissions, or contact the Editor-in-Chief.

SUBSCRIPTIONS

Gem-A members receive *The Journal* as part of their membership package, full details of which are given at https://gem-a.com/membership. Laboratories, libraries, museums and similar institutions may become direct subscribers to *The Journal*; download the form from *The Journal*'s home page.

ADVERTISING

Enquiries about advertising in *The Journal* should be directed to advertising@gem-a.com. For more information, see https://gem-a.com/news-publications/media-pack-2021.

DESIGN & PRODUCTION

Zest Design, London. www.zest-uk.com

PRINTER

DG3 Group (Holdings) Ltd, London. https://dg3.com

Mixed Sources
Product group from well-managed forests and other controlled sources
www.fsc.org Cert no. TT-COC-002454
© 1996 Forest Stewardship Council
FSC

ISSN 1355-4565 (Print), ISSN 2632-1718 (Online)

Gem-A
THE GEMMOLOGICAL ASSOCIATION OF GREAT BRITAIN

21 Ely Place
London EC1N 6TD
UK
t: +44 (0)20 7404 3334
f: +44 (0)20 7404 8843
e: information@gem-a.com
w: https://gem-a.com

Registered Charity No. 1109555
A company limited by guarantee and registered in England No. 1945780
Registered office: Palladium House, 1–4 Argyll Street, London W1F 7LD

What's New

INSTRUMENTATION

Inspectrum Spectrometer

In late 2021, Gemetrix Pty Ltd (Perth, Western Australia) released the Inspectrum, an instrument that records the visible-range (410–750 nm) photoluminescence (PL) and transmission spectra of loose and mounted gems. These measurements can help determine if a sample is natural, synthetic or treated. The Inspectrum can also be used to obtain reflection spectra for opaque gems such as jade. The unit is portable and can be powered by an external battery pack, but it requires connection to a computer in order to observe and record spectra. A switch enables the user to change modes from absorption to PL without repositioning the stone being tested. Visit https://www.gemetrix.com.au/Inspectrum.html.

NEWS AND PUBLICATIONS

GIT Information Center Reports

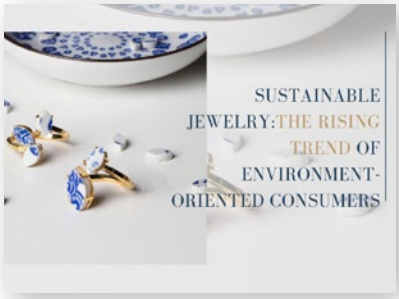

The Gem and Jewelry Institute of Thailand (GIT, Bangkok) posts articles primarily about gem and jewellery marketing in the online GIT Information Center at https://infocenter.git.or.th/en/category/article. The most recent ones from 2021 cover 'Sustainable Jewelry: The Rising Trend of Environment-Oriented Consumers' (December); 'Jewelry for the YOLD Market' (the 'too young to be old' senior population; November); and 'Circular Economy for Sustainable Gem and Jewelry Industry' (October). Other articles from 2021 cover handcrafted Thai jewellery, carbon-footprint reduction by the gem and jewellery industry, the 'Country Brand' marketing strategy, and ethics and sustainability. Many other articles have been posted since 2008, making this website a good resource for information on industry trends relevant to all those positioned along the gem and jewellery market chain.

Global Diamond Industry Report 2021–2022

Bain & Co. released its 11th annual report on the worldwide diamond industry in February 2022. Subtitled 'A Brilliant Recovery Shapes Up', the report focuses on the effects of the global pandemic, the diamond industry's 'impressive recovery' and projections for the future. Much of the year's success was the result of creative online sales platforms, even by small retailers. However, it also came from strong consumer demand. In 2021, revenue increases across the board included 62% for the mining segment, 55% for cutting and polishing, and 29% for diamond retail jewellery. By the year's end, both rough and polished prices were near their pre-pandemic levels, and rough diamond production had begun to recover, but still had not reached 2019 levels. Download the report at https://www.bain.com/insights/a-brilliant-recovery-shapes-up-the-global-diamond-industry-2021-to-22.

Gold Demand Trends 2021

The World Gold Council released a combined report in January 2022 that covers all of 2021 and its fourth quarter. Overall demand for gold rose 10% to 4,021 tonnes, mostly due to an increase of almost 50% in the fourth quarter, to its highest level in more than two years. The demand for gold jewellery rose in all regions, but especially in India and China. Jewellery fabrication grew 67% in response to consumer demand. Read the report online or download it (after logging in) at https://www.gold.org/goldhub/research/gold-demand-trends/gold-demand-trends-full-year-2021.

The Journal's Cumulative Index and Bibliography Lists Updated

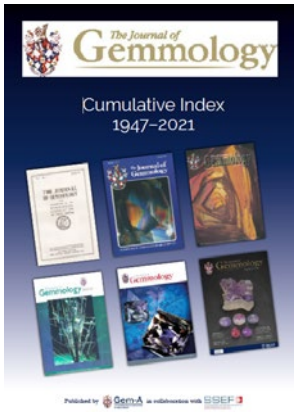

The Journal of Gemmology's cumulative index and subject bibliographies have been updated to cover all issues through 2021 (since its inception in 1947). The PDF files can be searched for specific authors as well as topics. The subject bibliographies, covering articles and notes published in *The Journal*, include the following topics: asterism and chatoyancy, biogenic gems, chrysoberyl and alexandrite, colour-change gems, corundum, diamond, emerald and other beryls, feldspars, garnet, historical gems and jewels, jades, opal, pearl, quartz-family gems, spinel and tourmaline. Download the index and bibliography files at https://gem-a.com/membership/journal-of-gemmology.

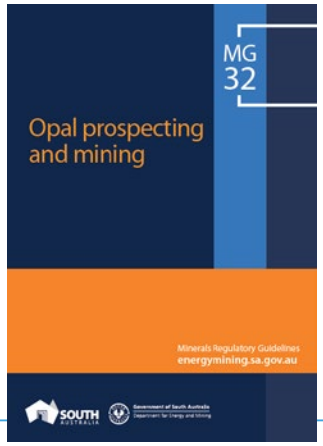

Opal Prospecting and Mining in South Australia

In January 2021, the Government of South Australia's Department for Energy and Mining issued a 36-page report titled *Opal Prospecting and Mining*, which describes resources and guidelines for opal fields in South Australia that were set aside for prospecting and mining in 1971 (i.e. Andamooka, Coober Pedy, Mintabie and Stuart Creek). It provides information on the fields, how to obtain a prospecting permit and 'requirements to prospect and mine for opal both within and outside' a field. Also covered are land access and environmental requirements. Download the report at https://sarigbasis.pir.sa.gov.au/WebtopEw/ws/samref/sarig1/image/DDD/MRGMG32.pdf.

Photoluminescence Poster for Diamonds

In March 2022, Gemetrix Pty Ltd (Perth, Western Australia) updated its reference poster that displays typical fluorescence and phosphorescence reactions for natural and synthetic diamonds and diamond simulants. The poster is organised by diamond colour, including colourless, yellow and orange, pink/purple, blue/violet, brown and green. Download the free poster at https://www.gemetrix.com.au/PL%20poster%202.pdf.

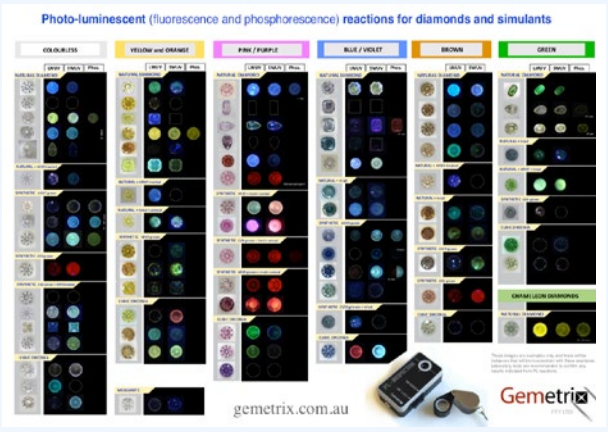

Responsible Sourcing by Jewellery Companies

In February 2021, Human Rights Watch released a one-page document titled '"Is Our Jewelry Company Sourcing Responsibly?" 20 Questions Company Officials Should Ask to Guide Action'. It provides a list of questions that deal with supply chain policy, traceability, human rights assessments, response to human rights risks, verification and grievance mechanisms, public reporting, and artisanal and small-scale mining. Read about—and download—the document at https://www.hrw.org/news/2021/02/11/valentines-day-traceable-transparent-jewelry-supply-chains.

TRAFFIC Report on Hong Kong Ivory Ban

In July 2021, TRAFFIC released *Ebbing Away: Hong Kong's Ivory Trade*, on the progress following Hong Kong's landmark decision in 2018 to prohibit the trade of ivory by the end of 2021 in an attempt to stem elephant poaching. Government records for 2020 indicate a decline in the availability of commercial ivory stocks, but the report suggests additional measures are needed. Download the report at https://www.traffic.org/publications/reports/ebbing-away-hong-kongs-ivory-trade.

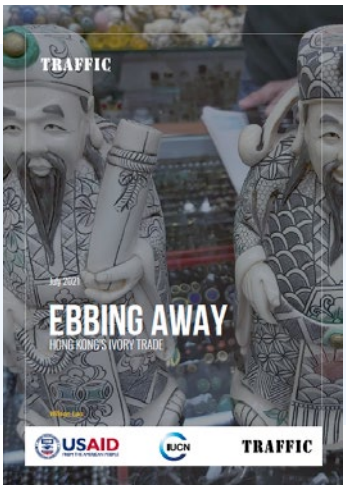

OTHER RESOURCES

Webinars and Other Online Gemmological Education

Due to the ongoing COVID-19 pandemic, a number of gem industry organisations and other groups continue to provide webinars (and other archived video and audio content) on their websites or YouTube channels that are of interest to gemmologists. See also those listed in previous What's New sections starting with Vol. 37, No. 2, 2020.

- The **GIA Alumni Association**'s Washington DC (USA) chapter offers recordings of their 2021 and 2022 presentations and webinars under 'Recent Posts' on their home page at https://dcgia.org. The videos currently available are: 'Diamonds of the Forbidden Zone' by Denise Nelsen (about visiting diamond mines on the Namibian coast); 'Afghanistan Gemstone Industry' by Gary Bowersox; and 'Victorian Jewelry: A Many-Splendored Thing' by Elyse Zorn Karlin.

- Launched in April 2021, **If Jewels Could Talk** is a series of podcasts hosted by jewellery historian and contributing jewellery director of *British Vogue* Carol Woolton. Now numbering 17, the podcasts feature the glitterati side of jewellery, including interviews with entertainment celebrities and prominent jewellers and jewellery experts. Wide-ranging topics include gem and jewellery history, notable and historic collections, past and current style trends, and much more. Visit http://www.carolwoolton.com/podcasts.

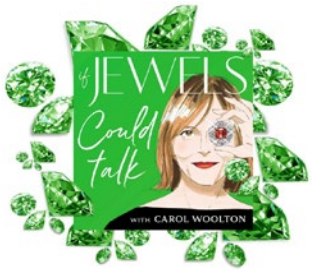

- **Jewellery World Awards** (previously JNA Awards) offers a webinar series on its YouTube channel at https://www.youtube.com/channel/UCZuG43DB_LGPguWo130k_4A. Videos posted in 2022 include 'Exploring AI in the Jewellery Industry' and 'The Key to Build a Successful Branding and Marketing Campaign'. Each one features a keynote speaker and a panel of experts.

- The **Responsible Jewellery Council** offers a series of podcasts under the title 'Creating Beautiful', which feature presentations by various industry leaders, including Susan M. Jacques of the Gemological Institute of America, Elliot Tannenbaum of Leo Schachter Diamonds and Diana Mitkov of De Beers. Visit https://open.spotify.com/show/0GQxe9T9oDBq7Xfd7pG5DE.

- The **Vancouver Kimberlite Cluster** is a seminar series organised by the University of British Columbia (Vancouver, Canada) and supported by SRK Consulting that covers diamond mining and exploration, kimberlite geology, and related topics. Several presentations from 2018–2022 are available on their YouTube channel at https://tinyurl.com/2p8hb49m, including the discovery and geology of the Argyle AK1 diamond deposit in Australia (by Murray Rayner), diamonds from South Africa's Koffiefontein mine and their inclusions (by Dr Nicole Meyer), and historical and modern mining methods for diamonds (by Jarek Jakubec).

DIAMOND EXPLORATION LAB, UBC vpl ubc srk consulting

- The **World Diamond Museum** in London launched a series of webinars in 2022. The first featured Dr Jack Ogden, who presented 'On the Trail of Some Famous Diamonds'. The series will continue through 2022 with talks by various authors who contributed to the book *Diamonds Across Time: Facets of Mankind* (see book review in *The Journal*, Vol. 37, No. 6, 2021, pp. 652–654). Visit https://www.youtube.com/channel/UC0PZeEzBGFqF3HDuiJSClgw.

What's New provides announcements of new instruments/technology, publications, online resources and more. Inclusion in What's New does not imply recommendation or endorsement by Gem-A. Entries were prepared by Carol M. Stockton unless otherwise noted.

An innovator in gemstone reporting

• Identification of colored gemstones • Country of origin determination • Full quality and color grading analysis

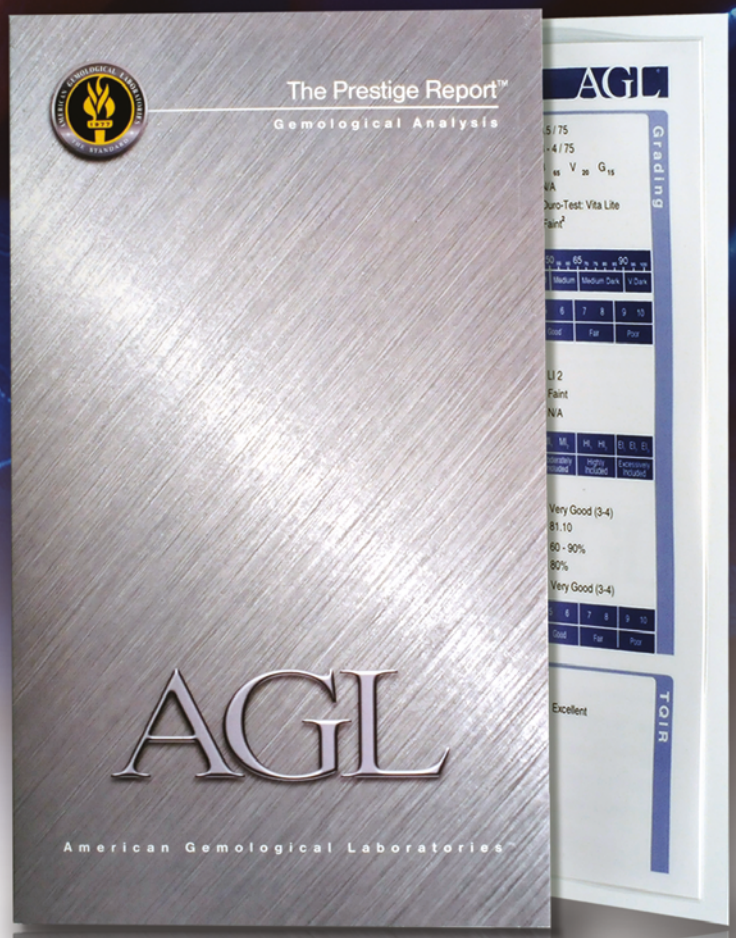

AMERICAN GEMOLOGICAL LABORATORIES AGL

580 5th Ave • Suite 706 • New York, NY 10036, USA
www.aglgemlab.com • +1 (212) 704 - 0727

Gem Notes

COLOURED STONES

Aquamarine from Manakana, Madagascar

Madagascar is well known as a source of aquamarine and other pegmatite-related gem materials (e.g. Pezzotta 2001), but in recent years most gem exploration and mining activities there have been curtailed by circumstances related to the COVID-19 pandemic and government regulations. Nevertheless, according to Dr Federico Pezzotta (pers. comm. 2022), in early 2021 there was a new find of aquamarine (Figures 1 and 2) that entered the market in the capital city of Antananarivo. The material was represented as coming from an area called Manakana, which is the name historically used for the region encompassing the pegmatitic districts on the west side of Lake Alaotra in central Madagascar. In this case, the specific aquamarine locality is Andilana, which is situated near the north-western shore of Lake Alaotra. Hundreds of kilograms of good-quality aquamarine were mined from near-surface deposits by thousands of miners from all over Madagascar who rushed there despite COVID-19 restrictions. In early May, the Malagasy government sent the military to gain control over the situation, and subsequently the export of aquamarine from Madagascar was made illegal.

According to information learned by Dr Pezzotta, as well as photos and videos seen by him, the deposit produced large aquamarine crystals frozen in quartz, as well as etched aquamarine in cavities. Much of it was of high quality and some fine gemmy crystals exceeding 4 kg were produced. The rough material is notable for

Figure 1: This rough aquamarine from a relatively new find at Manakana, Madagascar, weighs about 160 g. Photo courtesy of Dudley Blauwet.

Figure 2: Some of the gems cut from the Manakana aquamarine include (**a**) these faceted stones weighing 2.89–5.37 ct, and (**b**) a 5.15 ct cabochon and a 3.90 ct faceted oval cut that were examined for this report. Photos by (a) Aria Thomas/Dudley Blauwet Gems and (b) C. Williams.

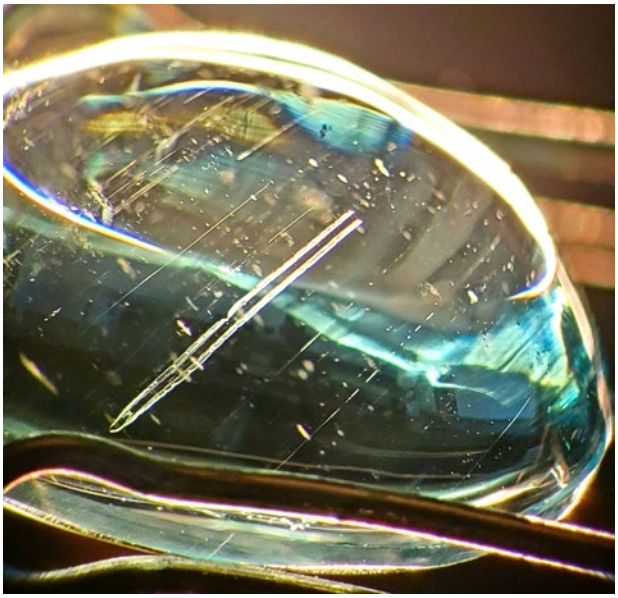

Figure 3: Flattened growth tubes—sometimes with a serrated appearance—are seen in the aquamarine cabochon. Photomicrograph by B. Williams; image width approximately 10 mm.

its attractive blue colour and the relatively large average size of clean stones.

In April 2021, at gem and mineral shows in Tucson, Arizona, USA, Dudley Blauwet (Dudley Blauwet Gems, Louisville, Colorado, USA) was shown three rough parcels of Manakana aquamarine totalling about 1 kg, and subsequently he was offered two large clean rough pieces weighing about 80 and 160 g (e.g. Figure 1). He obtained a 400 g parcel and sent a selection of the pieces to his cutting factory. Most of the resulting faceted gems were in the 1–5 ct range (e.g. Figure 2a). The overall yield was low (around 13%) due to the presence of veils and dark inclusions, as well as the cutting of all the smaller stones as calibrated and matched pairs.

Blauwet loaned two of the polished stones—an oval cabochon weighing 5.15 ct and a faceted oval of 3.90 ct (Figure 2b)—to authors CW and BW for examination of the inclusions. Gemmological data collected on the faceted stone showed RIs of 1.572–1.581 (birefringence 0.009) and a hydrostatic SG of 2.71, consistent with aquamarine. The cabochon contained a parallel array of growth tubes (Figure 3), and both stones hosted black dendritic inclusions (Figure 4) resembling the skeletal ilmenite previously documented in aquamarine (e.g. Gübelin & Koivula 1986, p. 240).

So far, the best faceted stone that Blauwet is aware of weighed 132 ct with excellent colour and minor inclusions. More aquamarine from this find is expected to enter the market as additional material is cut.

Brendan M. Laurs FGA

Cara Williams FGA and Bear Williams FGA
(info@stonegrouplabs.com)
Stone Group Laboratories
Jefferson City, Missouri, USA

References

Gübelin, E.J. & Koivula, J.I. 1986. *Photoatlas of Inclusions in Gemstones*. ABC Edition, Zurich, Switzerland, 532 pp.

Pezzotta, F. 2001. *extraLapis English No. 1: Madagascar—A Mineral and Gemstone Paradise*. M.D. Jarnot, G.A. Neumeier, W.B. Simmons and G.A. Staebler (eds), Lapis International LLC, East Hampton, Connecticut, USA, 98 pp.

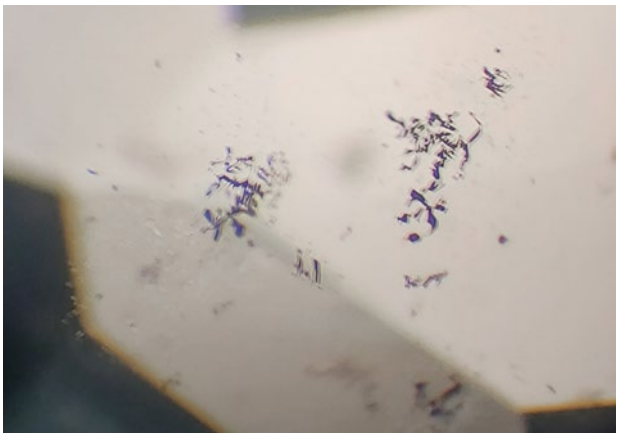

Figure 4: These black dendritic inclusions (probably ilmenite) are present in the faceted aquamarine in Figure 2b. Photomicrograph by C. Williams; image width 4 mm.

Star Augite from Vietnam

Augite is a common and widespread pyroxene mineral that occurs in various rocks (e.g. those of mafic igneous composition, especially basalt and gabbro). However, it is not known to occur in gem quality. In early 2021, during field studies of Cenozoic alkaline basalts associated with alluvial sapphires and other gems in Dong Nai Province, southern Vietnam, the authors found several fractured pieces and whole crystals of augite—and most of them displayed a six-rayed star after cutting. Augite has been previously reported as phenocrysts in Cenozoic basalts of southern Vietnam (Hoang & Flower 1998), but according to the authors' knowledge this is the first time that asterism has been documented in this mineral, notably as pieces large enough for use as gemstones.

Figure 5: A 50.56 ct free-form cabochon of augite from Dong Nai Province, Vietnam, appears (**a**) semi-transparent dark brown in transmitted light, and (**b**) displays a six-rayed star in reflected light. Photos by Le Ngoc Nang.

The sample described here was cut from an irregular piece of rough that weighed 19.6 g. The free-form cabochon weighed 50.56 ct and measured 25.5–24.39 × 8.88 mm. In transmitted light, the stone appeared dark brown and was semi-transparent, while strong illumination from above revealed a white six-rayed star (Figure 5). Standard gemmological testing and Raman spectroscopy were performed at the Liu Gemmological Research and Application Center. The RIs were 1.681–1.703 (taken on the flat base) and the hydrostatic SG value was 3.35. Observation with a polariscope showed the stone was biaxial and strongly pleochroic (in brown and black). It was inert to both long- and short-wave UV radiation.

Examination with a gemmological microscope revealed an abundance of white, straight and curved, silk-like inclusions (Figure 6) that we infer to be magnetite (cf. Bown & Gay 1959), along with 'fingerprints' composed of elongated fluid inclusions. In addition, we observed a set of well-developed twinning planes, which is consistent with augite (cf. Anthony *et al*. 1995). The sample's Raman spectrum included two major peaks at 669 and 1008 cm^{-1}, and four weaker bands at 740, 879, 936 and 1108 cm^{-1}, confirming the stone is augite (cf. Buzatu & Buzgar 2010).

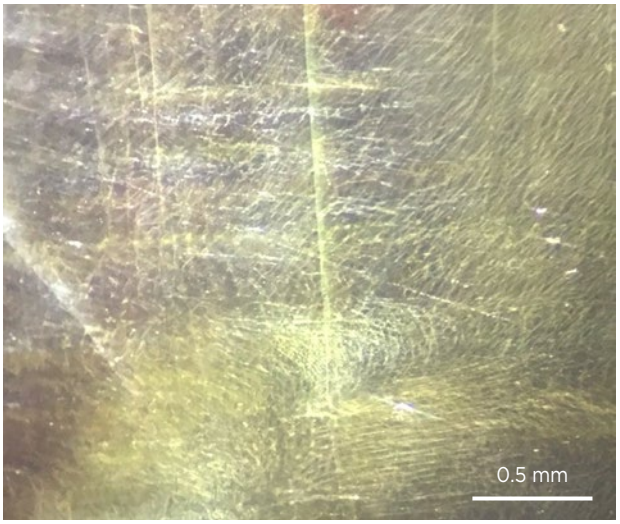

Figure 6: Straight and curved silk-like inclusions (probably magnetite) are responsible for the asterism shown by the augite. The more continuous subvertical lines in this image probably correspond to polysynthetic twin planes. Photomicrograph by Le Ngoc Nang.

The asterism in the augite was produced by light reflecting from clusters of the elongated silk-like inclusions (again, see Figure 6). They were unevenly distributed but arranged in three main orientations, resulting in a six-rayed star composed of relatively broad rays.

The discovery of star augite from Dong Nai adds an intriguing aspect to this common mineral, which has so far received little interest in the gem trade.

LE Ngoc Nang[1,2] (nang@liulab.edu.vn)
and PHAM Minh Tien[2]
[1]University of Science, Vietnam National University
[2]Liu Gemmological Research and Application Center
Ho Chi Minh City, Vietnam

References

Anthony, J.W., Bideaux, R.A., Bladh, K.W. & Nichols, M.C. 1995. *Handbook of Mineralogy*, Vol. 2: Silica, Silicates (Part 1). Mineral Data Publishing, Tucson, Arizona, USA, 446 pp. (see p. 48).

Bown, M.G. & Gay, P. 1959. The identification of oriented inclusions in pyroxene crystals. *American Mineralogist*, **44**(5–6), 592–602.

Buzatu, A. & Buzgar, N. 2010. The Raman study of single-chain silicates. *Analele Ştiinţifice ale Universităţii "Al. I. Cuza" Iaşi*, **56**(1), 107–125.

Hoang, N. & Flower, M. 1998. Petrogenesis of Cenozoic basalts from Vietnam: Implication for origins of a 'diffuse igneous province'. *Journal of Petrology*, **39**(3), 369–395, https://doi.org/10.1093/petroj/39.3.369.

Crocoite from Tasmania, Australia

Crocoite ($PbCrO_4$) was first found in Russia in 1763, later in a few European localities, and then in Australia (Tasmania) and Brazil. At one time it was the main ore of chromium, and it has also been used as a yellow pigment, such as in Van Gogh's paintings and on school buses. To the mineral collector, Tasmanian crocoite surpasses others because the specimens occur as well-formed crystals, and they are larger and more abundant than at any other locality. The (monoclinic) crystals are elongated and prismatic, and almost always vertically striated with a nearly square outline. They most often form reticulated aggregates and acicular groups; less commonly they occur as individual prismatic crystals that are sometimes partially hollow. Although crocoite possesses a remarkably saturated orange to orange-red colour, it is unknown to most gemmologists since its low hardness (Mohs 2½–3) relegates it to a collectors' stone. Crocoite's colour can fade to brown or even black over a long period (i.e. a century) if exposed to light, as observed in Van Gogh's paintings (Tan *et al*. 2013) and in some mineral specimens (Grguric 2015).

The 0.35 ct crocoite gemstone described here (Figure 7) is reportedly from Tasmania (i.e. possibly from the Adelaide or Red Lead mines in Dundas, Zeehan District). The following properties were recorded: colour—orange; pleochroism—weak orange and orange-red (sometimes described as trichroic since the mineral is biaxial); lustre—vitreous to sub-adamantine; diaphaneity—transparent; RI—over the limits of a standard refractometer; birefringence—strong (estimated by facet-edge doubling as 0.35); hydrostatic SG—6.0; magnetism—inert to an N52 neodymium magnet; Chelsea Colour Filter reaction—red; and fluorescence—inert to long- and short-wave UV radiation. These data are consistent with those previously published for crocoite (O'Donoghue 2006, who also reported RIs of 2.29–2.66 and a biaxial positive optic character). Microscopic examination revealed long thin growth tubes aligned parallel to the stone's length (likely the prism axis), very small negative crystals and a reflective partially healed fracture.

Figure 7: This 0.35 ct crocoite (3.9 × 2.8 × 2.1 mm), reportedly from Tasmania, exhibits an attractive vivid orange colour. Near the bottom, a partially healed fracture is visible as a dark elongated area. Photo by T. Cathelineau.

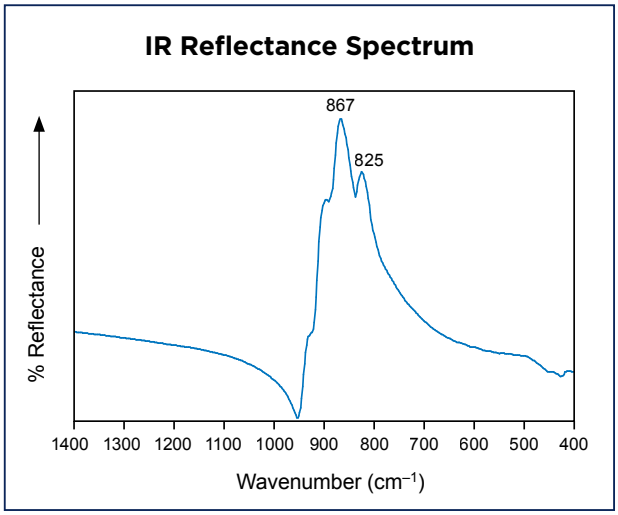

Figure 8: The IR reflectance spectrum of the stone in Figure 7 is representative of crocoite, and is characteristic of a chromate anion with dominant bands due to ν_3 asymmetric stretching vibrations in the 800–950 cm^{-1} range (Campbell 1965).

Infrared reflectance spectra were collected from several orientations of the stone's table, and all yielded essentially the same pattern (Figure 8), which is comparable with published spectra of crocoite from Russia (Chukanov 2014; Cr6 sample after log(1/T) transformation) and Tasmania (author's database: www.spec4gem.info/index.php/databases/irs/100).

A Raman spectrum (Figure 9) was collected from the gem's table with a homemade Raman spectrometer using a 638 nm LED laser without any polarisation consideration. The resulting spectrum was consistent with published crocoite spectra (e.g. Wilkins 1971; RRUFF R160016).

Visible-near infrared (Vis-NIR) spectra were collected over the 360–1000 nm range (Figure 10; cropped to 400–800 nm) with the help of a polarising filter oriented to obtain the maxima corresponding to the observed pleochroic colours: orange and orange-red. The two spectra showed very strong absorption in the violet, blue and green regions, with a remarkably steep absorption edge between 570 and 620 nm (the strength of which surpassed the capacities of the spectrophotometer), and no other features above 650 nm. The

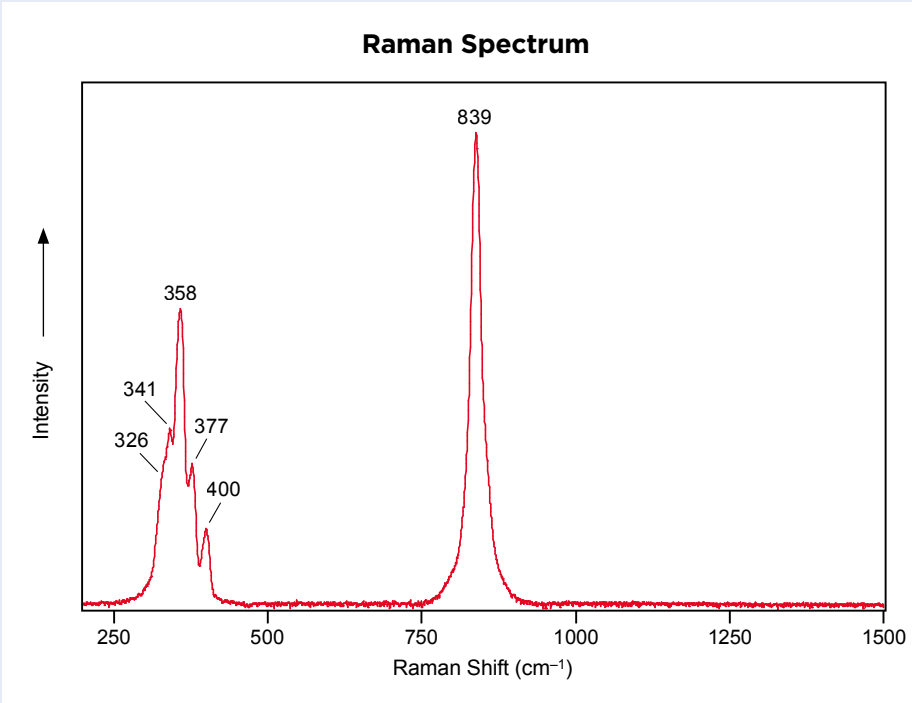

Figure 9: The Raman spectrum of the stone in Figure 7 is also representative of crocoite. The bands at 326, 341, 358, 377 and 400 cm^{-1} are produced by ν_2 and ν_4 bending vibrations, while the 839 cm^{-1} (multicomponent) band results from ν_1 and ν_3 stretching vibrations in the CrO_4^{2-} anion (Wilkins 1971).

absorption edge bordered, respectively, the transmission in the yellow and the red regions, which explains the observed colours; the shift between the two represents the pleochroism. Such a strong absorption is often associated with oxygen-metal charge transfer, in this case $O^{2-} \rightarrow Cr^{6+}$ within the CrO_4^{2-} anion (Loeffler & Burns 1976). Unlike some published spectra (Reddy & Sarma 1981), there was no band at about 605 nm.

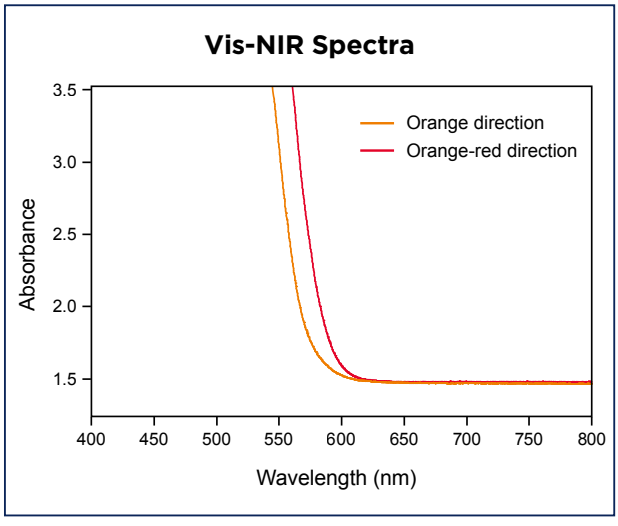

Figure 10: Polarised Vis-NIR spectra of the crocoite display a strong absorption over the violet-to-yellow range, with a remarkably steep absorption edge causing the orange and orange-red pleochroic colours. The path length of the beam was about 2.0 mm.

Crocoite has sometimes been described as fluorescent (O'Donoghue 2006) or as showing deep red luminescence, with a broad band peaking at about 700 nm (RFUFF R040053, 532 nm broad-scan spectrum) or 750 nm (with 337 nm excitation at liquid-nitrogen temperature; Gorobets & Rogojine 2002). Photoluminescence spectra of the present sample were collected using 254, 280, 375, 405 and 532 nm excitations, but none showed any luminescence. Similarly, none was observed in the Raman spectrum.

(*Author's note*: Crocoite is toxic, as it contains both lead and hexavalent chromium, so it is important to avoid breathing its dust and to wash hands after handling it.)

Thierry Cathelineau
(thierry.cathelineau@spec4gem.info)
Paris, France

References

Campbell, J.A. 1965. Spectral evidence for interionic forces in crystals—Chromates and dichromates. *Spectrochimica Acta*, **21**(7), 1333–1343, https://doi.org/10.1016/0371-1951(65)80215-6.

Chukanov, N.V. 2014. *Infrared Spectra of Mineral Species*. Springer, Dordrecht, Germany, 1,726 pp., https://doi.org/10.1007/978-94-007-7128-4.

Gorobets, B.S. & Rogojine, A.A. 2002. *Luminescent Spectra of Minerals*. RCP VIMS, Moscow, Russia, 300 pp.

Grguric, B. 2015. The light sensitivity of crocoite. https://www.mindat.org/article.php/2252/The+Light+Sensitivity+of+Crocoite, 13 August, accessed 3 February 2022.

Loeffler, B.M. & Burns, R.G. 1976. Shedding light on the color of gems and minerals. *American Scientist*, **64**(6), 636–647.

O'Donoghue, M. (ed) 2006. *Gems*. Butterworth-Heinemann, Oxford, 873 pp.

Reddy, B.J. & Sarma, K.B.N. 1981. Optical properties of chromate centres in crocoite. *Physics Letters A*, **86**(6–7), 386–388, https://doi.org/10.1016/0375-9601(81)90564-8.

Tan, H., Tian, H., Verbeeck, J., Monico, L., Janssens, K. & Van Tendeloo, G. 2013. Nanoscale investigation of the degradation mechanism of a historical chrome yellow paint by quantitative electron energy loss spectroscopy mapping of chromium species. *Angewandte Chemie International Edition*, **52**(43), 11360–11363, https://doi.org/10.1002/anie.201305753.

Wilkins, R.W.T. 1971. The Raman spectrum of crocoite. *Mineralogical Magazine*, **38**(294), 249–250, https://doi.org/10.1180/minmag.1971.038.294.15.

Hexagonal Growth Structures Displaying *Gota de Aceite* Effect in Colombian Emerald

Figure 11: This 1.27 ct emerald cabochon revealed some unusual internal features when examined with a microscope. Photo by Kaiyin Deng.

In September 2021, Guild Gem Laboratories examined a 1.27 ct green cabochon (Figure 11), which was identified as emerald by standard gemmological testing (RI of approximately 1.57 and hydrostatic SG of 2.70). Ultraviolet-visible (UV-Vis) spectroscopy and energy-dispersive X-ray fluorescence (EDXRF) analysis revealed low Fe and relatively high Cr, consistent with the composition of Colombian emeralds.

The *c*-axis was determined to be perpendicular to the base of the cabochon using a polariscope and conoscope. Microscopic observation down the *c*-axis showed hexagonal growth structures with clear outlines (Figure 12). These growth structures were composed of three main parts: a dark green rim, a medium green transition area, and a lighter green core, as diagrammed in Figure 13.

In addition, the *gota de aceite* ('oil drop', or roiled appearance) phenomenon was present within the dark green and medium green hexagonal structures. Closer examination showed three smaller sub-areas of hexagonal zoning (again, see Figures 12 and 13). The smallest of these hexagonal sub-zones was light green, while the two larger ones displayed a more saturated green colour, comparable with colour trends noted previously in emerald (Ringsrud 2008; Gao *et al.* 2017). Two of the sub-zones were parallel to the outer hexagonal prism of the host crystal, while the third was rotated by 30° (Figure 13), also consistent with the crystal habit of beryl.

We deduce that this emerald formed by the simultaneous growth of several hexagonal prisms proceeding in the same direction parallel to the *c*-axis. Various factors

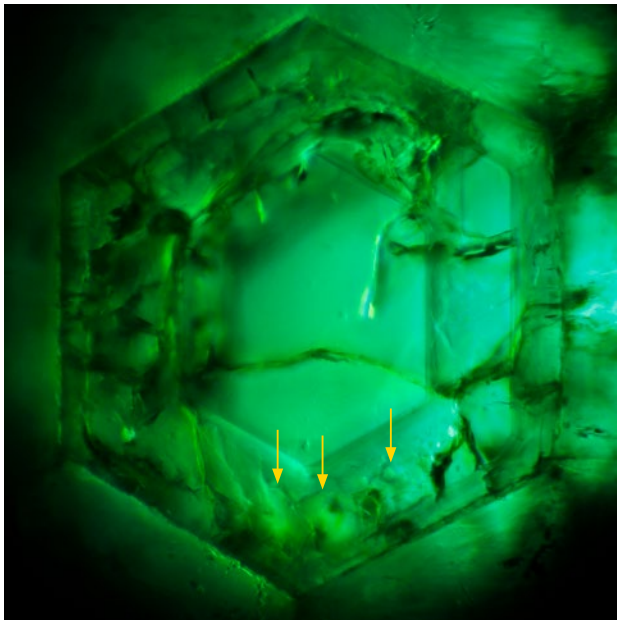

Figure 12: Viewed along the *c*-axis, the emerald displays hexagonal growth structures that locally contain the *gota de aceite* phenomenon within the outer zones. In addition, the locations of three smaller hexagonal sub-zones (diagrammed in Figure 13) are indicated by arrows. Photomicrograph by Xueying Sun; image width 2.24 mm.

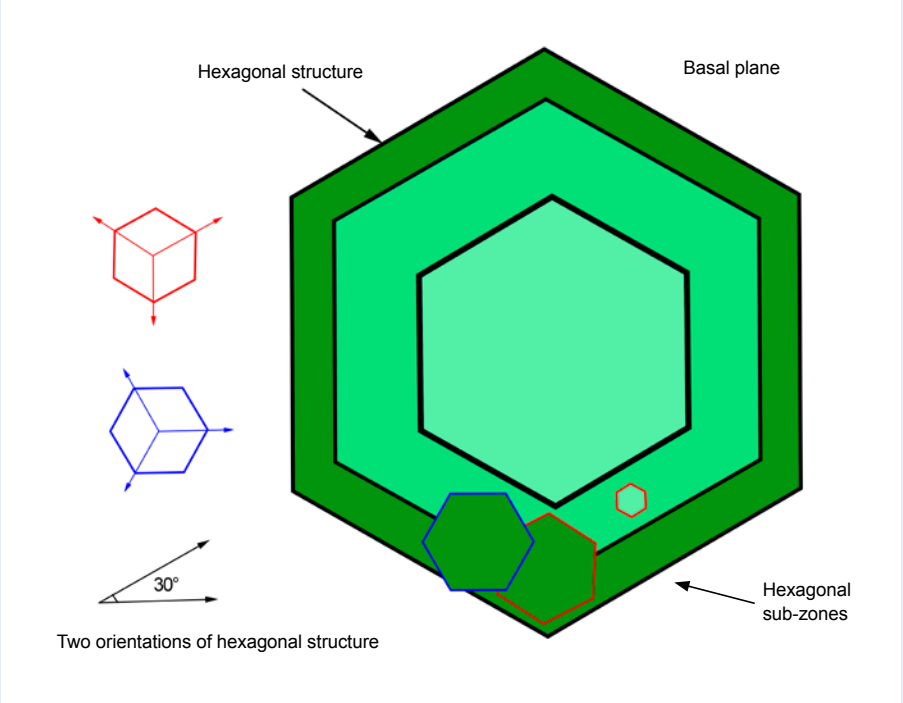

Figure 13: This diagram shows the hexagonal growth structures in the emerald corresponding to the view in Figure 12. The *gota de aceite* phenomenon is restricted to the two outer (dark green and medium green) hexagonal growth structures. The angle between the two orientations of hexagonal sub-zones is 30°. Drawing by Xueying Sun.

such as differential growth rate, the supply of nutrients and the particular conditions during emerald crystallisation may have given rise to the interesting growth disturbances in this emerald.

Xueying Sun and Yujie Gao
(peter.gao@guildgemlab.com)
Guild Gem Laboratories
Shenzhen, China

References

Gao, Y., Carmona, C. & Lin, Q. 2017. "Gota de aceite" effect in emerald: Observation and cause. *Gems & Technology 2017*, Beijing, China, 95–97.

Ringsrud, R. 2008. *Gota de aceite*: Nomenclature for the finest Colombian emeralds. *Gems & Gemology*, **44**(3), 242–245, https://doi.org/10.5741/GEMS.44.3.242.

Iolite from the Czech Republic

Transparent and pleochroic in shades of violet-blue to blue, yellow and colourless, cordierite is sometimes used as a gemstone (i.e. iolite). Cordierite, $Mg_2Al_4Si_5O_{18}$, is the Mg-rich end member of a series with sekaninaite (Fe-rich end member). These minerals have long been the subject of systematic research in the Bohemian Massif (e.g. Černý & Povondra 1966; Povondra *et al.* 1992; Hanus *et al.* 2016). Samples of gem-quality cordierite were recently found during mineralogical research in the central Moldanubian pluton, at the Vanov quarry near Telč in the central part of Moldanubicum Zone. This quarry is located about 300 m north-west of Vanov village and is actively being mined for aggregate by the company Colas CZ a.s.

Cordierite-biotite paragneisses with intensive migmatisation (streaked and veined with granitic rock)—typical for the eastern rim of the central Moldanubian pluton—are predominant in the general area. The most abundant rocks in the quarry are layered migmatites, with less-frequent massive migmatites and agmatites (migmatites containing xenoliths). Quartzites, calc-silicate rocks and amphibolites are occasionally present (René 2010). Cordierite occurs in leucosomes within migmatite, and altered aggregates of cordierite have been less frequently found in simple pegmatites.

Gem-quality cordierite from Vanov is characterised by vitreous lustre and an overall violetish blue colour, and it is only very rarely altered to microscopic sec-

Figure 14: Three iolites (0.09–0.10 ct) from Vanov quarry, Czech Republic, were faceted for this study. They were cut from material kindly provided by Václav Krčal. Photo by Ľubomír Kyrc.

ondary phyllosilicates (mostly chlorite and biotite). Chemical analyses by electron probe microanalysis (EPMA; 17 analytical points on two polished thin sections) revealed an average content of 1.14 apfu Mg, 0.80 apfu Fe, 0.02 apfu Mn and 0.06 apfu Na. In addition, laser ablation inductively coupled plasma mass spectrometry (LA-ICP-MS) of one sample (11 points across a grain mount) showed the presence of Ca, Rb, F, Li and Be (all <0.07 apfu).

For this study, we faceted three round-brilliant cuts (Figure 14) with the following diameters and weights: 2.94 mm (0.09 ct), 3.04 mm (0.10 ct) and 3.07 mm (0.10 ct). Viewed face up, they showed a characteristic violetish blue hue with very slightly greyish saturation and a tone ranging from medium to dark. They were characterised by strong pleochroism in blue and yellow. The gemmological properties were consistent with iolite: RIs of 1.529–1.539 (birefringence 0.010) and a hydrostatic SG ranging from 2.63 to 2.77. Microscopic examination revealed platelets of biotite (confirmed by EPMA) and planar fluid inclusions that were mainly present in a single orientation (Figure 15). The samples' identity as cordierite was confirmed by Raman spectroscopy, which showed bands at 258, 300, 365, 572, 672, 919, 972, 1183 and 1383 cm^{-1}. A band due to CO_2 vibrations in cordierite was also observed at 1383 cm^{-1} (Culka *et al.* 2016; Figure 16). UV-Vis spectroscopy showed absorptions at 436, 456, 492, 544, 585, 593 and 610 nm (Figure 17), and the broad feature centred at about 600 nm is consistent with Fe^{2+}–Fe^{3+} intervalence charge transfer, which is the main cause of colour in iolite (http://minerals.caltech.edu/files/visible/cordierite).

To the authors' knowledge, this is the first description of gem-quality cordierite from the Czech Republic (although facetable sekaninaite was documented previously by Hanus *et al.* 2016). Because it only rarely occurs in the Vanov quarry, it is unlikely that commercial quantities of this iolite will be produced in the future. Still, additional material could be found as mining operations continue.

Sebastián Hreus[1,2] and Prof. Milan Novák[1]
[1]Department of Geological Sciences, Masaryk University, Brno, Czech Republic
[2]Institute of Geosciences, Technical University of Košice, Slovakia

Dr Ján Štubňa (janstubna@gmail.com)
Gemmological Laboratory, Constantine the Philosopher University, Nitra, Slovakia

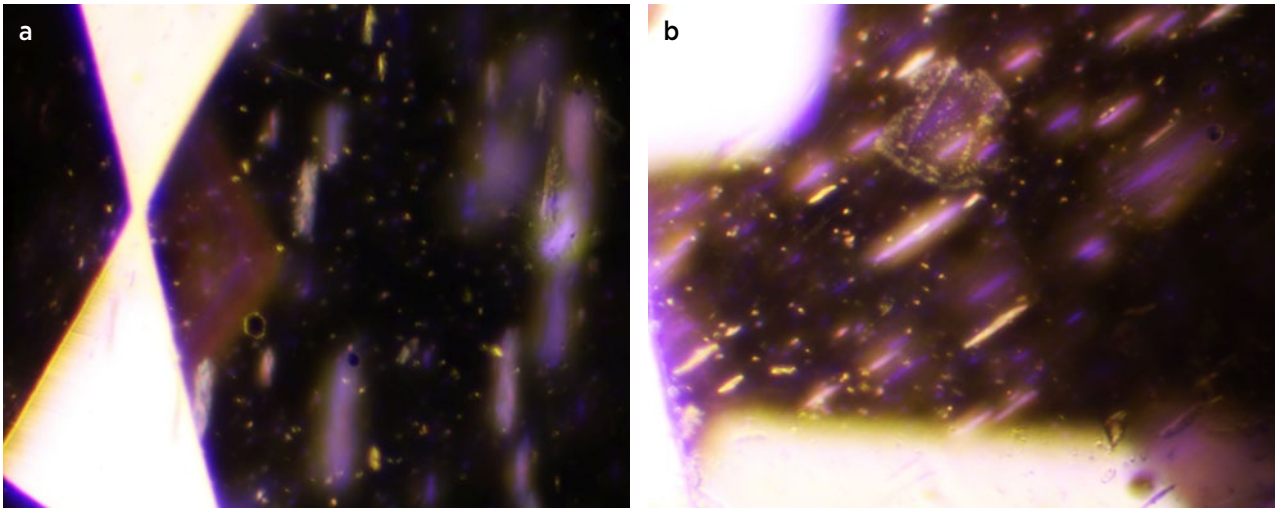

Figure 15: Internal features observed in the Vanov iolite samples include (**a**) biotite platelets and (**b**) oriented planar fluid inclusions. Photomicrographs by J. Štubňa; magnified 50×.

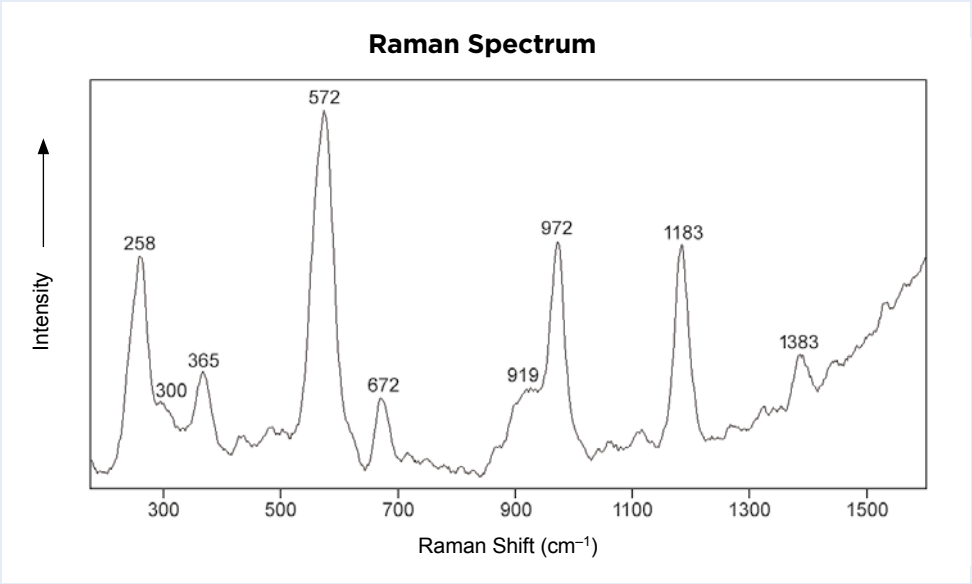

Figure 16: Raman spectroscopy of a Vanov iolite shows characteristic peaks for cordierite at 258, 300, 365, 572, 672, 919, 972 and 1183 cm^{-1}. The band at 1383 cm^{-1} is associated with CO_2 vibrations in channels within the cordierite structure.

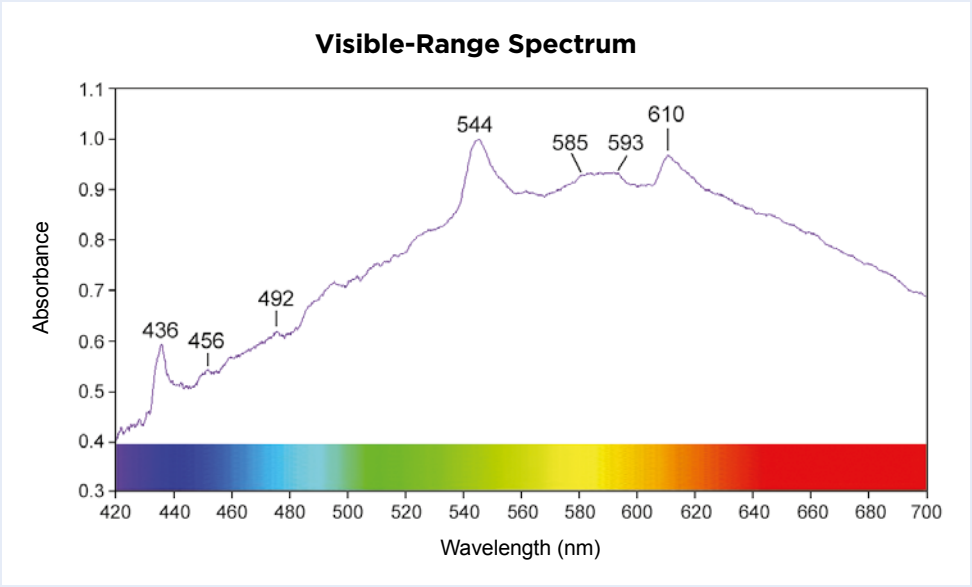

Figure 17: A representative visible-range spectrum of a violet-blue iolite from Vanov shows absorption bands at about 436, 456, 492, 544, 585, 593 and 610 nm. The path length of the beam was about 2.0 mm.

References

Černý, P. & Povondra, P. 1966. Beryllian cordierite from Věžná: (Na,K)+Be→Al. *Neues Jahrbuch für Mineralogie, Monatshefte*, **44**, 36–44.

Culka, A., Hyršl, J. & Jehlička, J. 2016. Gem and mineral identification using GL Gem Raman and comparison with other portable instruments. *Applied Physics A*, **122**(11), 1–9, https://doi.org/10.1007/s00339-016-0500-2.

Hanus, R., Kusá, I. & Kasíková, J. 2016. Gem-quality sekaninaite from the Czech Republic. *Journal of Gemmology*, **35**(2), 148–154, https://doi.org/10.15506/JoG.2016.35.2.148.

Povondra, P., Staňková, J. & Staněk, J. 1992. CO_2-bearing cordierite of Moldanubian leptynite rock series from Horní Bory, Czech Republic. *Acta Universitatis Carolinae, Geologica*, **3–4**, 331–349.

René, M. 2010. Petrografie a Geochemie Migmatitů z Lomu Vanov u Telče [Petrography and geochemistry of migmatites from the Vanov quarry near Telče]. *Geologické výzkumy Moravy a Slezska*, **17**(1–2), 162–165.

Sailboat-like Inclusion in Ruby from China

Marble-hosted rubies from Mogok (Myanmar) are world renowned for their high quality, particularly their bright red colouration. However, other localities such as Afghanistan, Tajikistan, Vietnam and China are known to produce rubies of the same petrogenetic type (Garnier *et al*. 2008). These rubies often host multiphase inclusions consisting of solid, liquid and/or gas phases. The paleo-fluids trapped in these cavities represent remnants of the growth medium. Previous studies have revealed that the multiphase inclusions are CO_2-dominated, with minor components such as COS, H_2S and native sulphur (Giuliani *et al*. 2015; Huang *et al*. 2022). In addition, H_2O is inferred to have been present in the paleo-fluids, although it cannot be observed directly in the inclusions.

The authors recently examined a ruby from the marble-hosted deposit at Yuanjiang in south-central Yunnan Province, China, that was of particular interest because it contained a multiphase inclusion resembling a sailboat (Figure 18). What makes this inclusion notable is that the sailboat it mimics has special meaning in China, where it symbolises smooth sailing (*yi fan feng shun* in Chinese, being analogous to the meaning of 'roses all the way' in the West). In China, the sailboat is traditionally used as a subject of carvings made from various gem materials (e.g. nephrite, jadeite and serpentine).

Further microscopic examination revealed this inclusion to be composed of liquid and gas phases, as well as a tabular transparent crystal. Raman spectroscopy—using a confocal Horiba LabRAM HR Evolution spectrometer coupled to an Olympus BX51 microscope, together with 473 nm laser excitation and a 100× objective—identified the tabular crystal as diaspore (Figure 19). Diaspore is a common constituent of fluid inclusions in Asian rubies (Garnier *et al*. 2008) and in Sri Lankan sapphires (Schmetzer & Medenbach 1988). It is regarded as a daughter mineral formed during the cooling of fluid inclusions via a reaction between the corundum host and water in the inclusion cavity (Schmetzer & Medenbach 1988; Huang *et al*. 2022).

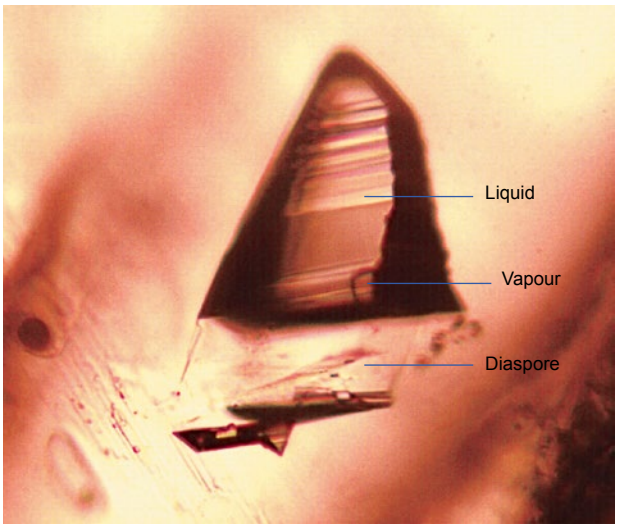

Figure 18: This sailboat-like multiphase inclusion is contained within a ruby from a marble-hosted deposit in Yuanjiang, China. Photomicrograph by T. Shui; image width 0.23 mm.

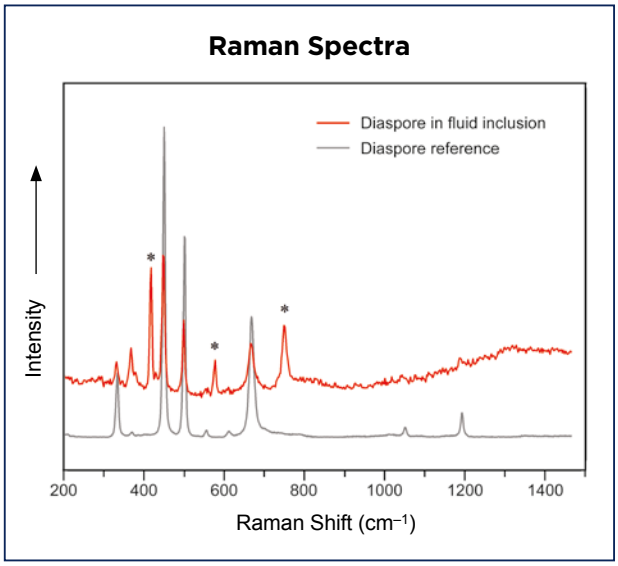

Figure 19: Raman spectroscopy of the transparent crystal within the inclusion shown in Figure 18 yielded a spectrum consisting of several bands from the corundum matrix (marked by asterisks) along with signals corresponding to the vibrations of diaspore. Also shown for comparison is a diaspore reference spectrum from the RRUFF database.

The micro-world of gem materials is especially fascinating when inclusion scenes present distinctive patterns, as shown by this sailboat-like example. In addition, the presence of diaspore in this multiphase inclusion is consistent with marble-hosted rubies from China and elsewhere in Asia (e.g. Huang 2021).

Prof. Ting Shui
Nanjing Center, China Geological Survey
Nanjing, China

Dr Wenqing Huang (67019822@qq.com)
National Center of Supervision and Inspection on Quality of Gold and Silver Products
Nanjing Institute of Product Quality Inspection
Nanjing, China

References

Garnier, V., Giuliani, G., Ohnenstetter, D., Fallick, A.E., Dubessy, J., Banks, D., Vinh, H.Q., Lhomme, T. *et al.* 2008. Marble-hosted ruby deposits from Central and Southeast Asia: Towards a new genetic model. *Ore Geology Reviews*, **34**(1–2), 169–191, https://doi.org/10.1016/j.oregeorev.2008.03.003.

Giuliani, G., Dubessy, J., Banks, D.A., Lhomme, T. & Ohnenstetter, D. 2015. Fluid inclusions in ruby from Asian marble deposits: Genetic implications. *European Journal of Mineralogy*, **27**(3), 393–404, https://doi.org/10.1127/ejm/2015/0027-2442.

Huang, W. 2021. *G&G* Micro-World: Fascinating fluid inclusions in Chinese ruby. *Gems & Gemology*, **57**(3), 272–273.

Huang, W., Ni, P., Zhou, J., Shui, T., Pan, J., Fan, M. & Yang, Y. 2022. Fluid inclusion and titanite U-Pb age constraints on the Yuanjiang ruby mineralization in the Ailao Shan-Red River metamorphic belt, southwest China. *Canadian Mineralogist*, **60**, 1–26, https://doi.org/10.3749/canmin.2100009.

Schmetzer, K. & Medenbach, O. 1988. Examination of three-phase inclusions in colorless, yellow, and blue sapphires from Sri Lanka. *Gems & Gemology*, **24**(2), 107–111, https://doi.org/10.5741/gems.24.2.107.

Raman Spectroscopy of Zircon Inclusions in Unheated Pink Sapphires from Ilakaka, Madagascar: Opening New Perspectives

Most high-quality pink sapphires on the market today come from Ilakaka, Madagascar, and can sometimes exceed 10 ct (Figure 20). Heat treatment under various conditions has been used to improve their colour, in order to remove or decrease their violet-to-purple (and sometimes brown) tint and reveal their pink appearance (Wang *et al.* 2006; Saeseaw *et al.* 2020). Pink sapphires from Ilakaka frequently contain zircon and, less commonly, monazite inclusions, from several to more than 100 µm in dimension (Figure 21). Heat treatment performed at relatively high temperature can be identified by using a microscope to visually observe the alteration of the zircon and monazite inclusions, as well as by using techniques such as Raman microanalysis of these inclusions or Fourier-transform infrared (FTIR) spectroscopy of the host sapphire. However, heat treatment at relatively low temperature (<1000°C) gives very little indication when the inclusions are viewed with a microscope, and identification can only be done by spectroscopic means (Saeseaw *et al.* 2020).

Band broadening—that is, an increase in the full width at half maximum (FWHM)—of the anti-symmetric stretching vibration (ν_3) of SiO_4 in zircon near 1000 cm^{-1}, as measured by Raman spectroscopy, can be used to estimate the degree of structural (radiation) damage. Nasdala *et al.* (1995) suggested that a FWHM of <5 cm^{-1} corresponds with well-crystallised ('high') zircon, while a FWHM over 30 cm^{-1} is found in structurally damaged ('low') zircon. The FWHM reported in the literature for zircon inclusions in unheated pink sapphires from Ilakaka varies from 10.1–13.5 cm^{-1} (average of 11.5 cm^{-1}; Wang *et al.* 2006) to 8.8–13.8 cm^{-1} (Saeseaw *et al.* 2020) and 7.5–17.6 cm^{-1} (median value below 10 cm^{-1}; Krzemnicki *et al.* 2021). By comparison, the FWHM reported in the literature for zircon inclusions in heat-treated pink sapphires from Ilakaka averages 8.7 cm^{-1} for samples heated to 1400°C (Wang *et al.* 2006) and from 6.6 to 12.7 cm^{-1} for samples heated to 1000°C (Saeseaw *et al.* 2020). The importance of the spatial and spectral resolutions when making these measurements was recently revealed by Karampelas *et al.* (2022), who analysed more than 100 zircon inclusions in 15 unheated purplish

Figure 20: These five pink sapphires, reportedly unheated and from Ilakaka, Madagascar, range from 4.15 to 10.75 ct. Composite photo by U. Hennebois.

Figure 21: A 0.34 ct unheated purplish pink sapphire from Ilakaka examined for this study contains transparent colourless zircon inclusions of various shapes and sizes that occur as isolated grains and in clusters. Photomicrograph by U. Hennebois; image width 3 mm.

pink sapphires from Ilakaka. The resulting FWHM varied from 7.1 to 21.7 cm^{-1} with a median value of 11.3 cm^{-1} and an average of 11.6 cm^{-1}.

Additional data were recently collected at the Laboratoire Français de Gemmologie (LFG) on unheated samples of known Ilakaka origin that were collected by one of the authors (VP). The analyses were done with the same instrumentation and conditions used by Karampelas *et al.* (2022): a Renishaw inVia Raman spectrometer with a 514 nm DPSS laser, about 10 mW laser power on the sample, a 50× long-working-distance objective lens, confocal mode (20 µm entrance slit), a grating of 1,800 grooves/mm and about 1.5 cm^{-1} spectral resolution. In one purplish pink rough sapphire, the FWHM of the zircon band ranged from 7.2 to 16.1 cm^{-1}, and within a single zircon inclusion it varied from 8.2 to 16.1 cm^{-1} (Figure 22). These differences in FWHM indicate significant heterogeneous radiation damage (Zeug *et al.* 2017). Such zoning was also illustrated by Elmaleh *et al.* (2015) in cathodoluminescence (CL) images of zircon inclusions in sapphires from the same region. Our preliminary studies of zircon inclusions in heated samples do not show large variations in their FWHM values, because heat treatment leads to structural reconstitution and a decrease in FWHM.

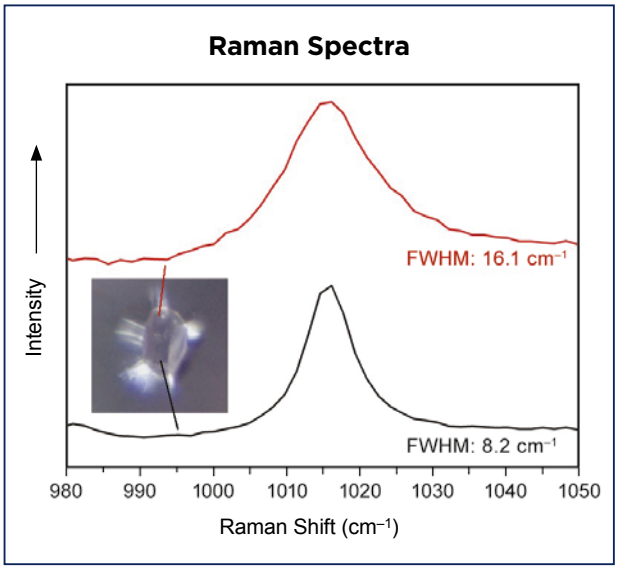

Figure 22: Raman spectra in the range 980–1050 cm^{-1} from a single zircon inclusion in the unheated sapphire show that the main Raman band is broader (FWHM about 16.1 cm^{-1}) at one end compared with the spectrum taken at the other end (FWHM about 8.2 cm^{-1}) of the inclusion. Photomicrograph by U. Hennebois; image width 100 µm.

Raman spectroscopy of zircon inclusions in pink sapphires from Ilakaka is used by gemmological laboratories as an additional tool to separate heated from non-heated samples. The parameters used for such analyses have an important effect, and published results should be used with caution. In this note, for the first time, significant variations in FWHM are reported for a single zircon inclusion in a pink sapphire from this region. Additional studies with CL will help to better explain the phenomenon. Similar variations may also be present in monazite inclusions. The zonation within individual zircon inclusions, as well as variations in FWHM for zircon inclusions in the same sample, are much less pronounced in heated samples, so this might provide additional evidence for separating unheated from heated pink sapphires from Ilakaka. Our research is ongoing and will be published in a full article in the future.

Dr Stefanos Karampelas (s.karampelas@lfg.paris), Ugo Hennebois and Aurélien Delaunay
LFG, Paris, France

Vincent Pardieu
VP Consulting, Manama, Bahrain

Dr Jean-Yves Mevellec FGA and Prof. Emmanuel Fritsch FGA
IMN-CNRS and University of Nantes, France

References

Elmaleh, E., Karampelas, S., Smith, S.T. & Galster, F. 2015. Zircon inclusions in blue sapphires. *34th International Gemmological Conference*, Vilnius, Lithuania, 26–30 August, 51–52.

Karampelas, S., Hennebois, U., Mevellec, J.-Y., Pardieu, V., Delaunay, A. & Fritsch, E. 2022. Identification of heated pink sapphires from Ilakaka (Madagascar). *The 7th International Gem & Jewelry Conference* (GIT2021), Chanthaburi, Thailand, 2–3 February, 212.

Krzemnicki, M.S., Lefèvre, P., Zhou, W. & Wang, H.A.O. 2021. Zircon inclusions in unheated pink sapphires from Ilakaka, Madagascar: A Raman spectroscopic study. *Online International Gemmological Conference (IGC 2021)*, 20–21 November, 21–23.

Nasdala, L., Irmer, G. & Wolf, D. 1995. The degree of metamictization in zircon: A Raman spectroscopic study. *European Journal of Mineralogy*, **7**(3), 471–478, https://doi.org/10.1127/ejm/7/3/0471.

Saeseaw, S., Khowpong, C. & Vertriest, W. 2020. Low-temperature heat treatment of pink sapphires from Ilakaka, Madagascar. *Gems & Gemology*, **56**(4), 448–457, https://doi.org/10.5741/gems.56.4.448.

Wang, W., Scarratt, K., Emmett, J.L., Breeding, C.M. & Douthit, T.R. 2006. The effects of heat treatment on zircon inclusions in Madagascar sapphires. *Gems & Gemology*, **42**(2), 134–150, https://doi.org/10.5741/gems.42.2.134.

Zeug, M., Rodríguez Vargas, A.I. & Nasdala, L. 2017. Spectroscopic study of inclusions in gem corundum from Mercaderes, Cauca, Colombia. *Physics and Chemistry of Minerals*, **44**(3), 221–233, https://doi.org/10.1007/s00269-016-0851-4.

Spessartine from Tongbei, China

Figure 23: These spessartines from Tongbei, Fujian Province, China (0.56–1.04 ct) were faceted and examined for this study. Photo by J. Štubňa.

Spessartine makes an attractive gem material due to its bright orange colour (caused by Mn^{2+}), high RI (1.81) and reasonably high hardness (Mohs 7½). Over the past three decades, several deposits have been discovered worldwide (e.g. in Namibia, Mozambique, Nigeria, China and Madagascar), and spessartine gems are readily found in the trade.

In late 2001, mineral specimens consisting of spessartine with smoky quartz and feldspar appeared on the market from a deposit in Tongbei, near Yunxiao, Fujian Province, China (e.g. Ottens 2005). This spessartine continues to be commonly available, but to the authors' knowledge it has not been documented in the gemmological literature. In June 2018, the authors obtained some rough spessartine from this locality at the Sainte-Marie-aux-Mines gem and mineral show, consisting of 40 pieces (30 g total) of gem-quality samples that measured up to 1 cm in diameter. For this study, we faceted three round-brilliant gemstones (5.27, 5.46 and 6.06 mm in diameter; 0.74, 0.86 and 0.84 ct, respectively), two triangular brilliant cuts (6.69 and 5.42 mm across; 1.04 and 0.56 ct, respectively) and one oval brilliant cut (6.06 × 4.51 mm; 0.79 ct; Figure 23).

The gemmological properties were consistent with spessartine, with the RI ranging from 1.805 to 1.810 and a hydrostatic SG of 4.04–4.13. All stones were inert to both long- and short-wave UV radiation. Microscopic examination revealed mainly fluid inclusions and growth structures (Figure 24), as well as

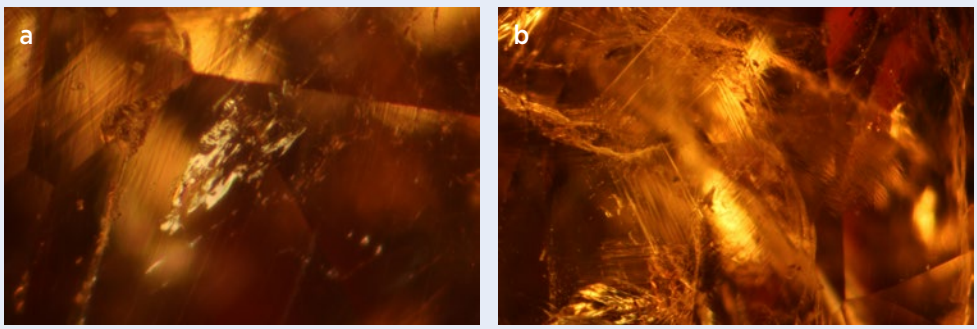

Figure 24: Internal features observed in the Tongbei spessartines include (**a**) fluid inclusions and (**b**) rhombic growth structures. Photomicrographs by J. Štubňa; magnified 40× (a) and 20× (b).

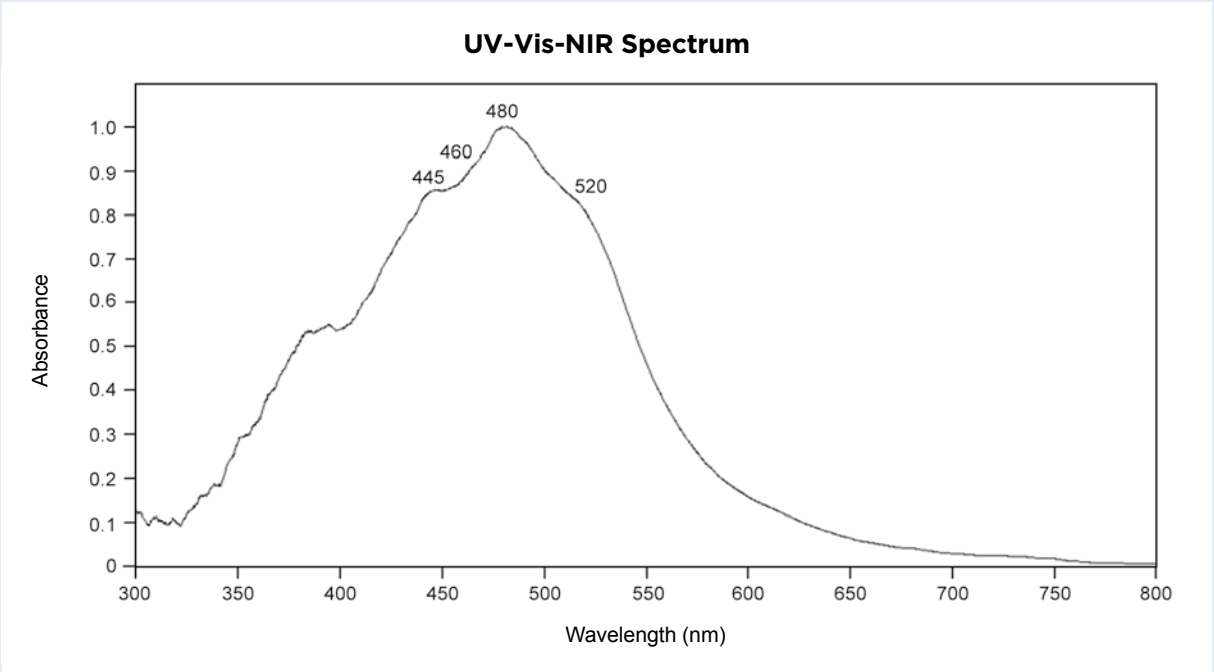

Figure 25: This representative UV-Vis-NIR spectrum of Tongbei spessartine shows absorptions at approximately 445, 460, 480 and 520 nm that are characteristic of Mn^{2+} in garnet. The path length of the beam was about 3.6 mm.

anomalous lamellar birefringence when viewed with crossed polarisers. The samples' identity as spessartine was confirmed using Raman spectroscopy, which showed bands at 222, 348, 469, 555, 631, 732, 904 and 1020 cm^{-1}. UV-Vis-NIR spectroscopy with a GL Gem Spectrometer revealed a series of absorptions at approximately 445, 460, 480 and 520 nm (Figure 25). These bands are characteristic of Mn^{2+} in garnet (Laurs & Knox 2001; Stephan *et al*. 2019).

Electron-microprobe analysis of a Tongbei spessartine by Antao and Cruickshank (2018) yielded a chemical formula of $(Mn_{2.82}Fe^{2+}_{0.14}Ca_{0.04})_{\Sigma 3}(Al_{1.95}Fe^{3+}_{0.05})_{\Sigma 2}[(SiO_4)_{2.61}(O_4H_4)_{0.28}(F_4)_{0.11}]_{\Sigma 3}$. These authors showed that the elevated contents of OH and F in this spessartine causes a large deviation from cubic symmetry that results in the garnet having tetragonal symmetry. The overall composition of $Sps_{94}Alm_5Grs_1$ of this spessartine is similar to some material from Zambia and the USA (Ramona, California), and is among the most spessartine-rich garnet in the gem trade (cf. analyses summarised in Laurs & Knox 2001).

Dr Ján Štubňa (janstubna@gmail.com)
Gemmological Laboratory, Constantine the Philosopher University, Nitra, Slovakia

Dr Radek Hanus
Gemological Laboratory of e-gems.cz
Prague, Czech Republic

Dr Jana Fridrichová and Dr Peter Bačík
Comenius University
Bratislava, Slovakia

References

Antao, S.M. & Cruickshank, L.A. 2018. Crystal structure refinements of tetragonal (OH,F)-rich spessartine and henritermierite garnets. *Acta Crystallographica Section B*, **74**(1), 104–114, https://doi.org/10.1107/s2052520617018248.

Laurs, B.M. & Knox, K. 2001. Spessartine garnet from Ramona, San Diego County, California. *Gems & Gemology*, **37**(4), 278–295, https://doi.org/10.5741/gems.37.4.278.

Ottens, B. 2005. Tongbei: Spessartine localities, Fujian Province, China. *Mineralogical Record*, **36**(1), 35–43.

Stephan, T., Lind, T., Huaysan, B. & Müller, S. 2019. Gem Notes: Spessartine reportedly from Ethiopia. *Journal of Gemmology*, **36**(7), 592–593, https://doi.org/10.15506/jog.2019.36.7.592.

Paraíba or Not? Cu-bearing Tourmaline with a Distinct Fe Concentration

Copper-bearing tourmaline, also known as Paraíba-type tourmaline (or paraiba tourmaline; LMHC 2012), is one of the most sought-after and appreciated coloured stones in the trade. This is mostly due to its vivid colour, which in the best cases is described as 'neon' or 'electric' blue. However, Cu-bearing tourmalines are found in many colours, ranging from saturated blue (sapphire-like colour) to vivid and light blue, greenish blue to bluish green, green, and even greenish yellow and purple. Known sources include Brazil (Paraíba and Rio Grande do Norte states), where this attractive variety of tourmaline was first discovered, Mozambique (Mavuco and Maraca in the Alto Ligonha pegmatite field) and Nigeria (Fritsch *et al*. 1990; Smith *et al*. 2001; Abduriyim *et al*. 2006; Laurs *et al*. 2008; and references therein).

Interestingly, Cu-free indicolite tourmaline with Fe^{2+} as a chromophore can sometimes show a greenish blue colour very similar to that of Paraíba-type tourmaline. This material is often marketed as Lagoon tourmaline and is known, for example, from Namibia and Afghanistan. The separation of non-Cu-bearing indicolite from Paraíba-type tourmaline is usually straightforward, based on chemical analysis, UV-Vis absorption spectroscopy or both (Merkel & Breeding 2009).

Here we describe an intermediate variety of tourmaline (Figure 26, centre—sample B), that was recently submitted to the Swiss Gemmological Institute SSEF (Krzemnicki 2021). This stone of impressive size and weight (61 ct) shows an attractive greenish blue colour and exceptional clarity. Here we compare it to a similar Cu-bearing tourmaline from Nigeria (Figure 26, left—sample A) and a Cu-free indicolite from Namibia (Figure 26, right—sample C). Chemical variations among these three samples are best revealed by comparing the concentrations of their chromophores Cu and Fe (Table I), as measured by laser ablation inductively coupled plasma time-of-flight mass spectrometry (LA-ICP-TOF-MS) using SSEF's GemTOF system (see Wang *et al*. 2016). The Paraíba-type tourmaline from Nigeria (sample A) is strongly dominated by Cu, resulting in a Cu/Fe ratio of 18, while the Cu concentration in the indicolite from Namibia (sample C) is near the detection limit of our instrument (0.08 ppm for Cu), resulting in a very low Cu/Fe ratio of 0.000025. By contrast, sample B contains both Fe and Cu, with an intermediate Cu/Fe ratio of 0.16.

Although very similar in their visual appearance, these three tourmaline samples can be separated by their UV-Vis-NIR absorption spectra (Figure 27). The colour of the Paraíba-type tourmaline (sample A) is primarily related to two broad Cu^{2+} absorption bands extending into the near-infrared range (centred at around 700 and 900 nm). The distinct predominance of the absorption band at 900 nm over the band at 700 nm is characteristic for any Cu-dominated (Paraíba-type) tourmaline. By contrast, the indicolite (sample C) is coloured by a single broad absorption band centred at around 720 nm due to Fe^{2+} (Merkel & Breeding 2009). The colour of the intermediate Fe-Cu tourmaline (sample B) is related to

Figure 26: The three tourmalines of similar greenish blue colour examined for this study consist of (from left to right): a Cu-bearing Paraíba-type tourmaline from Nigeria (sample A, 19 ct) with a Cu/Fe ratio of 18; a tourmaline of intermediate composition (sample B, 61 ct) that is probably from Nigeria, with a Cu/Fe ratio of 0.16; and an Fe-bearing indicolite from Namibia (sample C, 23 ct) with a Cu/Fe ratio of 0.000025. Composite photo by M. S. Krzemnicki, © SSEF.

Table I: Fe and Cu contents of the three tourmalines in Figure 26, obtained by LA-ICP-TOF-MS.

Element	Sample A (Cu bearing)		Sample B (Fe-Cu bearing)		Sample C (Fe bearing)	
	Average (4)	Std. dev.	Average (4)	Std. dev.	Average (4)	Std. dev.
Fe (ppm)	113	15	4181	107	6194	444
Cu (ppm)	2037	69	670	12	0.16	0.04
Cu/Fe ratio	18		0.16		0.000025	

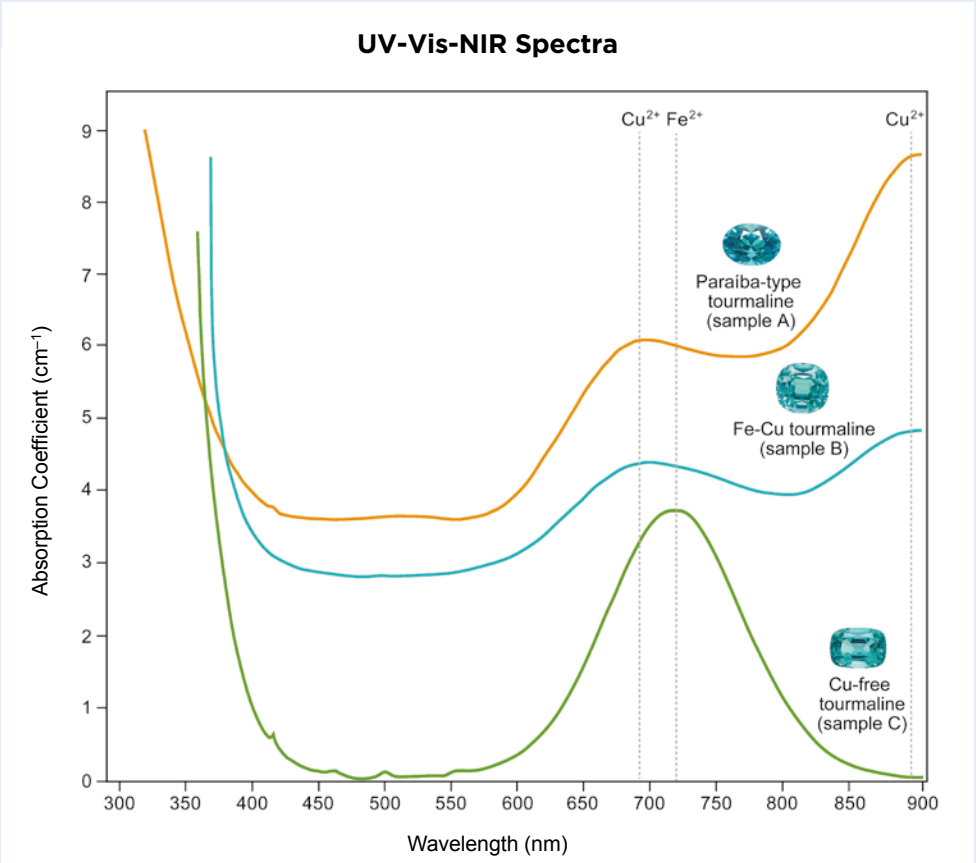

Figure 27: The UV-Vis-NIR spectra of the three tourmaline samples in Figure 26 are dominated by broad absorption bands of Cu^{2+} (sample A), Fe^{2+} (sample C), and a combination of both (sample B). The spectra are normalised to a path length of 1 cm and are offset vertically for clarity.

the absorption bands of both Cu^{2+} and Fe^{2+}. Because the bands at 700 and 900 nm have nearly equal intensity in this sample, it can be deduced that its colour is due to a combination of Cu and Fe.

Based on statistical processing of the trace-element data with a machine-learning algorithm (unsupervised non-linear t-SNE; Wang & Krzemnicki 2021), the origin of the intermediate Fe-Cu tourmaline (sample B) is in our opinion most likely Nigeria, although an independent confirmation of the mining site is still pending.

The recent appearance of greenish blue tourmaline with low Cu but distinctly higher Fe concentrations than typically found in Paraíba-type tourmaline (such as sample B) opens up interesting nomenclature considerations, similar to those long known for emerald and green beryl (related in that case to a gradual shift from Cr towards Fe). For the time being, given the relatively distinct concentration of Cu and the absorption spectrum with obvious Cu-related absorption bands, we feel that it is appropriate to call this particular stone 'Paraíba-type tourmaline' or 'paraiba tourmaline'. However, this would not be the case for a stone (such as sample C here) that contains significantly less Cu or when Fe-related absorption features dominate the Cu^{2+} bands.

In an ongoing study, we are currently focusing on this nomenclature issue with the aim of better defining to what extent an Fe-Cu-bearing tourmaline should be referred to using the Paraíba name and at what point it should be properly called an indicolite tourmaline with low traces of Cu.

Dr Michael S. Krzemnicki FGA
(michael.krzemnicki@ssef.ch)
and Dr Hao A. O. Wang FGA
Swiss Gemmological Institute SSEF
Basel, Switzerland

References

Abduriyim, A., Kitawaki, H., Furuya, M. & Schwarz, D. 2006. "Paraíba"-type copper-bearing tourmaline from Brazil, Nigeria, and Mozambique: Chemical fingerprinting by LA-ICP-MS. *Gems & Gemology*, **42**(1), 4–21, https://doi.org/10.5741/gems.42.1.4.

Fritsch, E., Shigley, J.E., Rossman, G.R., Mercer, M.E., Muhlmeister, S.M. & Moon, M. 1990. Gem-quality cuprian-elbaite tourmalines from São José da Batalha, Paraíba, Brazil. *Gems & Gemology*, **26**(3), 189–205, https://doi.org/10.5741/gems.26.3.189.

Krzemnicki, M.S. 2021. New copper-bearing tourmalines from Nigeria. *Facette Magazine*, No. 27, 21.

Laurs, B.M., Zwaan, J.C., Breeding, C.M., Simmons, W.B., Beaton, D., Rijsdijk, K.F., Befi, R. & Falster, A.U. 2008. Copper-bearing (Paraíba-type) tourmaline from Mozambique. *Gems & Gemology*, **44**(1), 4–30, https://doi.org/10.5741/gems.44.1.4.

LMHC 2012. Paraiba tourmaline. Laboratory Manual Harmonisation Committee, Information Sheet #6, 1 pp.

Merkel, P.B. & Breeding, C.M. 2009. Spectral differentiation between copper and iron colorants in gem tourmalines. *Gems & Gemology*, **45**(2), 112–119, https://doi.org/10.5741/gems.45.2.112.

Smith, C.P., Bosshart, G. & Schwarz, D. 2001. Gem News International: Nigeria as a new source of copper-manganese-bearing tourmaline. *Gems & Gemology*, **37**(3), 239–240.

Wang, H.A.O. & Krzemnicki, M.S. 2021. Multi-element analysis of minerals using laser ablation inductively coupled plasma time of flight mass spectrometry and geochemical data visualization using t-distributed stochastic neighbor embedding: Case study on emeralds. *Journal of Analytical Atomic Spectrometry*, **36**(3), 518–527, https://doi.org/10.1039/d0ja00484g.

Wang, H.A.O., Krzemnicki, M.S., Chalain, J.-P., Lefèvre, P., Zhou, W. & Cartier, L. 2016. Simultaneous high sensitivity trace-element and isotopic analysis of gemstones using laser ablation inductively coupled plasma time-of-flight mass spectrometry. *Journal of Gemmology*, **35**(3), 212–223, https://doi.org/10.15506/JoG.2016.35.3.212.

PEARLS

Art Nouveau Pendant with a Large Blister Pearl

Natural pearls are, and always have been, a rarity. Particularly fine natural pearls are highly treasured and attain top prices at auctions. Sometimes natural pearls are attached to a shell, requiring them to be cut out and reworked slightly on the shell side. These are known as blister pearls (CIBJO 2021), and are usually not as highly valued as round natural pearls, but they are still rare (Zhou *et al*. 2017).

Similar in appearance to blister pearls are cultured blisters. These half-pearls are cultivated on the inside surface of a mollusc's shell. A small nucleus, usually made from mother-of-pearl, is attached to the shell and left to accumulate nacre over a period of usually about two or three years. Cultured blisters have a lower value than natural blister pearls, similar to the price difference between cultured and natural spherical pearls (Hänni 2012 and references therein).

Recently, a goldsmith submitted a pendant mounted with a pearl to the DDI Foundation German Diamond Institute for testing (Figure 28a). It contained delicate

Figure 28: (**a**) This pendant featuring an oval-shaped blister pearl (17 mm wide) was submitted for testing. (**b**) A side view of the pendant shows the delicate Art Nouveau gold artwork and how a portion of the pearl's rim is covered by the mounting. (**c**) The open back of the pendant reveals concentric rings that follow the outline of the pearl. Photos by T. Jordi and L. Kiefert.

Figure 29: The number '9885' (about 3 mm tall) is stamped on top of the pendant's bail, but no maker's mark could be found. Photomicrograph by L. Kiefert.

gold work (Figure 28b), and the design was indicative of the Art Nouveau period. According to the owner, it was made by Edouard Colonna (1862–1948), an architect and designer who worked in New York, USA, for Tiffany & Co. and later in France (Koch & Posseme 1989). We could not locate a maker's mark, but the number '9885' was visible on top of the pendant's bail (Figure 29).

The pendant weighed 9.97 g, and the pearl itself measured approximately 20.5 × 17.0 × 8.5 mm, yielding a calculated weight of approximately 20 ct. Because the mounting covered part of the pearl's outline, it gave the impression of containing a cultured blister. When the pendant was viewed from the back side, concentric rings were visible around the worked surface, following the shape of the pearl (Figure 28c).

X-radiography did not show any sign of a bead or other inserted nucleus, which was indicative of a natural blister rather than a cultured blister pearl. In addition, a few weak lines visible in the X-ray images followed the outline of the pearl in the same way as the surface lines that are visible in Figure 28c.

The pearl was chemically analysed by EDXRF spectroscopy to determine its saltwater vs freshwater origin based on its MnO to SrO contents (Gutmannsbauer & Hänni 1994). With values of 33.9 ppm MnO and 964.5 ppm SrO, it was clearly identified as a saltwater pearl (Figure 30).

Considering also the delicate artwork of the gold mounting, we therefore concluded that the pendant is from the early 1900s and contains a natural blister pearl.

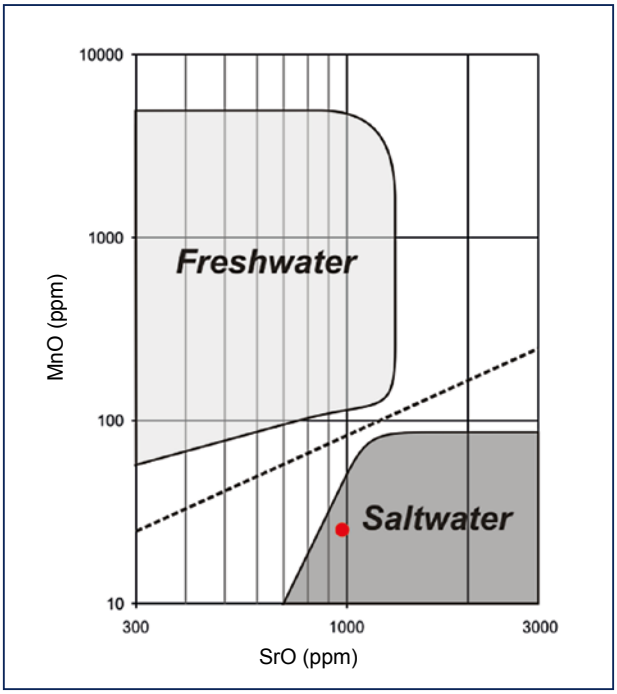

Figure 30: A plot of the MnO and SrO contents (red dot) identifies the pearl as being of saltwater origin. Modified after Gutmannsbauer & Hänni (1994).

Dr Lore Kiefert FGA (info@gemlabhelp.com)
Gemmology Consulting
Heidelberg, Germany

Jeanette Fiedler
DDI Foundation German Diamond Institute
Pforzheim, Germany

Pierre Hardy
Gübelin Gem Lab, Lucerne, Switzerland

References

CIBJO 2021. *CIBJO Guide for Classifying Natural Pearls and Cultured Pearls*. CIBJO Pearl Commission 2021-1, 4 February, 62 pp.

Gutmannsbauer, W. & Hänni, H.A. 1994. Structural and chemical investigations on shells and pearls of nacre forming salt- and fresh-water bivalve molluscs. *Journal of Gemmology*, **24**(4), 241–252, https://doi.org/10.15506/JoG.1994.24.4.241.

Hänni, H.A. 2012. Natural pearls and cultured pearls: A basic concept and its variations. *Australian Gemmologist*, **24**(1), 258–266.

Koch, M. & Posseme, E. 1989. *Pariser Schmuck: Vom Zweiten Kaiserreich zur Belle Epoque*. Hirmer, Munich, Germany, 327 pp.

Zhou, C., Hodgins, G., Lange, T., Saruwatari, K., Sturman, N., Kiefert, L. & Schollenbruch, K. 2017. Saltwater pearls from the pre- to early Columbian era: A gemological and radiocarbon dating study. *Gems & Gemology*, **53**(3), 286–295, https://doi.org/10.5741/gems.53.3.286.

SYNTHETICS AND SIMULANTS

A Convincing Glass Imitation of Emerald

Recently, a bluish green oval-cut sample weighing 4.05 ct (Figure 31) was submitted to EGL South Africa's laboratory for certification as a natural emerald. At first the microscopic features—such as what appeared to be partially healed fractures, some with orangey stains, and oil- or resin-filled fissures (e.g. Figure 32)—suggested that it could be an emerald. However, a closer look revealed some anomalous features, including rounded facet edges, which indicated something was not right.

The pattern of the inclusions that resembled partially healed fractures was somewhat reminiscent of an elongated honeycomb structure (Figure 33), and the individual 'droplets' did not have the typical forms shown by fluid inclusions. Although the RI of 1.572 was in the range of beryl, only a single reading could be obtained, indicating the material was singly refractive. Also, the hydrostatic SG value of 3.01 was higher than the expected range for beryl.

Figure 31: This 4.05 ct faceted green specimen submitted to EGL South Africa's laboratory turned out to be a glass simulant of emerald. Photo by K. Khourie.

Figure 32: White residues within a surface-reaching fissure in the glass simulant indicate the presence of an oil or resin filling, which suggests a conscious attempt at fraud. Photomicrograph by K. Khourie; magnified 70×.

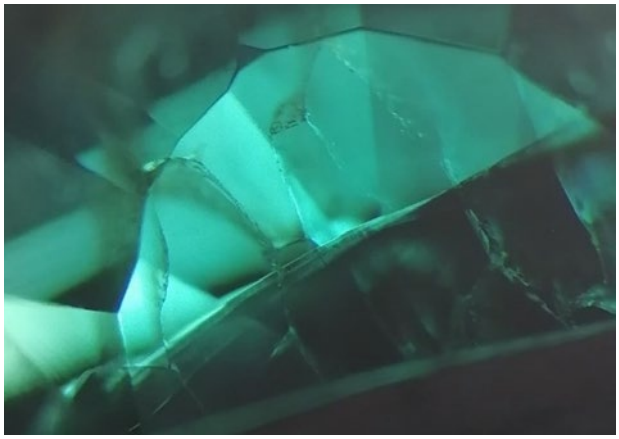

Figure 33: The glass sample contained fissures arranged in a honeycomb-like cellular formation. Photomicrograph by K. Khourie; magnified 40×.

The FTIR spectrum of the sample matched our reference for artificial glass. This is consistent with the rounded facet edges mentioned above, but interestingly no gas bubbles or flow lines were seen. The UV-Vis-NIR spectrum of the glass showed some similarities to that of natural emerald (Figure 34), suggesting that it was coloured by Cr^{3+} and Fe-related absorptions.

It is clear that this glass specimen was intended to defraud, as shown by the presence of fissures that were filled with oil or resin—a common clarity treatment in emerald. A similar clarity-enhanced glass imitation of emerald was recently reported by Stephan (2020), but the inclusions and RI of that sample were quite different from those reported here.

Kaylan Khourie FGA (research@egl.co.za)
EGL South Africa
Johannesburg, South Africa

Reference

Stephan, M. 2020. Lab Notes: Clarity-enhanced glass imitating emeralds. *Gems & Gemology*, **56**(1), 133.

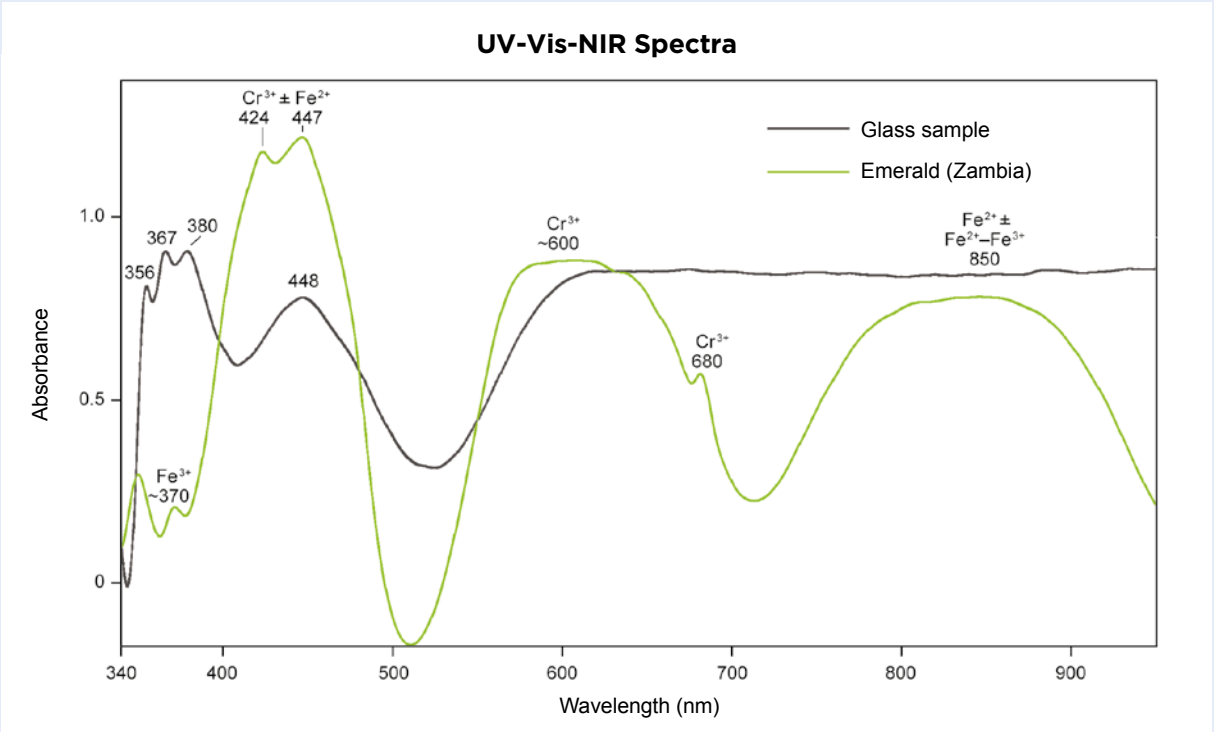

Figure 34: The UV-Vis-NIR spectrum of the glass sample is compared to that of a Zambian emerald. Peak attributions shown for the emerald suggest that the artificial glass may also be coloured by a combination of Cr^{3+} and Fe-related absorptions. The path length of the beam was about 6 mm for each sample.

Figure 1: This emerald crystal (45 × 8 × 8 mm) formed within a vein containing albite and pyrite on a matrix of black shale, and is from the Palo Arañado mine, Chivor mining district, Colombia. Photo courtesy of G. Martayan.

Colombian Emerald Oddities: Review and Formation Mechanisms

Isabella Pignatelli, Gaston Giuliani, Christophe Morlot, Lise Salsi and Gérard Martayan

ABSTRACT: Exceptional mineralogical oddities of gemmological interest have been found in Colombia's emerald deposits. Their particular sedimentary-hydrothermal geological environment is characterised by large fluid circulations and changes in thermodynamic conditions during emerald precipitation. In this context, various etching processes and growth perturbations affected the crystals in both the eastern and western belts of these emerald deposits. In the eastern belt, variations in post-growth etching are responsible for the formation of 'vaso' (cup), 'spongy' and spear-shaped emeralds, and etching associated with near-parallel growth of elongated crystals resulted in fibrous emerald specimens. In addition, rare sceptre emeralds formed by epitaxial lateral overgrowth due to the arrival of a later mineralising pulse in the hydrothermal system. 'Emerald gastropods' are also found in the eastern belt, and formed by the replacement of fossil aragonite by calcite which later dissolved away and was replaced by emerald. In the western emerald belt, hydrothermal fluid circulation sometimes resulted in non-uniform crystal growth, giving rise to horseshoe-shaped emeralds characterised by an incomplete hexagonal prismatic habit. An unusual sample of a calcitised trapiche emerald—due to fluid circulation affecting trapiche emerald-bearing black shale—is also described.

The Journal of Gemmology, **38**(1), 2022, pp. 26–43, https://doi.org/10.15506/JoG.2022.38.1.26

Colombian emerald crystals (Figure 1) are prized for their clarity, size and attractive colour, which is sometimes referred to as *Muzo green* (Peretti & Falise 2018). Among these famous emeralds are various peculiarities, such as trapiche emeralds from the Muzo, Coscuez and Peñas Blancas deposits, which are renowned for their distinctive texture resembling a wheel with six spokes (e.g. Pignatelli *et al.* 2015).

In this study, we characterise some additional emerald oddities from Colombia using non-destructive techniques. They are true rarities with unusual features that were produced under exceptional conditions. From the eastern Colombian emerald belt come sceptre, fibrous, 'vaso' (Figure 2), 'spongy' and spear-shaped emeralds, as well as the famous 'emerald gastropods' (Vuillet *et al.* 2002). From the western emerald belt come horseshoe-shaped and calcitised trapiche emeralds—new oddities that are described here for the first time. We also propose explanations for the formation of these specimens on the basis of experimental data and observations by the authors.

GEOLOGICAL SETTING

Colombian emerald deposits are hosted by black shales of the Eastern Cordillera sedimentary basin. They define two belts: (1) a western one containing the La Glorieta-Yacopí, Muzo, Coscuez, La Pita, Cunas and Peñas Blancas deposits, and (2) an eastern belt that includes the Gachalá, Buenavista, Chivor, Agua Blanca and Macanal deposits (e.g. Figure 3). The structural control of the mineralisation is markedly different in the two emerald belts (Branquet *et al.* 1999a, b). The Coscuez and Muzo deposits show compressive structures (folds, thrusts and tear faults), while the Chivor mines are hosted by extensional structures formed above an evaporite regional level (Branquet *et al.* 2015; Giuliani *et al.* 2015, 2016). These tectonic structures allowed the circulation of hydrothermal fluids and the formation of emerald. The fluids consisted of hot basinal brines (300–330°C) in the H_2O + NaCl (± CO_2) system (with a very high salinity of about 40 wt.% NaCl equivalent) that locally contained Ca, K, Mg, Fe, Li and SO_4 (Roedder 1984; Ottaway *et al.* 1994; Giuliani *et al.* 1991, 1993). The brines altered the black shales, which mobilised the Be, Cr and V necessary for emerald precipitation (Ottaway 1991; Giuliani *et al.* 1993; Mantilla Figueroa *et al.* 2007).

Fluid overpressures, due to the circulation of hydrothermal fluids along faults, caused the formation of hydraulic breccias and the opening of veins containing carbonates and pyrite, in which emerald precipitated along with other minerals such as quartz, albite, parisite and fluorite (Hall 1976). The thermal reduction of evaporitic sulphates in the presence of organic matter is a fundamental process for the mobilisation of Be, Cr and V in the black shales and in emerald formation (Ottaway *et al.* 1994). This exothermic reaction produces HCO_3^- and H_2S, which in turn react with the Ca^{2+} and Fe^{2+} transported by the fluids to form calcite, pyrite and hydrothermal organic matter (bitumen) in the veins (Giuliani *et al.* 2000).

Figure 2: 'Vaso' (cup) emeralds occur with calcite, albite and pyrite on this specimen (25 × 20 × 8 mm) from the Chivor mining district. Photo by G. Martayan.

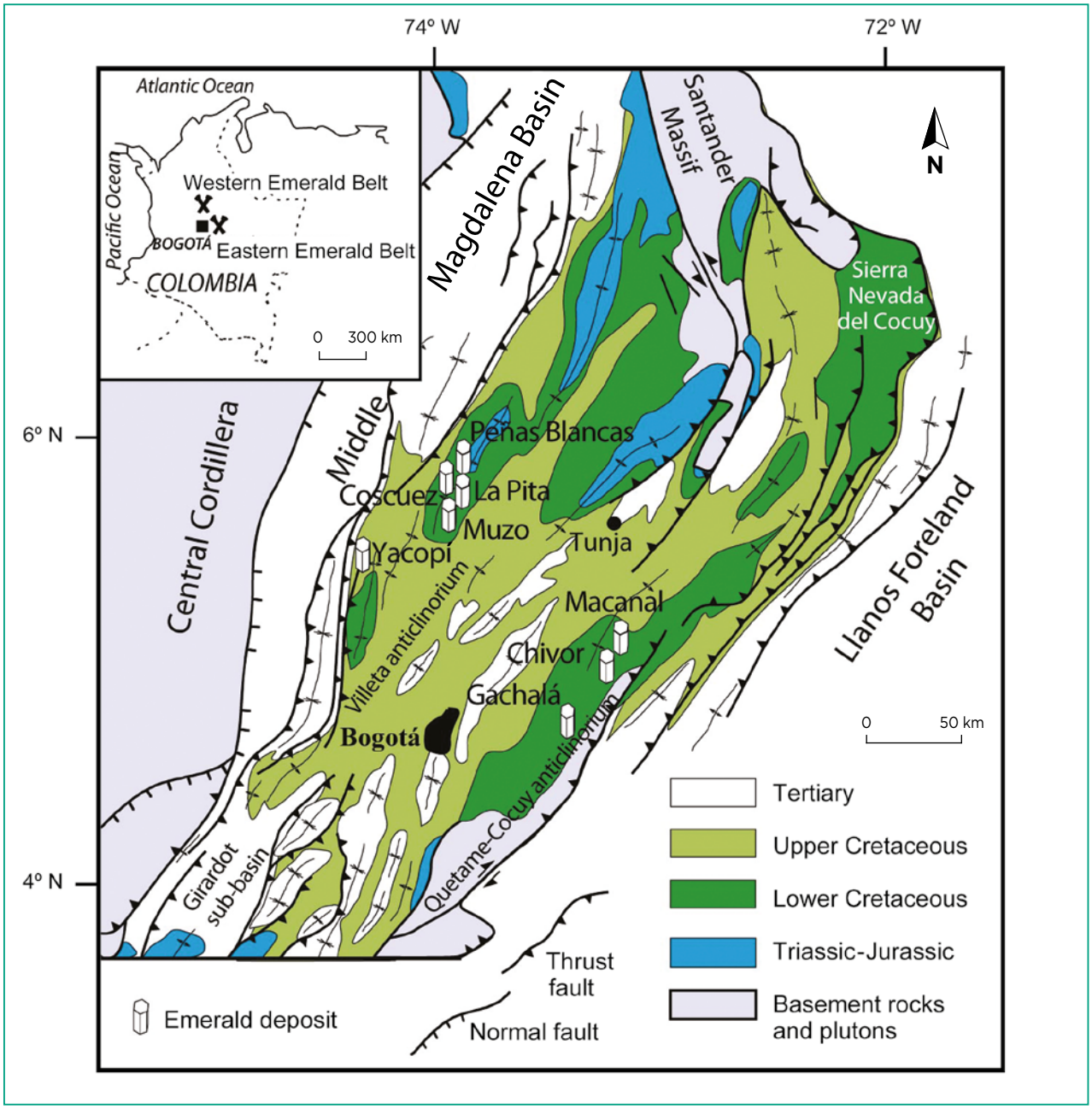

Figure 3: In this simplified geological map, many of Colombia's emerald deposits are shown hosted by Lower Cretaceous sedimentary rocks along two mineralised belts located on the western and eastern borders of a sedimentary basin of the Eastern Cordillera. The western belt includes the mining districts of Yacopí, Muzo, Coscuez, La Pita and Peñas Blancas, and the eastern belt hosts the Gachalá, Chivor and Macanal deposits. Modified from Branquet *et al.* (2015).

MATERIALS AND METHODS

We examined 28 specimens for this report that were loaned by museums or private collectors: a sceptre emerald, a fibrous emerald, two so-called vaso emeralds (or 'emerald cups'; Weldon *et al.* 2016), a 'spongy' emerald, a spear-shaped emerald, a horseshoe-shaped emerald, a calcitised trapiche emerald and 20 'emerald gastropods'. The last are centimetre-sized fossil prosobranches, exceptional because they have been replaced by emerald.

The horseshoe-shaped and calcitised trapiche emeralds are from the Muzo mine. The other samples analysed in this study are from the Chivor mining district (the exact mines are unknown), with the exception of the fossil gastropods, which are from the Gachalá mining district. The fossils were discovered in 1994 in the Matecaña mine, located in Lower Cretaceous sedimentary rocks that are part of the Guavio Formation (145–140 million years [Ma] old). Although the time period for the mining of the vaso emeralds is unknown, their sporadic

appearance on the Bogotá market in the last few years testifies to their presence in recent production.

The specimens were investigated using optical microscopy and X-ray computed tomography (CT), which is non-destructive and does not require sample preparation. It provides detailed three-dimensional (3D) imaging of textures and surfaces, as well as calculation of volume and the distribution of phases with different densities and states (i.e. liquid, solid or gas for three-phase inclusions; Morlot *et al*. 2016; Richard *et al*. 2019). The images were collected with a Phoenix Nanotom S scanner, using resolutions between 1.5 and 19.11 µm/voxel, and an X-ray tube with a tungsten anode and variable nanofocus tension of 75–105 kV. The tomography files had voxel (3D pixel) resolutions between 0.8 and 30 µm/voxel as a function of sample size. Virtual cross-sections were extracted using VGStudio and Avizo 9.5 software. A segmentation process was used to identify each phase, assigning different colours to the images according to X-ray attenuation. For this study we used a greyscale, in which the denser phases appear white.

CT was coupled to micro-X-ray fluorescence (XRF) mapping to visualise the distribution of chemical elements in the volume of the calcitised trapiche emerald. Semi-quantitative chemical maps were obtained using a Bruker M4 Tornado spectrometer. The system had an Rh X-ray tube with a Be side window and polycapillary optics, providing an X-ray beam diameter of 25–30 µm on the sample. The X-ray tube was operated at 50 kV and 200 µA. X-rays were detected by a 30 mm^2 XFlash silicon drift detector with an energy resolution up to 135 eV. All analyses were done under vacuum (20 mbar). Semi-quantitative maps were generated for Al, Si, S, Ca, Ti, Cr, Mn and Fe on areas of 22 × 17 mm over a period of 300 seconds. The data acquisition and processing were carried out using the Bruker software supplied with the instrument (Flude *et al*. 2017).

RESULTS AND DISCUSSION

Sceptre Emerald

To our knowledge, the sceptre emerald (Figure 4a) is an exceptional rarity, and this is its first description in the literature. The specimen is 13 mm long and consists of two hexagonal prismatic portions: the trunk and the cap. Both are characterised by striations parallel to the *c*-axis along the prism faces. The light green trunk is slender, with a diameter of 2.5 mm. The darker green cap is shorter and stubby, with a diameter of 3.5 mm. The trunk and cap are separated by macroscopically

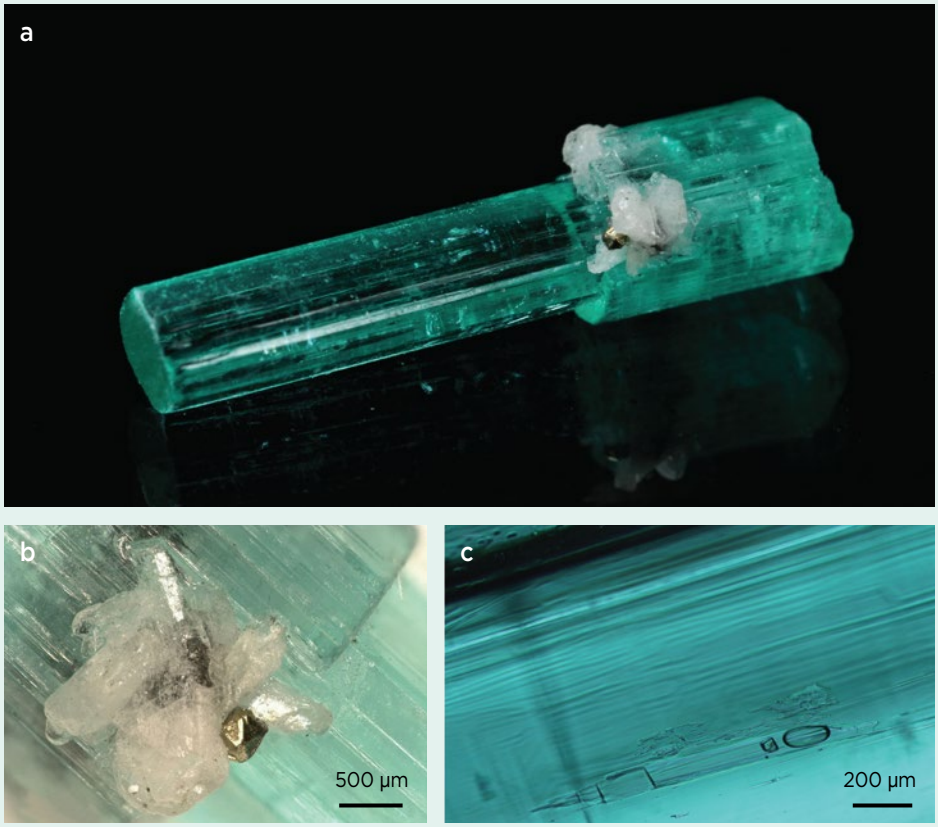

Figure 4: (**a**) This 13-mm-long sceptre emerald from Chivor is made up of two portions: a thicker, darker cap (3.5 mm diameter) and a narrower lighter green trunk (2.5 mm diameter). (**b**) Inclusions of quartz and pyrite are present between the cap and the trunk. (**c**) A large multiphase fluid inclusion within the cap area contains gas and liquid phases, a cube of halite, a carbonate and an opaque mineral. Photos by (a) G. Martayan, (b) I. Pignatelli and (c) G. Giuliani.

recognisable inclusions of quartz and pyrite (Figure 4b). Both portions of the emerald contain three-phase or multiphase fluid inclusions in the H_2O + NaCl (± CO_2) system, as previously described for Colombian emeralds (Giuliani *et al.* 1991, 1993). One of the largest is present in the cap and measures 2 mm long. It consists of a multiphase fluid inclusion with a gas (bubble), a liquid phase, a cube of halite and two crystals of different sizes: a carbonate and a tiny opaque mineral (Figure 4c). We identified the solid inclusions using optical microscopy, and we assume the liquid and gas phases are the same as those described in the previous studies cited above. At the end portion of the trunk near the cap, we also observed elongated fluid inclusions with spindle-shaped terminations.

The distribution of fluid inclusions in the sample is inhomogeneous. CT images revealed that their quantity is higher in the cap (Figure 5a), where they are concentrated in proximity to the trunk, particularly in the centre of the cap and around inclusions of quartz, carbonate and pyrite (Figure 5b). CT images of the contact area between trunk and cap show that the cap overhangs the trunk laterally, forming a stepped rough surface (Figure 6a).

Our observations suggest that the formation mechanism of this emerald specimen is likely the same as that of sceptre quartz, based on the following features: (1) the structurally continuous coexistence of a larger, shorter cap portion and a slender trunk portion; (2) a high density of fluid inclusions trapped in the trunk near the boundary with the cap; (3) the presence of pyrite and quartz partially covering the trunk surface; and (4) differences in colour and in the quantity of inclusions between the cap and the trunk. All these features indicate that physicochemical conditions changed between the formation of trunk and cap (Sunagawa 2005). On the basis of the genetic model proposed for sceptre quartz found in pegmatites and hydrothermal veins (Takahashi *et al.* 2004), the sceptre emerald formed in two stages. First, the trunk portion crystallised, and it was then partially or completely covered by solid inclusions, which interrupted its growth. During the second stage, the growth of the cap was favoured by the arrival of a newly mineralised fluid or changes in the thermodynamic conditions of the initial parental fluid from which the trunk formed. The fact that the cap and trunk formed under different conditions explains their differences in colour and concentrations of inclusions (cf. Takahashi *et al.* 2004). The cap grew on the trunk by epitaxy (i.e. keeping the same crystallographic orientation as the trunk). However, considering the trunk surface was partially masked by the precipitation of other minerals (quartz, carbonate and pyrite in the case of this emerald), this is a special case of epitaxy that has been referred to in the literature as *epitaxial lateral overgrowth* or *ELO* (Nishinaga *et al.* 1988; Nishinaga 2002), meaning that

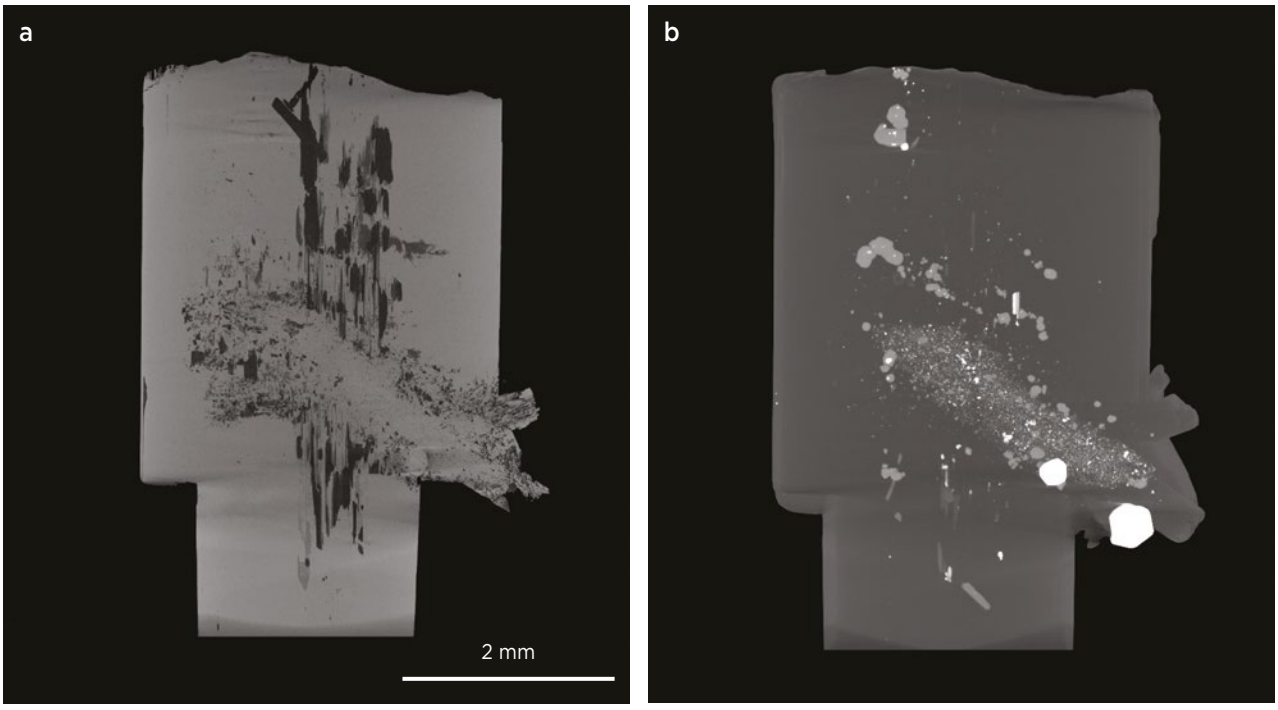

Figure 5: CT images of the sceptre emerald show: (**a**) dark areas corresponding to voids (fluid inclusions); and (**b**) lighter areas marking the locations of mineral inclusions, including quartz and carbonate (light grey), as well as pyrite (white). Images by C. Morlot.

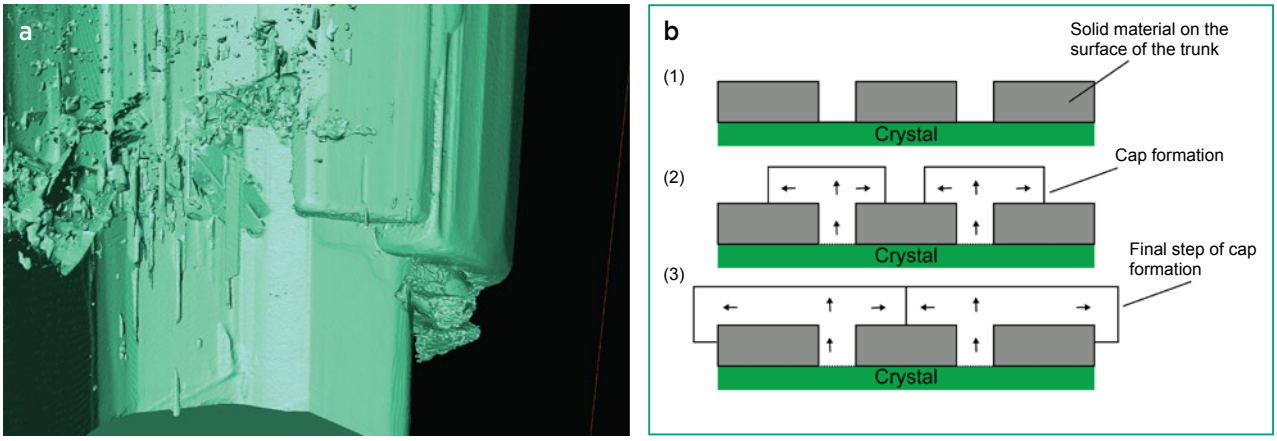

Figure 6: (**a**) This false-colour CT image of the sceptre emerald shows that the cap protrudes laterally from the trunk, forming steps with a rough surface. The diameter of the trunk is 2.5 mm; image by C. Morlot. (**b**) The schematic diagram (modified from Takahashi *et al.* 2004) illustrates the formation process by epitaxial lateral overgrowth for sceptre crystals.

the cap started to grow on unmasked areas of the trunk surface and then developed further on masked areas, as shown in Figure 6b.

Although there are many similarities between sceptre quartz and this sceptre emerald, the cap portion in quartz usually contains fewer inclusions and defects than the trunk (especially in samples found in hydrothermal veins), suggesting formation under a lower driving-force condition (Takahashi *et al.* 2004). By comparison, the cap of the sceptre emerald is characterised by more fluid inclusions and a higher content of chromophore elements, resulting in a darker colour than that of the trunk. This indicates that the cap grew faster, under higher driving force, probably due to chemical changes in the growth solution, such as a combined effect of supersaturation and greater impurity concentration.

Fibrous Emerald

The fibrous emerald is a long, thin specimen (2 × 1 × 15 mm) of pale green colour, elongated on the *c*-axis (Figure 7a). It lacks sharply defined faces, although relics of pinacoidal faces are visible with a microscope. Tomographic imaging revealed a number of interesting characteristics:

1. It exhibits grooved, striated portions of prism faces that result from the coexistence of several crystals parallel to the *c*-axis, as well as relics of pinacoidal faces characterised by rough surfaces (Figure 7b).
2. It contains many tube-like voids, with different diameters, that are probably fluid inclusions oriented parallel to the *c*-axis (Figure 7c). A detail of the fluid inclusions is shown in Figure 7d, encompassing a large three-phase fluid inclusion that contains a gas bubble (about 126 µm diameter), a liquid phase and an unidentified crystal.
3. It consists of an aggregate of crystals elongated parallel to the *c*-axis, with hexagonal sections visible on CT images taken perpendicular to the *c*-axis (Figure 7e). They are more-or-less misoriented and turned slightly relative to the *c*-axis direction, as previously observed in some pegmatitic beryls (Graziani *et al.* 1981; Tempesta *et al.* 2011).

This specimen is the result of irregular growth due to several 'fluxes of matter' (cf. Graziani *et al.* 1981, p. 242) that caused the crystallisation of multiple crystals, the formation of small voids between them (corresponding to the dark zones in Figure 7e) and striations on the morphological faces. The fact that sharply defined faces are no longer visible could be due to post-growth etching, which could have contributed to enlarging the empty zones. Dissolution along dislocation bundles could explain the formation of the tube-like voids visible in the CT scans (Figure 7c, d) when supersaturation of the growth medium decreased after growth (Scandale & Zarka 1982; Authier & Zarka 1994).

Vaso Emeralds

The name *esmeralda vaso* (for 'emerald cup') indicates the presence of eye-visible single or multiple cavities that give an emerald crystal the appearance of a cup without a handle. Vaso emeralds have been found only in the Chivor mining district and were described for the first time by Fritz Klein in his book *Smaragde unter dem Urwald* (*Emeralds Under the Jungle*; Klein 1941). On pages 128 and 129, a hand-painted plate by Walter Wild illustrates several emeralds from Chivor and Muzo,

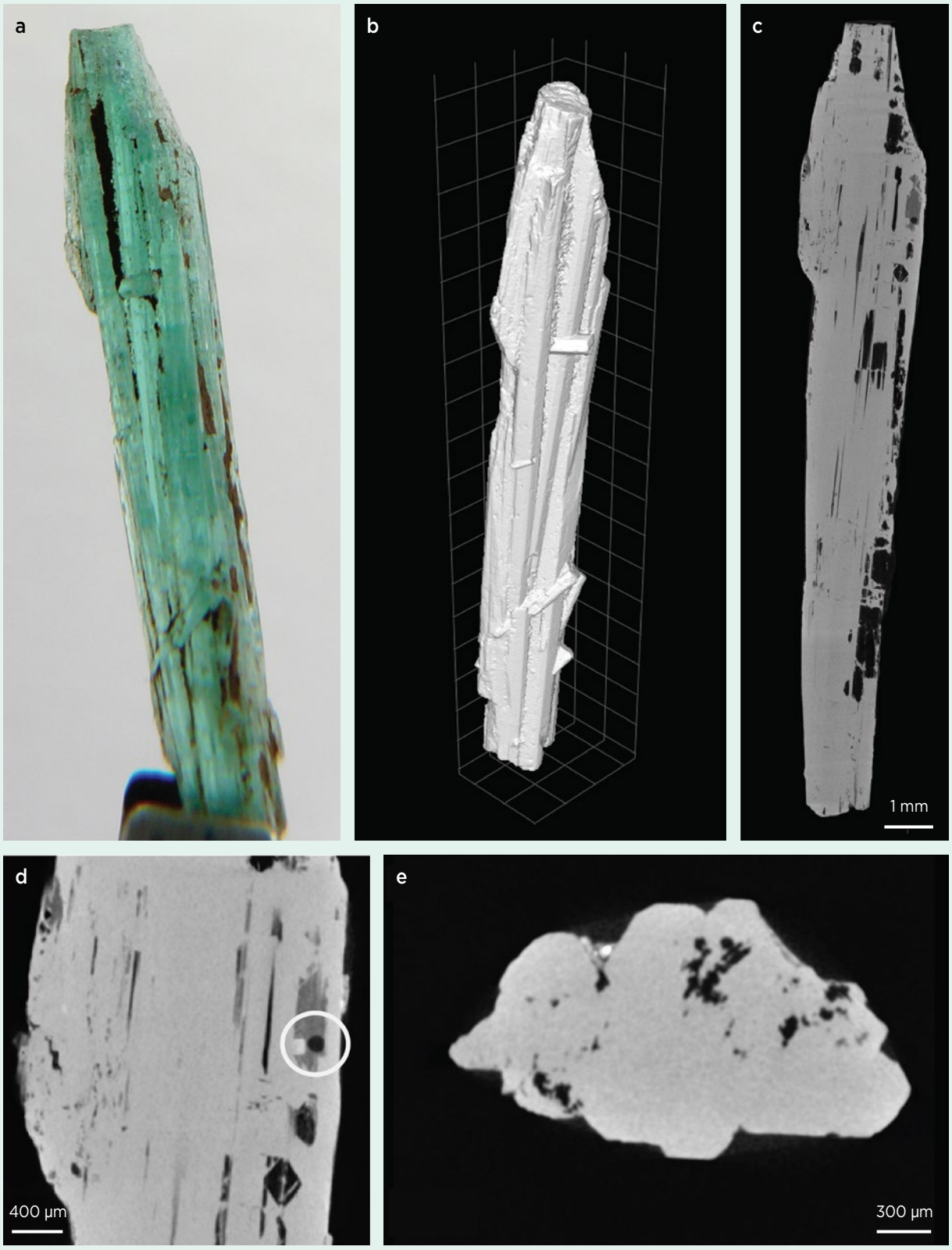

Figure 7: (**a**) This fibrous emerald (2 × 1 × 15 mm) is from Chivor. (**b**) A 3D CT image (grid is in millimetres) shows relics of pinacoidal faces, as well as grooved, striated portions of prism faces. (**c**) Another CT image shows tube-like voids (fluid inclusions and empty spaces) of various diameters oriented parallel to the *c*-axis. (**d**) CT imaging of a large three-phase inclusion shows that it contains a gas bubble (diameter about 126 µm; indicated by a white circle), a liquid phase and an unidentified crystal. (**e**) A CT image taken parallel to the *c*-axis of the sample reveals the hexagonal sections of the elongated crystals that make up the fibrous emerald specimen. Photo by G. Giuliani and CT images by C. Morlot.

among which are two vaso-type crystals. However, the author only mentions their origin without adding further details. Later, Weldon *et al*. (2016, figure 11) compared four vaso emeralds exhibited at the International Emerald Museum in Bogotá to those illustrated in Klein's book.

Twenty years after Klein's book, Johnson (1961, p. 138) described this kind of emerald from the Coliflor tunnel at Chivor:

> Some of the tapered emeralds have a hollow cavity in the centre which extends from an opening on the termination the entire length of the crystal. Completely tapered emeralds are rare since the cavity in the centre causes most of them to fracture in the middle along a plane perpendicular to the *c*-axis. Most of these emeralds do not exceed 2 cm in length.

Vaso emeralds have a typical hexagonal prismatic habit (Figures 2 and 8), and small dipyramidal $\{11\bar{2}2\}$ faces are sometimes present (Figure 8b). The crystals are characterised by the presence of either several small cavities or one large central cavity extending from the pinacoidal (0001) face (Figures 2 and 8a). Tomographic images show that the cavities have irregular or roughly hexagonal cross-sections (Figure 9a), and their long sides are oriented parallel (or nearly parallel) to the prism faces. The walls of the cavities are steep and have vertical steps oriented in the *c*-axis direction. These steps originated from the presence of several neighbouring cavities with hexagonal sections (Figure 9b, c).

As seen with an optical microscope, the ends of the cavities appear rounded (Figure 10a, b) or pointed (Figure 11a–c), but tomographic images reveal that the rounded ends are, in reality, pointed (Figures 9d and 10d–f) and the cavities are of variable length (Figure 10e). Their bottoms sometimes contain solid inclusions, such as carbonates (Figure 10d), which made it impossible to clearly see the cavities' ends with the optical microscope and caused them to appear rounded. Their pointed shape was also sometimes obscured in the microscope by residues of oil used for emerald clarity enhancement (Figure 11a, b, d).

The pointed ends were located near the boundary between different-coloured portions of one of the emerald crystals we examined (Figure 11a, d). This boundary also corresponded to a trapping front for three-phase and multiphase fluid inclusions (Figure 11d, e). These inclusions are similar to those observed in other Colombian emeralds (Ottaway 1991; Giuliani *et al*. 1991, 1993; Cheilletz *et al*. 1994), and are easily recognised by the presence of one or more cubic halite crystals (Figure 11e). The fluid inclusions near the trapping front appear jagged and are characterised by the presence of a CO_2 gas phases (Figure 10c).

Observations with the optical microscope indicated

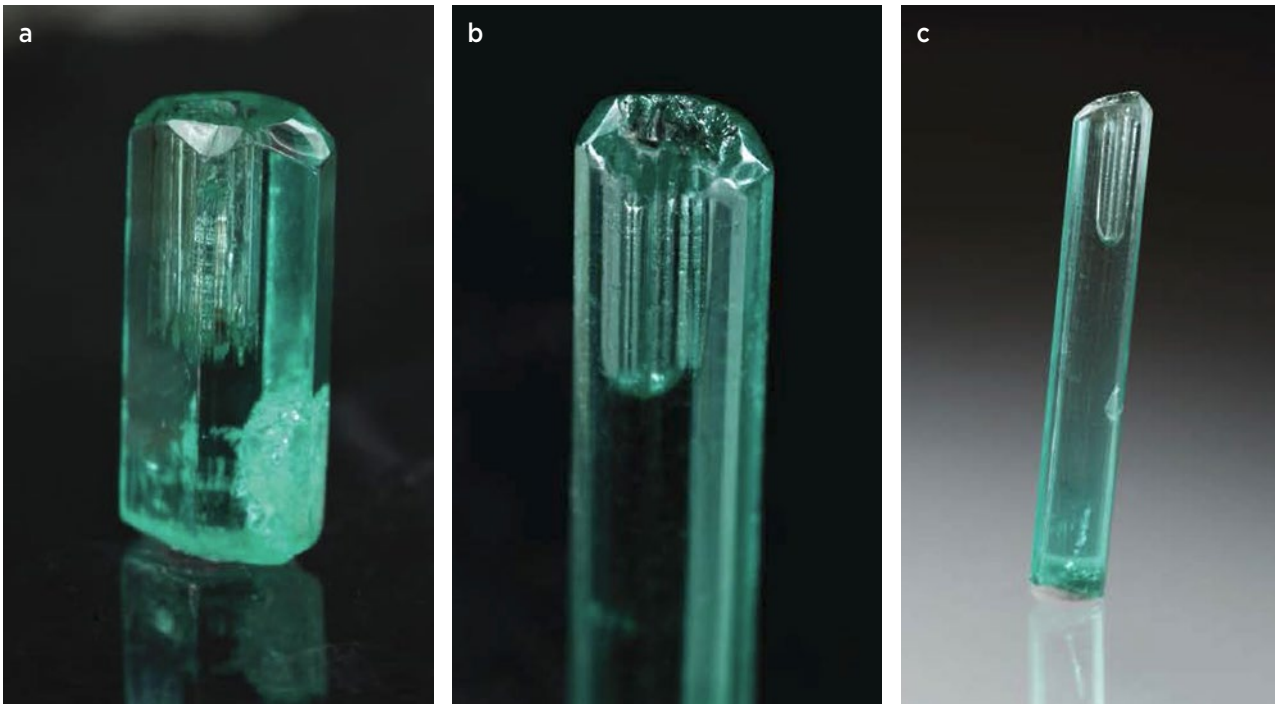

Figure 8: These vaso emeralds are from the Chivor mining district (probably from the Oriente mine). The crystals measure 11 × 5 × 5 mm (**a**) and 20 × 3 × 3 mm (**b** and **c**). Photos by G. Martayan.

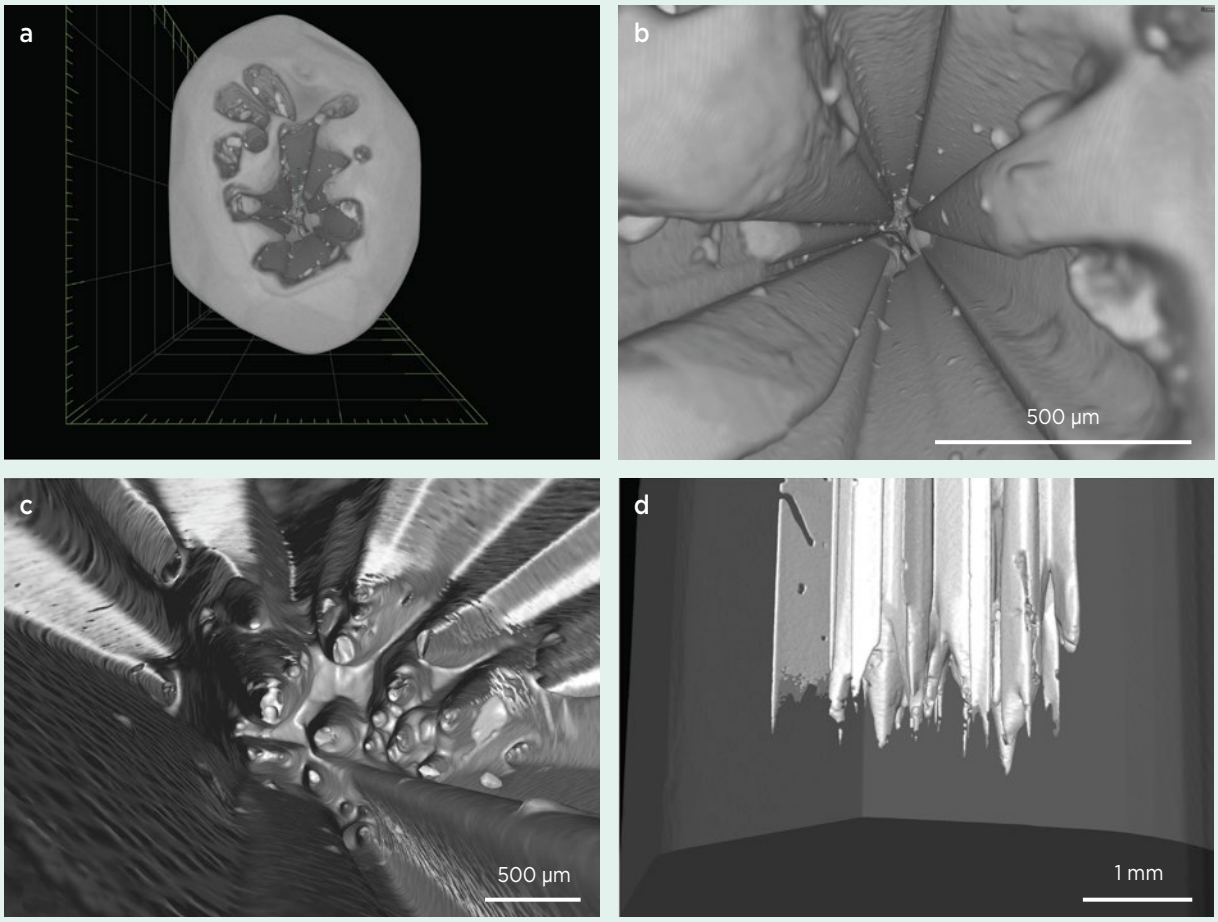

Figure 9: CT images reveal various details of the vaso emeralds. (**a**) This view looking down the *c*-axis shows several irregular or roughly shaped hexagonal cavities on the pinacoidal face of the crystal in Figures 8b and 8c (grid is in millimetres). The cavities are bounded by vertical steps extending in the *c*-axis direction, as seen in (**b**) the crystal in Figures 8b and 8c, and in (**c**) the specimen in Figure 8a. (**d**) The pointed ends of the cavities in the crystal in Figures 8b and 8c are clearly evident in this view. Images by C. Morlot.

that the base of one vaso emerald had a high concentration of solid and fluid inclusions (Figure 11f). CT provided better visualisation of this area, and shows a large amount of solid inclusions of pyrite and carbonates surrounded by fluid cavities, negative crystals and a trapped piece of the host rock (Figure 12).

The open cavities on the pinacoidal faces of vaso emeralds (again, see Figures 2 and 8) correspond to etch pits caused by post-growth, preferential etching along dislocation lines, as previously observed in pegmatitic beryls from Australia, China and Brazil, as well as in Colombian emeralds from the Muzo and Yacopí mines (Medina *et al*. 1983; Sunagawa & Urano 1999; Tempesta *et al*. 2011). The etch pits have pointed bottoms (called P-type) and are oriented parallel to the *c*-axis. Their shape in cross-section depends on (1) the symmetry of the face where they formed at the outcrop of dislocations and (2) the dissolution conditions (Sunagawa & Urano 1999). On the basis of our data, it was not possible to identify the type(s) of dislocations. Thus, they could be edge, screw or mixed dislocations, given that these dislocations play the same role in etching but not in growth (Sunagawa 2005). Some of them are probably screw dislocations, which generate growth spirals and could explain the formation of the large central cavity in some vaso emeralds. The hollow core can form in either of the two following ways: (1) along dislocation lines with a large Burgers vector (generally >10 Å), at the centre of a growth spiral; or (2) from a basin-like depression generated by a number of dislocations with a small Burgers vector concentrated in a narrow area (Sunagawa & Bennema 1981; Sunagawa 2005).

Etching is favoured where the density of dislocations is higher (Scandale & Zarka 1982; Tempesta *et al*. 2011), so the original presence of bundles of parallel dislocations is plausible in vaso emeralds. Due to the high

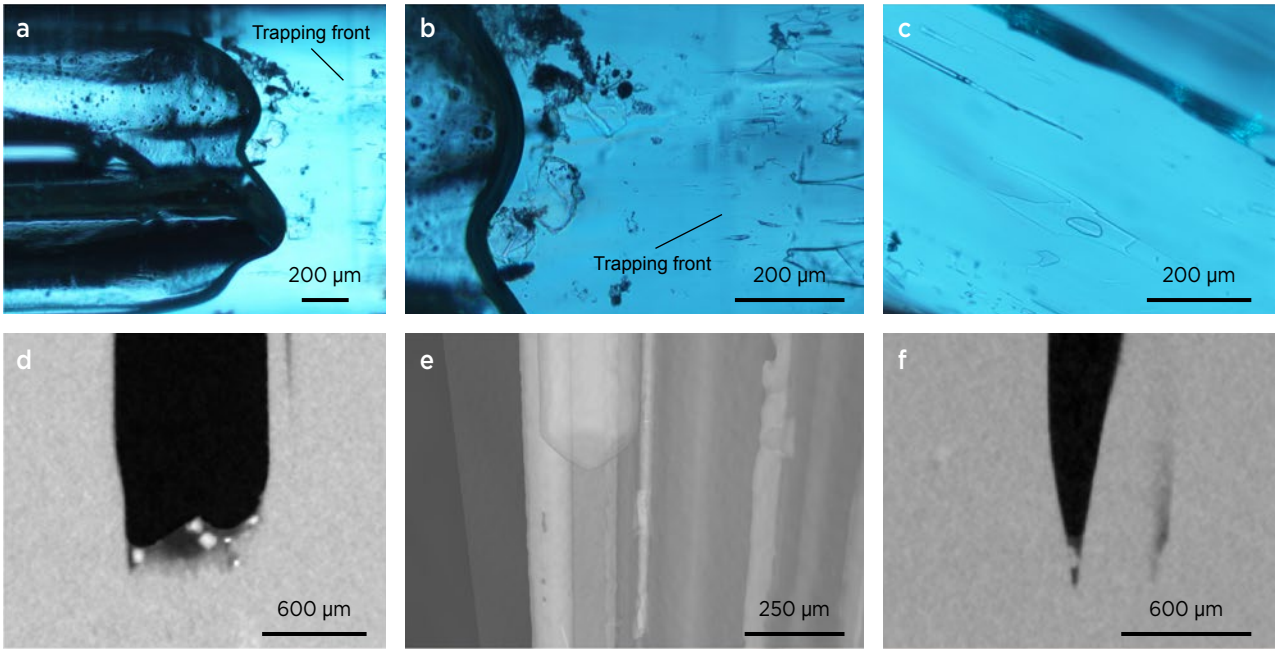

Figure 10: Images taken with an optical microscope (**a**–**c**) show that the ends of the cavities in the vaso emerald in Figures 8b and 8c appear rounded. (a, b) The cavities are located near the trapping front of fluid inclusions and a boundary in the chemical composition of the crystal. (c) Most of the fluid inclusions appear jagged and are characterised by the presence of a CO_2 gas phase and halite crystals. CT images (**d**–**f**) show that cavities that initially appear round-ended are actually composed of several pointed ends. This is due to the fact that, as seen with the microscope, the bottom of the cavity is obscured by micro-inclusions (e.g. carbonates and other minerals). Photomicrographs by G. Giuliani and CT images by C. Morlot.

strain concentrated along their surface outcrops, etching will generate several etch pits, resulting in parallel cavities (Figures 9 and 11). These cavities are characterised by steps with minute unevenness (Figure 9b, c), which differentiates them from smooth growth steps (Sunagawa 2005). The steepness of the cavities' walls is determined by the relative rates of dissolution parallel to the crystal surface and along the dislocation lines. If the dissolution rate along the dislocation is much higher than it is parallel to the surface, the walls are steep, as

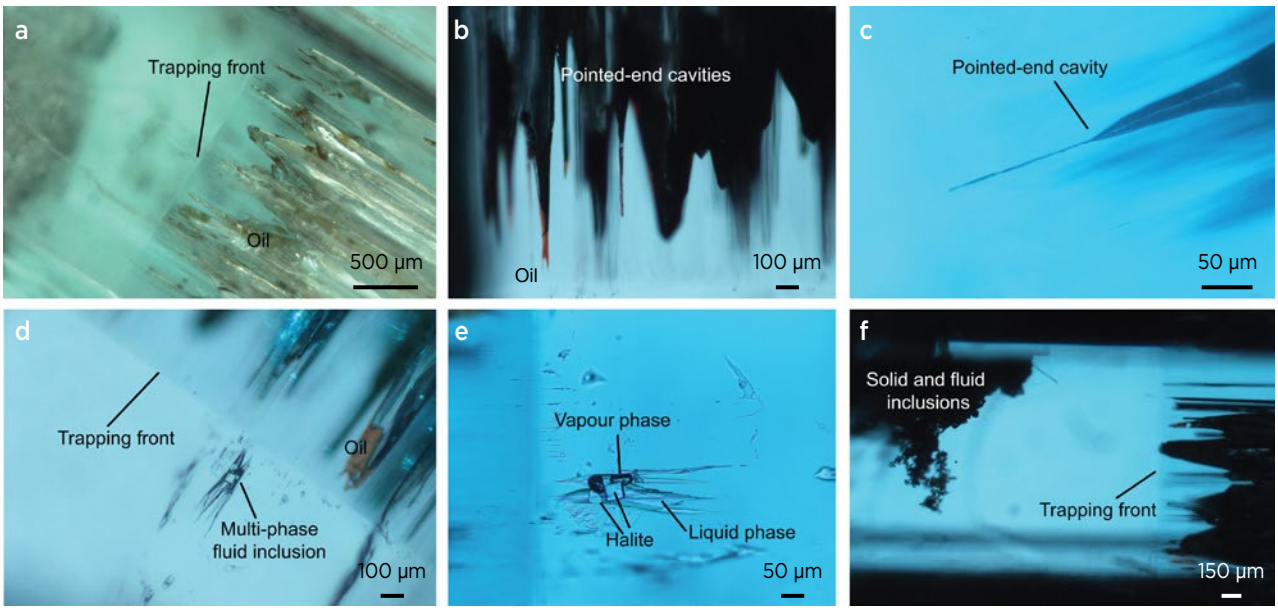

Figure 11: Optical photomicrographs of the cavities in the vaso emerald in Figure 8a reveal that their pointed ends (**a**–**c**) terminate near a trapping front of three-phase fluid inclusions. Some of the cavities are partially filled by oil used for clarity enhancement (a, b and d). On the other side of the trapping front are fluid inclusions containing one or more halite crystals, along with vapour and liquid phases (**d**, **e**). High concentrations of solid and fluid inclusions (**f**) located near the base of the crystal are shown in greater detail in Figure 12. Photomicrographs by G. Giuliani.

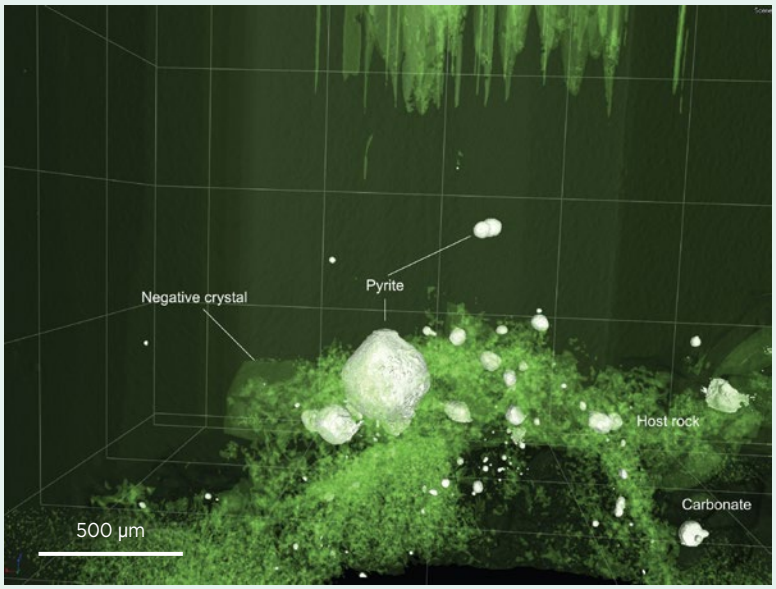

Figure 12: A false-colour CT image shows details of the concentration of solid and fluid inclusions near the base of the vaso emerald shown in Figure 8a (also seen in Figure 11f). This zone consists of pyrite and carbonate inclusions associated with fluid cavities, negative crystals and a fragment of the host rock. Image by C. Morlot.

in our samples (Kurumathoor & Franz 2018). When the dislocation line ends, dissolution in that direction stops, which explains why the cavities do not extend along the entire length of a crystal. This is probably related to variations in physicochemical conditions during the emeralds' growth, as indicated by two features: (1) The dislocations end near a growth band that is visible as a change in the emerald's colour (Figure 11a, d). This growth band corresponds to a compositional fluctuation. The saturation degree likely changed too, because the dislocation ceased at the same location. (2) This growth band also corresponds to fluctuations in the number of fluid inclusions, which is emphasised by a sharply demarcated trapping front (Figure 11d, e).

Spongy Emerald

The spongy emerald sample (1.7 × 1.1 × 1.1 cm ; Figure 13a) is stubby with large pinacoidal faces and relicts of prism $\{10\bar{1}0\}$ faces that appear to be striated vertically. Its name reflects the appearance resulting from the presence of many cavities with irregular cross-sections that are visible on the pinacoidal faces (Figure 13b). These cavities extend through the crystal and have steep walls (Figure 13c, d), similar to those in the vaso emeralds. The coexistence of neighbouring cavities explains the presence of the striations on the prism faces. The cavities can be partially filled by dolomite (Schmetzer *et al.* 2020) and in some cases pyrite (as in the present specimen), which accumulate on their bottoms (Figure 13c, d). Sometimes the filling occupies nearly the entire length of the cavity (Figure 13b, d).

This sample could be considered a special case of vaso emerald. When dislocations extend the full length of a crystal, dissolution can proceed all the way through a hexagonal prism, creating a spongy emerald.

Spear-Shaped Emerald

The spear-shaped emerald (23 × 1.5 × 1.5 mm) has a hexagonal prismatic habit bounded by first-order prism $\{10\bar{1}0\}$ faces, as well as small dipyramidal $\{11\bar{2}2\}$ and dihexagonal prism $\{12\bar{3}0\}$ faces. The pinacoidal termination (0001) was replaced by a sharp point, which gives this emerald a spear-like shape (Figure 14).

The pointed tip is the result of etching that proceeds not only from outcrops of dislocations but also from tube-like inclusions on pinacoidal faces, in addition to etching along corners and edges. This was previously documented by Sunagawa (2005), who described the effects of hydrothermal dissolution on pegmatitic beryls.

Emerald-Replaced Fossil Gastropods

The fossil gastropods are exceptional samples resulting from the epigenetic replacement of aragonite by calcite and then emerald (Vuillet *et al.* 2002). The samples examined for this report show various degrees of deformation due to synsedimentary compaction. All are incomplete (Figure 15), having been more-or-less fragmented because of their fragility compared to the surrounding black shale matrix. Details pertaining to the identification of the gastropods, and their ages, are given in Box A.

The timeline of the shell mineralisation process can be reconstructed as follows: Approximately 135 Ma ago (Lower Cretaceous) the gastropods lived in a low-energy marine environment on a loose substrate. After

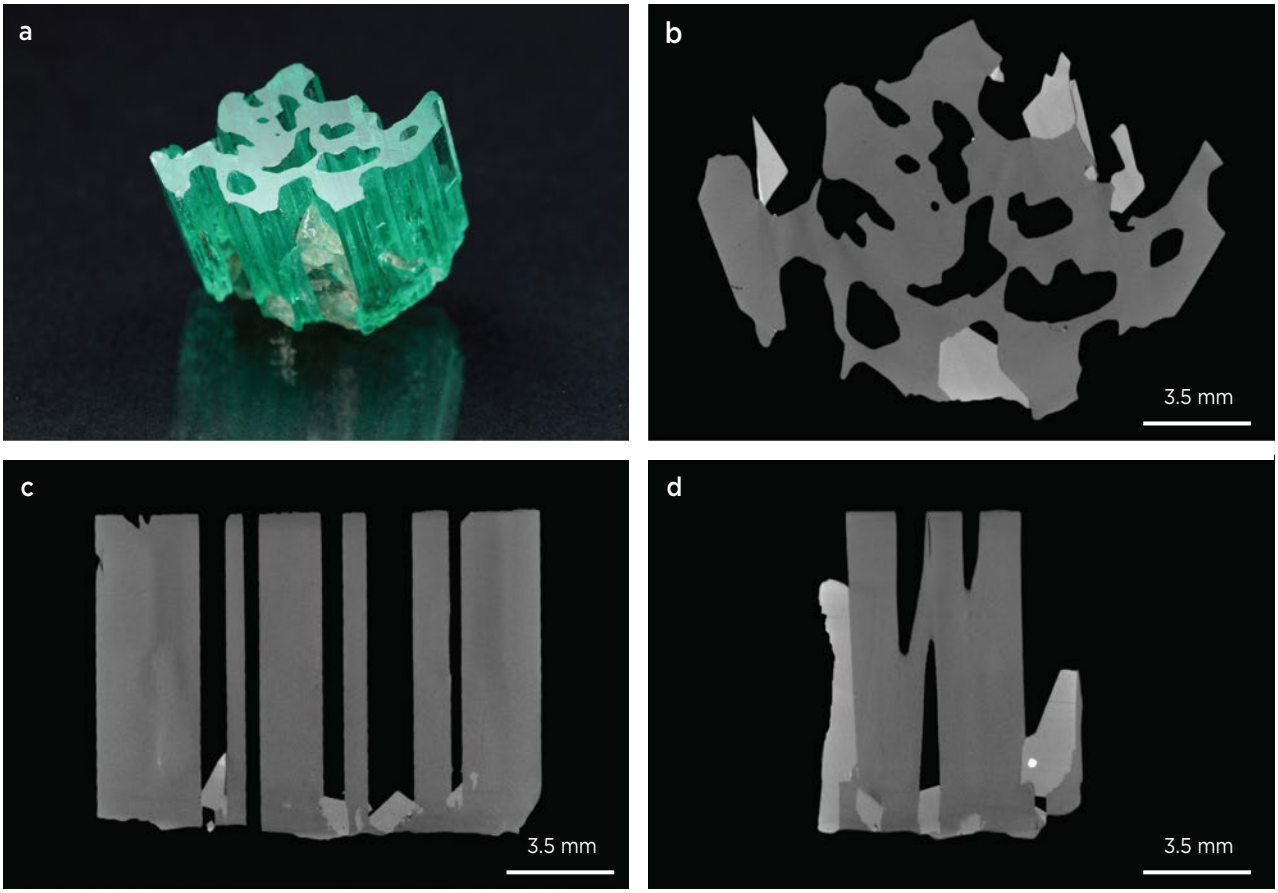

Figure 13: (**a**) A spongy emerald (1.7 × 1.1 × 1.1 cm) from Chivor is characterised by cavities parallel to the *c*-axis. CT images show three cross-sections of this sample: (**b**) A section perpendicular to the *c*-axis illustrates the irregular outlines of the cavities. (**c**, **d**) Two sections parallel to the *c*-axis (and perpendicular to one another) indicate that the cavities developed along the entire crystal length and are often partially filled by solid inclusions, especially carbonates. Photo by G. Martayan and CT images by C. Morlot.

their death, they were buried in the sediment. The aragonitic shells of the gastropods (1.5–2 mm thick) were completely replaced by calcite, and then dissolved by fluid circulation in the black shale, leaving only their imprints. About 70 Ma later, tectonic constraints in the sedimentary basin of the Eastern Cordillera favoured the circulation of hot basinal brines along faults and fractures in the fossil-bearing calcareous black shales of the Guavio Formation. The brines transported Al, Be, Si, Cr and V, allowing for the precipitation of emerald (Giuliani *et al*. 2019). The emerald filled the spaces left vacant by the shells' dissolution, replicating the external morphologies of the gastropods.

Thus, the emerald-replaced gastropods resulted from a combination of the following conditions: (1) the development of fractures in a fossil-bearing level of the host black shale; (2) the circulation of hot brines enriched in emerald-forming components; (3) the high permeability of the sediment, in part due to the cavities left by the dissolved shells; and (4) preservation of the emerald-replaced fossils within the black shales until their discovery.

Figure 14: On this 0.75 ct spear-shaped emerald (23 × 1.5 × 1.5 mm) from Chivor, the pinacoidal termination was etched into a sharp point, which gives the specimen its spear shape. Photo by G. Martayan.

Figure 15: These emerald-replaced gastropods (*Pictavia* and *Pseudomelania*) are some of those studied for this report. From left to right, their dimensions are 2.2 × 1.5 cm, 1.1 × 1.0 cm, 1.4 × 1.0 cm, 1.9 × 1.0 cm and 1.2 × 0.6 cm. From the collection of R. Titeux; photo by L.-D. Bayle.

Box A: Taxonomy and Age of the Emerald-Replaced Fossil Gastropods

Our observations of the emerald-replaced gastropods from the Matecaña mine in the Gachalá mining district enabled us to identify the genera of 15 of the 20 specimens.

Specimen OTH118-4 (Figure A-1) is an intact coiled shell, except for the missing base and operculum, and could be attributed to the genus *Ataphrus* s. str. (superfamily Trochacea, family Ataphridae). This and similar specimens had a slightly cyrtoconoid shell formed by four convex turns with a smooth surface, separated by a linear suture. The sample in Figure A-1 has a height of 10 mm and a width of 12 mm, with a growth angle ranging from 97° (first turns) to 92° (last turns). The genus *Ataphrus* is known from the mid-Jurassic to the Upper Cretaceous in Mesogean regions (e.g. maritime areas located, during the Mesozoic, between two large continental blocks consisting of Eurasia and North America on one side and India, Africa and South America on the other).

Specimen OTH081-8 (Figure A-2) consists of a coiled shell fragment with internal filling at the base and operculum (which is partially preserved). Despite its rather poor preservation status, it can be attributed to the genus *Pseudomelania* and subgenus *Oonia* (superfamily Loxonematacea, family Pseudomelaniidae). Its last three turns—relatively high, very slightly domed and apparently smooth—are separated by a linear suture; the growth angle of the last turn is 35°. The base is not umbilicated, and the internal section of the operculum is oval, distinctly higher than wide. Specimen OTH118-1 in Figure A-2 was also identified as the subgenus *Pseudomelania* (*Oonia*), which is known from the Triassic to the Lower Cretaceous (Barremian age), but the species of Gachalá is much narrower in shape than those so far described

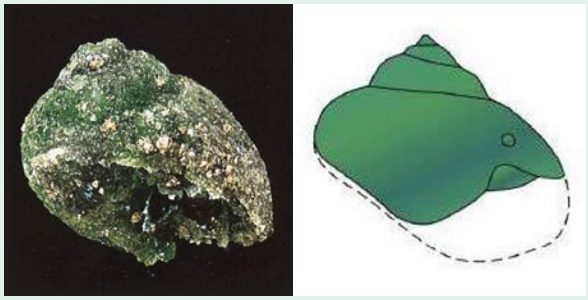

Figure A-1: Emerald-replaced gastropod specimen OTH118-4 (10 × 12 mm) is possibly of the genus *Ataphrus*. The accompanying reconstruction diagram shows the completeness of the fossil. From the collection of G. Eringer (MultiAxes); photo by L.-D. Bayle.

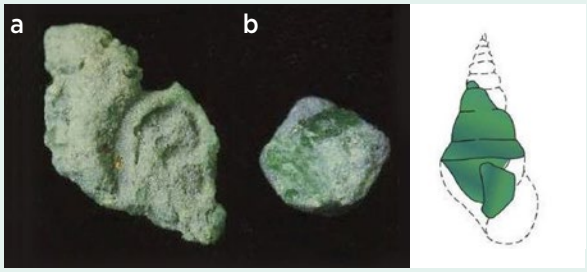

Figure A-2: Emerald-replaced gastropod specimens OTH081-8 (**a**: 12.0 mm long) and OTH118-1 (**b**: 5.5 mm diameter) are of the genus *Pseudomelania*, subgenus *Oonia*. The completeness of OTH081-8 is illustrated in the accompanying reconstruction diagram. From the collection of R. Titeux; photo by H. Conge.

Figure A-3: Specimens OTH081-4 (left, 22 × 15 mm) and OTH081-5 represent the genus *Ampullospira*, sub-genus *Pictavia*. The accompanying reconstruction diagram is a composite from the two specimens. From the collection of R. Titeux; photo by L.-D. Bayle.

(Leymerie 1841–1842) in the Tithonian and in the Lower Cretaceous of the Mesogean regions.

Twelve specimens (JR001-1 and -2, OTH081-3 to -7, OTH118-2, -3, -5 and -6, and VC001-1; e.g. Figure A-3) belong to a species of the genus *Ampullospira* and subgenus *Pictavia* (superfamily Naticacea, family Globulariidae). The summary description and reconstruction given here are based on the five best-preserved specimens (OTH081-4, -5, -7, OTH118-5 and JR001-2). They have a regular shell formed from five to six turns that are weakly domed, smooth and separated by a finely canaliculated suture. The last turns occupy almost two-thirds of the total height. The holostome is markedly higher than wide, with a thick, concave columellar border, and an orthoclinic labral border. The maximum dimensions of the samples of this species are: total height 21 mm, height of the last turns 15 mm, operculum height 12 mm, width 14.5 mm and growth angle 67.5°. The subgenus *Ampullospira* (*Pictavia*) appeared in the Triassic, but this species is clearly more slender than *Ampullospira* (*Pictavia*) *laevigata* (Deshayes, in Leymerie 1841–1842), from the Hauterivian-age Paris basin and is the only post-Jurassic *Pictavia* known so far.

The three taxonomic genera of gastropods among the examined samples probably represent new species so far not reported from any other localities of the Guavio Formation or elsewhere. However, it is not possible to give them species names due to the insufficient state of their preservation. They are certainly of the same age (Berriasien) as the ammonites found in the Chivor mining district (Berriasellidae subfamily of the Berriasellinae and Neocomitinae subfamilies; Branquet 1999). Based on the three taxonomic genera that were identified (*Ataphrus*, *Pseudomelania* and *Ampullospira*), the gastropods had an indisputable marine origin, belonging to benthic communities typical for internal platforms and/or loose paleosubstrates (i.e. sediments). The specimens we examined showed no signs of superficial degradation, which implies a paleobiotope (i.e. living environment) with weak hydrodynamics.

Horseshoe-shaped Emerald

The horseshoe-shaped emerald specimen exhibits an unusual habit with only four of the six prism faces fully developed (Figure 16a). The other two prism faces, as well as the two pinacoidal faces, are incomplete due to the growth of proto- or syngenetic solid inclusions, (i.e. calcite crystals and a larger, doubly terminated quartz crystal; Figure 16b).

The formation mechanism of a horseshoe-shaped emerald was previously described by Graziani *et al.* (1981), who studied crystals from Brazil that formed during a metasomatic-hydrothermal episode in pegmatitic veins. According to those authors, non-uniform growth due to directional fluid flow resulted in a trough-like crystal with a horseshoe-shaped cross-section. Crystal growth occurred mainly where the flow of fluids was highest and, thus, a euhedral beryl bounded by prism faces developed. Where the flow of fluids was weaker and growth was hampered by the presence of proto-syngenetic minerals, the beryl could not grow properly, so it could not develop all the prism faces. This resulted in an incomplete hexagonal prismatic habit that took the appearance of a horseshoe in cross-section.

Calcitised Trapiche Emerald

This specimen exhibits elements characteristic of trapiche texture (Figure 17a), with a core, prismatic growth sectors and sector boundaries (for details, see Pignatelli *et al.* 2015). The core and sector boundaries were found to consist of calcite with fragments of the calcitised black shale matrix. This specimen appears whitish instead of green because the original emerald was almost totally replaced by calcite (the presence of which was confirmed by X-ray diffraction).

CT imagery was coupled with chemical mapping by micro-XRF in order to better understand the 3D distribution of elements in the sample's volume. The mapping helped distinguish relict emerald in the different zones where it was replaced by calcite. In the element maps, areas enriched in Ca correspond to the presence of calcite

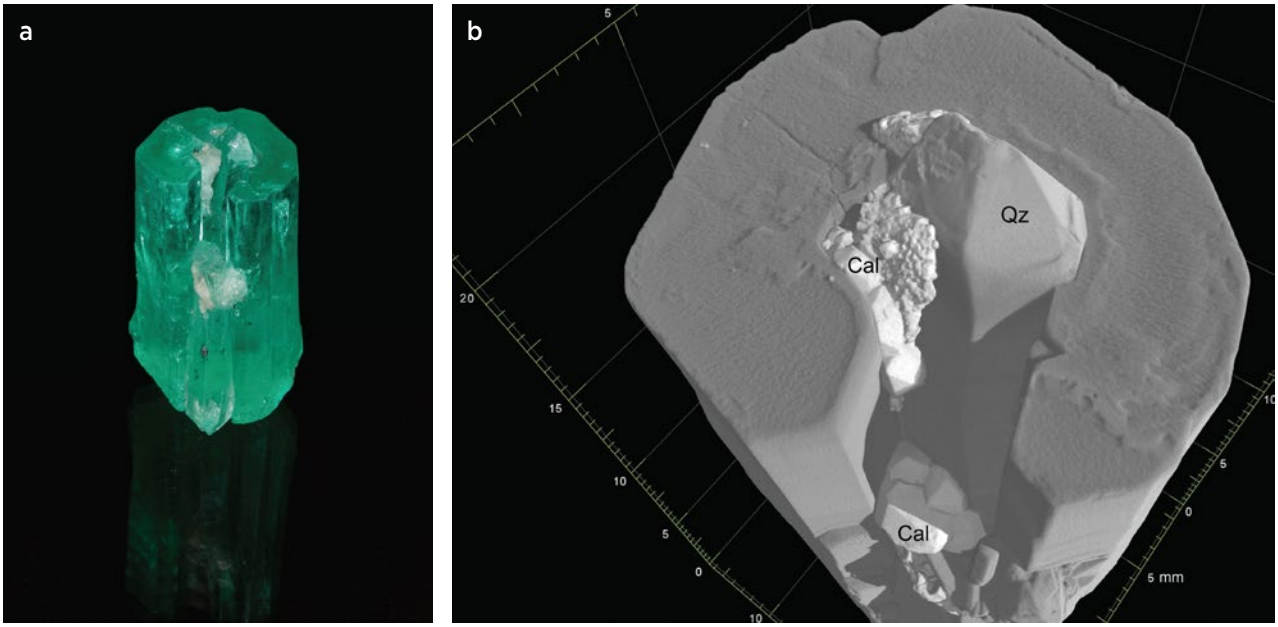

Figure 16: Optical (**a**) and CT (**b**) images of the horseshoe-shaped emerald (19 mm high × 11 mm diameter) from Muzo show that the crystal did not develop into a regular hexagonal prism due to the presence of proto- or syngenetic solid inclusions of calcite (Cal) and quartz (Qz). Photo by G. Martayan and CT image by C. Morlot.

(Figure 17b, c), while the superposition of Cr and Al suggest that relict portions of emerald remain in the prismatic growth sectors (Figure 17d). The Si distribution shows that this element was not always associated with Al (Figure 17e), implying the presence of another silicate in addition to beryl. Analysis of all the compositional maps points to it being quartz (Figure 17f), which was found in the sector boundaries, as well as in the core. Quartz also occurred in prismatic growth sectors, between emerald relics (Figure 17b, c). The presence of S, Ti, Fe and Mn (analysed but not shown in these maps) around the calcitised trapiche emerald and in its fractures indicates the formation of a reaction edge consisting of oxides/hydroxides and anhydrite. The oxides/hydroxides contain Fe and/or Mn, and are mixed with disseminated crystals of rutile, according to the distribution of these elements in the XRF maps. The distribution of S partially coincided with that of Ca (due to the precipitation of anhydrite), but it also indicates the presence of native sulphur in some portions of the sample.

According to the XRF and CT data, a four-stage formation model can be proposed for this sample:

1. A trapiche emerald formed in black shale, as described by Pignatelli *et al.* (2015).
2. The subsequent circulation of hydrothermal fluids in fractures and brecciated zones caused metasomatism of the black shale, leading to the leaching of major components (Al, Si, K, Ti and Mg), trace elements (Ba, Be, Cr and V) and rare-earth elements from the host rock. This also caused dissolution of the trapiche emerald, as well as the crystallisation of calcite.
3. The precipitation of quartz in the fractures and in areas of higher porosity—in particular the sector boundaries and core of the trapiche emerald—suggests the circulation of a Si-rich fluid following the metasomatic episode.
4. Late weathering processes favoured the deposition of Fe oxides/hydroxides, anhydrite and native sulphur by the destabilisation of pyrite.

CONCLUSIONS

The formation of these rare and unique mineralogical oddities is related to the specific geological context of emerald deposits in Colombia. The key to understanding their formation is the circulation of fluids along tectonic structures or lithological contacts: the fluid overpressure in black shales caused hydraulic fracturing and brecciation, the opening of veins that were filled by carbonates and pyrite, and the precipitation of emerald itself. During subsequent decompression, the composition of the fluids locally changed, modifying the emerald-fluid equilibrium and leading to etching processes after the cessation of emerald growth. Different degrees of etching gave rise to the spongy, spear-shaped and vaso emeralds described in this study.

The calcitised trapiche emerald provides an example of another effect of post-growth mineral-fluid

interactions. The circulation of hydrothermal fluids other than those from which emerald precipitated was responsible for the dissolution of emerald and its replacement by calcite, as well as the later crystallisation of quartz after the metasomatism of the host black shale.

Variations in composition and flow of fluids affected the growth of the sceptre and horseshoe-shaped emeralds, respectively, resulting in their particular forms. However, the sceptre emerald was formed in two growth steps under different conditions, while the horseshoe-shaped emerald resulted from non-uniform and incomplete growth. The fibrous emerald is the result of a combination of growth and post-growth processes: aggregation of crystals elongated parallel to the *c*-axis, followed by etching, which contributed to enlarging the voids between the crystals.

Fluid circulations are also responsible for the formation of emerald-replaced gastropods in fossil-bearing calcareous black shales. After the aragonitic shell material was replaced by calcite, fluids caused the dissolution of the carbonate and the spaces were epigenetically filled by emerald.

The spectacular forms and attractive green colour of these Colombian emerald oddities make them unique and very interesting gemmological samples not found elsewhere in the world.

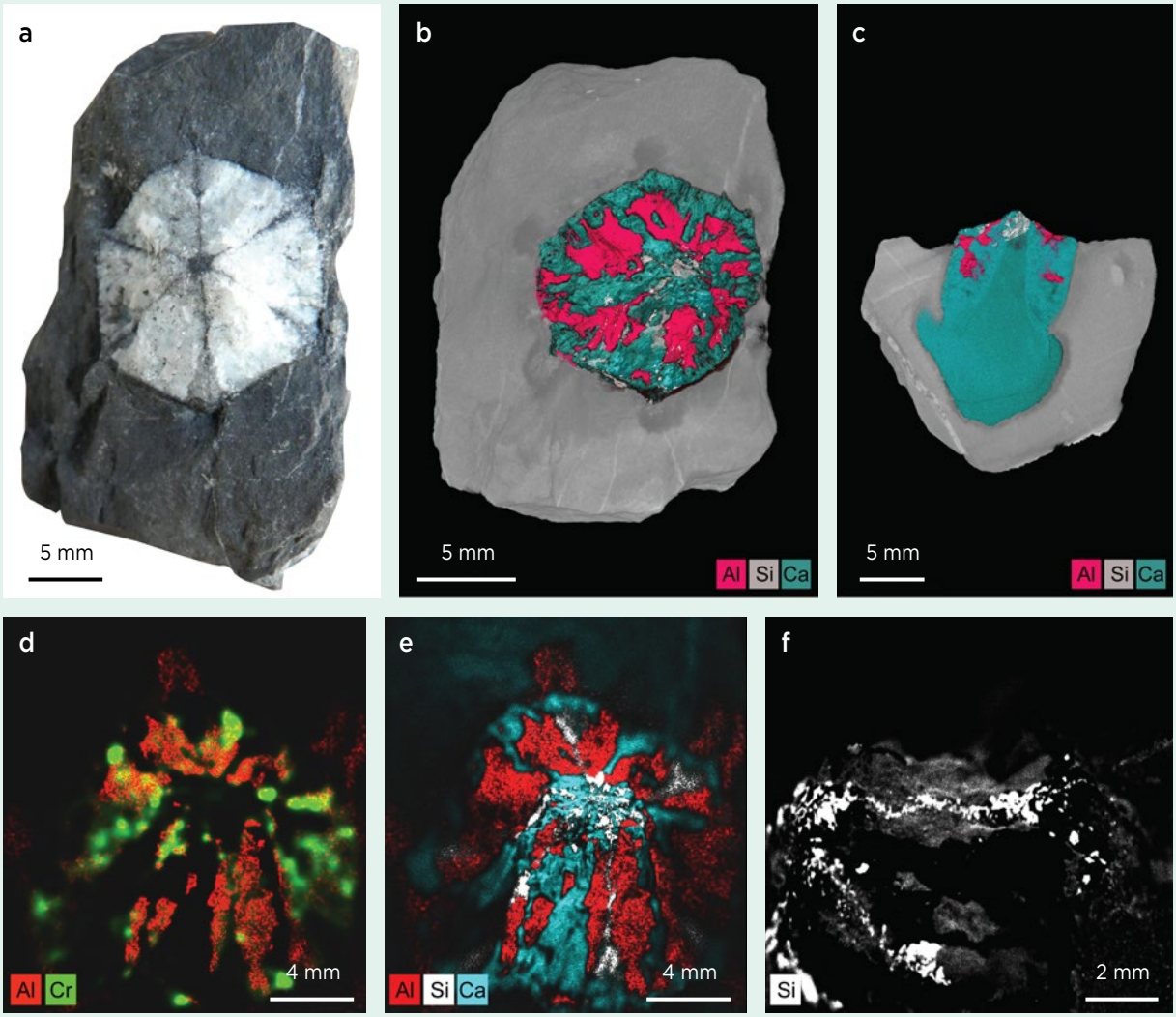

Figure 17: (**a**) This calcitised trapiche emerald sample is from Muzo. Combined CT and XRF mapping images illustrate the distribution of chemical elements in the sample. Sections of the sample are shown (**b**) parallel and (**c**) perpendicular to the *c*-axis. (**d**) The presence of Cr and Al help locate relict areas of emerald. (**e**) The distribution of Si, Al and Ca indicates the presence of another silicate and calcite. (**f**) The Si map shows that quartz is present in the growth sectors and in the core of the calcitised trapiche emerald. Images d and e are taken at the core of the trapiche texture; image f is a lateral view of d and e. Specimen courtesy of H. Ramírez; photo and CT/XRF mapping images by C. Morlot and L. Salsi.

REFERENCES

Authier, A. & Zarka, A. 1994. X-ray topographic study of the real structure of minerals. *In*: Marfunin, A.S. (ed) *Composition, Structure, and Properties of Mineral Matter: Concepts, Results, and Problems*. Advanced Mineralogy, **1**, Springer-Verlag, Berlin, Germany, 221–233, https://doi.org/10.1007/978-3-642-78523-8_12.

Branquet, Y. 1999. *Étude structurale et métallogénique des gisements d'émeraude de Colombie: Contribution à l'histoire tectono-sédimentaire de la Cordillère Orientale de Colombie*. PhD thesis, Université de Lorraine, Nancy, France, 295 pp.

Branquet, Y., Cheilletz, A., Giuliani, G., Laumonier, B. & Blanco, O. 1999a. Fluidized hydrothermal breccia in dilatant faults during thrusting: The Colombian emerald deposits. *Geological Society, London, Special Publications*, **155**, 183–195, https://doi.org/10.1144/gsl.Sp.1999.155.01.14.

Branquet, Y., Laumonier, B., Cheilletz, A. & Giuliani, G. 1999b. Emeralds in the Eastern Cordillera of Colombia: Two tectonic settings for one mineralization. *Geology*, **27**(7), 597–600, https://doi.org/10.1130/0091-7613(1999)027<0597:Eiteco>2.3.Co;2.

Branquet, Y., Giuliani, G., Cheilletz, A. & Laumonier, B. 2015. Colombian emeralds and evaporites: Tectono-stratigraphic significance of a regional emerald-bearing evaporitic breccia level. *13th Biennial Meeting of the Society for Geology Applied to Mineral Deposits*, Nancy, France, 24–27 August, 1291–1294.

Cheilletz, A., Féraud, G., Giuliani, G. & Rodriguez, C.T. 1994. Time-pressure and temperature constraints on the formation of Colombian emeralds: An $^{40}Ar/^{39}Ar$ laser microprobe and fluid inclusion study. *Economic Geology*, **89**(2), 361–380, https://doi.org/10.2113/gsecongeo.89.2.361.

Flude, S., Haschke, M. & Storey, M. 2017. Application of benchtop micro-XRF to geological materials. *Mineralogical Magazine*, **81**(4), 923–948, https://doi.org/10.1180/minmag.2016.080.150.

Giuliani, G., Cheilletz, A., Dubessy, J. & Rodriguez, C.T. 1991. H_2O-NaCl-$CaCl_2$-bearing fluids in emeralds from the Vega San Juan mine, Gachalá District, Colombia. *Plinius*, No. 5, 90.

Giuliani, G., Cheilletz, A., Dubessy, J. & Rodriguez, C.T. 1993. Chemical composition of fluid inclusions in Colombian emerald deposits. *Proceedings of the Eighth Quadrennial IAGOD Symposium*, Ottawa, Ontario, Canada, 12–18 August 1990, 159–168.

Giuliani, G., France-Lanord, C., Cheilletz, A., Coget, P., Branquet, Y. & Laumomnier, B. 2000. Sulfate reduction by organic matter in Colombian emerald deposits: Chemical and stable isotope (C, O, H) evidence. *Economic Geology*, **95**(5), 1129–1153, https://doi.org/10.2113/gsecongeo.95.5.1129.

Giuliani, G., Branquet, Y., Fallick, A.E., Groat, L.A. & Marshall, D. 2015. Emerald deposits around the world, their similarities and differences. *InColor*, December (special issue), 56–69.

Giuliani, G., Branquet, Y., Fallick, A.E., Groat, L.A. & Marshall, D. 2016. Classification géologique des gisements d'émeraude. *Revue de Gemmologie* A.F.G., No. 196, 12–20.

Giuliani, G., Groat, L.A., Marshall, D., Fallick, A.E. & Branquet, Y. 2019. Emerald deposits: A review and enhanced classification. *Minerals*, **9**(2), article 105 (63 pp.), https://doi.org/10.3390/min9020105.

Graziani, G., Scandale, E. & Zarka, A. 1981. Growth of a beryl single crystal – History of the development and the genetic medium. *Journal of Applied Crystallography*, **14**(4), 241–246, https://doi.org/10.1107/s002188988100928x.

Hall, M.L. 1976. *Mineralogía y Geoquímica de las Vetas Esmeraldíferas de Muzo, Departamento de Boyacá con Implicaciones en la Prospección Futura de Esmeraldas en Otras Partes de Colombia.* Compilación de los Estudios Geológicos Oficiales en Colombia, Boyacá, 326 pp.

Johnson, P.W. 1961. The Chivor emerald mine. *Journal of Gemmology*, **8**(4), 126–152, https://doi.org/10.15506/JoG.1961.8.4.126.

Klein, F. 1941. *Smaragde unter dem Urwald: Meine Entdeckungs- und Erlebnisreisen in Lateinamerika*. Oswald Arnold Verlag, Berlin, Germany, 285 pp.

Kurumathoor, R. & Franz, G. 2018. Etch pits on beryl as indicators of dissolution behaviour. *European Journal of Mineralogy*, **30**(1), 107–124, https://doi.org/10.1127/ejm/2018/0030-2703.

Leymerie, A. 1841–1842. Mémoire sur le terrain crétacé du département de l'Aude, contenant des considérations générales sur le terrain néocomien. *Mémoire de la Société Géologique de France*, **4**, 291–364 (1841); 1–34 (1842).

Mantilla Figueroa, L.C., Silva Arias, A., Serrano Dominguez, J.J., Conde Gómez, J., Gómez Durán, C., Ramírez Arias, J.C., Meza Ortíz, J.A., Pelayo Serrano, Y. *et al.* 2007. *Investigación Petrográfica y Geoquímica de las Sedimentitas del Cretácico Inferior (K1) y sus Manifestaciones Hidrotermales Asociadas; Planchas 169, 170, 189, 190 (Cordillera Oriental): Implicaciones en la Búsqueda de Esmeraldas*. Instituto Colombiano de Geología y Minería (INGEOMINAS), Bogotá, Colombia, Acuerdo Especifico N°01 – Complementario al Convenio Marco de Cooperación 005/2001, 330 pp.

Medina, J.A., Morante, M. & Leguey, S. 1983. Natural etch pits in beryl related with the structure. *Bulletin de Minéralogie*, **106**(3), 293–297, https://doi.org/10.3406/bulmi.1983.7708.

Morlot, C., Pignatelli, I., Giuliani, G., Sterpenich, J., Boiron, M.C., Ohnenstetter, D., Andriamamonjy, A., Raoul, J. *et al.* 2016. La tomographie à rayons X et ses applications en gemmologie : Exemples de l'émeraude trapiche et

du grenat démantoïde. *Revue de Gemmologie A.F.G.*, No. 198, 13–18.

Nishinaga, T. 2002. Microchannel epitaxy: An overview. *Journal of Crystal Growth*, **237–239**(2), 1410–1417, https://doi.org/10.1016/s0022-0248(01)02227-8.

Nishinaga, T., Nakano, T. & Zhang, S. 1988. Epitaxial lateral overgrowth of GaAs by LPE. *Japanese Journal of Applied Physics*, **27**(6A), L964–L967, https://doi.org/10.1143/jjap.27.L964.

Ottaway, T.L. 1991. *The geochemistry of the Muzo emerald deposit, Colombia*. MS thesis, University of Toronto, Ontario, Canada, xii + 216 pp.

Ottaway, T.L., Wicks, F.J., Bryndzia, L.T., Kyser, T.K. & Spooner, E.T.C. 1994. Formation of the Muzo hydrothermal emerald deposit in Colombia. *Nature*, **369**(6481), 552–554, https://doi.org/10.1038/369552a0.

Peretti, A. & Falise, T. 2018. *Magnificent Green: On the Trail of the Legendary Colombian Emerald*. GRS GemResearch Swisslab, Lucerne, Switzerland, 337 pp.

Pignatelli, I., Giuliani, G., Ohnenstetter, D., Agrosi, G., Mathieu, S., Morlot, C. & Branquet, Y. 2015. Colombian trapiche emeralds: Recent advances in understanding their formation. *Gems & Gemology*, **51**(3), 222–259, https://doi.org/10.5741/gems.51.3.222.

Richard, A., Morlot, C., Créon, L., Beaudoin, N., Balistky [*sic*], V.S., Pentelei, S., Dyja-Person, V., Giuliani, G. *et al*. 2019. Advances in 3D imaging and volumetric reconstruction of fluid and melt inclusions by high resolution X-ray computed tomography. *Chemical Geology*, **508**, 3–14, https://doi.org/10.1016/j.chemgeo.2018.06.012.

Roedder, E. 1984. *Fluid Inclusions*. Reviews in Mineralogy, **12**, Mineralogical Society of America, Washington DC, USA, vi + 646 pp., https://doi.org/10.1515/9781501508271.

Scandale, E. & Zarka, A. 1982. Sur l'origine des canaux dans les cristaux. *Journal of Applied Crystallography*, **15**(4), 417–422, https://doi.org/10.1107/s0021889882012291.

Schmetzer, K., Martayan, G. & Ortiz, J.G. 2020. History of the Chivor emerald mine, part 1 (1880–1925): From rediscovery to early production. *Gems & Gemology*, **56**(1), 66–109, https://doi.org/10.5741/gems.56.1.66.

Sunagawa, I. 2005. *Crystals: Growth, Morphology and Perfection*. Cambridge University Press, Cambridge, 308 pp.

Sunagawa, I. & Bennema, P. 1981. Observations of the influence of stress fields on the shape of growth and dissolution spirals. *Journal of Crystal Growth*, **53**(3), 490–504, https://doi.org/10.1016/0022-0248(81)90130-5.

Sunagawa, I. & Urano, A. 1999. Beryl crystals from pegmatites: Morphology and mechanism of crystal growth. *Journal of Gemmology*, **26**(8), 521–533, https://doi.org/10.15506/JoG.1999.26.8.521.

Takahashi, Y., Imai, H., Hosaka, M., Kawasaki, M. & Sunagawa, I. 2004. Epitaxial lateral overgrowth (ELO): The mechanism of formation of scepter, skeletal, cathedral and related quartz morphologies. *European Journal of Mineralogy*, **16**(6), 1009–1017, https://doi.org/10.1127/0935-1221/2004/0016-1009.

Tempesta, G., Scandale, E. & Agrosì, G. 2011. Striations and hollow channels in rounded beryl crystals. *Periodico di Mineralogia*, **80**(1), 75–87, https://doi.org/10.2451/2011PM0006.

Vuillet, P., Giuliani, G., Fischer, J.-C. & Chiappero, P.-J. 2002. Les émeraudes de Gachalá : Historique, genèse et curiosités paléontologiques. *Le Règne Minéral*, No. 46, 5–18.

Weldon, R., Ortiz, J.G. & Ottaway, T. 2016. In Rainier's footsteps: Journey to the Chivor emerald mine. *Gems & Gemology*, **52**(2), 168–187, https://doi.org/10.5741/gems.52.2.168.

The Authors

Dr Isabella Pignatelli, Christophe Morlot and Lise Salsi
Université de Lorraine,
GeoRessources UMR 7359 CNRS-UL, BP 70239,
54506 Vandœuvre-lès-Nancy cedex, France
Email: isabella.pignatelli@univ-lorraine.fr

Dr Gaston Giuliani
Université Paul Sabatier, GET/IRD,
UMR CNRS-IRD-CNES 5563,
14 avenue Edouard Belin, 31400 Toulouse, France
and
Université de Lorraine, CRPG UMR 7358 CNRS-UL,
15 rue Notre-Dame-des-Pauvres, BP 20,
54501 Vandœuvre-lès-Nancy cedex, France

Gérard Martayan
Independent researcher, Paris, France
Email: gmartayan@gmail.com

Acknowledgements

The authors thank the emerald collectors who made it possible to carry out this study. Specifically, Hernán Ramírez (MinEmeralds) is acknowledged for supplying the calcitised trapiche emerald sample. We also thank Louis-Dominique Bayle and H. Conge for the gastropod photos. Author GG wishes to pay special tribute to his travelling companions, now deceased—Pierre Vuillet (consultant gemmologist) and Jean-Claude Fischer (honorary professor of paleontology and gastropod specialist at MNHN in Paris, with whom he studied emerald-replaced gastropods in 2002)—and also appreciates the assistance of Daniel Ohnenstetter, a researcher at CPRG/CNRS who worked on Colombian trapiche emeralds and contributed to our team's first publication in 1998.

Pink-Orange Euclase from Bahia, Brazil

Lætitia Gilles-Guéry, Luiza Almeida Villar de Queiroz, Jurgen Schnellrath, Bear Williams, Cara Williams, Tiago Campolina Barbosa, Brendan M. Laurs, Laurence Galoisy and Georges Calas

ABSTRACT: Gem-quality pink-orange euclase was discovered in Bahia, Brazil, in 2015–2016, but did not enter the international gem and mineral trade until mid-2018. There has been limited production to date from two different occurrences, located about 30 km apart, with an estimated production of less than 1 kg total from both sources. Although the pink-orange euclase from each occurrence has distinctive internal features, crystal morphology and colour zoning—allowing rough or cut stones from each locality to be readily separated from one another—their gemmological and chemical properties are similar, indicating they probably formed in a similar geological context. Some notable internal features exhibited by samples from the second reported occurrence include curly/woolly 'fibres' and associated circular/cylindrical inclusions. The unusual pink-orange colouration of this euclase is due to traces of Mn^{3+}.

The Journal of Gemmology, **38**(1), 2022, pp. 44–62, https://doi.org/10.15506/JoG.2022.38.1.44

Euclase—$BeAl(SiO_4)(OH)$—is a rare mineral (especially in facetable quality), which crystallises in the monoclinic system and has a Mohs hardness of 7½. Crystal specimens are highly sought after by collectors, but euclase's perfect cleavage can make it challenging to facet or use in jewellery. The mineral is most often colourless, but also can be blue (sometimes with sharply defined colour zoning), bluish green, green and yellow (e.g. Chaves & Karfunkel 1994). In addition, pale pink euclase has been reported as a few millimetre-sized crystals from the Borborema Pegmatitic Province in Brazil (Eeckhout *et al*. 2002; Cassedanne & Philippo 2015).

Recent finds of pink-orange euclase (Figures 1 and 2) in Brazil have attracted considerable attention due to the material's unusual and beautiful colour, relatively high clarity and well-formed crystals. Interestingly, despite such material being unknown in the mineral world until recently, it was found at two localities in Bahia State in eastern Brazil at approximately the same time. The crystals from both occurrences make attractive mineral specimens and are occasionally facetable into gemstones

Figure 1: This 2.99 ct shield-shaped euclase was characterised for this article (i.e. sample 2). Courtesy of Dudley Blauwet; cutting and photo by Brett Kosnar.

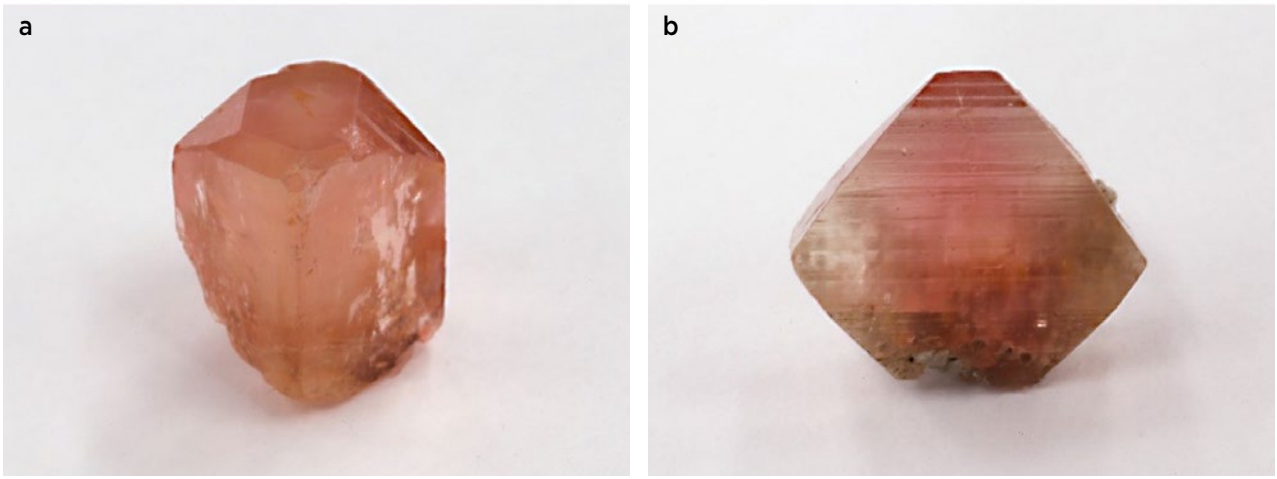

Figure 2: These photos show the typical appearance of euclase crystals from (**a**) the first occurrence (15.1 mm tall) and (**b**) the second occurrence (15.2 mm tall). Photos by J. Schnellrath and L. V. A. de Queiroz.

(see Figure 1 and the cover of this issue). A recent study by Gilles-Guéry *et al*. (2022) ascribes the pink-orange colouration to the presence of Mn^{3+}. That study also includes results of heat-treatment experiments that changed the colour from pink-orange to pink. The present article covers the history and geological aspects of this euclase, as well as its gemmological, chemical and spectroscopic properties, and highlights differences between samples from the two occurrences.

HISTORY AND PRODUCTION

In March 2016, a pink-orange crystal was brought to the attention of author JS, who identified it as euclase using Raman spectroscopy and standard gemmological testing at the Centro de Tecnologia Mineral (CETEM) laboratory. The origin of the sample was reported as Livramento de Nossa Senhora in Bahia State. In May 2017, four pink-orange crystals were submitted to CETEM to confirm their identity after a gem lab in Belo Horizonte (Brazil) identified them as Imperial topaz, and these crystals also proved to be euclase. These four specimens, together with the initial sample analysed in 2016, were subsequently sent to Sorbonne University in Paris, France, to study the cause of their colour (Gilles-Guéry *et al*. 2022).

In June 2018, one of the authors (LG-G) saw similar pink-orange euclase crystals exhibited at the mineral and gem show in Sainte-Marie-aux-Mines, France. In late 2020, two of the authors (LAVQ and JS) learned of a specific location where such euclase crystals had been mined in 2015–2016. In December 2020 they visited the occurrence, which is located approximately 18 km west-north-west of the town of Livramento de Nossa Senhora (Figure 3) in the Paramirim mountain range of Bahia State. Only 300 g of euclase crystals/fragments had been mined there, and the entire production was bought by local mineral dealer Julio Martins Cardoso dos Santos, who generously donated a parcel of lower-quality pieces for the authors' research.

During the February 2020 Tucson gem shows, dealer Dudley Blauwet bought a cleaved crystal of pink-orange euclase weighing 1.93 g that was represented as coming from the Brumado area (in southern Bahia State). It was faceted in April 2021 by Brett Kosnar (Kosnar Gem Co., Golden, Colorado, USA) into the 2.99 ct shield-cut stone in Figure 1. This euclase, as will be demonstrated in this article, shares the same general physical and chemical properties as the five crystals studied at Sorbonne University and the samples donated by Julio Martins, but its internal features proved very different, causing the authors to suspect that it came from a separate occurrence or locality.

Our search led us to the office of Álvaro Lúcio, a well-known Brazilian mineral collector and dealer in Belo Horizonte. He reported having purchased the entire known production of pink-orange euclase from Bahia State, including the samples from the first occurrence mentioned above (sold to him by Julio Martins). From this first occurrence he retained only one top-quality crystal for his own collection and sold the rest. In addition, he had purchased material from gem and mineral dealer 'Tião of Diamantina', who is based in Minas Gerais State. It was evident that those samples were from a separate occurrence because of significant differences in colour zoning and crystal morphology, as well as the presence of numerous distinctive fibrous inclusions. Álvaro Lúcio generously loaned a parcel of crystals from the second occurrence for our research.

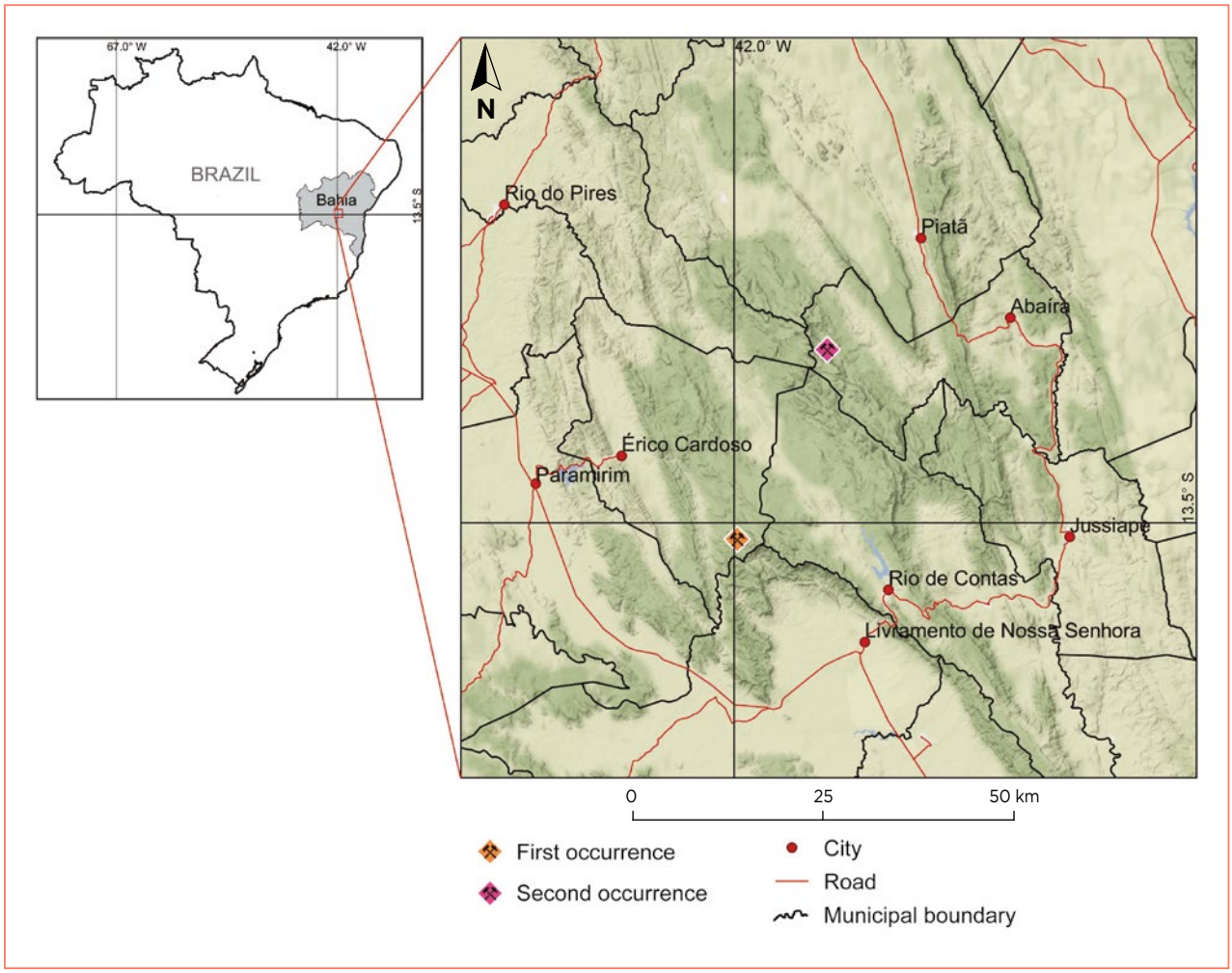

Figure 3: The pink-orange euclase comes from central Bahia State in eastern Brazil. The first reported occurrence was found several kilometres north-west of Livramento de Nossa Senhora in the Paramirim mountain range (in the municipality of Érico Cardoso). The position of the second occurrence is not known precisely, but is located in the Catolés mountain range within the municipality of Abaíra. Terrain background from http://maps.stamen.com.

Subsequently, the authors learned from Mr Tião that on different occasions he had bought two lots of this euclase in Brumado from a local *garimpeiro* (artisanal miner): one weighing approximately 300 g and the other 200 g.

In total, the entire known production of pink-orange euclase from Brazil is probably less than 1 kg, and of this, only a small part consists of facet-grade material or collector-quality crystals. In October 2021, three of the present authors (LG-G, LAVQ and JS) made a second trip to Livramento de Nossa Senhora to investigate the source of the pink-orange euclase crystals containing the fibrous inclusions. After visiting the Paramirim mountain range and finding no indication that another euclase occurrence had been found there, they learned from local dealers that the crystals with fibrous inclusions came from the Catolés mountain range, also in Bahia State and located approximately 30 km north-north-east of the first occurrence (again, see Figure 3).

GEOLOGY

Bahia State is well known for its production of diamond (de Carvalho *et al.* 2018), emerald, amethyst and rutilated quartz, but also for unusual mineral occurrences such as Mn-bearing andalusite (Schnellrath 1989). Besides gems, this region is noted for its mineral commodities, mainly gold and barite, but also manganese, tin, copper and dimension stone. Due to the presence of these mineral resources, the Geological Survey of Brazil (CPRM—Companhia de Pesquisa de Recursos Minerais), in cooperation with the Mineral Research Company of Bahia (Companhia Baiana de Pesquisa Mineral or CBPM), has made detailed geological maps of the region. Based on one of these maps (de Souza *et al.* 2003) and on field observations by the present authors, both of the pink-orange euclase occurrences are hosted by the Ouricuri do Ouro Formation, which is composed of

metamorphosed sedimentary rocks (arenite, conglomerate, breccia and graywacke; Figure 4). This formation is part of the Espinhaço Supergroup, a thick metasedimentary sequence deposited, beginning around 1,750 million years ago (Ma), over the Archean basement of the São Francisco Craton in eastern Brazil.

This region has a long tectonic history. During the Neoproterozoic Era, a basin adjacent to the Espinhaço rift was uplifted in response to the propagation of an orogenic front. The tectonics evolved into a continental collision zone producing crustal shortening and thickening, manifested by extensive fold belts and major shear zones (sericite Ar-Ar age of 497 Ma; Guimarães *et al*. 2005). The processes involved in the generation of most of the mineral resources of this region were tectonically controlled and associated with the circulation of low-temperature metamorphic-hydrothermal fluids (Guimarães *et al*. 2005).

A rugged landscape was observed by authors LAVQ and JS along their 7 km traverse to the first euclase occurrence (Figure 5a). The trail followed an east-north-east direction, crossing different rock layers almost perpendicularly, some of which exhibited mylonitic foliation. The subvertical dips (again, see Figure 5a) were probably related to vertical tectonic movement of blocks on a regional scale. In addition, some stratified metaarenite and metaconglomerate lithologies were observed dipping at low angles and showing cross-bedding (Figure 5b). The existence of diverse dip angles can be explained by variations in the ductile-brittle behaviour of different lithologies along the shear zones. The most vertical foliations were seen mainly in the more schistose rocks, locally containing pyrophyllite (Figure 6a) and sometimes green (Mn-bearing) andalusite (cf. Schnellrath 1989; see Figure 6b). Indeed, de Souza *et al*. (2003) described six pyrophyllite occurrences in four different municipalities, revealing the regional scale of this type of mineralisation. Mn-bearing andalusite has also been found in alluvial deposits at Paramirim das Crioulas, only 6.5 km from the first euclase occurrence, and at a pyrophyllite occurrence at Ibitiara located about 90 km north (Cassedanne & Cassedanne 1980; Schnellrath 1989).

During our hike to the first euclase occurrence, we also observed various quartz veins that were either concordant or discordant to the rock foliation. Among them were numerous, closely clustered (<100 m apart) areas with pockets containing quartz crystals, some with fibrous inclusions and others totally transparent. At the euclase deposit itself, we were unfortunately not able to see any mineralisation *in situ* because the diggings had been backfilled by the miners after the crystals were extracted.

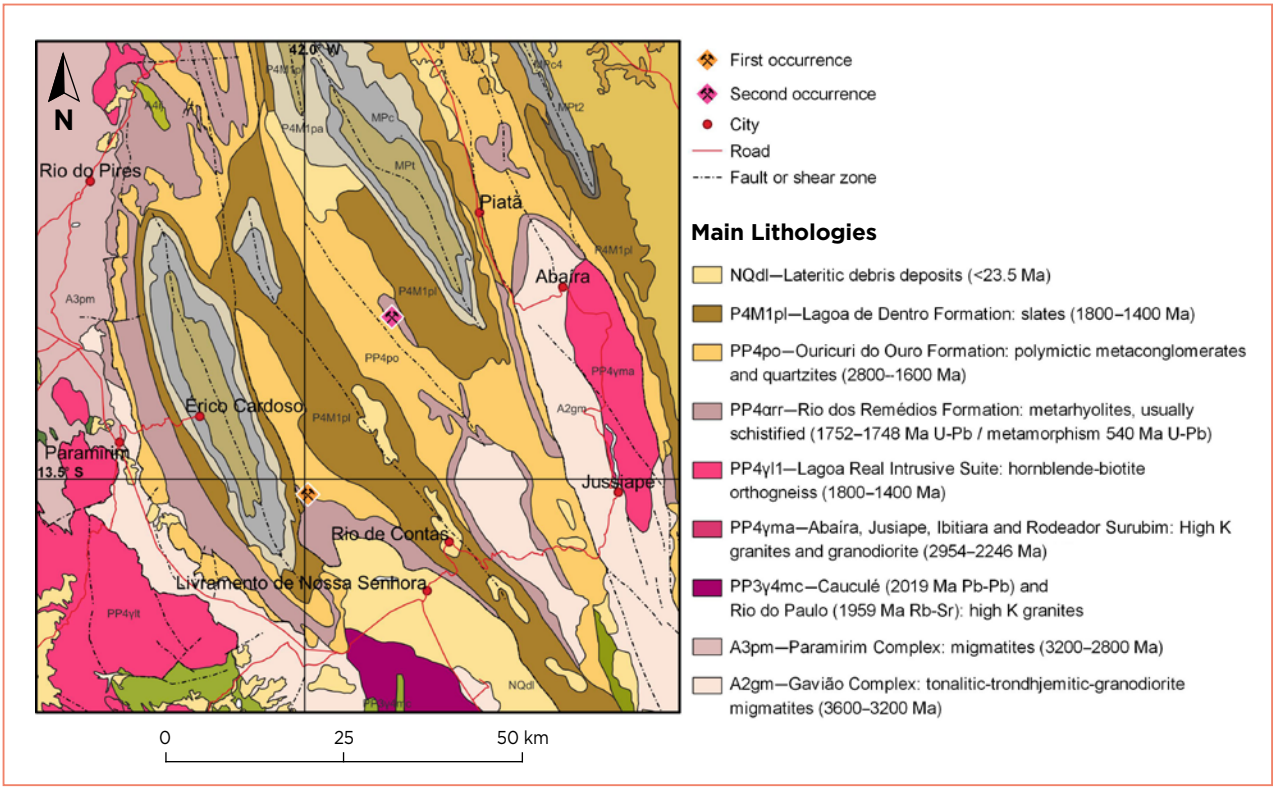

Figure 4: This generalised regional geological and structural map (modified from de Souza *et al*. 2003) shows the major lithologies and linear structures in the area hosting the pink-orange euclase. The host rocks consist of metasedimentary rocks (metaarenites) of the Ouricuri do Ouro Formation.

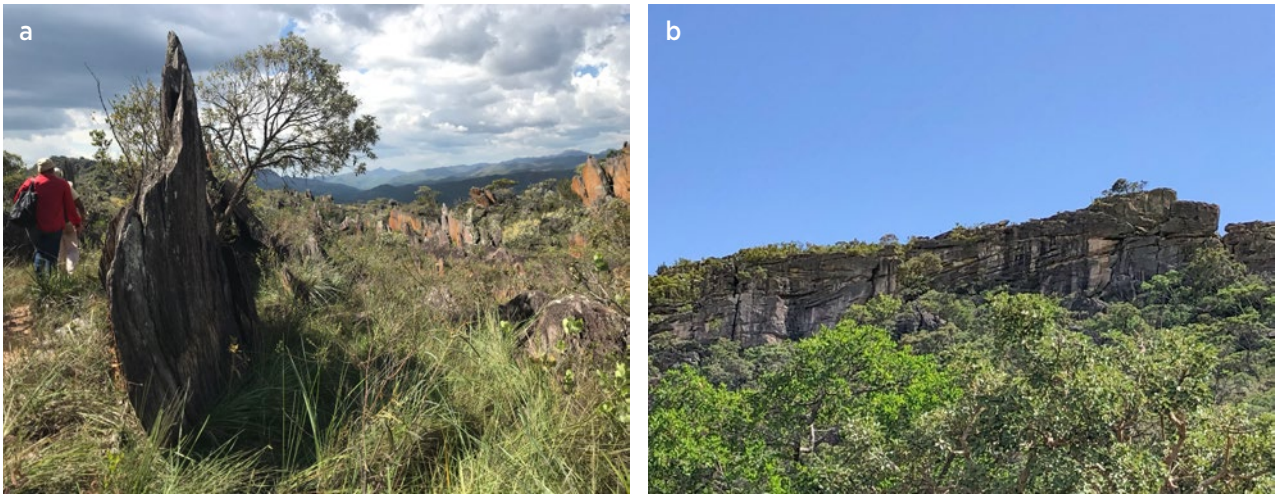

Figure 5: (**a**) An outcrop of a schistose rock with subvertical dip is seen here during the authors' 7 km hike to the first euclase occurrence. Photo by L. Bloomfield. (**b**) Shallowly dipping metaarenites with cross-bedding are also present in the euclase mining area. Photo by L. V. A. de Queiroz.

However, we found tiny loose fragments of pink-orange euclase at the site. According to the *garimpeiros*, the euclase was hosted by the more schistose host rocks and associated with well-formed transparent quartz crystals without any fibrous inclusions in a very limited area (probably a small vug). This suggests that the euclase is genetically related to the quartz veins, which were derived from hydrothermal fluids.

At the time of our visit to the first euclase occurrence, small-scale mining was taking place at the second euclase locality by *garimpeiros* who work in the Catolés mountain range. The precise location of the deposit is yet unknown to the authors, but the Catolés area is geologically equivalent to the first occurrence (again, see Figure 4). Considering the similarity in the geological environment of the two localities, and that in both cases the garimpeiros were prospecting for quartz crystals containing fibrous inclusions when they accidently found euclase crystals with the same very unusual pink-orange colour, we conclude that both occurrences are related to the same mineralising event (i.e. the percolation of hydrothermal fluids). Unlike the crystallisation of quartz, euclase needs Be to form, and this indicates that there must be a source of this light element that is yet unknown to us. Ongoing studies are further investigating the geological conditions for the formation of these euclase crystals.

MATERIALS AND METHODS

Thorough examination and testing were performed on two polished euclase samples (Figure 7) representing the two occurrences: one from the area near Livramento de Nossa Senhora (sample 1) and the other, loaned by Dudley Blauwet, presumably from the second area based

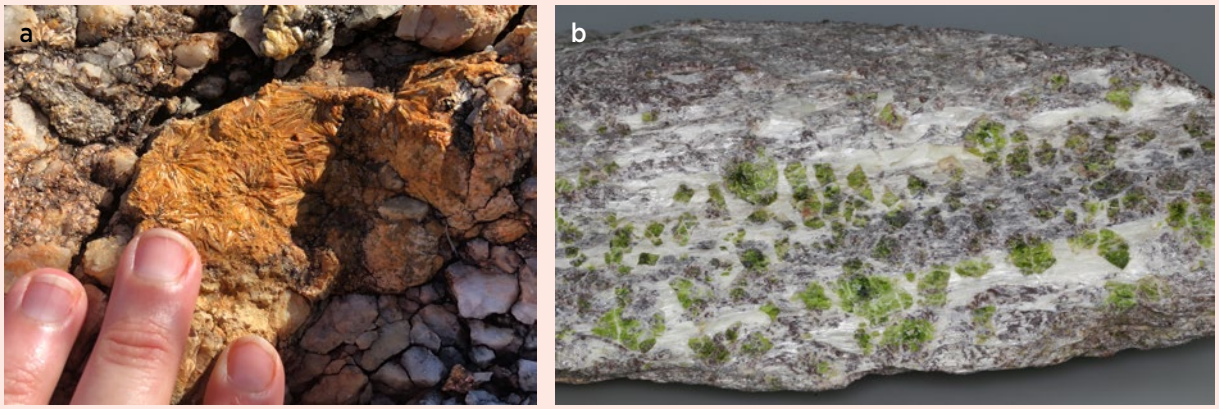

Figure 6: (**a**) Pyrophyllite is associated with quartz veins in the region near the first euclase occurrence. Photo by L. Bloomfield. (**b**) Schist in the same area contains concentrations of green Mn-bearing andalusite. Photo by J. Schnellrath; image width 11.2 cm.

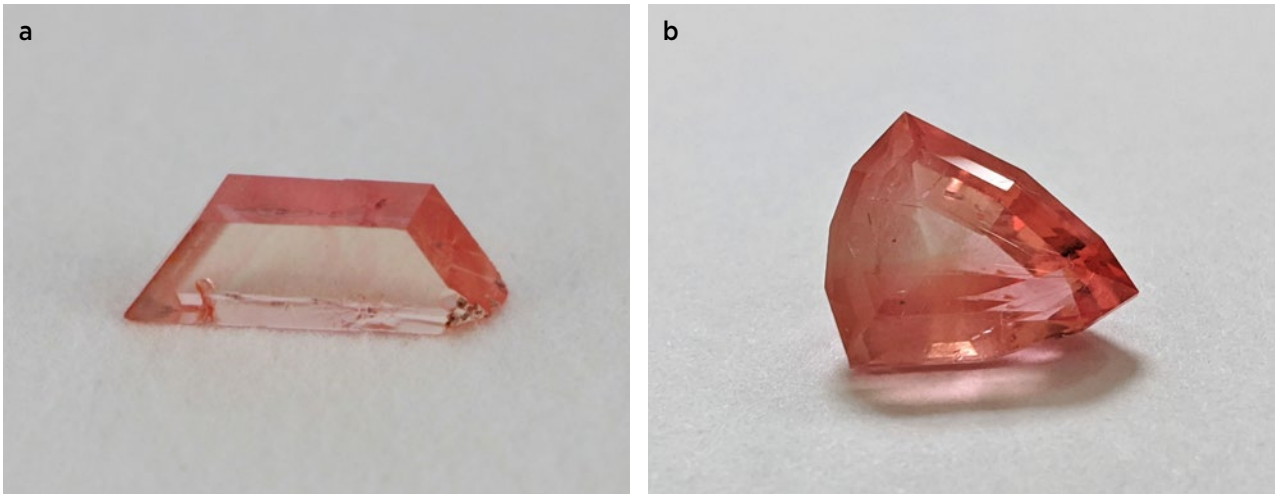

Figure 7: (**a**) Euclase sample 1 (from the first occurrence) consists of a 3.5 ct parallel-polished plate measuring 15.02 × 3.89 × 5.08 mm. Photo by L. Gilles-Guéry. (**b**) Euclase sample 2 (from the second occurrence) is a 2.99 ct shield-shaped gemstone measuring 10.74 × 9.09 × 5.87 mm. Photo by Aria Agarwal/Dudley Blauwet Gems.

on its inclusion features (sample 2). Sample 1 (Figure 7a) was a parallel-polished plate weighing 3.5 ct, which was also studied by Gilles-Guéry *et al.* (2022). Sample 2, a 2.99 ct faceted stone (Figures 1 and 7b), was characterised for the present study by authors BW and CW.

The gemmological properties of sample 1 were obtained at Sorbonne University. Refractive indices were measured with a Krüss refractometer. Specific gravity was obtained by the hydrostatic method using a Mettler Toledo JS1603C balance. UV fluorescence was observed in a darkened room using a standard long-wave (365 nm) and short-wave (254 nm) UV lamp. The colour of the sample was described before and after heating to 300°C and 500°C using the chromatic coordinate system *Yxy*, calculated from unpolarised optical spectra, with a D65 illuminant (average midday light in western Europe) and plotted on a CIE 1931 diagram (Hunt & Pointer 2011). Raman spectroscopy of the sample was performed with a B&W Tek GemRam spectrometer (785 nm red laser) and a GL Gem Raman PL532 TEC spectrometer (532 nm green laser). Optical absorption spectra were obtained using a PerkinElmer Lambda 1050 ultraviolet-visible-near infrared (UV-Vis-NIR) spectrometer in transmission mode, in the 330–2000 nm (30,000–5000 cm^{-1}) range with a resolution of 1 nm and a 4 × 4 mm beam size. Chemical composition was measured with a Cameca SX 100 electron probe micro-analyser (EPMA). The results were averaged from over 100 analytical points. The standards used were diopside (Si*K*α), orthoclase (Al*K*α), $MnTiO_3$ (Ti*K*α and Mn*K*α), Fe_2O_3 (Fe*K*α) and pure Ge (Ge*K*α). For Al, Si and Ge we used an accelerating voltage of 25 kV, a beam current of 10 nA and a counting time of 5 s. For Ti, Mn and Fe we used an accelerating voltage of 25 kV, a beam current of 200 nA and a counting time of 30 s. The data were processed using Cameca's PAP procedure. The amounts of BeO and H_2O, which cannot be quantified using the electron microprobe, were calculated by difference. Detection limits were about 10 ppm for trace elements such as Fe, Ti and Mn, and 20 ppm for Ge.

The gemmological properties of sample 2 were obtained at Stone Group Laboratories. Refractive indices were measured with a Gem-A desktop refractometer. Specific gravity was obtained by the hydrostatic method using a Scientech SP150 balance. Raman spectroscopy was done with a Magilabs GemmoRaman-532SG spectrometer (532 nm laser) and an Enwave Raman unit (785 nm red laser). The UV-Vis-NIR absorption spectrum in the 365–1000 nm range was collected with a Magilabs GemmoSphere spectrometer; the resulting colour calculated from the spectrum was also plotted on the chromaticity diagram mentioned above. Chemical composition was measured by energy-dispersive X-ray fluorescence (EDXRF) spectroscopy using an Amptek X123-SDD spectrometer (Au target X-ray tube) operated at 25 kV and 35 µA. Minor and trace elements were quantified by Dr George Rossman at California Institute of Technology (Pasadena, California, USA) using an INAM Expert 3L desktop EDXRF analyser with a Ti target X-ray tube. The beam had a spot size of approximately 3 mm in diameter, and was centred over the area of the sample with the smallest amount of inclusions. The analysis was conducted in two stages: first a 90 s scan using 45 kV excitation to measure the heavier elements, followed by a 90 s scan using 13 kV excitation for the lighter elements. As this equipment does not use a vacuum chamber, elements lighter than Mg could not be detected.

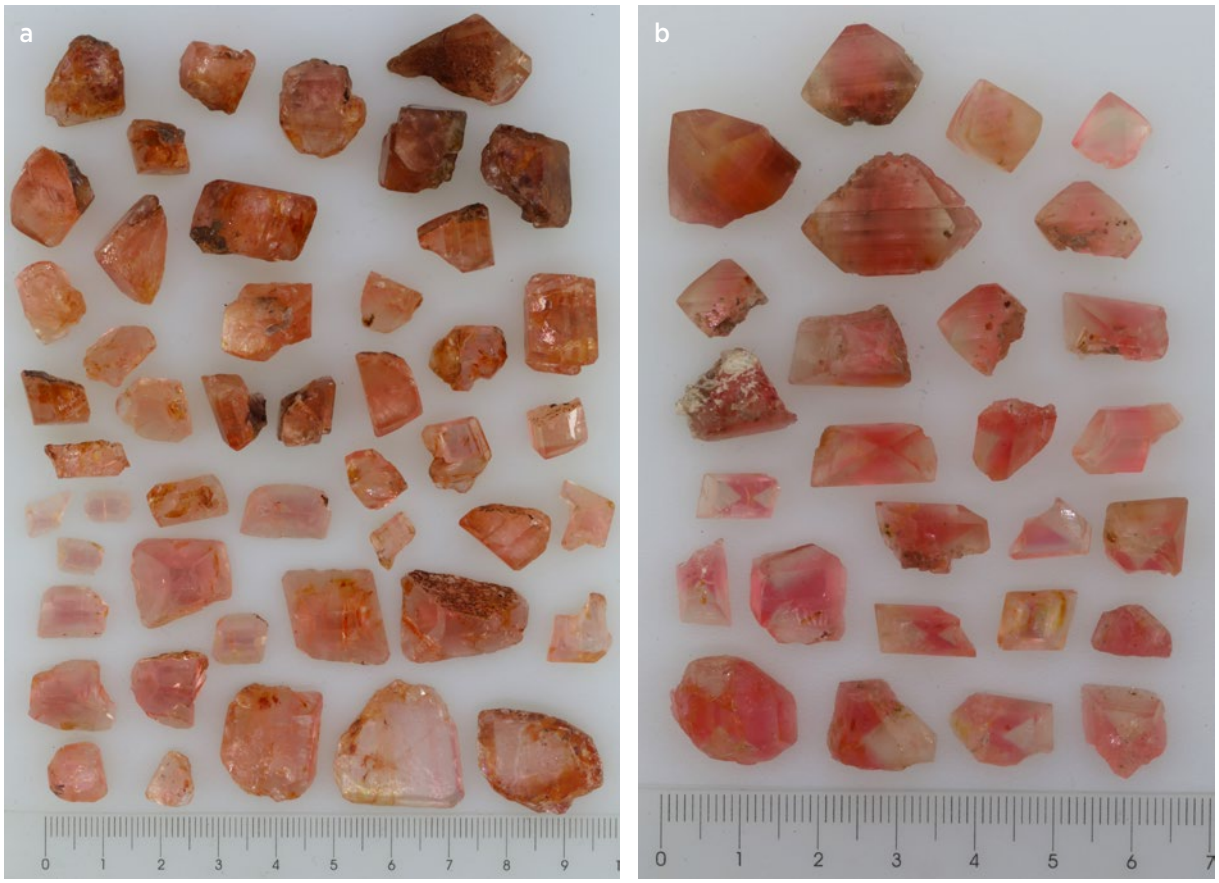

Figure 8: These euclase crystals and fragments were studied for their internal features, and include (**a**) a parcel weighing 104.8 g from the first reported occurrence, and (**b**) a lot consisting of 35.5 g from the second occurrence. The ruler in each photo is in centimetres. Photos by J. Schnellrath and L. V. A. de Queiroz.

An additional 104.8 g of pink-orange euclase specimens (mostly crystal fragments) from the first reported occurrence (Figure 8a) and another 35.5 g of euclase from the second source (Figure 8b) were examined for their inclusions and other notable internal features at the CETEM laboratory. Photomicrographs of internal features were taken with a Canon EOS 6D camera affixed to a Schneider immersion microscope with Zeiss Stemi 508 trinocular optics using 1-bromonaphthalene as an immersion liquid. Unless stated otherwise, images were taken using diffused, polarised transmitted light.

Due to the presence of a diverse suite of inclusions in the euclase from the second occurrence, selected samples from that locality were studied at CETEM by scanning electron microscopy–energy-dispersive spectroscopy (SEM-EDS), using a Hitachi TM3030Plus tabletop SEM coupled with a Bruker Quantax 70 EDS system. In addition, Raman spectroscopy of selected inclusions was performed at the Centro de Tecnologia em Nanomateriais e Grafeno (Universidade Federal de Minas Gerais, Belo Horizonte), using a WITec alpha300 R Raman microscope with a 50× objective, a 532 nm laser and a maximum power of 20 mW. Spectra were collected by accumulating six consecutive readings with an integration time of 5 s each, yielding a resolution of about 5 cm^{-1}.

RESULTS

Crystal Morphology

Euclase crystals from the first and second occurrences are distinctive from one another, and can be readily separated by their visual appearance (see Figures 2, 8 and 9). Those from the first occurrence are more elongated parallel to the *c*-axis (although they are commonly broken along their main {010} cleavage direction), and also exhibit pinacoidal {001} faces, which are typically not seen on crystals from the second occurrence. In addition, crystals from the second occurrence commonly show more pronounced striations, as well as conspicuous sector zoning visible as distinct pink-orange and near-colourless areas.

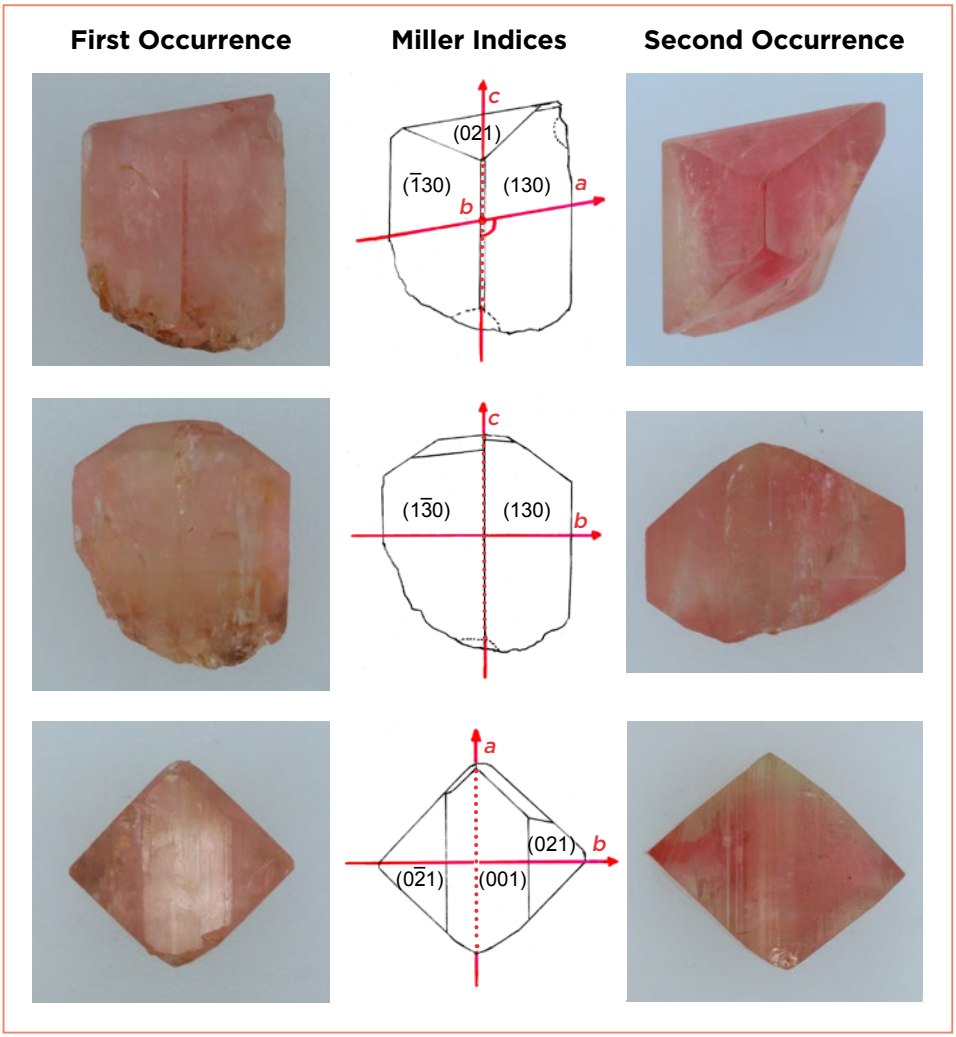

Figure 9: Crystals of pink-orange euclase from the two Brazilian occurrences exhibit similar principal forms but also show some differences. The accompanying line drawings are based on the crystal from the first occurrence, but the Miller indices (indexed according to the monoclinic $P2_1/c$ space group, per Gilles-Guéry *et al.* 2022) apply to crystals from both occurrences. The crystal from the first occurrence measures 14.9 × 12.6 × 11.6 mm, and the one from the second occurrence is 19.2 × 20.4 × 17.0 mm (dimensions are for the *c*-, *b*- and *a*-axis directions, respectively). Photos by J. Schnellrath.

Gemmological Properties

The gemmological properties of the two euclase samples are summarised in Table I. While the colour of sample 1 was an almost homogeneous pink-orange, sample 2 was strongly colour zoned, varying from orange-pink at the pointed end of the faceted stone to almost colourless at its wider end. Slight differences in the overall colouration of the euclase from each occurrence can also be seen in the rough samples in Figure 8. Both samples 1 and 2 had RIs of 1.652–1.673 (birefringence 0.021) and an SG value of 3.10. They were inert to long- and short-wave UV radiation. Euclase sample 2 was also tested for magnetic susceptibility but was not magnetic. When excited with both red (785 nm) and green (532 nm) lasers, no laser-induced luminescence was observed in the Raman spectra.

Sample 1 displayed orange to pink pleochroism that was visible to the unaided eye. Figure 10 presents the colour coordinates for the two pleochroic orientations of the crystal sections (001) and (010); for further discussion, see Gilles-Guéry *et al.* (2022). The colour of euclase

Table I: Gemmological properties of pink-orange euclase from Bahia, Brazil.[a]

Property	Sample 1	Sample 2
Origin	Livramento de Nossa Senhora (Paramirim mtns.)	Abaíra municipality (Catolés mtns.)
Weight	3.5 ct	2.99 ct
Colour	Pink-orange	Orange-pink[b]
Pleochroism	Orange to pink	Pink to pale pinkish orange
RIs	1.652–1.673	1.652–1.673
Birefringence	0.021	0.021
Optic character	Biaxial	Biaxial positive
SG	3.10	3.10

[a] Both samples were inert to long- and short-wave UV radiation.

[b] Overall face-up colour; it was near-colourless at the wide end.

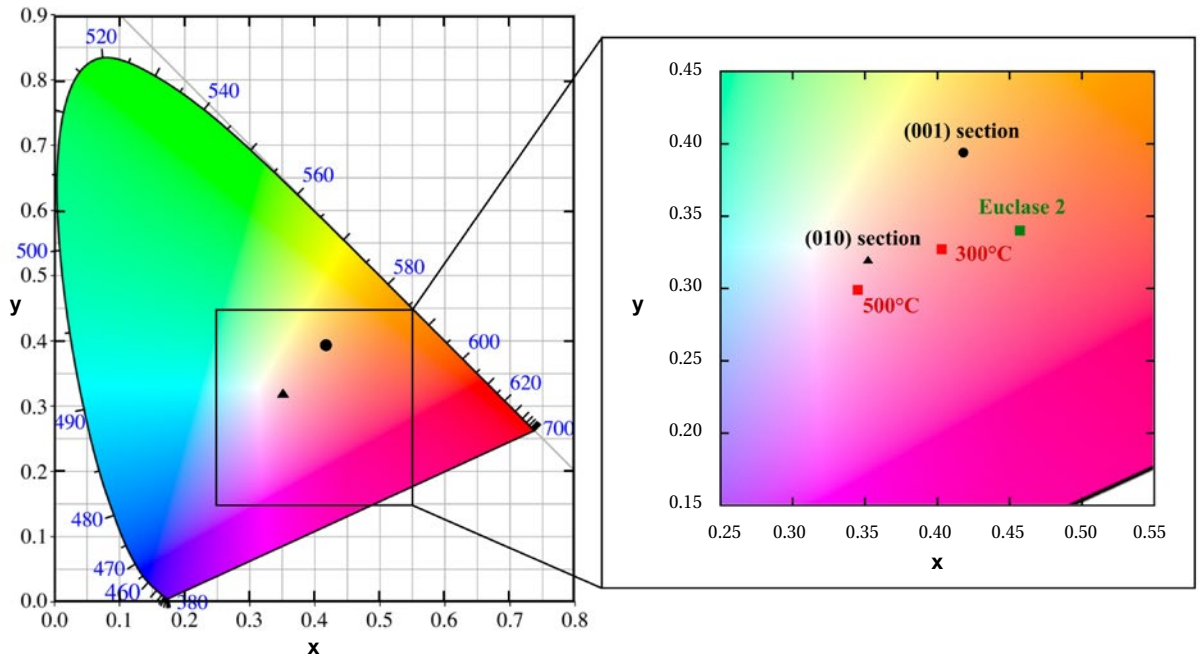

Figure 10: Colorimetric representations of the two euclase samples are shown in this CIE chromaticity diagram (calculated from optical spectra in the 380–780 nm range for the system *Yxy* with D65 illumination). The pleochroism (black points) and colours produced by heat treatment (red points) are shown for euclase sample 1, and the hue of sample 2 is also plotted (green point). Around the horseshoe-shaped diagram, the wavelengths (labelled in blue) are indicated in nanometres. Modified from Gilles-Guéry *et al.* (2022).

sample 2 is an intermediate hue between the colours of the two orientations of sample 1 (again, see Figure 10). This is due to the crystallographic orientation of the faceted stone, which caused it to appear slightly more pinkish. The pleochroism of euclase sample 2 was strong, and varied from pink to pale pinkish orange (Figure 11).

Figure 11: Strong pleochroism from pink to pale pinkish orange is shown by euclase sample 2, which weighs 2.99 ct. Photo by C. Williams.

Internal Features

Samples from the First Occurrence. These were typically less included than those from the second occurrence and therefore could be cut into cleaner faceted stones. Complex colour-zoning patterns were typically seen when viewed with the microscope (e.g. Figure 12). Partially healed fissures with fluid inclusions were also commonly observed, including those consisting of a liquid and a vapour phase (Figure 13a), and those containing two immiscible liquids and a vapour phase (Figure 13b). Also seen were colour concentrations near the rims of some crystals, as well as dark 'phantoms' (Figure 14a) derived from the accumulation of tiny platelets (possibly pyrophyllite/talc) parallel to certain crystal faces during successive growth phases. Figure 14b shows these tiny platelets between crossed polarising filters, as well as larger birefringent idiomorphic solid inclusions with characteristics of quartz. Both the dark 'phantoms' and colour concentrations near the rims were observed in many of the better-formed crystals.

Samples from the Second Occurrence. These were typically more included than those from the first occurrence and therefore exhibited lower transparency. In addition, they consistently showed hourglass-shaped

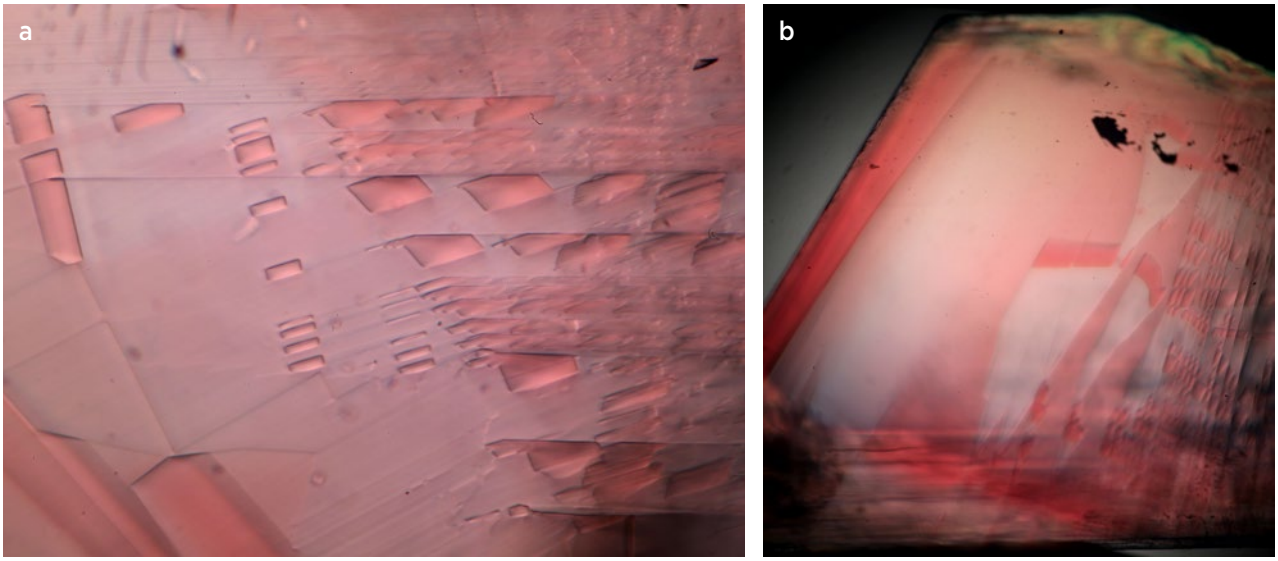

Figure 12: Complex patchy colour zoning, shown here in two different crystals, is typical of the euclase from the first occurrence when viewed with a microscope. Photomicrographs by J. Schnellrath and L. V. A. de Queiroz; (**a**) image width 3.2 mm and (**b**) crystal height 7.6 mm.

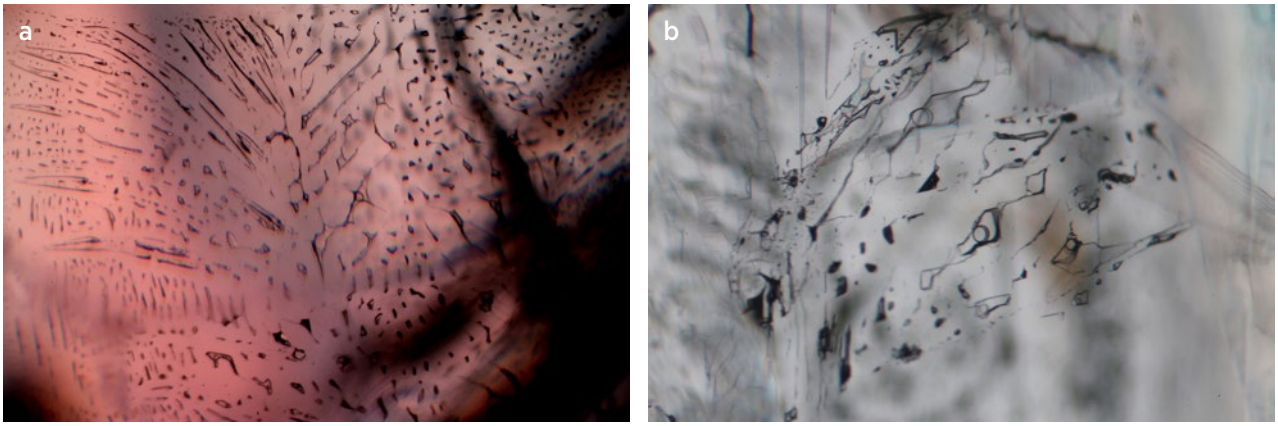

Figure 13: Euclase from the first occurrence commonly contains partially healed fissures consisting of two-phase fluid inclusions. Shown here are fluid inclusions with (**a**) a liquid and a vapour phase, and (**b**) a gaseous phase with two immiscible liquids. Photomicrographs by J. Schnellrath and L. V. A. de Queiroz; image widths (a) 5.2 mm and (b) 3.2 mm.

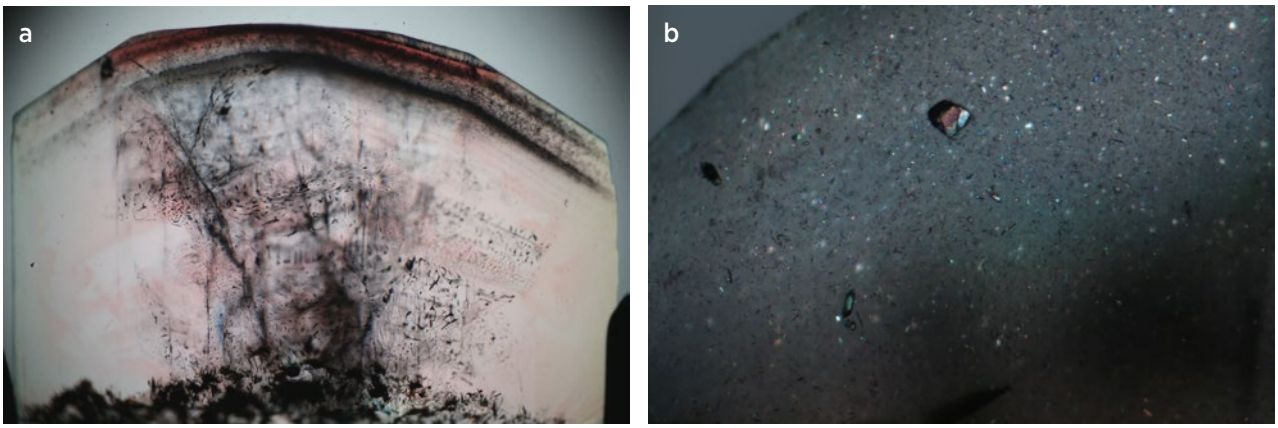

Figure 14: (**a**) Euclase from the first occurrence sometimes contains dark 'phantoms' composed of tiny platelets as well as strong colour concentrations near the rims of the crystals. Also seen here are several partially healed fissures and faint complex colour zoning. (**b**) The tiny platelets composing the phantoms are seen here with crossed polarisers, together with some larger birefringent idiomorphic solid inclusions that are probably quartz. Photomicrographs by J. Schnellrath and L. V. A. de Queiroz; (a) crystal width 11.3 mm and (b) image width 3.7 mm.

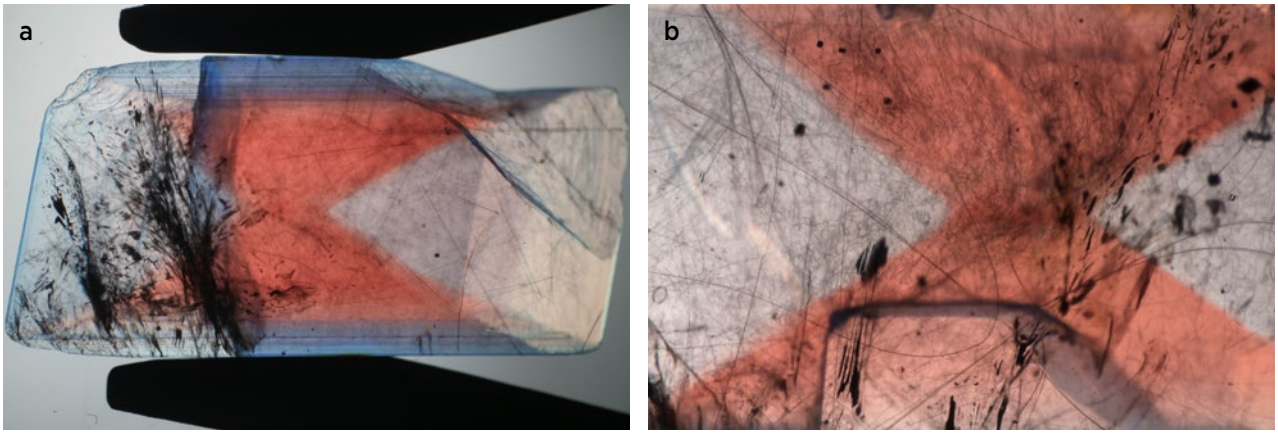

Figure 15: Euclase from the second occurrence shows prominent hourglass-shaped colour zoning, which is seen here down the *b*-axis, perpendicular to the cleavage plane. Photomicrographs by J. Schnellrath and L. V. A. de Queiroz; (**a**) crystal length 14.8 mm and (**b**) image width 6.0 mm.

sector zoning of orange-pink colour that contrasted with the adjacent near-colourless sectors (Figure 15). This colour zoning could best be seen by looking down the *b*-axis, perpendicular to the cleavage plane.

The most characteristic inclusions in our samples consisted of various types of fibrous channels (e.g. Figure 16), which herein are referred to simply as 'fibres'. We observed two main varieties, both present in almost all the crystals examined from the second occurrence. The first type consisted of fine-to-coarse, straight or gently curved fibres. They occurred mostly as isolated needles, but occasionally also formed bundles (Figure 16a). In both cases they did not have a preferential orientation. Microscopic observation revealed that these fibres might consist of a mineral phase (perhaps tremolite/actinolite) that was subsequently dissolved away, leaving narrow empty channels. This presumption was corroborated by SEM imagery showing empty voids with lozenge-shaped cross-sections, as well as the absence of a Raman signal from anything other than the host euclase. This is also consistent with the yellowish to brownish colouration of the fibres due to epigenetic staining or infiltration of foreign material during weathering. The second type of fibre had a curly or woolly appearance (Figure 16b). They were much finer than the first type, and seemed to be related to other structures/inclusions, as described below. Based on SEM and Raman analyses, this type of fibre also consisted of empty channels.

Other inclusions commonly encountered in euclase from the second occurrence were euhedral rhombohedra resembling a carbonate mineral (Figure 17). Closer observation revealed two types: (1) high-relief, dark-appearing larger-sized rhombs that did not exhibit birefringence (again, see Figure 17); and (2) much less common ones consisting of low-relief, transparent, minute, birefringent crystals (see the lower-right inclusion in Figure

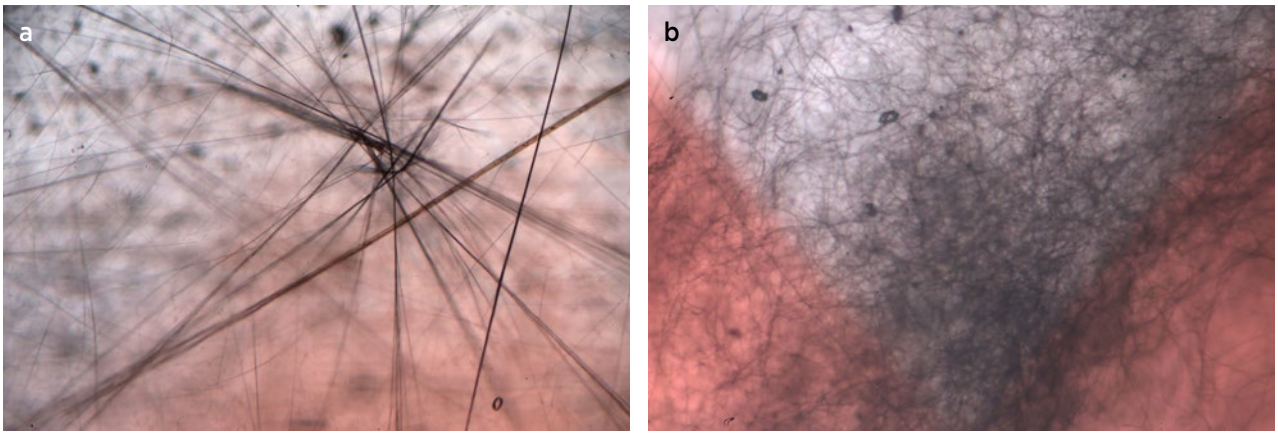

Figure 16: Various types of fibres are the most characteristic inclusion feature in euclase from the second occurrence. They appear as (**a**) straight or slightly curved fine-to-coarse fibrous inclusions; and (**b**) very fine curly/woolly fibres, which here are mostly concentrated in the centre of this stone. Photomicrographs by J. Schnellrath and L. V. A. de Queiroz; image widths (a) 3.9 mm and (b) 2.5 mm.

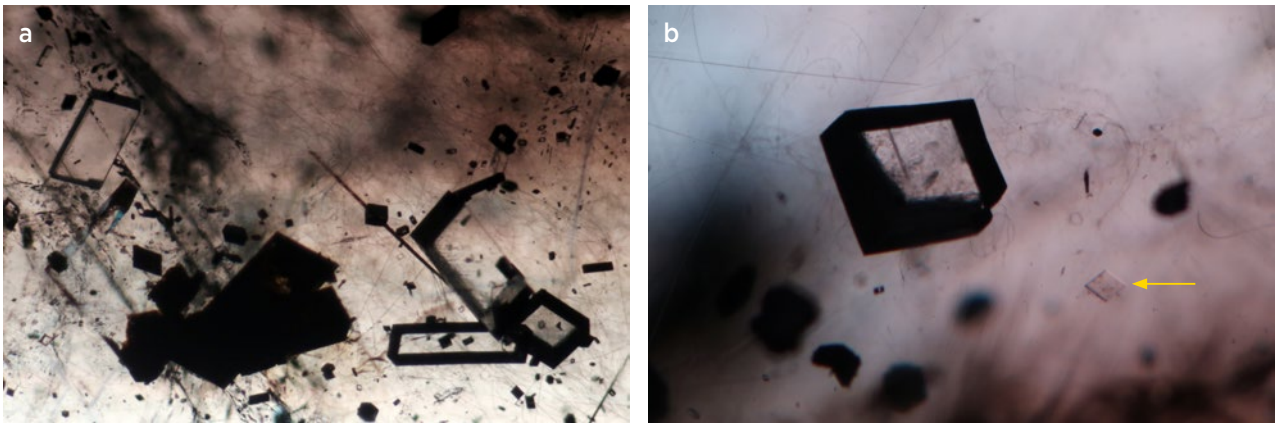

Figure 17: (**a**) Large, high-relief rhombs in a euclase sample from the second occurrence do not exhibit birefringence. (**b**) Another high-relief rhomb in the same sample is flanked by a much smaller low-relief rhomb (see arrow), which was birefringent when viewed with crossed polarisers and proved to be dolomite. Photomicrographs by J. Schnellrath and L. V. A. de Queiroz; image widths (a) 2.8 mm and (b) 3.1 mm.

17b). Raman and SEM-EDS analyses revealed these latter inclusions to be dolomite. The high-relief rhombs only produced a Raman signal from the host euclase, and were probably cavities resulting from the dissolution of dolomite inclusions. It seems likely that these larger inclusions were preferably dissolved during the post-growth leaching process because their greater size provided a higher likelihood of being penetrated by the fibrous channels mentioned above, which apparently served as conduits for the etching solutions.

Additional inclusions in euclase from the second occurrence included tabular crystals with a pseudo-hexagonal shape—consistent with the morphology of a phyllosilicate mineral—which formed either isolated tablets or stacked plates that gave the appearance of nearly spherical aggregates (Figure 18). The dark, high-relief appearance of these aggregates in transmitted light suggests that the minerals in these inclusions were partially or completely dissolved by the same solutions that dissolved those in the fibrous and rhombic inclusions. In fact, Raman and SEM-EDS analyses of the tabular crystals and spherical aggregates failed to detect signs of any phase other than the host euclase.

Two types of birefringent idiomorphic inclusions were also present in euclase from the second occurrence. A quartz inclusion seen in Figure 18a displays bright interference colours. In Figure 19a, the two larger crystals with intense interference colours were also identified as quartz. Additionally present is an elongated prismatic crystal showing low relief that was identified as euclase included in the euclase host. Figure 19b shows an as-yet-unidentified hydrated La-Al phosphate/arsenate mineral—possibly

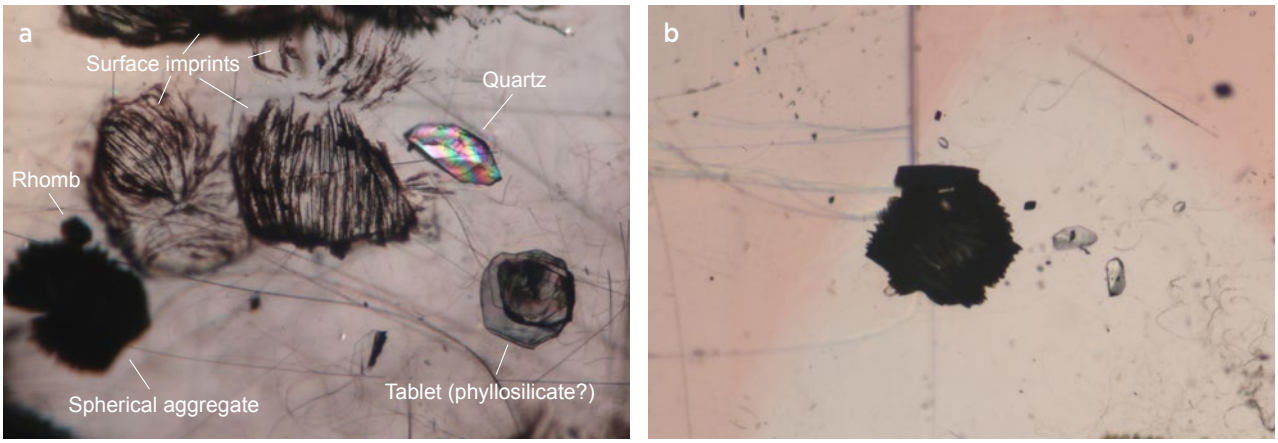

Figure 18: Some of the euclase from the second occurrence contains platy inclusions with the appearance of a phyllosilicate mineral. (**a**) This scene includes an individual tabular crystal with a pseudo-hexagonal shape (to the lower right) accompanied by a quartz crystal showing intense interference colours. Also visible is a dark spherical aggregate made up of the same type of plates, a dark rhomb, some fibres, and imprints of some spherical aggregates on the surface of the crystal. (**b**) This dark spherical aggregate of plates is located near a colour-zoning boundary. Smaller colourless crystals (composed of an unknown hydrated La-Al phosphate/arsenate mineral) and various fibres are also present. Photomicrographs by J. Schnellrath and L. V. A. de Queiroz; image widths (a) 2.1 mm and (b) 2.6 mm.

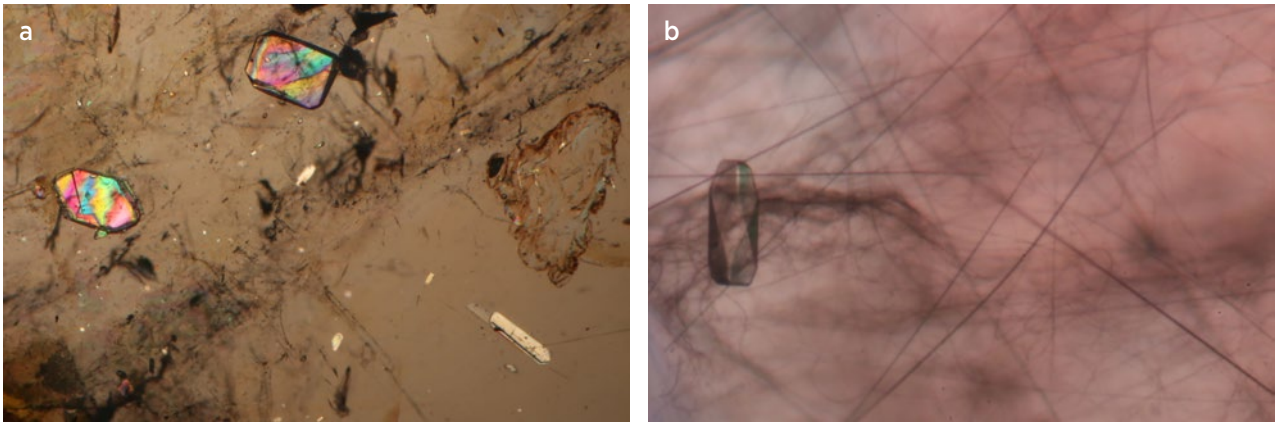

Figure 19: (**a**) Solid birefringent inclusions in euclase from the second occurrence are seen with partially crossed polarisers. The two larger crystals with intense interference colours proved to be quartz, and the prismatic inclusion at the bottom right is euclase. (**b**) On the left side of this image is an as-yet-unidentified hydrated La-Al phosphate/arsenate mineral, which is surrounded by fine curly/woolly fibres and coarser straight or slightly bent fibres. Photomicrographs by J. Schnellrath and L. V. A. de Queiroz; image widths (a) 5.5 mm and (b) 0.6 mm.

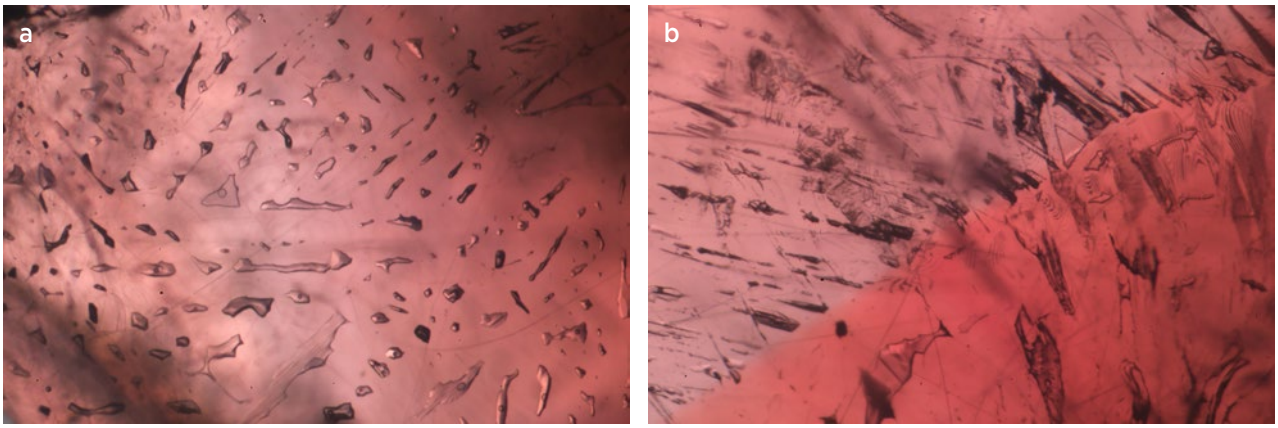

Figure 20: (**a**) Partially healed fissures with two-phase fluid inclusions also occur in euclase from the second occurrence. (**b**) These fluid inclusions exhibit different shapes and orientations on either side of a colour-zoning boundary. Photomicrographs by J. Schnellrath and L. V. A. de Queiroz; image width 4.0 mm each.

an intermediate phase between florencite-(La) and arsenoflorencite-(La)—that is surrounded by both types of fibrous inclusions. More crystals of this unknown inclusion are visible in Figure 18b.

Some of the euclase samples from the second occurrence contained partially healed fissures consisting of two-phase fluid inclusions (Figure 20a), as well as fluid inclusions showing different shapes and orientations according to colour boundaries defining the sector zoning (Figure 20b).

Particularly intriguing were circular inclusions in the form of flattened negative crystals that showed high relief and an internal polygonal shape (Figure 21). Also seen were ring-like structures (Figures 21, 22 and 23a) and cylindrical rods (Figure 23). Figure 22a shows a flattened circular negative crystal that seems to be uncoiling to produce curly/woolly fibres. Figure 22b depicts a ring-like structure that seems to be made up of coiled fibres. The cylindrical rods in Figure 23 are seen in proximity to circular and spring-like features, as well as curly/woolly fibres. Raman and SEM-EDS analyses of the negative crystals and cylindrical rods led to the conclusion that both are empty structures. On the other hand, analysis of the interior space within the ring-like features showed that it is occupied by the host euclase. These observations suggest that perhaps the thickness of these circular structures determined whether their interior was occupied by the host euclase or was filled with empty space (i.e. a negative crystal). Further studies are needed to better understand these unusual inclusions.

Chemical Composition

The chemical composition of euclase samples 1 and 2 is summarised in Table II.

EPMA analysis of sample 1 corresponds with the theoretical formula of euclase, with 33.22 wt.%

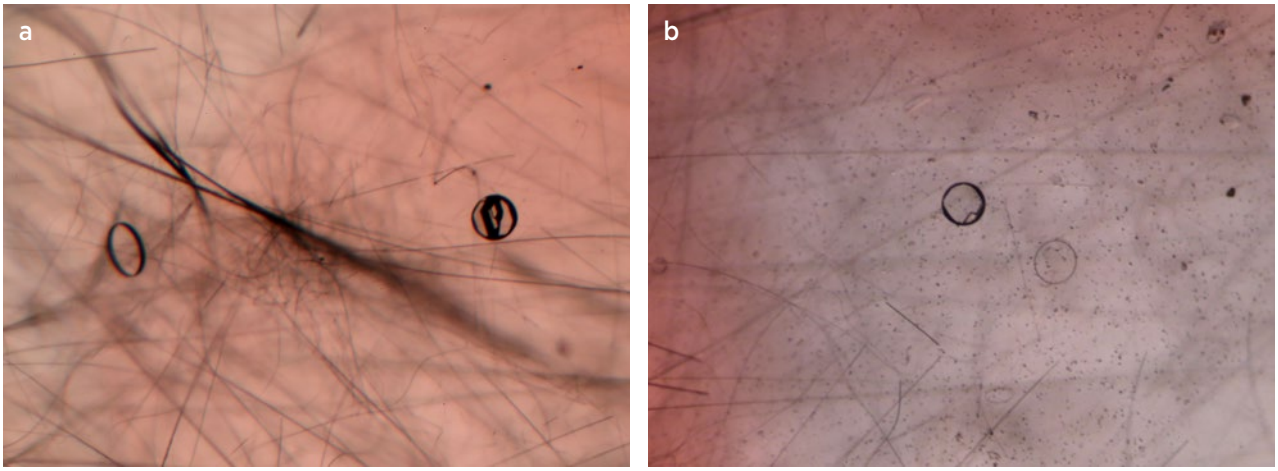

Figure 21: Flattened circular negative crystals show high relief and internal polygonal shapes near ring-like structures in euclase from the second occurrence. (**a**) Abundant fibres are also seen in one sample, while (**b**) another is accompanied by fewer fibres. Photomicrographs by J. Schnellrath and L. V. A. de Queiroz; image widths (a) 1.7 mm and (b) 2.6 mm.

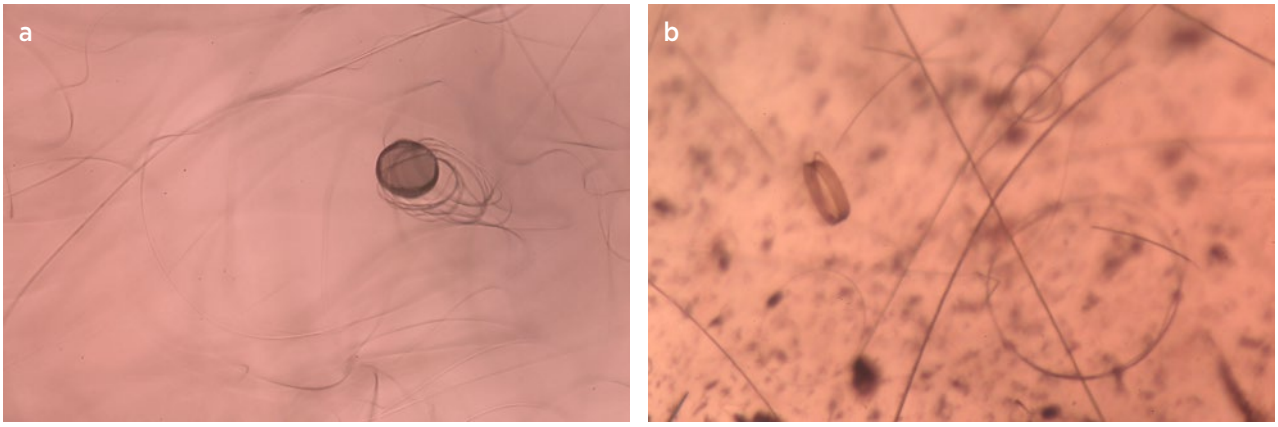

Figure 22: Euclase from the second occurrence exhibits unusual circular features. (**a**) This flattened circular negative crystal seems to be uncoiling to produce curly/woolly fibres. (**b**) Another ring-like structure (on the left side of the image) appears to be made up of coiled fibres. Photomicrographs by J. Schnellrath and L. V. A. de Queiroz; image widths (a) 0.8 mm and (b) 0.9 mm.

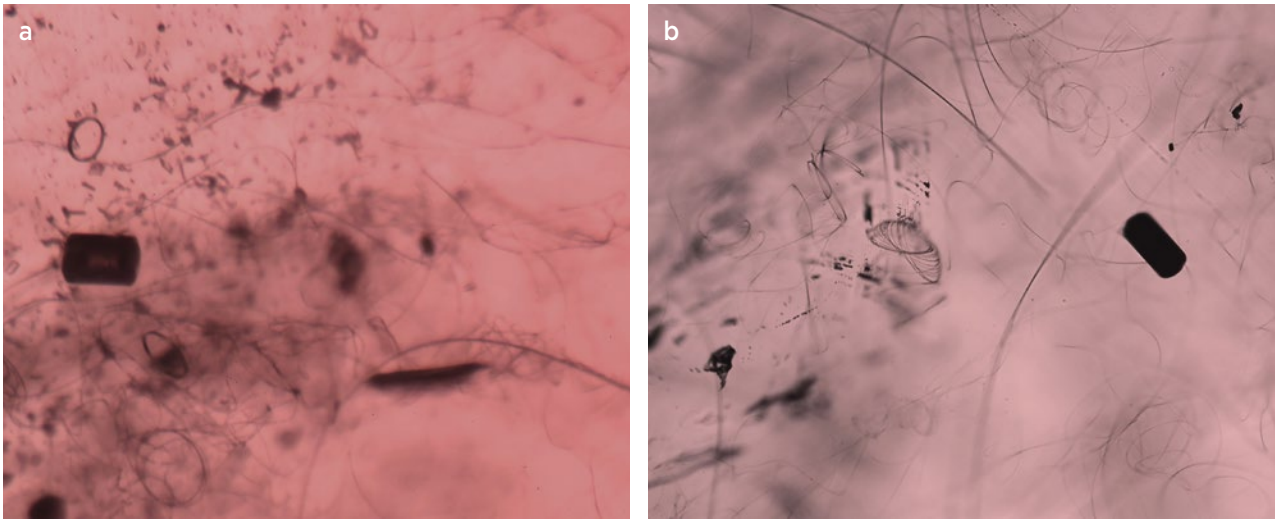

Figure 23: Also present in euclase from the second occurrence are distinctive cylindrical rod-shaped inclusions. (**a**) This dark-appearing rod is surrounded by curly/woolly fibres and ring-like structures. (**b**) In another sample, a rod is surrounded by curly/woolly and spring-like fibres. The rods were found to consist of empty space. Photomicrographs by J. Schnellrath and L. V. A. de Queiroz; image widths (a) 1.3 mm and (b) 1.1 mm.

Table II: Chemical composition of pink-orange euclase from Bahia, Brazil.[a]

Sample (analytical technique) / Element/oxide	Sample 1 (EPMA)	Sample 2 (EDXRF)
Al_2O_3	33.22 wt.%	na
SiO_2	43.09 wt.%	na
Fe	992 ppm	2200 ppm
Mn	73 ppm	63 ppm
Ti	46 ppm	Trace[b]
Ge	142 ppm	154 ppm
Ga	na	11 ppm
As	na	5 ppm
Total	76.31 wt.%	–
$\Sigma(BeO+H_2O)$	23.69 wt.%	–

[a] Abbreviation: na = not analysed.

[b] It was not possible to analyse low concentrations of Ti because the EDXRF instrumentation at Caltech used a Ti X-ray tube; the detection limit for Ti was probably in the range of several hundred ppm.

Al_2O_3 and 43.09 wt.% SiO_2. Minor and trace elements consisted of Fe, Ge, Mn and Ti. Thus, this euclase has a relatively pure chemical composition, with very low impurity contents (Gilles-Guéry *et al.* 2022).

EDXRF spectroscopy of sample 2 performed at Stone Group Laboratories revealed significant amounts of Fe, as well as sufficient Mn to explain the pink colour. Traces of Ge and Ti were also present. A second EDXRF measurement of this sample performed at Caltech quantified the minor and trace elements Fe, Mn and Ge (see Table II).

Optical Spectroscopy

The polarised optical spectra of euclase sample 1 are described and the attribution of the bands are presented by Gilles-Guéry *et al.* (2022). Here we compare the spectral features of an unpolarised spectrum for sample 2 to those of the oriented spectra obtained for sample 1 (Figure 24). In the IR range, a sharp peak was observed at 980 nm (10,200 cm^{-1}), which can be attributed to the second overtone of the OH-stretching mode (Gilles-Guéry *et al.* 2022). A peak at 756 nm (13,227 cm^{-1}) has not yet been attributed and is also present in the optical spectra of sample 1. In the visible range, two major bands were recorded at 481 nm (20,790 cm^{-1}) and 532 nm (18,796 cm^{-1}). These are attributed to Mn^{3+} substituting for Al^{3+} in the octahedral site (Gilles-Guéry *et al.* 2022). However,

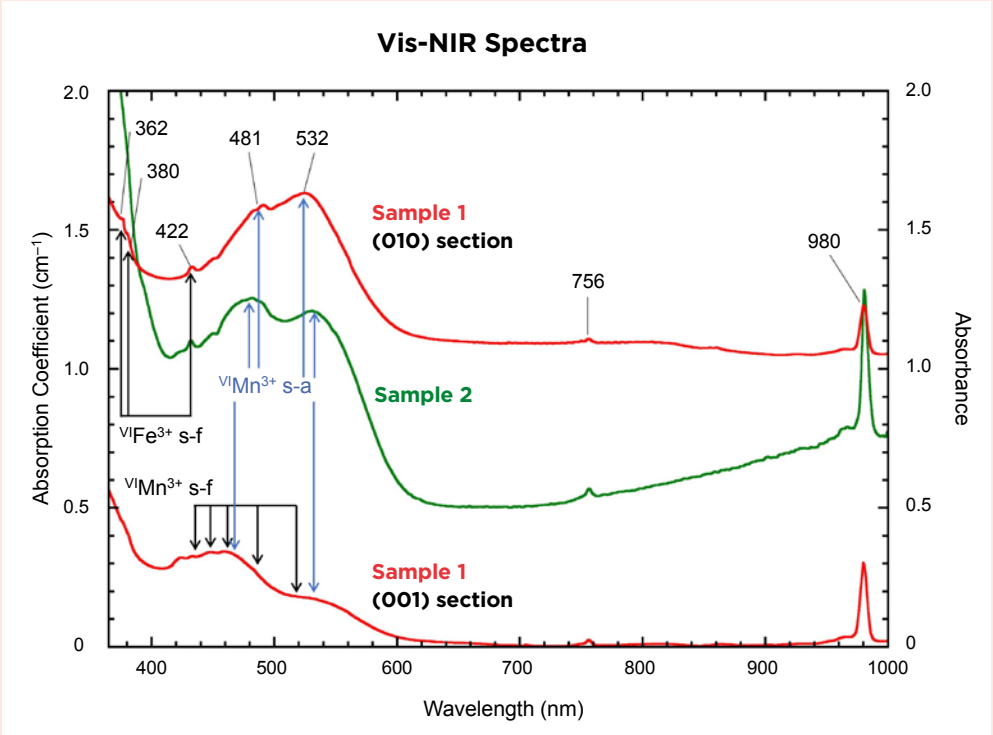

Figure 24: Vis-NIR absorption spectra of euclase sample 1 (in two orientations) and sample 2 (unpolarised) show spin-allowed (s-a) and spin-forbidden (s-f) transitions of Mn^{3+} and Fe^{3+} in the octahedral site. The major absorption bands responsible for the pinkish colouration of the euclase are due to Mn^{3+} in the octahedral Al site.

the positions of these two bands were slightly different for the two samples. This can be explained by the pleochroic nature of euclase and differences in sample orientation. (Because sample 2 was faceted it could not be oriented the same as sample 1.) Three minor bands at 362 nm (27,610 cm^{-1}), 380 nm (26,250 cm^{-1}) and 422 nm (23,680 cm^{-1}) are attributed to Fe^{3+} spin-forbidden transitions (Gilles-Guéry *et al.* 2022). The rising slope in the UV range is attributed to oxygen-metal charge transfer $O \rightarrow Fe^{3+}$ with a possible contribution of thermally unstable defects (Gilles-Guéry *et al.* 2022). The Mn^{3+} spin-forbidden transitions that were recorded in the optical spectra of sample 1 (Gilles-Guéry *et al.* 2022) cannot be seen in the spectrum of sample 2 due to its lower resolution.

DISCUSSION

Gemmological Properties and Identification

The gemmological properties that we recorded are similar to those given by Sasaki *et al.* (2021) for a 4.08 ct orangey pink euclase. The RI and SG values fall within the reported ranges for euclase in general, and are comparable with those published in previous studies of colourless and coloured euclase (Sharp 1961; Graziani & Guidi 1980; Sauer 2006). The SG of euclase has been shown to vary depending on chemical composition, which also affects the colour of the mineral: a colourless sample from Colorado (USA) had an SG value of 3.00 (Sharp 1961), an Fe-bearing euclase from Minas Gerais (Brazil; colour not indicated) had a slightly higher SG of 3.07 (Graziani & Guidi 1980), and a blue euclase from Chivor (Colombia) had an SG of 3.10 (Sauer 2006). The SG value of the pink-orange euclase samples in the present study (3.10) matches that of the blue euclase documented by Sauer (2006).

Because the RIs of euclase can overlap those of spodumene and phenakite, careful measurements of birefringence, SG and optic character are important for effective separation. The euclase RIs of 1.652–1.673 and birefringence of 0.021 are clearly above those of topaz and tourmaline, but below those of rhodochrosite. Similarities to spodumene might cause greater confusion, although the pink-orange colour of this euclase is distinct from kunzite's violetish pink, and the birefringence is greater (0.021 vs 0.015). Although a biaxial optic figure can be observed for euclase, this is not helpful because topaz and kunzite are also biaxial (however, phenakite is uniaxial). Nevertheless, the lack of a fluorescence reaction to long-wave UV radiation will immediately separate euclase from Imperial topaz and kunzite.

Inclusions

To the authors' knowledge, many of the inclusion features in the pink-orange euclase from the second occurrence have not been documented previously in euclase, and some of them appear to be unknown in any other gem material. The curly/woolly 'fibres' in the euclase are similar to some microscopic features seen in pyrope from the Czech Republic, which have been inferred as etch channels that formed along dislocations (Gilg *et al.* 2015). Our observations of the intriguing circular inclusions in this euclase lead us to believe that they are closely linked to the curly/woolly fibres, and that these may represent the final stage of 'uncoiling' of rod-like structures. The flattened circular negative crystals might be an intermediate stage, while the ring-like structures could represent a final manifestation of such an uncoiling process.

Recently, Koivula *et al.* (2021, p. 275) described a similar rod in pink-orange euclase as a 'tiny hollow cylindrical void containing a dark brown fluid and a mobile gas bubble'. We were not able to observe any filling (including fluids) within these rods in our samples, and therefore we assume that they are empty and contain only air. As explained above, any 'fibres' that may have built up these rods are no longer apparent, and in most cases any liquid that these negative crystals originally contained apparently escaped, probably via the hollow fibrous inclusions.

Chemical Composition

The pink-orange euclase samples we studied were relatively pure, and many of the trace elements found in euclase from other occurrences—such as Na, K, Ca, Sc, Cu or Sn—were not detected (Sharp 1961; Graziani & Guidi 1980; Hanson 1985). The Fe content of our sample 1 (average of 992 ppm) was similar to the amount of Fe in blue and colourless euclase from north-east Brazil (cf. Graziani & Guidi 1980; Guedes *et al.* 2006). The Fe content in sample 2 was higher (2200 ppm), but this might be explained by the different analytical methods. The EDXRF technique used for euclase no. 2 encompassed a relatively large area of the sample, while euclase no. 1 was analysed by EPMA across 100 points and showed a range of 449–2132 ppm Fe.

Based on chemical analyses presented in the literature, Mn and Ti are not common in euclase. For example, these elements were not reported in colourless or greenish blue euclase (Graziani & Guidi 1980; Pignatelli *et al.* 2017). The Mn contents of our samples, although low (73 ppm in no. 1 and 63 ppm in no. 2), are anomalous in euclase and compare well with a value of around 60 ppm Mn obtained from an orangey pink stone

by Sasaki *et al.* (2021). Similar low Mn contents have also been found in pink beryl: 150 ppm in material from Minas Gerais, Brazil (Blak *et al.* 1982), and 60–82 ppm in samples from Elba Island, Italy (Caucia *et al.* 2016).

Our chemical analyses showed that both stones contained similar amounts of Ge (142 and 154 ppm). Germanium is commonly present in trace amounts in some granitic pegmatite minerals (e.g. topaz, mica and spodumene; Bernstein 1985), and has also been found in blue and colourless euclase from Minas Gerais, Brazil (Graziani & Guidi 1980). In addition, a Ge content of 230–530 ppm was reported in greenish blue euclase from Colombia (Pignatelli *et al.* 2017), which is not associated with pegmatites but rather with hydrothermally altered black shales. Our analyses of green Mn-bearing andalusite from Paramirim das Crioulas (in the municipality of Érico Cardoso, Bahia State) showed a Ge content of 97–105 ppm. This raises questions about the geochemistry of the region, which could offer additional clues to the formation of pink-orange euclase at both occurrences.

Cause of Colour and Pleochroism

The causes of colour, pleochroism and heat-induced change of colour in this pink-orange euclase were studied by Gilles-Guéry *et al.* (2022). The colour and pleochroism from orange to pink are related to the substitution of Mn^{3+} in the octahedral Al site. An additional component, which might contribute to thermally unstable defects together with the rising slope towards the UV region, was assigned to $O \rightarrow Fe^{3+}$ oxygen–metal charge transfer.

Gilles-Guéry *et al.* (2022) found that heat treatment modifies the colour of this euclase from pink-orange to pure pink by removing the thermally unstable defects that cause the yellow tint. The colour of the samples after heat treatment to 300°C and 500°C (in red) is plotted in Figure 10. The heat-treated colour was shown to be stable by comparing the optical spectra and chromatic coordinates, at least within the two-year period of the study (Gilles-Guéry *et al.* 2022).

Formation of Pink-Orange Euclase

We infer that the pink-orange euclase from Bahia, Brazil, formed in hydrothermal veins hosted by a schistose unit within metaarenite. Abundant green Mn-bearing andalusite crystals were found by the authors in nearby schists (Figure 6b). The presence of Mn^{3+} in the andalusite (Hålenius 1978; Abs-Wurmbach *et al.* 1981; Smith *et al.* 1982; Schnellrath 1989) indicates local oxidising conditions. The absence of Mn^{2+} in the euclase and its stable pink colour (even after heat treatment) due to Mn^{3+} is consistent with oxidative formation conditions (Gilles-Guéry *et al.* 2022).

During the formation of Mn^{3+}-bearing gems (e.g. Tarantola *et al.* 2019), a low fluid:rock ratio throughout the geodynamic evolution and an Fe-poor character of the hydrothermal fluid are necessary to buffer the oxygen activity to high levels and create adequate oxidising conditions. This allows the preservation of Mn^{3+} during interactions between hydrothermal fluids and the surrounding rocks. The presence of Ge in the pink-orange euclase is consistent with the contamination of the hydrothermal fluid by the surrounding rocks, similar to Colombian euclase (Pignatelli *et al.* 2017).

The overall gemmological properties and chemical composition of the euclase samples from both occurrences were very similar, and we infer that they have the same geochemical signature. Based solely on these characteristics, and not looking at the internal features, there is nothing to distinguish material from the two occurrences. However, based on our observation of internal features, we could clearly separate euclase samples from both occurrences. Although they both probably formed in the same geological environment, the differences in their inclusion scenarios could be due to contamination from the surrounding rocks. Quartz crystals mined from the same regions may be relatively pure or contain fibrous inclusions. As for the quartz, differences in the inclusions present in the euclase from each occurrence could be associated with slight variations in host-rock composition.

CONCLUSION

Gem-quality pink-orange euclase was unknown before being found in the past few years in Bahia, Brazil. Surprisingly, two separate occurrences of this new gem material were found at approximately the same time. Based on information provided by dealers and local miners, the euclase comes from both the Paramirim and Catolés mountain ranges, but only small amounts have been recovered so far. Although the rarity of this pink-orange euclase means that it is not likely to be encountered by most gemmologists or appraisers at the present time, additional production is certainly possible in the future. The properties presented in this article will help separate this euclase from similar-looking gem materials such as Imperial topaz.

Although the pink-orange euclase from each occurrence shares the same overall gemmological properties and chemical characteristics, samples from the two localities show different crystal morphology, colour zoning

and inclusion suites. Euclase from the second reported occurrence, in the Catolés mountain range, contains a particularly interesting diversity of internal features (e.g. Figure 25), including unusual curly/woolly fibres as well as associated circular, cylindrical and ring-like structures that have not been seen previously in any gem material to the authors' knowledge.

Compared to many pink-coloured gem materials (e.g. topaz, tourmaline, garnet, beryl, etc.), this pink-orange euclase presents an unusual pleochroic hue that makes it quite attractive to collectors. The cause of its pink-orange colour is related to the substitution of Mn^{3+} in the octahedral Al site. The heat-treatment study performed by Gilles-Guéry *et al*. (2022) revealed an additional contribution to the colouration, which is possibly due to thermally unstable defects.

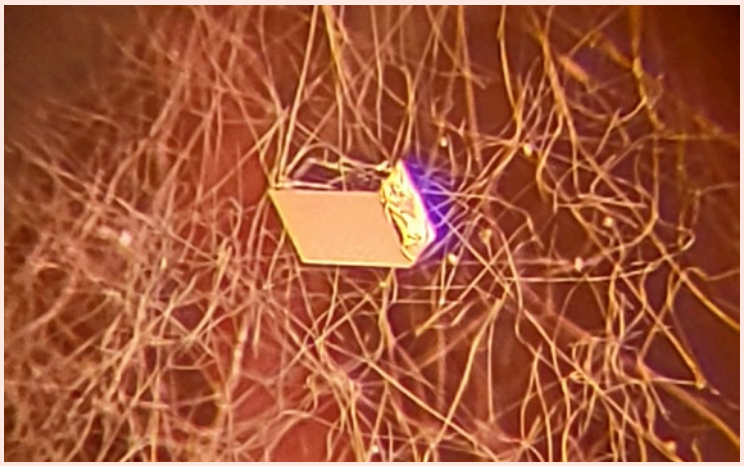

Figure 25: Pink-orange euclase from Brazil contains a variety of interesting inclusions that are not commonly encountered by gemmologists, such as the curly/woolly fibres and the rhomb-shaped cavity (probably a dolomite crystal that was etched away), shown here in the faceted stone from the second occurrence that is seen in Figure 1. Photomicrograph by B. Williams; image width 1.5 mm.

REFERENCES

Abs-Wurmbach, I., Langer, K., Seifert, F. & Tillmanns, E. 1981. The crystal chemistry of (Mn^{3+}, Fe^{3+})-substituted andalusites (viridines and kanonaite), $(Al_{1-x-y}Mn^{3+}_xFe^{3+}_y)_2(O|SiO_4)$: Crystal structure refinements, Mössbauer, and polarized optical absorption spectra. *Zeitschrift für Kristallographie*, **155**(1–2), 81–113, https://doi.org/10.1524/zkri.1981.155.1-2.81.

Bernstein, L.R. 1985. Germanium geochemistry and mineralogy. *Geochimica et Cosmochimica Acta*, **49**(11), 2409–2422, https://doi.org/10.1016/0016-7037(85)90241-8.

Blak, A.R., Isotani, S. & Watanabe, S. 1982. Optical absorption and electron spin resonance in blue and green natural beryl. *Physics and Chemistry of Minerals*, **8**(4), 161–166, https://doi.org/10.1007/bf00308238.

Cassedanne, J. & Philippo, S. 2015. *Minerals and Gem Deposits of the Eastern Brazilian Pegmatites*, Vols. 1 and 2. Natural History Museum of Luxembourg, Luxembourg, 672 pp.

Cassedanne, J.P. & Cassedanne, J. 1980. Note sur l'andalousite gemme de la Chapada Diamantina. *Revue de Gemmologie A.F.G.*, **63**, 15–17.

Caucia, F., Marinoni, L., Callegari, A.M., Leone, A. & Scacchetti, M. 2016. Gem-quality morganite from Monte Capanne pluton (Elba Island, Italy). *Neues Jahrbuch für Mineralogie, Abhandlungen*, **193**(1), 69–78, https://doi.org/10.1127/njma/2015/0293.

Chaves, M.L.S.C. & Karfunkel, J. 1994. Novas ocorrências de euclásio em Minas Gerais. *Boletim IG-USP. Série Científica*, **25**, 53–60.

de Carvalho, L.D.V., Schnellrath, J. & de Medeiros, S.R. 2018. Mineral inclusions in diamonds from Chapada Diamantina, Bahia, Brazil: A Raman spectroscopic characterization. *REM – International Engineering Journal*, **71**(1), 27–35, https://doi.org/10.1590/0370-44672016710160.

de Souza, J.D., de Melo, R.C., Kosin, M., Santos, R.A., Teixeira, L.R., Sampaio, A.R., Guimarães, J.T., Vieira Bento, R. *et al*. 2003. *Mapa Geológico do Estado da Bahia. Escala 1:1.000.000. Versão 1.1*. Programas Carta Geológica do Brasil ao Milionésimo e Levantamentos Geológicos Básicos do Brasil, CPRM—Serviço Geológico do Brasil, Salvador, Brazil.

Eeckhout, S.G., Castañeda, C., Ferreira, A.C.M., Sabioni, A.C.S., de Grave, E. & Vasconcelos, D.C.L. 2002. Spectroscopic studies of spessartine from Brazilian pegmatites. *American Mineralogist*, **87**(10), 1297–1306, https://doi.org/10.2138/am-2002-1005.

Gilg, H.A., Gast, N. & Hyršl, J. 2015. Chromium pyropes from Bohemia: Characterization and identification in archaeological and historical jewellery. *13th Biennial SGA Meeting,* Nancy, France, 24–27 August, 1301–1304.

Gilles-Guéry, L., Galoisy, L., Schnellrath, J., Baptiste, B. & Calas, G. 2022. Mn^{3+} and the pink color of gem-quality euclase from northeast Brazil. *American Mineralogist*, **107**(3), 489–494, https://doi.org/10.2138/am-2021-7838.

Graziani, G. & Guidi, G. 1980. Euclase from Santa do Encoberto, Minas Gerais, Brazil. *American Mineralogist*, **65**(1–2), 183–187.

Guedes, K.J., Krambrock, K., Pinheiro, M.V.B. & Menezes Filho, L.A.D. 2006. Natural iron-containing blue and colorless euclase studied by electron paramagnetic resonance. *Physics and Chemistry of Minerals*, **33**(8–9), 553–557, https://doi.org/10.1007/s00269-006-0102-1.

Guimarães, J.T., Martins, A.A.M., Filho, E.L.A., Loureiro, H.S.C., Arcanjo, J.B.A., das Neves, J.P., Abram, M.B., da Silva, M.d.G. *et al*. 2005. *Projeto Ibitiara - Rio de Contas: Estado da Bahia. Programa Recursos Minerais do Brasil, Escala 1:200.000*. CPRM—Serviço Geológico do Brasil and CPBM—Companhia Baiana de Pesquisa Mineral, Salvador, Brazil, 157 pp. + appendixes and maps.

Hålenius, U. 1978. A spectroscopic investigation of manganian andalusite. *Canadian Mineralogist*, **16**(4), 567–575.

Hanson, A. 1985. Découverte d'euclase dans un filon de quartz à Ottré, massif de Stavelot, Belgique. *Bulletin de Minéralogie*, **108**(2), 139–143, https://doi.org/10.3406/bulmi.1985.7863.

Hunt, R.W.G. & Pointer, M.R. 2011. *Measuring Colour*, 4th edn. John Wiley & Sons Ltd, Chichester, West Sussex, 469 pp.

Koivula, J.I., Renfro, N. & Nicastro, I. 2021. *G&G* Micro-World: Quarterly crystal: Fibers and rods in euclase. *Gems & Gemology*, **57**(3), 274–275.

Pignatelli, I., Giuliani, G., Morlot, C., Rouer, O., Claiser, N., Chatagnier, P.-Y. & Goubert, D. 2017. Recent advances in understanding the similarities and differences of Colombian euclases. *Canadian Mineralogist*, **55**(4), 799–820, https://doi.org/10.3749/canmin.1700011.

Sasaki, M., Miura, M. & Saruwatari, K. 2021. Lab Notes: Pink euclase. *Gems & Gemology*, **57**(4), 375–376.

Sauer, D.A. 2006. Gem News International: Faceted blue euclase from Colombia. *Gems & Gemology*, **42**(2), 173.

Schnellrath, J. 1989. *Brasilianische Andalusite und Zink-Staurolithe von Edelsteinqualitaet: Chemismus, Bildungsbedingungen, Optische und Kristallographische Eigenschaften*. PhD thesis, Johannes Gutenberg-Universität Mainz, Germany, 126 pp.

Sharp, W.N. 1961. Euclase in greisen pipes and associated deposits, Park County, Colorado. *American Mineralogist*, **46**(11–12), 1505–1508.

Smith, G., Hålenius, U. & Langer, K. 1982. Low temperature spectral studies of Mn^{3+}-bearing andalusite and epidote type minerals in the range 30000–5000 cm^{-1}. *Physics and Chemistry of Minerals*, **8**(3), 136–142, https://doi.org/10.1007/bf00311284.

Tarantola, A., Voudouris, P., Eglinger, A., Scheffer, C., Trebus, K., Bitte, M., Rondeau, B., Mavrogonatos, C. *et al*. 2019. Metamorphic and metasomatic kyanite-bearing mineral assemblages of Thassos Island (Rhodope, Greece). *Minerals*, **9**(4), https://doi.org/10.3390/min9040252.

The Authors

Dr Lætitia Gilles-Guéry*, Dr Laurence Galoisy and Prof. Georges Calas
Sorbonne Université, Muséum National d'Histoire Naturelle, CNRS, IRD, Institut de Minéralogie, de Physique des Matériaux et de Cosmochimie (IMPMC), 4 Place Jussieu, 75252 Paris Cedex 05, France

* Currently: Lætitia Gilles-Guéry Conseil, 19 rue Emile Dubois, 75014 Paris, France
Email: laetitia.gilles-guery@orange.fr

Luiza Almeida Villar de Queiroz and Dr Jurgen Schnellrath
Centro de Tecnologia Mineral (CETEM), Ilha da Cidade Universitária, 21941-908 Rio de Janeiro, Rio de Janeiro, Brazil

Bear Williams FGA and Cara Williams FGA
Stone Group Laboratories LLC, Jefferson City, Missouri, 65110, USA

Tiago Campolina Barbosa
Centro de Tecnologia em Nanomateriais e Grafeno (CTNANO), Rua Professor José Vieira de Mendonça, 520 31310-260 Belo Horizonte, Minas Gerais, Brazil

Brendan M. Laurs FGA
Gem-A, 1106 2nd St. #317, Encinitas, California, 92024, USA

Acknowledgements

We acknowledge technical support provided by Sorbonne University's IMPMC spectroscopy facility and Camparis microprobe facility. Dudley Blauwet (Dudley Blauwet Gems, Louisville, Colorado, USA) kindly loaned euclase sample 2 for this research. We thank Dr George Rossman (California Institute of Technology, Pasadena, California, USA) for his analysis of sample 2. Our appreciation also goes to Julio Martins Cardoso dos Santos for taking some of the authors to the first euclase occurrence near Livramento de Nossa Senhora, and for donating a considerable amount of rough material for our research. In addition, we thank Álvaro Lúcio, his son Eduardo Ribeiro Lúcio (in memoriam) and grandson Carlos Lúcio for loaning a parcel of euclase from the second occurrence.

Gem-A
THE GEMMOLOGICAL ASSOCIATION OF GREAT BRITAIN

Study gemmology online!

- Online class groups
- Virtual learning
- Interactive quizzes
- Start your journey to FGA Membership with online learning by leading provider, Gem-A

Contact **education@gem-a.com** for more information

Creating gemmologists since 1908

Gem-A, 21 Ely Place, London, EC1N 6TD, UK. T: +44 (0)20 7404 3334, W: www.gem-a.com. Registered charity no. 1109555.

Demantoid Garnet from Antetezambato, Northern Madagascar—Internal Characteristics and Their Use in Deciphering Geographic Origin

J. C. (Hanco) Zwaan

ABSTRACT: Demantoid garnets from Antetezambato, northern Madagascar, contain a characteristic inclusion suite typical of a skarn occurrence. Unlike demantoid from the classic deposits in the Ural Mountains, Russia, and from other serpentinite-related occurrences, the stones from Madagascar do not contain 'horsetail' inclusions, but instead host groups of small, rounded diopside grains, fluorapatite, dolomite, calcite, quartz, pyrite and wollastonite, as well as rare native bismuth. Partially healed fissures contain two-phase fluid inclusions (with H_2O and a gas bubble) of varying salinity. Negative crystals, commonly large and empty, sometimes also contain H_2O. Pronounced growth features and parallel hollow tubes are also present. Demantoid from Namibia likewise has a skarn origin and shows some similar internal features, as well as some that are different, such as the common presence of fluorapatite and small multiphase fluid inclusions, along with the absence of large negative crystals and native bismuth. A review of previously advocated methods for geographic origin determination of demantoid based on chemical fingerprinting alone shows that this technique is applicable only to stones with a nearly pure andradite composition when differentiating Malagasy and Namibian localities. In such cases, elevated traces of Mn are indicative of a Namibian origin.

The Journal of Gemmology, **38**(1), 2022, pp. 64–79, https://doi.org/10.15506/JoG.2022.38.1.64

In 2009, fine specimens and attractive faceted gemstones of green demantoid (as well as brown andradite) entered the market from a skarn deposit near Antetezambato in northern Madagascar (Rondeau *et al.* 2009; Pezzotta 2010; Pezzotta *et al.* 2011). The area was worked by artisanal miners until 2011 when production declined as the near-surface part of the deposit was exhausted. In 2013–2014, initial open-cast mining was done by a joint venture between the Malagasy company Ruby Red Madagascar (owner of the mining rights) and a local gem-trading company. In 2018, a new mining project was initiated by a joint venture between Ruby Red Madagascar and Prosperity Earth LLC, with mechanised equipment used to explore the deposit to a depth of 15–18 m (Gomelsky & Bates 2021). Mining is ongoing, and the company takes great pride in working in an ethical and responsible way with the local community—such as employing an all-Malagasy workforce and contributing to various initiatives pertaining to health, education, infrastructure and agriculture. The environmental footprint of the mining is also carefully considered, mainly through the replanting

Figure 1: These faceted samples of demantoid from Antetezambato, Madagascar, were selected to characterise their inclusions, with the possibility of identifying criteria for origin determination. Shown here are 19 stones (0.43–0.89 ct) of the 62 Madagascar samples in the study collection. Photo by J. C. Zwaan.

of mangroves in the area (Gomelsky & Bates 2021; J. Ferry, pers. comm. 2021).

In recent years, there has been increasing interest in the geographic origin determination of demantoid, with research focusing mainly on chemical analyses and chemometric methods (Schwarzinger 2019; Bindereif *et al.* 2020), but also on inclusion characteristics (Lewis 2018). The present study provides new data on the inclusion characteristics of demantoid from Madagascar (Figures 1 and 2), with the goal of refining criteria for origin determination. In addition, the internal microscopic features are compared to those seen in Namibian demantoid, which has a similar skarn origin. Finally, published chemical data for stones from these two deposits is evaluated further to assess the usefulness of trace-element content for aiding in their separation.

MATERIALS AND METHODS

For this study, 62 faceted Madagascar demantoids (six round brilliants and 56 round modified brilliants) ranging from 0.18 to 0.89 ct were examined (again, see Figures 1 and 2). They were loaned by Prosperity Earth LLC, and because they were selected for the presence of inclusions, these study samples are not representative of the highest-quality gem material from this locality. They were basically all transparent, moderately to heavily included (only one stone was slightly included), and some contained large fissures or cavities (or both). They varied from green to orangey yellow. Observation face-up with the unaided eye and a standard daylight-equivalent lamp showed evenly distributed colouration that ranged from an almost pure green (slightly yellowish green) to yellow-green (Munsell 10GY, 7.5GY, 5GY and 2.5GY) to greenish yellow and yellow (10Y, 7.5Y and 5Y) and, in one stone, orangey yellow (between 2.5Y and 10YR). Most colours showed light to moderate tones and were moderately saturated; the yellower stones typically appeared brownish. While samples showing a dominant green colour are classified as demantoid, the others are simply called andradite (or the trade name *topazolite*). However, boundaries between these varieties are not well

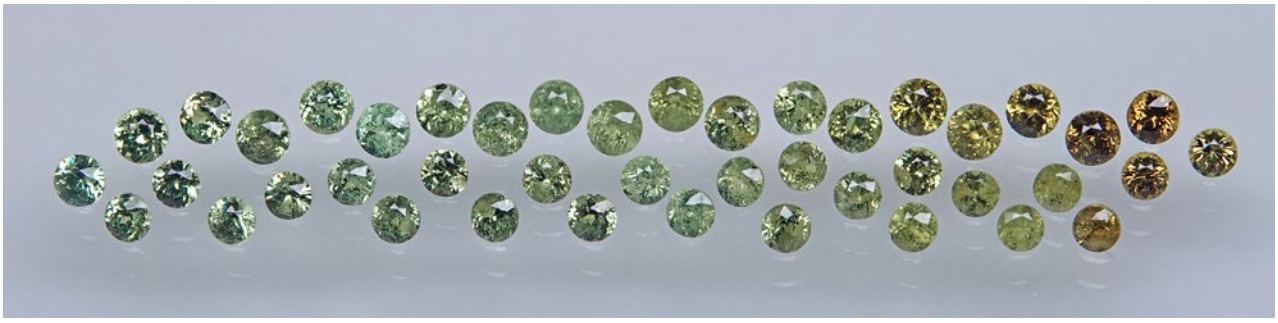

Figure 2: The remaining 43 garnets (0.18–0.36 ct) in the study collection are arranged in this photo to display the range of colour observed in the Madagascar material. Photo by J. C. Zwaan.

established, and they are not differentiated in this study. Overall the gems had a lively appearance, consistent with the optical properties of demantoid, which has a high (sub-adamantine) lustre and very high dispersion.

For comparison, internal characteristics were also examined in a selection of demantoid samples from the Erongo region, Namibia, showing a similar appearance. They consisted of 15 faceted stones (0.26–3.21 ct) and 23 transparent fragments (mostly with parallel polished windows; 0.79–26.24 ct). The majority of them were kindly loaned by the German-based company Paul Wild OHG, while one faceted stone and six fragments were from the Naturalis collection in Leiden, The Netherlands.

Internal features were observed with a standard gemmological microscope and a Nikon Eclipse E600 POL polarising microscope. For photomicrography, both were connected to a Nikon DS-Ri2 digital camera. Inclusions in 44 of the stones from Madagascar and 20 samples from Namibia were analysed by Raman spectroscopy using a Thermo Scientific DXR Raman microscope with 532 nm laser excitation. Scanning electron microscopy–energy dispersive X-ray spectroscopy (SEM-EDS) analyses of inclusions in two samples from Madagascar were performed using a JEOL JSM-8480LV scanning electron microscope coupled to an Oxford Instruments Inca x-act silicon drift detector (range of elements analysed: from B to U). Measurements were taken at 15 kV, with a 40 s acquisition time for each analysis and a 3 µm spot size.

MICROSCOPIC CHARACTERISTICS

The internal features described in this section all pertain to the Madagascar samples, while those observed in the demantoids from Namibia are compared further below in the Discussion section. All of the photomicrographs were taken by the author.

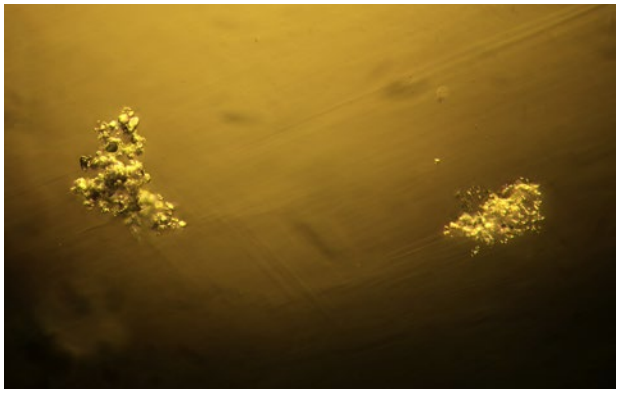

Figure 3: Clusters of small diopside crystals were encountered in most of the demantoids studied. The cluster on the right especially displays a 'bread-crumb' appearance due to the minute size of most of the individual crystals. Oblique illumination; image width 0.63 mm.

Mineral Inclusions

The most commonly encountered mineral inclusion (confirmed in 37 of the 44 samples analysed by Raman spectroscopy) was diopside, which occurred as small, mostly rounded, equidimensional grains that were grouped in clusters. Individual stones contained from one to many such clusters. When viewed with a loupe or with low magnification, the clusters looked like 'bread crumb' inclusions. At higher magnification, it became apparent that most of the individual diopside grains were very small and rounded (Figure 3). Occasionally, slightly larger grains and, rarely, euhedral crystals of diopside were present (Figure 4). Many of the clusters were analysed with Raman spectroscopy to see whether any other minerals were present, but none were found. Raman analysis gave the best match to clinopyroxene, and in particular to diopside. The positions of the Raman peaks and their comparatively low full-width-at-half-maximum values indicated a relatively pure diopside composition ($CaMgSi_2O_6$), compared to various

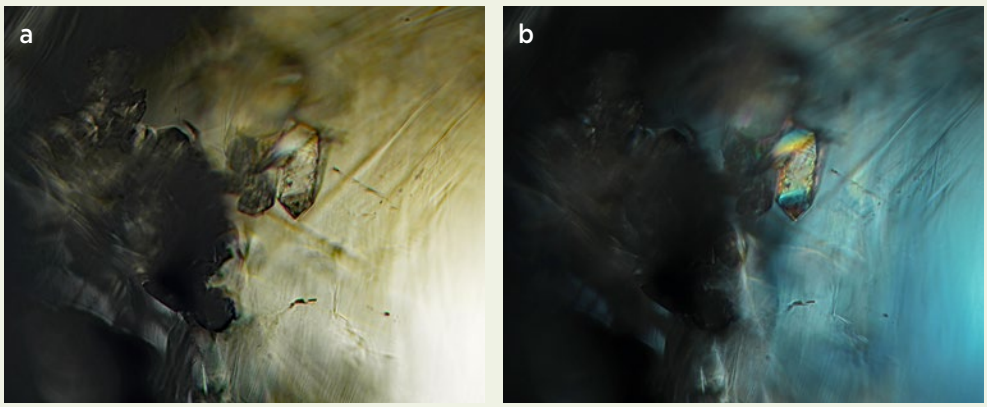

Figure 4: A rare euhedral diopside crystal is visible here at the edge of a larger cluster of diopside crystals, and is seen in (**a**) transmitted light and (**b**) cross-polarised light, where the euhedral diopside shows interference colours. Image width 0.6 mm.

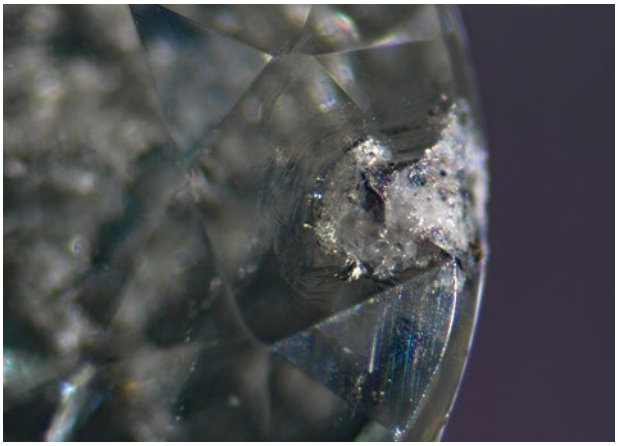

Figure 5: Carbonate inclusions in demantoid from Madagascar include whitish aggregates of dolomite. Image width 2.0 mm.

diopside-clinoenstatite mixtures ($CaMgSi_2O_6$–$Mg_2Si_2O_6$; cf. Tribaudino *et al.* 2012). An increase in Fe concentration—as expected for hedenbergite ($CaFeSi_2O_6$) and augite ($[Ca,Mg,Fe^{2+}]_2Si_2O_6$) components—would shift most Raman bands to lower wavenumbers (cf. Huang *et al.* 2000; Buzatu & Buzgar 2010). A semi-quantitative SEM-EDS analysis of a diopside inclusion at the surface of one demantoid sample confirmed its nearly pure composition (in wt.%): MgO 17.0, SiO_2 57.2, CaO 24.4 and FeO 1.35, giving $Ca_{50.0}Mg_{47.8}Fe_{2.2}$ (or $X_{Mg} = 0.96$).

Carbonate inclusions were confirmed in nine of the demantoids. They occurred as whitish aggregates of small grains (Figure 5) and as small, transparent crystals, some with a rhombohedral shape (Figure 6). Raman spectroscopy revealed that the whitish aggregates consisted of dolomite ($CaMg[CO_3]_2$) and the transparent crystals were calcite ($CaCO_3$).

Small, transparent apatite crystals were occasionally identified. They were mostly prismatic (Figure 7), although one rounded apatite grain was also found. Raman spectroscopy gave a best match with fluorapatite ($Ca_5[PO_4]_3F$) in the RRUFF database (https://rruff.info).

Quartz was not commonly observed, but it might have just been elusive, occurring as colourless grains in proximity to the many clusters of diopside and other inclusions. One quartz grain was spotted at the surface of a sample by its much lower lustre compared with the demantoid host (Figure 8). Another quartz inclusion

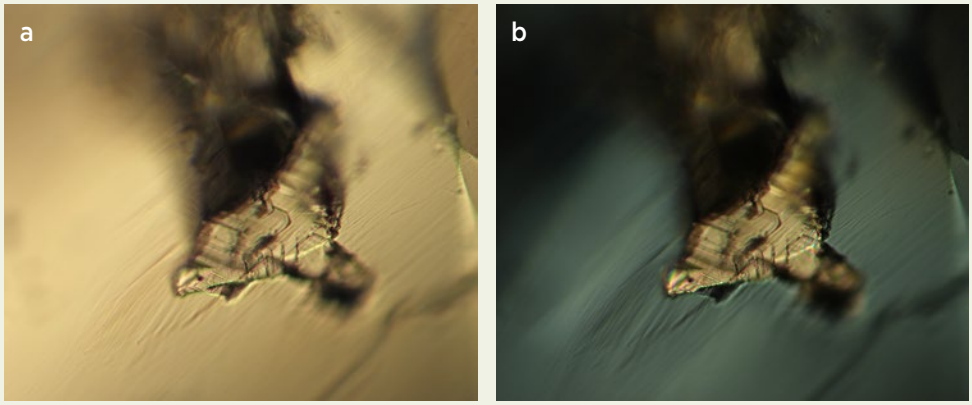

Figure 6: (**a**) Carbonate inclusions in Madagascar demantoid also consist of transparent calcite crystals. (**b**) Between crossed polarisers, the calcite shows characteristic high-order interference colours. Image width 0.6 mm.

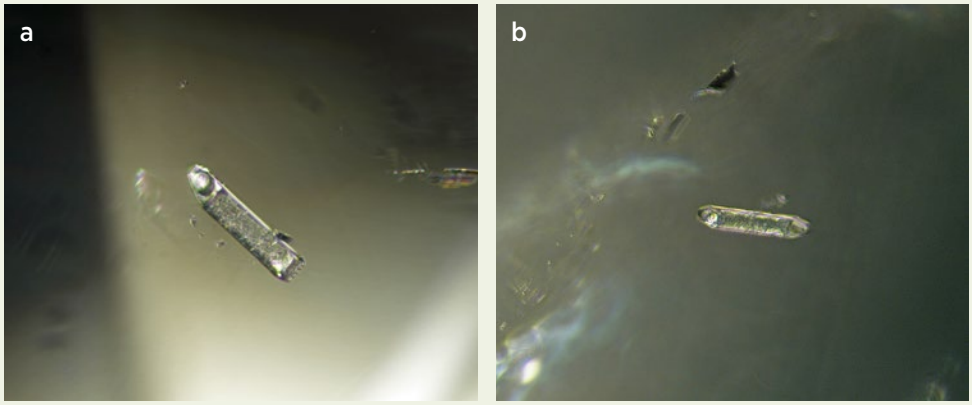

Figure 7: An elongated prismatic shape is typical of the fluorapatite inclusions in the Madagascar demantoid samples, although they were not commonly encountered. Examples are shown here in (**a**) darkfield illumination (image width 0.3 mm) and (**b**) oblique illumination (image width 0.4 mm).

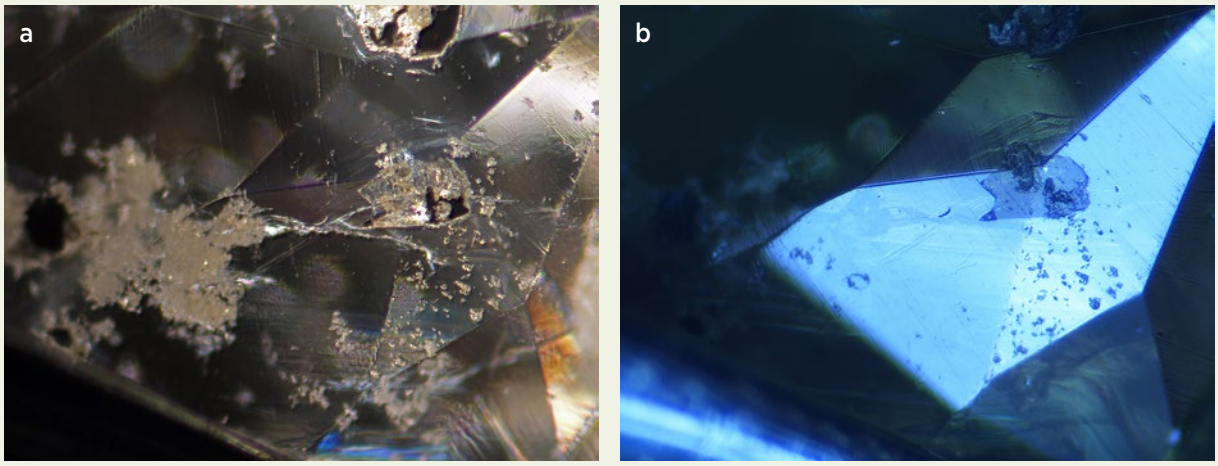

Figure 8: Quartz inclusions were rarely identified in the Madagascar demantoid samples. (**a**) A quartz inclusion is located near a cluster of diopside crystals in a rather heavily included stone, seen here in darkfield illumination. (**b**) Its presence is betrayed by a significantly lower lustre than the host demantoid where it intersects the surface when viewed with reflected light. Image width 1.6 mm.

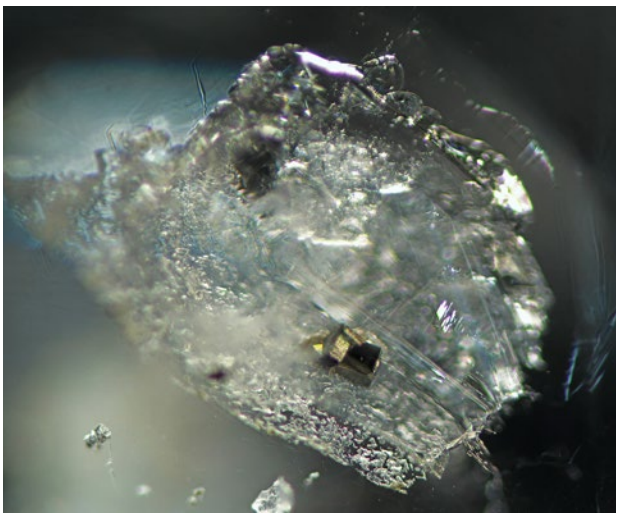

Figure 9: In this Madagascar demantoid, a transparent quartz inclusion is present above a partially healed fissure and hosts interpenetrant pyrite cubes. Darkfield and oblique illumination; image width 1.2 mm.

was positioned above a partially healed fissure and contained interpenetrant pyrite cubes (Figure 9).

Wollastonite ($CaSiO_3$) was identified in two of the stones. It occurred as transparent, long prismatic to needle-like crystals (Figure 10). Very small wollastonite inclusions varied from elongate to more equidimensional and slightly rounded. Although the Raman spectra obtained were mixed with the signals of the host demantoid, wollastonite could readily be identified, matching well with reference spectra in the RRUFF database.

Several of the studied demantoids contained iron-stained fissures (Figure 11), which were typically small. In one stone, Raman analysis confirmed the presence of goethite.

Notably, three of the stones contained opaque needle- or rod-like inclusions with a metallic lustre (Figure 12). Two of these inclusions were parallel-oriented, and Raman analysis where they intersected the surface revealed a

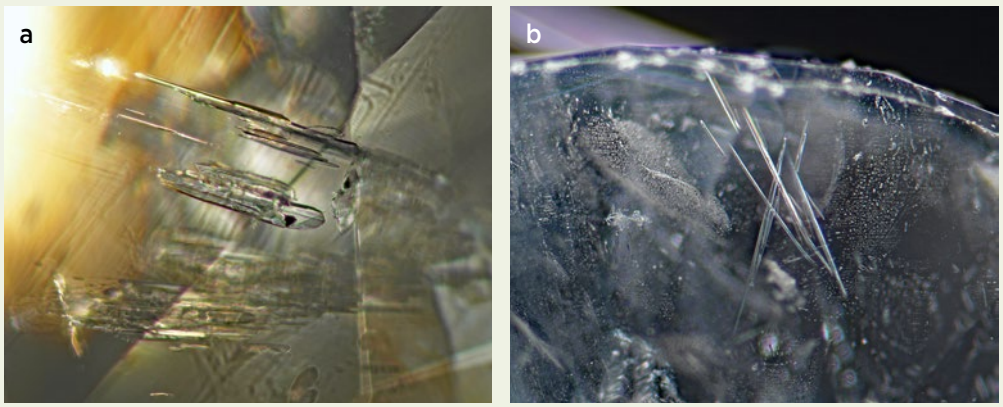

Figure 10: (**a**) Long prismatic crystals and (**b**) needles of wollastonite are rarely present in Madagascar demantoid. (a) Transmitted light, image width 1.1 mm; and (b) darkfield illumination, image width 1.8 mm.

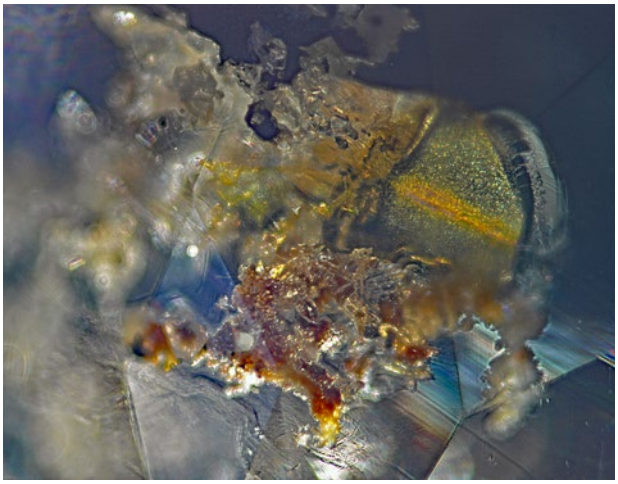

Figure 11: In this Madagascar demantoid, goethite is present in a relatively large fissure, appearing as small orangey brown flakes and brownish yellow microcrystals. Darkfield illumination, image width 2.5 mm.

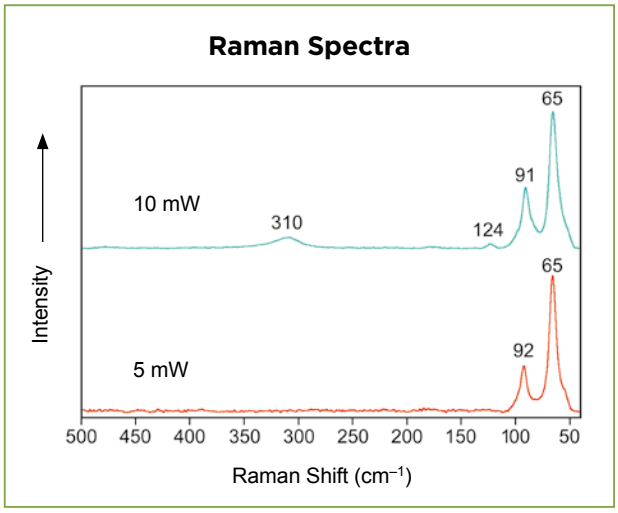

Figure 13: The Raman spectrum of a surface-reaching bismuth inclusion analysed with 10 mW excitation shows weak features at 310 and 124 cm^{-1}, which indicate the presence of bismite, as expected for the oxidation of bismuth. These features are not visible in the spectrum obtained with 5 mW excitation, consistent with the oxidation process being hastened by higher laser power.

spectrum (in the low-wavenumber range) characteristic of native bismuth, with a strong band at about 65 cm^{-1} and another pronounced feature at about 91 cm^{-1} (Chukanov & Vigasina 2020). Native bismuth is easily oxidised in air and can alter to bismite (Bi_2O_3), and this may be hastened by increasing the laser power during Raman analysis (Zepeda *et al.* 2012). After raising the laser power from 5 to 10 mW, relatively weak, broad features appeared at 310 and 124 cm^{-1}, indicating the presence of ß-Bi_2O_3 (Figure 13). SEM-EDS analysis confirmed the presence of Bi along with varying small amounts of oxygen. Ten analyses (four on one bismuth inclusion and six on another) gave Bi = 91.1–95.2 wt.% and O = 4.8–8.9 wt.%.

In one other demantoid, Raman analysis again confirmed the presence of native bismuth. This inclusion was a bit thicker and appeared bent and branch-like (Figure 14a). Its characteristic silvery grey-white colour and high lustre were apparent where it intersected the surface (Figure 14b).

In another demantoid, irregular grains were encountered that looked like an ore mineral and were associated with a partially healed fissure (liquid feather). The grains appeared steel-grey to black, with an olive green overtone (Figure 15). Raman spectroscopy suggested the presence of stannite (Cu_2FeSnS_4), which is consistent with the visual appearance of the grains. Because the inclusions were small and relatively deep under the surface, the resulting Raman spectra were mixed with strong bands of the host demantoid. Nevertheless, after multi-component analysis of a representative mixed spectrum, the strongest band generated by the inclusion had a peak

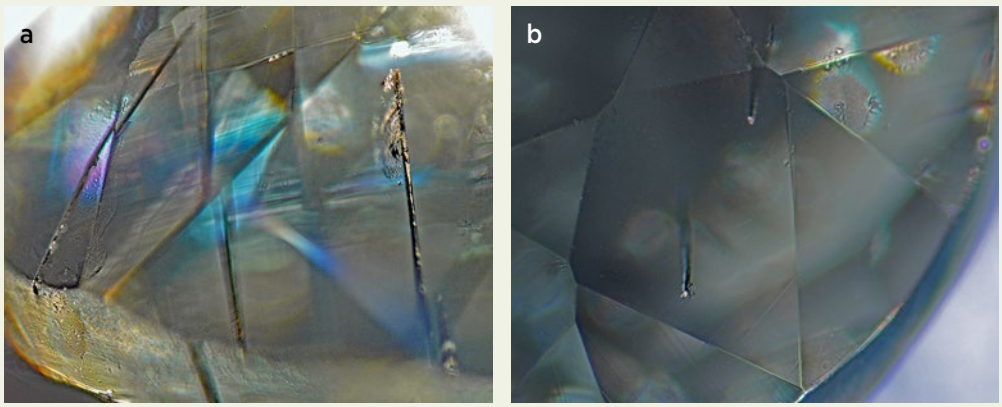

Figure 12: Opaque, needle-like inclusions with a metallic lustre in Madagascar demantoid are shown with (**a**) oblique illumination and (**b**) darkfield illumination. Raman analysis identified them as native bismuth. Image width 1.7 mm.

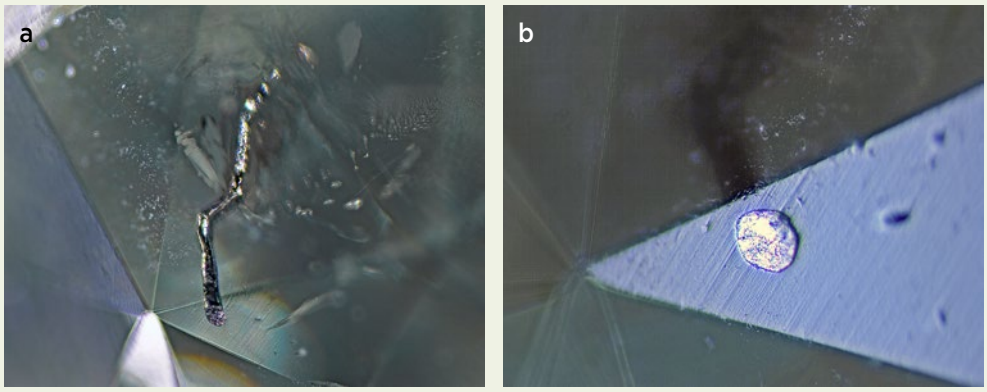

Figure 14: (**a**) Native bismuth is present in this Madagascar demantoid as a bent, branch-like inclusion. (**b**) With overhead lighting, its characteristic silvery grey-white colour can be seen where it intersects the surface. Image widths (a) 1.8 mm and (b) 0.7 mm.

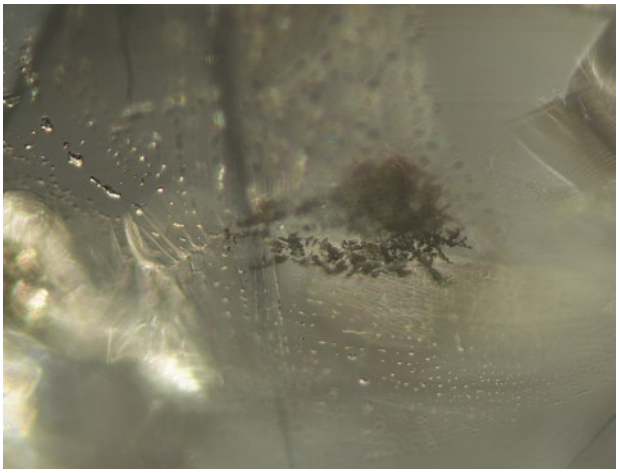

Figure 15: In one Madagascar demantoid, irregular metallic grey-to-black grains (probably stannite) are associated with a partially healed fissure. Image width 0.8 mm.

position of 322 cm^{-1} (Figure 16), which exactly matches with the principal peak of the stannite spectra in the RRUFF database.

Fluid Inclusions

Partially healed fissures were common, taking on various forms. Some contained clearly discernible two-phase inclusions with regular shapes, often elongated or rounded (or both; Figure 17a), but also with slightly jagged or irregular forms (Figure 17b) that were similar to those of 'trichites' in tourmaline. Other partially healed fissures were more veil-like, containing minute voids, and were fairly large or showed a characteristic triangular ('pine tree') shape (Figure 18).

Raman analysis confirmed that the two-phase inclusions consisted of aqueous liquid-vapour phases. Spectra

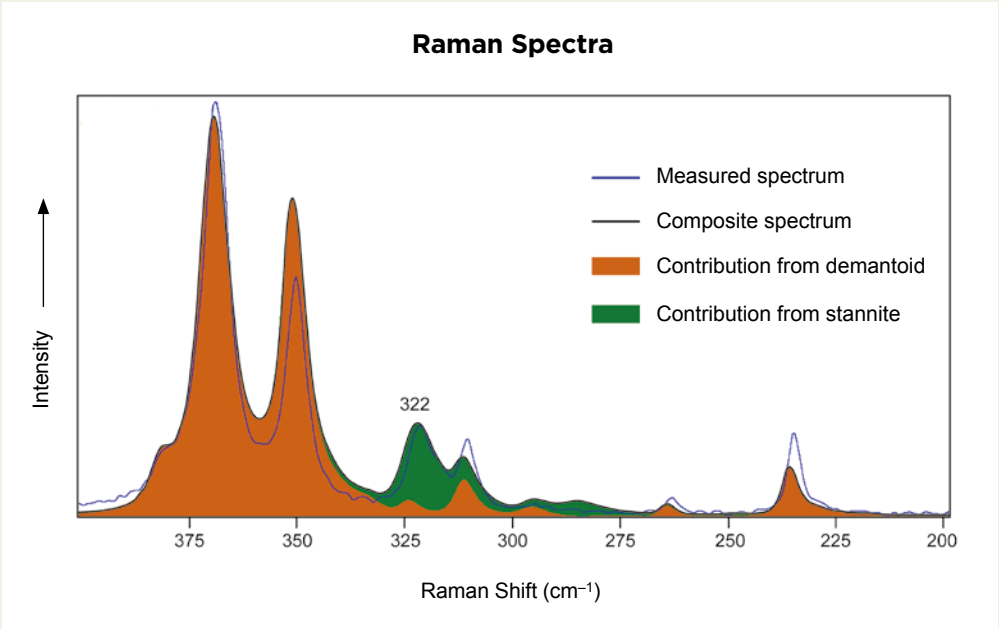

Figure 16: Raman analysis of the inclusion in Figure 15 yielded a mixed spectrum. The blue trace is the measured Raman spectrum and the black trace is the composite graph. Multicomponent analysis strongly suggests the presence of stannite.

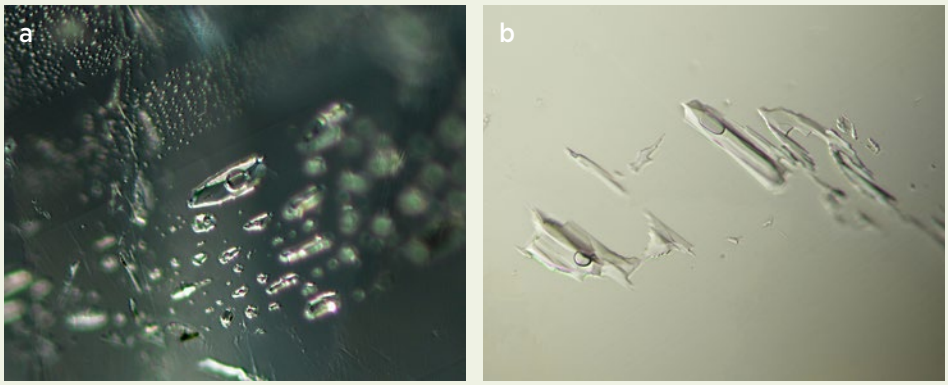

Figure 17: Partially healed fissures in Madagascar demantoid often contain clearly discernible two-phase inclusions, both as (**a**) elongated, rounded shapes and as (**b**) jagged or irregular forms. (a) Darkfield illumination, image width 0.4 mm; and (b) transmitted light, image width 0.3 mm.

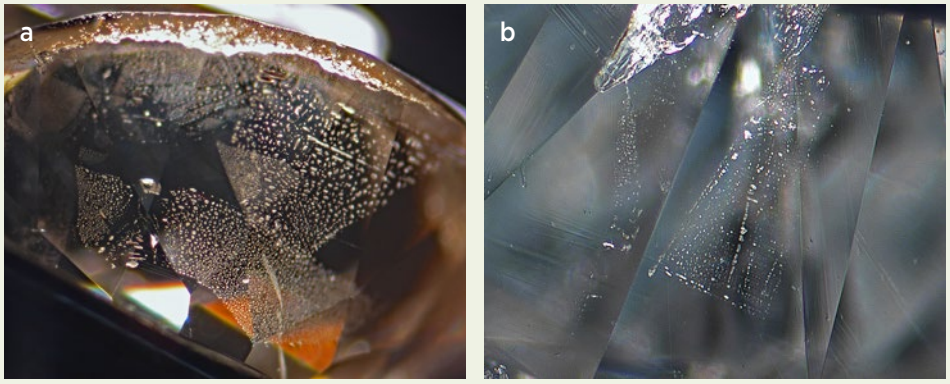

Figure 18: (**a**) Large, veil-like, partially healed fissures are common in Madagascar demantoid. (**b**) These fissures frequently occur in triangular shapes reminiscent of pine trees. Darkfield illumination, image widths (a) 2.3 mm and (b) 1.4 mm.

of both types of inclusions (elongated, rounded shapes and trichite-like ones) showed a typical O-H stretching band of liquid water. In general, Raman features at 3430 and 3232 cm^{-1} can be regarded as the most distinctive components of pure water (Sun 2010). However, the overall position and shape of the O-H stretching band depend on both the temperature at which they are analysed and the NaCl concentration in the fluid.

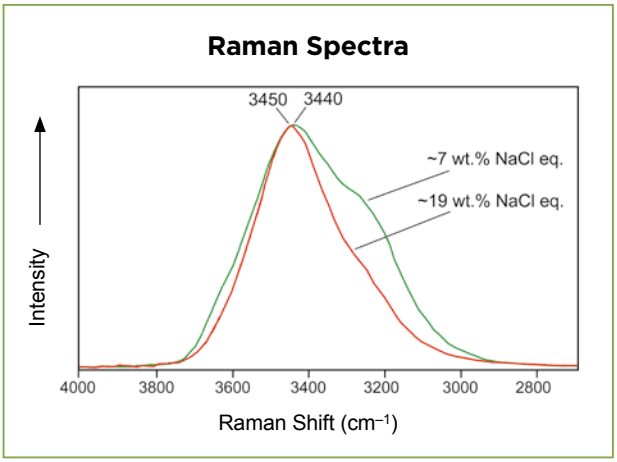

Measurements were done at a fixed room temperature of 20°C. At this temperature, as the NaCl concentration increases, the position of the O-H stretching band shifts to higher wavenumbers—in this case to 3440 and 3450 cm^{-1}, corresponding to lower and higher salinity, respectively—while the shoulder of this band diminishes and its slope steepens (see Figure 19). On this basis, using signal processing and equations given by Claverie *et al.* (2010), the rounded-shaped inclusions likely contain about 70 g/L NaCl and the trichite-like ones have up to about 190 g/L NaCl, which translates to salinities of 7 wt.% and 19 wt.% NaCl equivalent. Although the latter value is relatively high, it is not elevated enough to produce three-phase inclusions with halite cubes upon cooling, such as those seen in Colombian emeralds (Bodnar 2003).

Figure 19: Raman spectra of the aqueous liquid-vapour inclusions in Figure 17a (green trace) and 17b (red trace) show an O-H stretching band of liquid water. The shape and position of the band indicate that these aqueous inclusions contain different concentrations of NaCl, which reduces the strength of the shoulder at around 3200–3300 cm^{-1} as salinity increases.

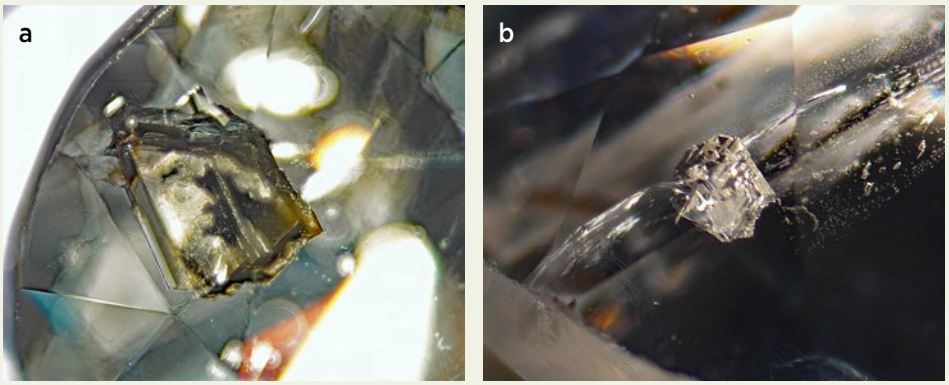

Figure 20: Negative crystals are common in Madagascar demantoid. In the study samples shown here, they exhibit (**a**) large size and (**b**) rhombohedral shape. Image widths (a) 1.2 mm and (b) 1.4 mm.

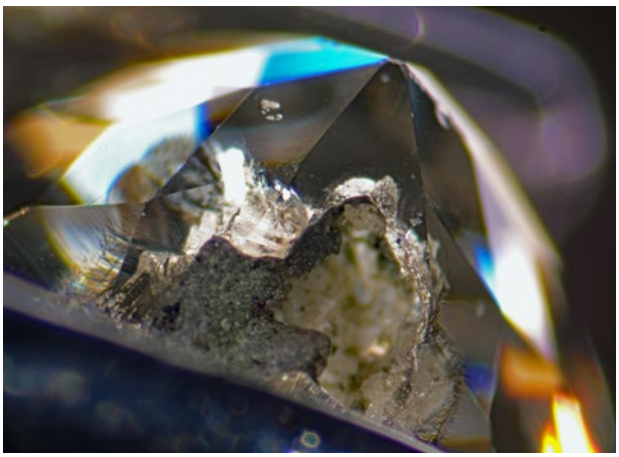

Figure 21: A large negative crystal on the pavilion of this Madagascar demantoid has collected some debris where it is open to the surface. Image width 2.5 mm.

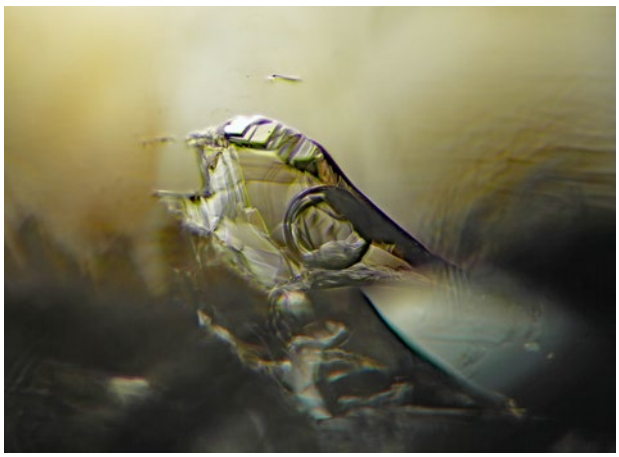

Figure 22: Negative crystals in Madagascar demantoid are mostly empty, but occasionally contain water (liquid and vapour), as seen in this example. Image width 0.9 mm.

Negative Crystals

Inclusions showing high relief and having the appearance of crystals were also very common (Figure 20a). When analysed with Raman spectroscopy, these 'crystals' mostly turned out to be empty, which identifies them as negative crystals. Many showed rhombohedral shapes (Figure 20b). Several large negative crystals intersected the surface of one faceted stone, creating a large empty cavity that was partially filled with foreign material (probably dirt and remnants of polishing powder; Figure 21). Occasionally, the negative crystals were found to contain a fluid and gas bubble (Figure 22). The ones that could be analysed showed a Raman spectrum of pure water (Figure 23), rather than the saline-type spectra of the fluid inclusions constituting the partially healed fissures (cf. Figure 19). However, establishing whether these trends for the water-containing inclusions are consistent would require many more measurements and a more detailed fluid inclusion study.

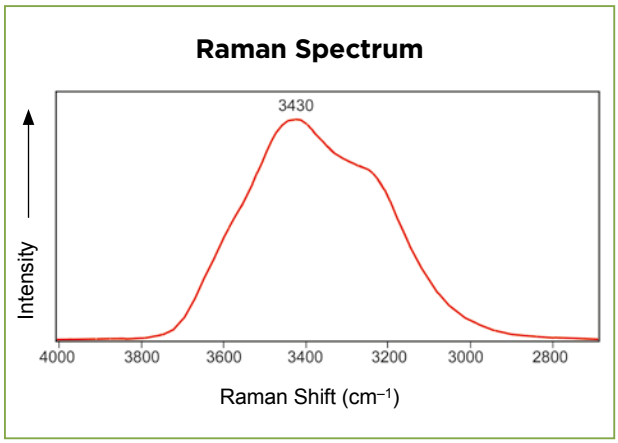

Figure 23: The Raman spectrum of the negative crystal in Figure 22 indicates the presence of relatively pure water when compared to the spectra in Figure 19 of the saline inclusions.

Growth Structures and Growth Tubes

Straight and angular growth zoning were observed in a number of stones. While the colour was usually even, the zoning had a similar appearance to the so-called graining observed in diamond: very narrowly spaced zones, with occasionally brown and reflective graining

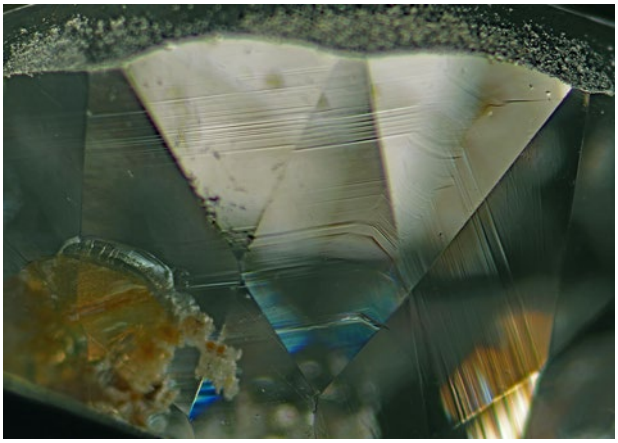

Figure 24: Straight and angular growth zoning observed in Madagascar demantoid sometimes resembles the narrow-spaced graining in diamonds. Image width 2.2 mm.

(Figures 24 and 25). Tube-like inclusions were oriented perpendicular to straight growth zoning. Some larger inclusions of this kind that reached the surface could be confirmed as hollow tubes (Figure 26a). Also perpendicular to the graining were minute, parallel-oriented, short needle-like inclusions (Figure 26b), as well as minute particles that remain undetermined. Unusual stepped growth zoning was found in one stone (Figure 27).

DISCUSSION

The assemblage of mineral inclusions in the Madagascar study samples—in particular diopside, wollastonite, calcite, dolomite and quartz—is consistent with the formation of this demantoid in a skarn environment, as described previously (Pezzotta 2010; Pezzotta *et al.* 2011). Based on these inclusions, the stones from Madagascar can readily be distinguished from demantoid of Russia, Italy, Pakistan, Iran, Eritrea and Slovakia, which is generally related to serpentinite resulting from hydrothermal/metamorphic alteration of ultramafic parent rocks. Demantoid from Russia and Italy contains radially arranged and curved fibres of asbestos (i.e. chrysotile, as so-called horsetail inclusions) and chromite grains (Gübelin & Koivula 2005; Adamo *et al.* 2009; Lewis 2018). Horsetail inclusions are also common in demantoid from Pakistan (i.e. Baluchistan; Adamo *et al.* 2015), Iran (Gübelin & Koivula 2005; Du Toit *et al.* 2006), Eritrea (Milisenda & Hunziker 1999) and

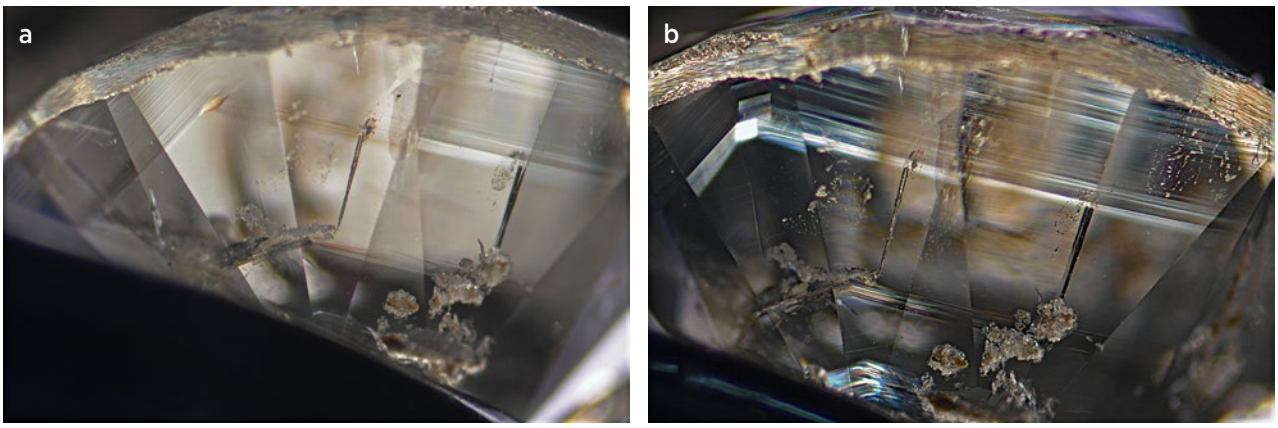

Figure 25: Occasionally, depending on the lighting direction, areas of brown graining (**a**) are seen as striking reflective graining (**b**) in Madagascar demantoid. Also visible are parallel tubes that are oriented perpendicular to the growth zoning. Near the bottom of each image, clusters of diopside are present. Image widths (a) 3.0 mm and (b) 2.6 mm.

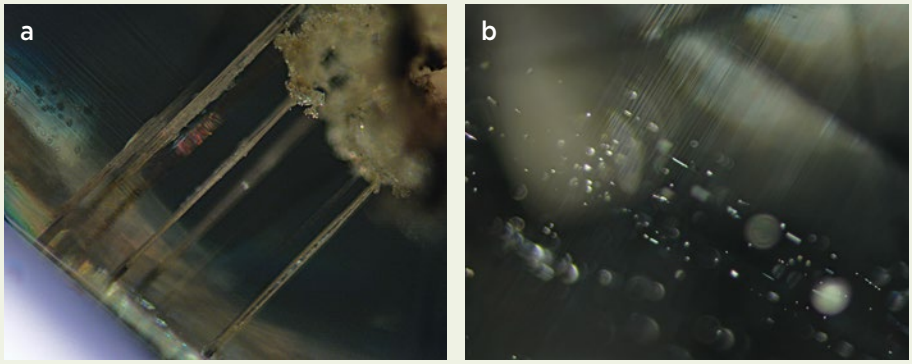

Figure 26: (**a**) Larger tubes oriented perpendicular to the growth zoning reach the surface of this Madagascar demantoid sample, allowing verification that they are indeed hollow. (**b**) Short, very fine needles, also perpendicular to the growth zoning, are occasionally present in Madagascar demantoid. Image width 1.2 mm for both.

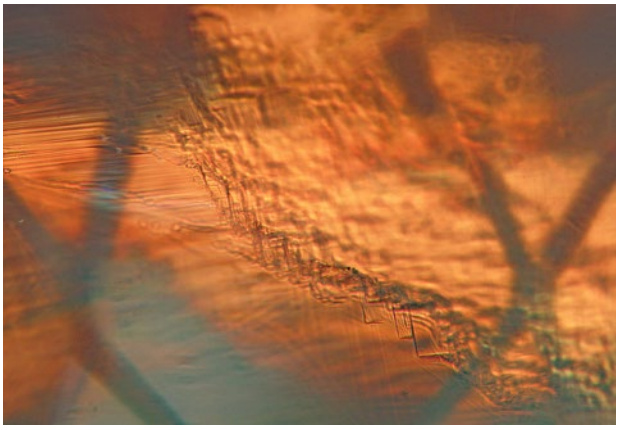

Figure 27: Unusual stepped growth zoning is visible in this Madagascar demantoid. Image width 1.0 mm.

Slovakia (Štubňa *et al*. 2019). In addition, demantoid from Italy and Baluchistan commonly contains white masses of a serpentine mineral, probably antigorite. Demantoid from Baluchistan also hosts equant octahedral (Cr-rich) magnetite which, together with the serpentine, resembles the chromite + serpentine assemblage in demantoid from Italy (Adamo *et al*. 2009, 2015; Palke & Pardieu 2014).

Demantoid found in the peridot mines within the Pakistan part of Kashmir (northern Pakistan) shows acicular, fibrous and felt-like chrysotile, but which is not radially arranged, as in demantoid from Russia (Milisenda *et al*. 2001). Only the partially healed fissures in demantoid from northern Pakistan and Iran (Milisenda *et al*. 2001; Du Toit *et al*. 2006) sometimes look similar to those encountered in this study. The equidimensional, rounded, small diopside crystals that occur in clusters in our study samples are very different from the stalk-like diopside inclusions that are sometimes present in demantoid from the Ural Mountains (Krzemnicki 1999; Gübelin & Koivula 2005).

The inclusions in demantoid from Madagascar are most similar to those in the stones from Namibia, which also formed in a skarn environment. It has been reported previously that Namibian demantoid contains diopside (X_{Mg} = 0.92–0.95), wollastonite, quartz, calcite and sphalerite, and it also shows similar growth zoning (Lind *et al*. 1998; Koller *et al*. 2012; Lewis 2018). Furthermore, Koller *et al*. (2012) stated that the fluid inclusions (two-phase and multiphase) in Namibian demantoid have a secondary origin, because the fluids were trapped along partially healed fractures. Based on micro-thermometric measurements, Koller *et al*. (2012) and Giuliani *et al*. (2017) suggested that the fluid inclusions in Namibian demantoid belong to the H_2O-$CaCl_2$ system (with or without CH_4), with the liquid phase having a salinity of 6–8 wt.% $CaCl_2$ and with CH_4 present in the vapour phase.

From the present author's observations of the 38 comparison samples from Namibia, at first glance they showed a similar inclusion scenery to Madagascar demantoid. Both contained diopside clusters and the common presence of partially healed fissures, as well as reflective, straight and angular growth zoning. Also seen in the Namibian demantoid were wollastonite (in three samples), a transparent calcite rhombohedron and small quartz grains.

However, closer examination revealed some notable differences. Raman analyses of a number of long prismatic and small, almost needle-like crystals in Namibian demantoid—with the same appearance as the wollastonite in the three other Namibian stones mentioned above—gave spectra of quartz or a mixture of calcite and quartz (suggesting calcite-quartz pseudomorphs after wollastonite; Figure 28). Also, fluorapatite was a common inclusion in Namibian demantoid, often occurring adjacent to or within the clusters of small diopside crystals, whereas fluorapatite was only occasionally encountered in the Madagascar samples. In Namibian demantoid, rounded, transparent grains of fluorapatite were more common and significantly larger than the long prismatic crystals present in the Madagascar stones. The largest of the few fluorapatite crystals encountered in the Madagascar demantoid were approximately 100-µm-long prisms (Figure 7b), while in the Namibian material equidimensional, rounded crystals up to approximately 200 µm were common (Figure 29). Sphalerite was reported previously in Namibian demantoid but was not found in this study. Titanite was identified (with Raman analysis) as a rare inclusion adjacent to a large cluster of diopside grains in a Namibian sample.

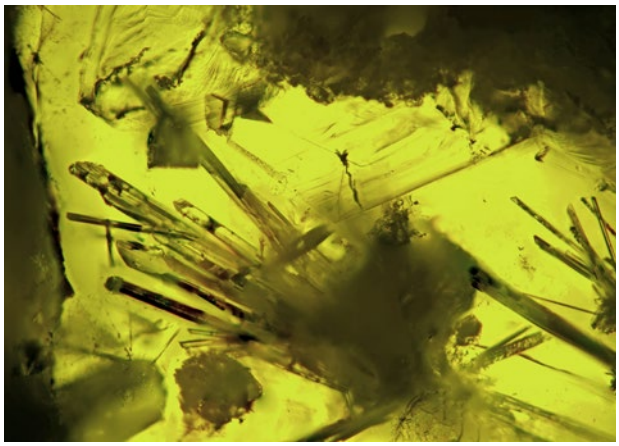

Figure 28: Long prismatic crystals of wollastonite occur in demantoid from Namibia. Interestingly, Raman analysis of the elongate inclusions shown here yielded quartz spectra, suggesting the presence of quartz pseudomorphs after wollastonite. Image width 1.4 mm.

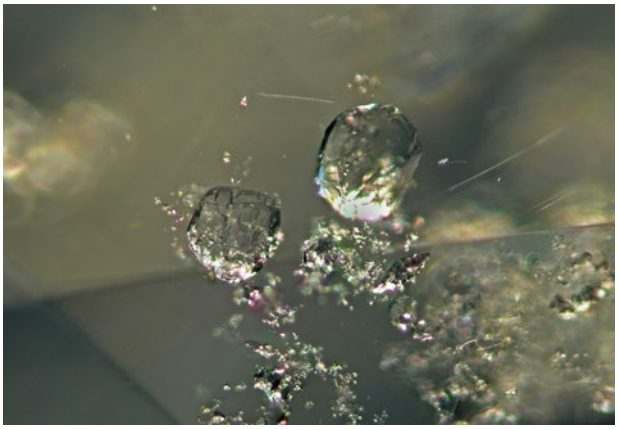

Figure 29: The transparent, rounded fluorapatite inclusions observed in Namibian demantoid are both much more common and somewhat larger than those occasionally seen in Madagascar material. Image width 0.9 mm.

Partially healed fissures in the Namibian demantoid samples were typically veil-like, commonly containing minute fluid inclusions, and sometimes showing trichite-like patterns, which often looked dark. Raman analysis suggested they were empty. In addition, small two-phase and multiphase fluid inclusions containing minute, doubly refractive solids were present in the Namibian stones. Some slightly larger fluid inclusions could be analysed, which revealed that they contained small grains of calcite, liquid H_2O and a gas bubble (Figure 30). This suggests the presence of Ca-bearing aqueous solutions during the formation process. Raman analysis of H_2O in some fluid inclusions did not reveal the presence of ClO_4^-, CCl_4 or $CaCl_2$, probably because, if present, their concentrations were not high enough to be detected (cf. Rudolph & Irmer 2013; Martinez-Uriarte *et al.* 2014). Either pure H_2O or water with very low salinity (up to ~10 wt.% NaCl equivalent) was found, corresponding to 6% in the $CaCl_2$-H_2O system (after Roedder 1984). This is consistent with findings by Koller *et al.* (2012), who inferred the presence of $CaCl_2$ by the measurement of low melting points during their micro-thermometric freezing-stage experiments. As in the Madagascar material, neither CH_4 nor CO_2 could be found in the vapour phase of the fluid inclusions in Namibian demantoid. In any case, an in-depth fluid inclusion study of the demantoids and their host rocks from both Madagascar and Namibia would be required to fully characterise the fluids involved with the formation environment of the garnets.

Negative crystals were rarely seen in the Namibian demantoid, and those encountered were comparatively small. Large, empty negative crystals on the order of 600–1000 µm that were seen in the Madagascar samples (Figures 20a and 21) were not present in either the faceted stones or the polished crystal fragments from Namibia. Only one Namibian demantoid hosted a negative crystal containing water (liquid and vapour) that was similar in appearance and size (slightly larger than 400 µm) to those seen in Madagascar material (Figure 31; compare to Figure 22).

In summary, demantoid from Madagascar shows a highly characteristic inclusion scenery: a combination of diopside clusters and negative crystals (the latter being commonly large and empty, but occasionally filled with aqueous liquid and vapour), along with partially healed fissures, in combination with the absence of calcite-bearing multiphase inclusions. Bismuth rods have not been reported as an inclusion in demantoid from any other occurrence, so when present these might serve to prove a Madagascar origin.

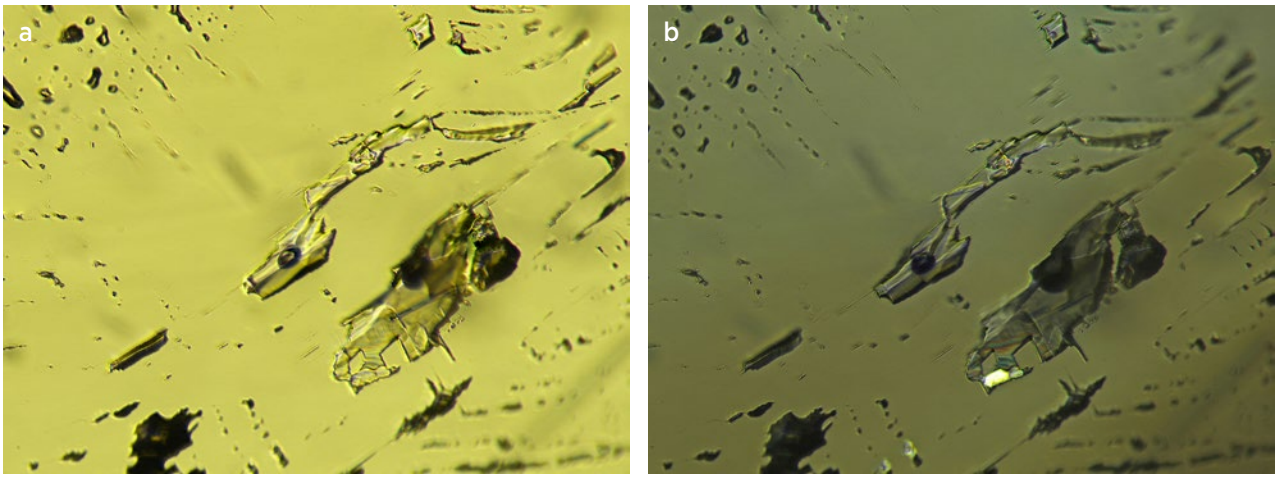

Figure 30: (**a**) Multiphase inclusions in Namibian demantoid were found to contain water (liquid and vapour), and no CH_4 or CO_2 in the vapour phase, similar to those analysed in the Madagascar samples. (**b**) Between crossed polarisers, a birefringent calcite crystal is revealed in one of the multiphase inclusions. Image width 0.7 mm.

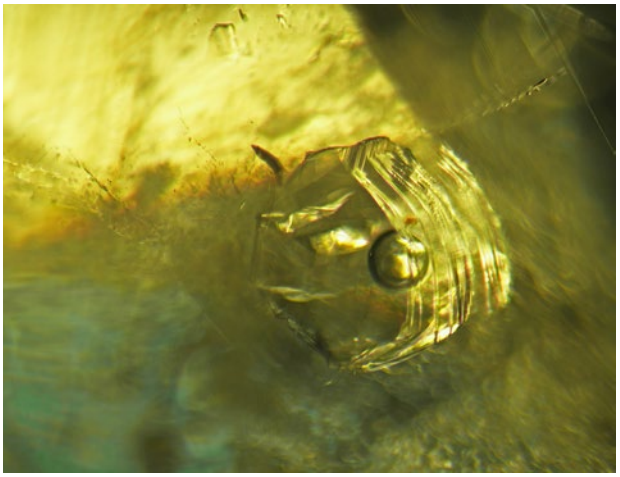

Figure 31: One of the Namibian demantoid samples hosts a negative crystal containing water, similar to those occasionally present in Madagascar demantoid. Image width 1.2 mm.

Evaluation of Previous Demantoid Chemical Data

Chemical data for Madagascar demantoid were initially given by Bocchio *et al.* (2010) and Pezzotta *et al.* (2011). Compared with those from serpentinised rocks, stones from Madagascar show no significant to very low Cr, V and Ti, low Mg and Mn, and high rare-earth element (REE) concentrations. Demantoid with a nearly pure andradite composition is typically enriched in light REEs, depleted in heavy REEs and shows a positive Eu anomaly (Bocchio *et al.* 2010).

Consistent with their formation in a skarn environment, demantoids from both Madagascar and Namibia have a similar chemical composition (Bocchio *et al.* 2010; see also data in Table I). Nevertheless, Schwarzinger (2019) and Bindereif *et al.* (2020) advocated distinguishing them based on chemical fingerprinting (using Al content and plotting V+Cr vs Mn/Ti ratio) or chemometric modelling using logarithms of trace-element concentrations for Mg, Al, Ti, V, Cr and Mn. However, some of their Madagascar data show extremely high Al, much higher Ti, and significantly higher V and Cr than the data presented by Pezzotta *et al.* (2011), who gave Mg, Al, Ti, V and Cr concentrations more similar in most cases to those for Namibian material (Table I). These differences might be due to the fact that compositional variations can occur on a very local scale. While most demantoid is almost pure andradite (Adr; end-member composition $Ca_3Fe^{3+}_2[SiO_4]_3$), it may also contain a significant grossular component (Grs; end-member composition $Ca_3Al_2[SiO_4]_3$). Bocchio *et al.* (2010) analysed a single zoned sample from Namibia that varied from almost pure andradite to a composition enriched in grossular ($Adr_{11}Grs_{89}$). Barrois *et al.* (2013) mentioned that samples from Madagascar sometimes show narrow Al-rich zones, with up to 5.9 wt.% Al_2O_3 (i.e. ~31,230 ppmw Al), alternating with Al-free zones or Al-rich second-generation andradite in small cavities. Bindereif *et al.* (2020) reported Al values up to 85,470 ppmw (which converts to 16.15 wt.% Al_2O_3) in samples from Madagascar, demonstrating a significant grossular component. A plot of the 14 point analyses of five samples of Madagascar demantoid reported in Bindereif *et al.* (2020) shows that elevated Ti,

Table I: Relevant element concentrations (by LA-ICP-MS) in demantoids from Madagascar and Namibia.

Property	Madagascar			Namibia	
	Pezzotta *et al.* 2011		Bindereif *et al.* 2020*	Bindereif *et al.* 2020*	
No. samples	13		5	25	
No. analyses	150		14	73	
Element (ppmw)	**Range**	**Median**	**Range**	**Range**	**Median**
Mg	307–1423	450	171–776	70–1145	321
Al	15–5467	38	40–85470	13–981	117
Ti	0.17–7.5	1.2	18–3325	0.63–98	4.4
V	nd–3.1	0.03	nd–109	nd–7.3	0.24
Cr	nd–2.7	0.98	nd–118	nd–407	0.79
Mn	9–91.5	35	15–209	219–4981	700

* Similar compositional ranges were indicated by Schwarzinger (2019), and it appears that those data were incorporated into the ranges given by Bindereif *et al.* (2020). Median values are not given for the Madagascar data of Bindereif *et al.* (2020) due to the presence of mixed andradite and andradite-grossular compositions. Abbreviation: nd = not detected.

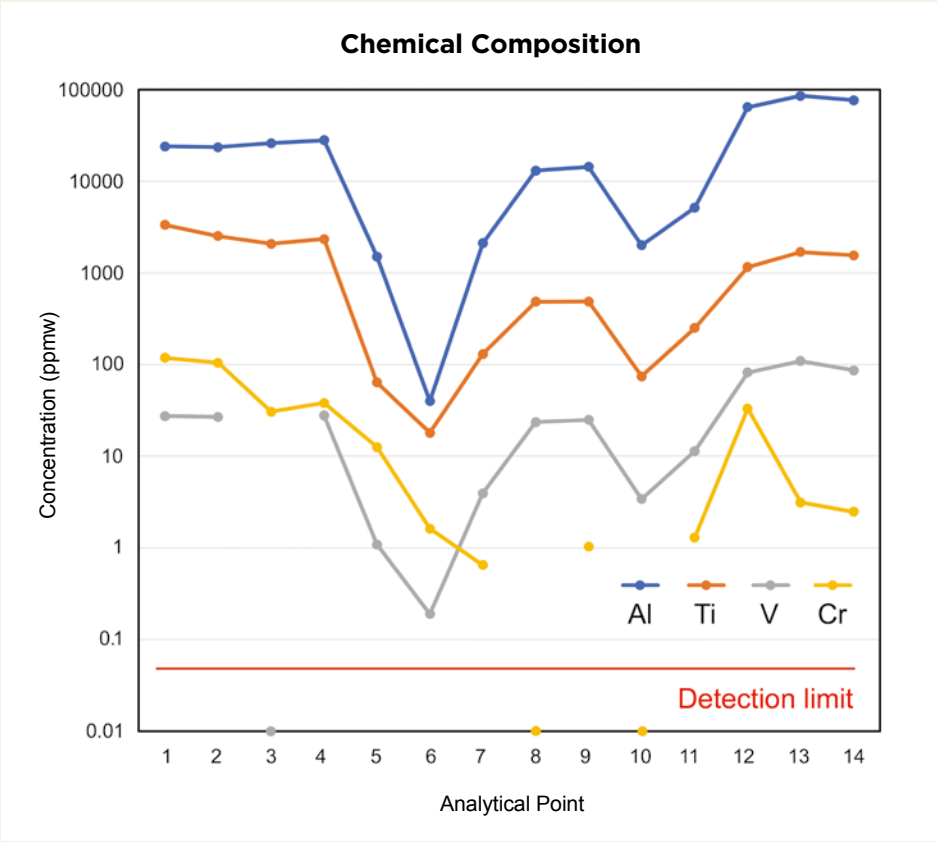

Figure 32: Trace-element data from 14 point analyses of five samples of Madagascar demantoid (Bindereif *et al.* 2020) show similar trends for Al, Ti and V, with elevated Ti and V when Al is high. Less correlation is shown by Cr, with concentrations that are higher only when Al is elevated.

V and Cr concentrations only occur where the Al concentration is high (Figure 32). Similarly, when the grossular component increases, the REE pattern will change, leading to a depletion in light REEs and an enrichment in moderately heavy REEs, as well as a trend towards a negative Eu anomaly (Bocchio *et al.* 2010).

From this, it can be concluded: (1) although an enriched Al content could help separate skarn-hosted from serpentinite-hosted demantoid, it cannot be used to confidently separate Malagasy from Namibian stones; and (2) only analyses showing a nearly pure andradite composition should be used for comparing and assessing geographic origin. From the available data (Pezzotta *et al.* 2011; Bindereif *et al.* 2020), plotting Mn vs Al concentrations provides a possible way to distinguish demantoid from Madagascar and Namibia (see Table I and Figure 33). However, more data are needed to test this hypothesis.

CONCLUSION

Detailed characterisation of mineral and fluid inclusions in demantoid from Madagascar showed distinctive features that can be used to determine their geological (skarn) origin. These include diopside clusters (with or without wollastonite, carbonates, quartz and fluorapatite), negative crystals (which are commonly large and empty, but occasionally filled with aqueous liquid and vapour), and partially healed fissures (showing various forms and containing aqueous liquid and vapour, with varying salinities of <20 wt.% NaCl equivalent). When present, native bismuth inclusions appear to be diagnostic for a Madagascar origin; to date they have not been reported in demantoid from any other locality.

Compared with demantoid from serpentinised rocks, stones from skarn-hosted deposits in Madagascar and Namibia show no significant or very low Cr, V and Ti, low Mg and Mn, high REE concentrations, and enriched Al in some samples. A review of available data indicates that only analyses showing a nearly pure andradite composition should be used for assessing geographic origin. For such samples, it appears that a very low Mn content is indicative of a Madagascar origin as compared to material from Namibia.

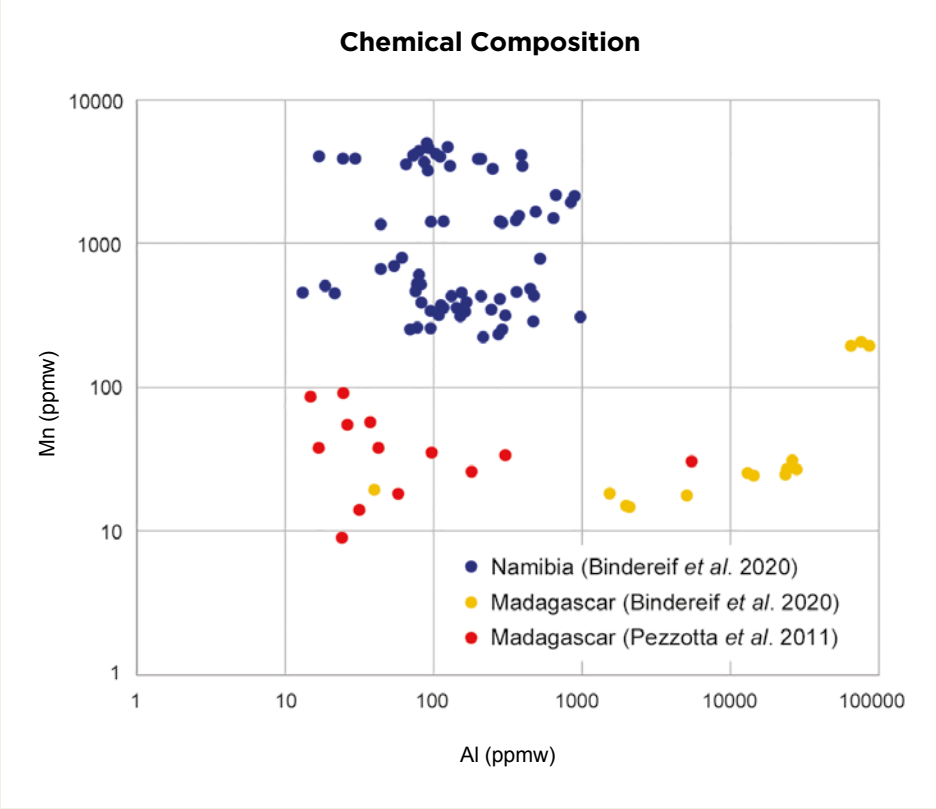

Figure 33: Previously published data for Al and Mn are plotted in this diagram to explore the possibility of chemically distinguishing demantoid from Madagascar and Namibia.

REFERENCES

Adamo, I., Bocchio, R., Diella, V., Pavese, A., Vignola, P., Prosperi, L. & Palanza, V. 2009. Demantoid from Val Malenco, Italy: Review and update. *Gems & Gemology*, **45**(4), 280–287, https://doi.org/10.5741/gems.45.4.280.

Adamo, I., Bocchio, R., Diella, V., Caucia, F. & Schmetzer, K. 2015. Demantoid from Balochistan, Pakistan: Gemmological and mineralogical characterization. *Journal of Gemmology*, **34**(5), 428–433, https://doi.org/10.15506/JoG.2015.34.5.428.

Barrois, O., Giuliani, G., Hafeznia, Y., Zeenabad, H.A., Rakotondrazafy, A.F.M., Ohnenstetter, D., Fallick, A.E., Mathieu, S. *et al*. 2013. Caractéristiques mineralogique et chimique des démantoides de Bagh Borj (Iran) et d'Antetezambato (Madagascar): Consequences geologiques, 2ème partie, études mineralogique et chimique. *Revue de Gemmologie A.F.G.*, No. 183, 10–15.

Bindereif, S., Rüll, F., Schwarzinger, S. & Schwarzinger, C. 2020. Chemometric modeling of trace element data for origin determination of demantoid garnets. *Minerals*, **10**(12), article 1046 (15 pp.) and supplementary table S1 (9 pp.), https://doi.org/10.3390/min10121046.

Bocchio, R., Adamo, I. & Diella, V. 2010. The profile of trace elements, including the REE, in gem-quality green andradite from classic localities. *Canadian Mineralogist*, **48**(5), 1205–1216, https://doi.org/10.3749/canmin.48.5.1205.

Bodnar, R.J. 2003. Introduction to aqueous-electrolyte fluid inclusions. *In*: Samson, I., Anderson, A. & Marshall, D. (eds) *Fluid Inclusions: Analysis and Interpretation*. Mineralogical Association of Canada, Québec, Canada, 81–100.

Buzatu, A. & Buzgar, N. 2010. The Raman study of single-chain silicates. *Analele Ştiinţifice Ale Universităţii "Al. I. Cuza" Iaşi*, **56**(1), 107–125.

Chukanov, N.V. & Vigasina, M.F. 2020. Raman spectra of minerals. *In*: *Vibrational (Infrared and Raman) Spectra of Minerals and Related Compounds*. Springer, Cham, Switzerland, 741–1255, https://doi.org/10.1007/978-3-030-26803-9_4.

Claverie, R., Fontana, M.D., Duričković, I., Bourson, P., Marchetti, M. & Chassot, J.-M. 2010. Optical sensor for characterizing the phase transition in salted solutions. *Sensors*, **10**(4), 3815–3823, https://doi.org/10.3390/s100403815.

Du Toit, G., Mayerson, W., van der Bogert, C., Douman, M., Befi, R., Koivula, J.I. & Kiefert, L. 2006. Demantoid from Iran. *Gems & Gemology*, **42**(3), 131.

Giuliani, G., Pignatelli, I., Fallick, A., Boyce, A., Andriamamonjy, A., Razafindratsimba, S. & Khan, T. 2017. Gem andradite garnet deposits demantoid variety. *InColor*, No. 36, 28–39.

Gomelsky, V. & Bates, R. 2021. Guest John Ferry. The Jewelry District podcast, episode 38, 16 February, https://www.jckonline.com/editorial-article/podcast-jewelry-district-ep-38.

Gübelin, E.J. & Koivula, J.I. 2005. *Photoatlas of Inclusions in Gemstones*, Vol. 2. Opinio Publishers, Basel, Switzerland, 829 pp.

Huang, E., Chen, C.H., Huang, T., Lin, E.H. & Xu, J. 2000. Raman spectroscopic characteristics of Mg-Fe-Ca pyroxenes. *American Mineralogist*, **85**(3–4), 473–479, https://doi.org/10.2138/am-2000-0408.

Koller, F., Niedermayr, G., Pintér, Z. & Szabó, C. 2012. The demantoid garnets of the Green Dragon mine (Tubussi [*sic*], Erongo region, Namibia). *Acta Mineralogica-Petrographica, Abstract Series*, **7**, 72, http://acta.bibl.u-szeged.hu/39436/1/mineralogica_as_007.pdf.

Krzemnicki, M.S. 1999. Diopside needles as inclusions in demantoid garnet from Russia: A Raman microspectrometric study. *Gems & Gemology*, **35**(4), 192–195, https://doi.org/10.5741/gems.35.4.192.

Lewis, Z. 2018. Beyond 'horse tails' in demantoid garnet. *Gems&Jewellery*, **27**(4), 32–35.

Lind, T., Henn, U. & Bank, H. 1998. New occurrence of demantoid in Namibia. *Australian Gemmologist*, **43**(3), 153–160.

Martinez-Uriarte, L., Dubessy, J., Bihannic, I., Boulet, P. & Robert, P. 2014. Reference Raman spectra of $CaCl_2.nH_2O$ solids (n= 0, 2, 4, 6). *11th International GeoRaman Conference*, St Louis, Missouri, USA, 15–19 June, abstract 5069.

Milisenda, C.C. & Hunziker, J. 1999. Demantoid aus Eritrea. *Zeitschrift der Deutschen Gemmologischen Gesellschaft*, **20**, 75–79.

Milisenda, C.C., Henn, U. & Henn, J. 2001. Demantoide aus Pakistan. *Gemmologie: Zeitschrift der Deutschen Gemmologischen Gesellschaft*, **50**(1), 51–56.

Palke, A.C. & Pardieu, V. 2014. Gem News International: Demantoid from Baluchistan Province in Pakistan. *Gems & Gemology*, **50**(4), 302–303.

Pezzotta, F. 2010. Andradite from Antetezambato, north Madagascar. *Mineralogical Record*, **41**(3), 209–229.

Pezzotta, F., Adamo, I. & Diella, V. 2011. Demantoid and topazolite from Antetezambato, northern Madagascar: Review and new data. *Gems & Gemology*, **47**(1), 2–14, https://doi.org/10.5741/gems.47.1.2.

Roedder, E. 1984. *Fluid Inclusions*. Reviews in Mineralogy, **12**, Mineralogical Society of America, Washington DC, USA, vi + 646 pp., https://doi.org/10.1515/9781501508271.

Rondeau, B., Fritsch, E., Mocquet, B. & Lulzac, Y. 2009. Ambanja (Madagascar) – A new source of gem demantoid garnet. *InColor*, No. 11, 22–24.

Rudolph, W.W. & Irmer, G. 2013. Hydration of the calcium(II) ion in an aqueous solution of common anions (ClO_4^-, Cl^-, Br^-, and NO_3^-). *Dalton Transactions*, **42**, 3919–3935, https://doi.org/10.1039/c2dt31718d.

Schwarzinger, C. 2019. Determination of demantoid garnet origin by chemical fingerprinting. *Monatshefte für Chemie - Chemical Monthly*, **150**(5), 907–912, https://doi.org/10.1007/s00706-019-02409-3.

Štubňa, J., Bačík, P., Fridrichová, J., Hanus, R., Illášová, Ľ., Milovská, S., Škoda, R., Vaculovič, T. *et al*. 2019. Gem-quality green Cr-bearing andradite (var. demantoid) from Dobšiná, Slovakia. *Minerals*, **9**(3), article 164 (12 pp.), https://doi.org/10.3390/min9030164.

Sun, Q. 2010. The single donator–single acceptor hydrogen bonding structure in water probed by Raman spectroscopy. *Journal of Chemical Physics*, **132**(5), article 054507 (4 pp.), https://doi.org/10.1063/1.3308496.

Tribaudino, M., Mantovani, L., Bersani, D. & Lottici, P.P. 2012. Raman spectroscopy of $(Ca,Mg)MgSi_2O_6$ clinopyroxenes. *American Mineralogist*, **97**(8–9), 1339–1347, https://doi.org/10.2138/am.2012.4057.

Zepeda, M.A., Picquart, M. & Haro-Poniatowski, E. 2012. Laser induced oxidation effects in bismuth thin films. *MRS Proceedings*, **1477**, 28–33, https://doi.org/10.1557/opl.2012.1720.

The Author

Dr J. C. (Hanco) Zwaan FGA
Netherlands Gem Laboratory,
Naturalis Biodiversity Center,
Darwinweg 2, 2333 CR Leiden,
The Netherlands
Email: hanco.zwaan@naturalis.nl

Acknowledgements

The author thanks John Ferry, founder and CEO of Prosperity Earth LLC (Greenwich, Connecticut, USA), for the loan of Madagascar demantoid samples for this study, and Markus Paul Wild, managing director of Paul Wild OHG (Kirschweiler, Germany), for the loan of demantoid samples from Namibia.

Photochromism and Photochromic Gems: A Review and Some New Data (Part 2)

Féodor Blumentritt and Emmanuel Fritsch

ABSTRACT: Part 2 of this article reports on photochromism in diamond, corundum and baryte. Diamond provides the greatest number of photochromic behaviours for a single gem species, with five varieties, only one of which is related to the well-known silicon-vacancy colour centre. The photochromic behaviour of chameleon (green/yellow) diamonds is probably related to various impurities (N, H, Ni and possibly O). Three of the other photochromic diamond varieties involve the addition of brown colour, but they are unlikely to originate from the exact same mechanism. For corundum, we propose that yellow-orange photochromism is linked to an electron moving in and out of a hole centre. For baryte, doubt remains with regard to published descriptions of the yellow-to-blue change in colour with exposure to sunlight, but involvement of sulphur is a possibility for this sulphate mineral. In general, since photochromism modifies the colours of gems, and since the effect is reversible, it is important for the gemmological community to be aware of its potential influence on colour grading.

The Journal of Gemmology, **38**(1), 2022, pp. 80–92, https://doi.org/10.15506/JoG.2022.38.1.80

The aim of the second half of this two-part article is to review research on inorganic photochromic gem materials other than silicates. Here we concentrate on diamond (with no less than five different photochromic behaviours; e.g. Figure 1), corundum (mostly its yellow variety) and the collector's gem material baryte. Compared with silicates, and especially the aluminosilicates with cages in their structures (as presented in part 1 of this article: Blumentritt & Fritsch 2021), diamond and corundum are chemically simpler materials. However, the large number of defects known in diamond makes it one of the most challenging gem materials for understanding the nature of the absorption centres responsible for photochromism. This is compensated in part by the extensive research on diamond for various material properties, which provides fairly detailed knowledge of many of its defects (e.g. Zaitsev 2001). Corundum offers a different challenge, in that absorption linked to metal ions is very well documented, but that of intrinsic defects and colour centres is lagging far behind. Baryte stands apart, with only a few publications describing a colour behaviour that could correspond to a photochromic property.

MATERIALS AND METHODS

Because we were unable to procure some of the rare photochromic materials covered in the present article, we report only the information available in the published literature for such cases (sometimes including photos or spectra). For diamond, we studied a 0.39 ct marquise-cut chameleon diamond from the collection of the University of Nantes. For corundum, we obtained four rough photochromic yellow-orange sapphires from Madagascar from gem dealer Emmanuel Piat, and the one showing the strongest photochromism (0.19 g) was selected for further examination.

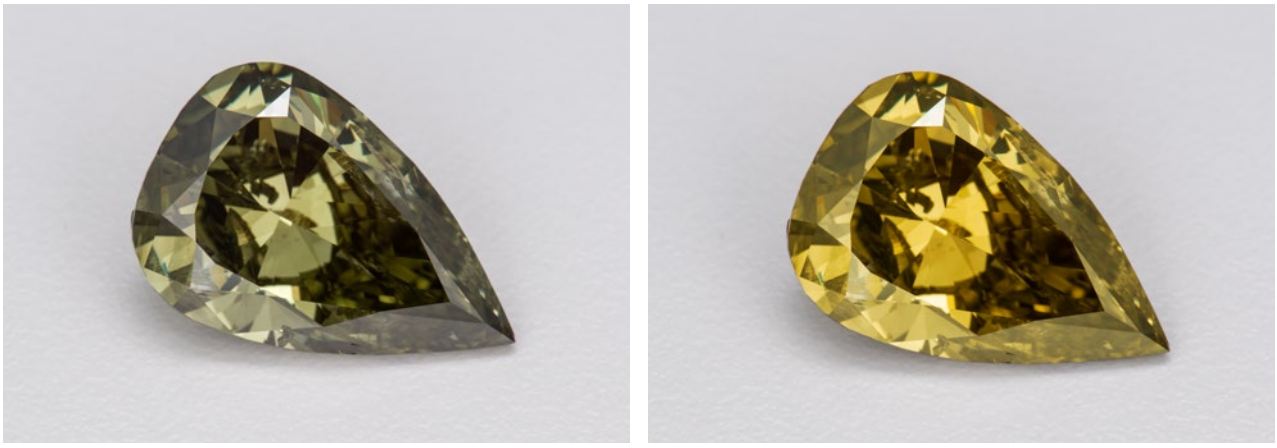

Figure 1: This 6.15 ct chameleon diamond exhibits photochromic behaviour. Its stable 'olive' green colour (left) turns orangey yellow after being kept in the dark (right). Courtesy of Alan Bronstein; photos by Robert Weldon.

The experimental setup by which we obtained ultraviolet-visible-near infrared (UV-Vis-NIR) absorption spectra of the two photochromic gems we procured is identical to the conditions described in the Materials and Methods section of part 1 of this article (Blumentritt & Fritsch 2021). A summary of the properties of the photochromic gems discussed in this article can be found in Table I.

DIAMOND

Articles on the photochromism of diamond have been published since the 1960s, but they are relatively uncommon. Nevertheless, interest in such gems has grown along with the increasing popularity of coloured diamonds, and they are now a well-known curiosity for gem collectors. Despite the relatively small number of

Table I: Properties of the photochromic gems diamond, corundum and baryte.

Gem material		Stable/ metastable colour	Photo-generated colour induced by	Approx-imate time to induce photo-generated colour	Photo-generated colour(s) reversed by	Approx-imate time to fade photo-generated colour	Proposed mechanism	Principal references
Diamond	Natural	Green/yellow* (chameleon)	White light	Seconds	Heat (around 100°C)	Seconds to minutes	Centre involving N, H, Ni and possibly O	Fritsch & Delaunay (2018)
					Darkness	Several days		
	Natural	Pink/ pinkish brown	Short-wave UV	Seconds to minutes	Visible light	Seconds to minutes	Colour centre	Byrne *et al.* (2012, 2014)
	Natural	Light yellow/ light brown	Long-wave UV	Seconds to minutes	Visible light	Seconds to minutes	Unknown	Butler *et al.* (2017)
	CVD synthetic	Yellow/brown	Short-wave UV	Minutes to hours	Heat (around 450°C)	Minutes to hours	Colour centre	Khan *et al.* (2010)
	CVD synthetic	Near-colourless/ greyish blue	Short-wave UV (~225 nm)	Minutes	Visible light	Seconds to minutes	$[Si\text{-}V]^{2-} \leftrightarrow [Si\text{-}V]^{-}$ $[Si\text{-}V]^{0} \leftrightarrow [Si\text{-}V]^{-}$	D'Haenens-Johansson *et al.* (2011); Breeze *et al.* (2020)
					Heat (around 550°C)	Seconds to minutes		
Corundum (sapphire)		Addition of yellow to orange component	Short-wave UV	Minutes to hours	Daylight or visible light	Minutes to hours	Hole centre	Nassau & Valente (1987)
					Heat (around 100°C)	Seconds to minutes		
Baryte		Colourless to greyish yellow/blue	Bright sunlight	Hours	Visible light or darkness	Months to years	Sulphur-related?	King (1987)

* From the point of view of an electronic energy diagram, Fritsch *et al.* (2007) indicated that the stable state shows the yellow to yellow-orange colour and the metastable state is greyish or 'olive' green.

photochromism-related publications, diamond probably remains one of the most-researched and well-documented photochromic gems. In the past, photochromic diamonds tended to be a subject of non-gemmological studies because the effect could be useful for various industrial applications such as quantum optics (Byrne *et al.* 2014; Breeze *et al.* 2020). However, work published to date is limited to observations and hypotheses, and lacks detailed interpretations for some reversible colour changes, partly because of the very large number of defects (i.e. hundreds) identified in diamond.

Information on five different varieties of photochromic behaviours in diamond is compiled below. Natural photochromic diamonds (chameleon, pink and cape) are presented first, followed by synthetic ones (brown and greyish blue). Since even subtle colour variations in diamond are closely tied to their value, photochromism should be checked for in gemmological laboratories before assigning a colour grade.

Chameleon Diamond

Today's most accepted definition of 'chameleon diamond' pertains to photochromism involving a greyish green (or 'olive' green) stable colour that turns yellow to yellow-orange when kept in the dark[1] (Figures 1 and 2). This change in colour can also occur via thermochromism with slight heating, typically below 300°C (Raal 1969; Fryer 1981, 1982; Koivula & Kammerling 1991; Fritsch *et al.* 1995, 2007; De Weerdt & Van Royen 2001; Hainschwang *et al.* 2005; Breeding *et al.* 2018), or even when cooled to liquid-nitrogen temperature (De Weerdt & Van Royen 2001).

Curiously, chameleon diamonds have long been presented to the public, owing to the famous French author Jules Verne, whose novels—such as *Journey to the Centre of the Earth*, *From the Earth to the Moon* and *Twenty Thousand Leagues Under the Sea*—often predicted events that happened long after the publication of his books (Fritsch & Delaunay 2018). In *L'Étoile du Sud* (*The Star of the South*; Verne 1884), his description of an extraordinary diamond was not purely the fantasy of his imagination or coincidence, because a chameleon diamond had already been reported by French scientific journalist Louis Figuier (1867). However, these two references mentioned only the thermochromic aspect.

[1] Fritsch *et al.* (2007) indicated that, from the point of view of an electronic energy diagram, the stable state of a chameleon diamond shows the yellow to yellow-orange colour, and the metastable state is greyish or 'olive' green.

The first published description of a photochromic diamond was in *The Diamond Dictionary* (Copeland *et al.* 1960, p. 44):

> A 2.24-carat diamond purported to change color from bronze to green when exposed to light. C. A. Kiger of Kansas City purchased the stone about 1953 and consigned it 'to a Texas dealer who sold it to an oil man.' No further information is available.

Chameleon diamonds have been described variously as type IaA (Fritsch *et al.* 1995; Hainschwang *et al.* 2005), a mixture of types IaA and Ib (De Weerdt & Van Royen 2001) or dominantly type IaA/B (with A>>B) including traces of type Ib (Fritsch *et al.* 2007). Even though diamond types for chameleons differ slightly, they are not in blatant contradiction.

All of the references cited below provide some explanation of the photochromism mechanism in chameleon diamonds, and they generally agree that the change in colour is due to a charge transfer between an acceptor and a donor defect. The articles mostly begin with a precise description of the defects present in such diamonds. These include defects that are Ni-related (De Weerdt & Van Royen 2001; Hainschwang *et al.* 2005; Ardon 2014), H- or N-related (Fritsch *et al.* 1995, 2007; De Weerdt & Van Royen 2001; Hainschwang *et al.* 2005), and even an O-related one (480 nm band; Hainschwang *et al.* 2008).

Cuboid growth sectors have been documented in chameleon diamonds and could explain the presence of Ni, which is very common in H-rich cuboid growth sectors (even in non-photochromic diamonds; Lang *et al.* 2004). For the charge transfer, both Ni- and N-related defects are considered good donors (De Weerdt & Van Royen 2001).

Hydrogen appears to be a necessary defect for photochromism. Theoretical calculations (Goss *et al.* 2011) show that some N-H-N complexes might form; they amount roughly to an A aggregate with a hydrogen atom. These complexes induce an absorption feature in the near-infrared (again, see Figure 2), which appears to be responsible in part for the photochromic effect. This absorption, induced by a charge transfer, causes a structural modification of the N-H-N complex (Fritsch *et al.* 2007; Goss *et al.* 2011). A complex of Ni-H-N has also been proposed to explain diamond photochromism (Fritsch *et al.* 2007). In general, though, the mechanism given by most authors implies an electronic structure with a trap level and a donor level.

However, Byrne *et al.* (2018) proposed another scheme, mostly to explain phosphorescence, but also to include photochromic behaviour. They suggested

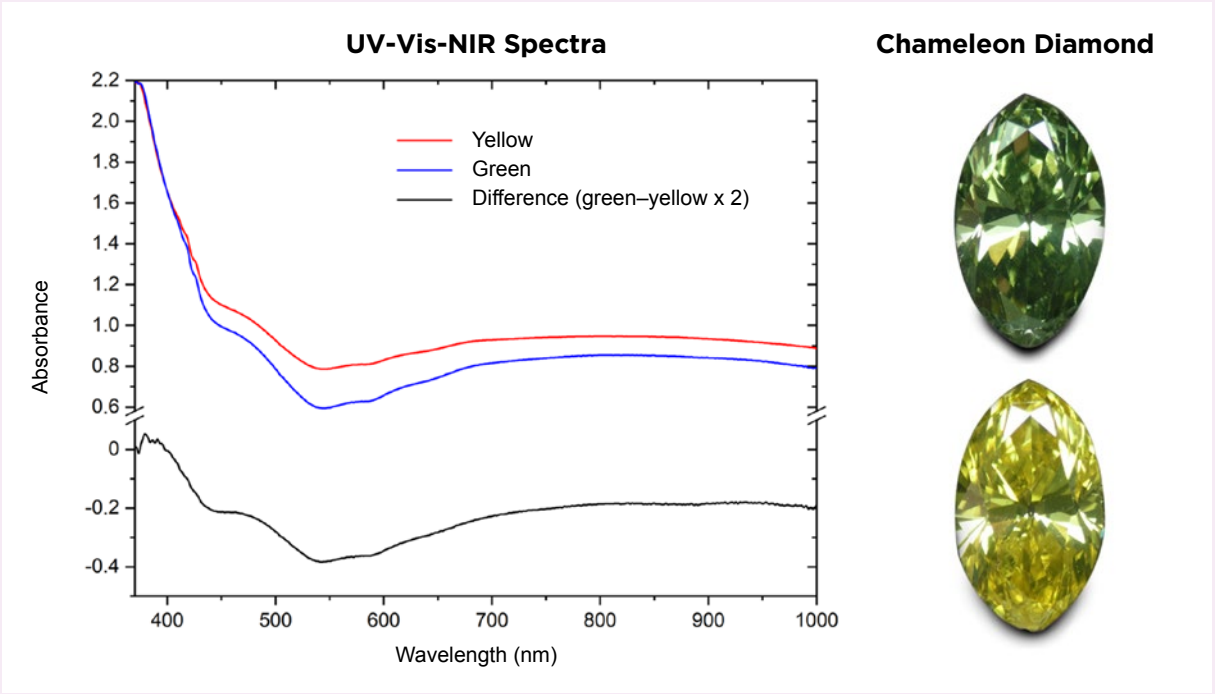

Figure 2: Spectra of the two colour states of a 0.39 ct chameleon diamond are shown here, together with the difference spectrum between the greyish green (stable) and yellow (unstable) colours. Other spectra recorded on chameleon diamonds show slightly variable but generally consistent results (cf. Hainschwang *et al.* 2005; Fritsch *et al.* 2007; Byrne *et al.* 2018). The path length of the beam was approximately 4 mm, and the difference spectrum is multiplied by a factor of 2 for clarity. Photos by Thomas Hainschwang.

that the change in colour is not directly induced by the trap level but by an electronic transition from the valence band to the donor level, which has already lost its electron. This transition occurs in the near-infrared to visible range and leads to the greenish colouration. This particular electronic model was designed exclusively to fit the luminescence of chameleon diamonds. Such diamonds generally show a long-lasting yellow persistent luminescence (phosphorescence; Fritsch *et al.* 1995; De Weerdt & Van Royen 2001; Byrne *et al.* 2018) and sometimes fluorescence that appears white (blue + yellow = white; Hainschwang *et al.* 2005; Fritsch & Delaunay 2018), but the link between photochromism and fluorescence has not yet been clearly established. Fritsch and Delaunay (2018) listed at least nine characteristics to define a chameleon diamond, demonstrating the complexity of the issue of photochromism in a gem material with many different defects.

Pink Diamond

The second variety of photochromism in diamond reported in the literature, known for several decades (Crowningshield 1960), occurs in some pink to purplish pink diamonds. These stones turn more brown (Figure 3) after short-wave UV irradiation and return to their initial pink colour after exposure to visible light (Fryer 1983a; De Weerdt & Van Royen 2001; Fisher *et al.* 2009; Byrne *et al.* 2012, 2014; Chapman 2014; Eaton-Magaña *et al.* 2018). To our knowledge, this behaviour has been observed only in diamonds with pink or purplish pink graining and that are coloured by the 550 nm band (see, e.g., Eaton-Magaña *et al.* 2018). Surprisingly, while some articles dealing with the grading of pink diamonds mention the photochromic property, none of them discuss its effect on colour grading, despite the obvious relationship (Hofer 1985; King *et al.* 2002), especially when the grading process includes photoluminescence analysis with UV excitation. This problem was specifically pointed out for photochromic brown synthetic diamonds grown by chemical vapour deposition (CVD; see below and Khan *et al.* 2010).

In general, pink and brown diamonds are coloured by plastic deformation. This process probably induces the formation of a variety of defects responsible, at least in part, for the pink colour (De Weerdt & Van Royen 2001; Fisher *et al.* 2009; Byrne *et al.* 2014; Gaillou & Rossman 2014). The absorption spectra of such photochromic pink diamonds typically show two bands centred at 390 and 550 nm (i.e. commonly reported in the literature as 3.18 and 2.25 eV, respectively; De Weerdt & Van Royen

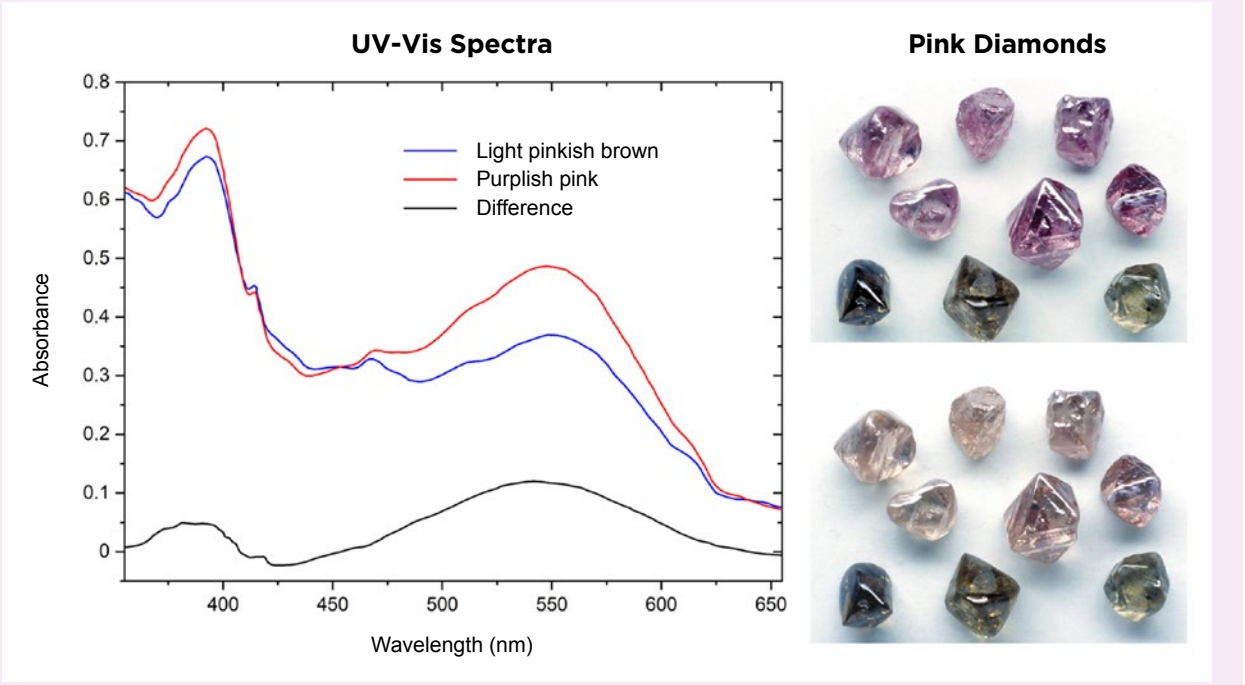

Figure 3: Spectra of a photochromic diamond from the Argyle mine, Australia (adapted from Byrne *et al.* 2012), illustrate the results before (purplish pink) and after (light pinkish brown) short-wave UV exposure, together with the associated difference spectrum. The photos show several diamond crystals (approximately 1 ct each) from Argyle displaying photochromic behaviour; the bottom three diamonds are not photochromic but are included for colour reference. Photos courtesy of John G. Chapman.

2001; Fisher *et al.* 2009; Byrne *et al.* 2014; Breeze *et al.* 2020), plus an underlying continuum rising towards the UV which induces the brown colour component (again, see Figure 3). A list of common defects found in such pink diamonds can be obtained by perusing the literature. Single substitutional nitrogen (N_s) might have an important implication for their pink colour, but it has not yet been proved (Noble 2001; Byrne *et al.* 2014). The vacancy clusters that often form with plastic deformation are indeed present in photochromic pink diamonds (Fisher *et al.* 2009; Byrne *et al.* 2014). Byrne *et al.* (2014) introduced a tentative electronic structure to explain their observations of a bleaching effect (from brown to pink colour) due to IR irradiation. The electronic structure clearly suggests that the photochromic reaction involves a colour center generating a charge transfer (Byrne *et al.* 2012, 2014).

'Foxfire' Cape Diamond

A third variety of photochromic natural diamond was reported by Butler *et al.* (2017) for the Foxfire diamond, the second-largest (187.63 ct) gem-quality rough diamond found in Canada to date, which was subsequently faceted into two pear brilliants weighing 37.87 ct and 36.80 (Figure 4). When exposed to a typical

Figure 4: The cape-yellow pear-shaped brilliants in these earrings (37.87 and 36.80 ct) were cut from the 187.63 ct Foxfire diamond, which was documented by Butler *et al.* (2017) as showing photochromism. Private collection; photo © Christie's Images/Bridgeman Images.

Figure 5: This 0.83 ct cape-yellow diamond (left) turns brown when exposed to strong long-wave UV radiation (right). It reverts to its normal cape-yellow colour by simple exposure to visible light. Composite photo courtesy of Thomas Hainschwang.

long-wave UV lamp, the light yellow crystal became light brown. It returned to its initial light yellow colour upon exposure to visible light. Interestingly, the authors further stated that such small colour changes are often observed in natural diamonds. However, there is no other mention of such a change in the published gemmological literature. The origin of this modification of colour is not clear, as no before-and-after absorption spectra were provided. However, Butler *et al.* (2017) point out that electric charges move very slowly in diamond, and photochromism could be an indirect consequence of this sluggish movement of electrons between defects, resulting in a slow change in colour. Possibly more interesting, King *et al.* (2016) mentioned that the only visible-range spectral features of this large rough diamond were the N3 and N2 absorptions associated with the N3 defect.

Thomas Hainschwang (pers. comm. 2021) has observed that this third photochromic behaviour seems common only for relatively pure cape diamonds (Figure 5)—in other words, gems with dominant N3-related absorptions and only minor contributions from other centres. Further work is necessary to explain the mechanism.

Brown CVD Synthetic Diamond

The fourth variety of photochromic diamond concerns CVD synthetic diamonds that are near-colourless (or light brown) in their stable state, but turn light brown (or deep brown) after prolonged exposure (typically more than 30 minutes) to short-wave UV radiation. They return to their initial near-colourless or light brown state after being heated to temperatures higher than 450°C (Khan *et al.* 2009; Figure 6).

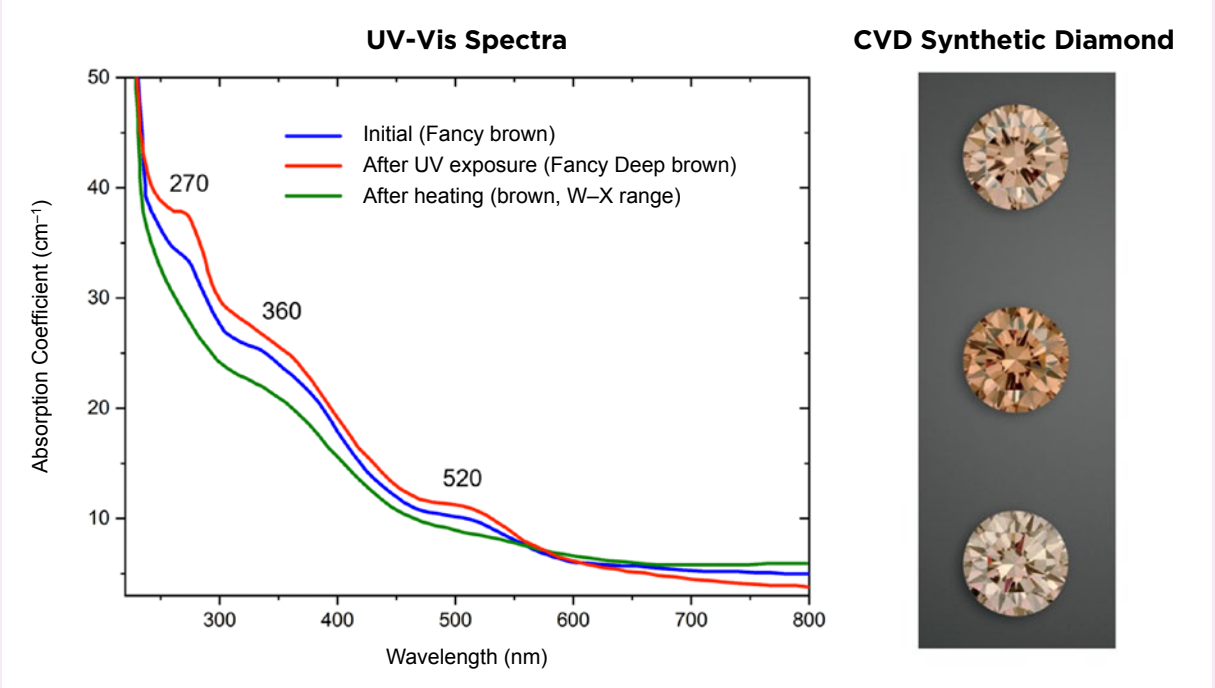

Figure 6: Photos and absorption spectra of a 0.40 ct photochromic CVD synthetic diamond (adapted from Khan *et al.* 2010) show the sample in its initial state, after exposure to ~225 nm UV radiation and after heating (seen in the images from top to bottom). The spectra have not been offset in order to directly compare the evolution of the absorption. Composite photo courtesy of R. Khan.

This behaviour satisfies the definition of photochromism—similar to the 'classic model' electronic structure described in part 1 of this article (see figure 2 in Blumentritt & Fritsch 2021). According to Khan *et al.* (2009), single nitrogen with a neutral charge (N_s^0) and nitrogen-vacancy-hydrogen (NVH) defects are involved, and the colouration is related to three absorption bands centred at 270, 360 and 520 nm (again, see Figure 6) that are responsible for the overall brownish appearance in the photogenerated state. The authors also suggested that a charge transfer is the source of the photochromism and proposed the following reaction mechanism: $N_s^0 + NVH^0 \leftrightarrow N_s^+ + NVH^-$. However, since the diminution of N_s^0 occurs faster than the growth of NVH^-, they proposed the existence of a secondary process with an unknown electron acceptor. A year later, the same authors confirmed their results (Khan *et al.* 2010) and also alerted gemmologists that the colour of a photochromic CVD synthetic diamond can be temporarily enhanced, thus influencing its colour grade. This observation concerns all varieties of photochromic diamonds.

Greyish Blue CVD Synthetic Diamond

A fifth variety of photochromic diamond concerns near-colourless CVD samples that change to greyish blue (Figure 7) from the UV radiation of a DiamondView (approximately 225 nm), and return to their initial near-colourless state after exposure to visible light or heating to around 550°C (Chauhan 2015; Breeze *et al.* 2020; Del Re 2020). This photochromic variety involves a completely different change in colour from the type exhibited by the brown CVD synthetic diamonds described above. The colour-causing defect is the silicon vacancy, $[Si\text{-}V]^-$, which absorbs in the green-to-red (and near-infrared) range and thus transmits blue. Breeze *et al.* (2020) proposed that a doubly charged silicon-vacancy complex, $[Si\text{-}V]^{2-}$, is responsible for this photochromic behaviour by forming $[Si\text{-}V]^-$ under short-wave UV excitation (approximately 225 nm). Absorption due to $[Si\text{-}V]^{2-}$ occurs entirely in the UV range, thus inducing no colour prior to UV excitation. Alternatively, $[Si\text{-}V]^-$ can be produced by charge transfer from $[Si\text{-}V]^0$ (D'Haenens-Johansson *et al.* 2011), since the latter also absorbs in the near-infrared and thus does not induce any colour prior to UV excitation. Clearly, this type of photochromism is related to silicon-vacancy defects.

Origin of Brown Colouration in Photochromic Diamonds

The photochromic change in colour involves a brown component for the pink, cape and CVD brown synthetic diamonds described above, and also for chameleon

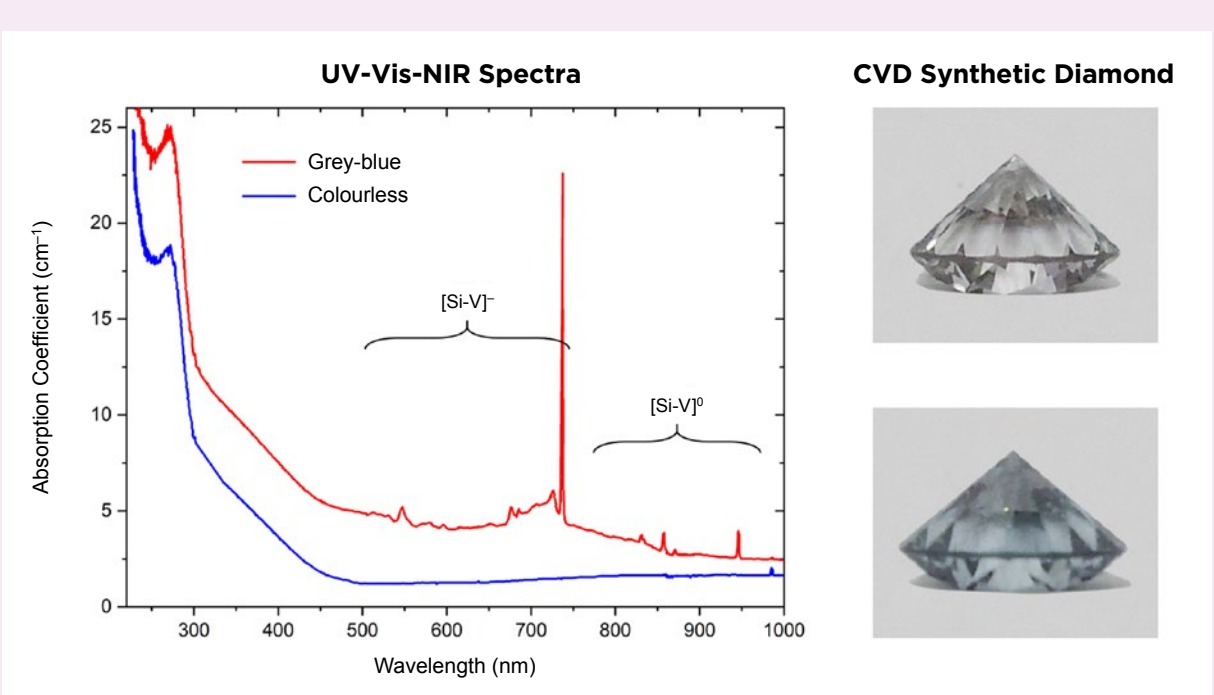

Figure 7: These photos (from Chauhan 2015) show a near-colourless 1.42 ct CVD synthetic diamond (top) and the same sample after exposure to short-wave UV radiation (bottom). The UV-Vis-NIR spectra, adapted from Breeze *et al.* (2020) and collected at 80 K, reveal the production of metastable $[Si\text{-}V]^-$ (500–750 nm) and $[Si\text{-}V]^0$ (780–980 nm) centres following UV exposure (225 nm in the DiamondView). Heating to 550°C causes it to return to its stable $[Si\text{-}V]^{2-}$ (near-colourless) state.

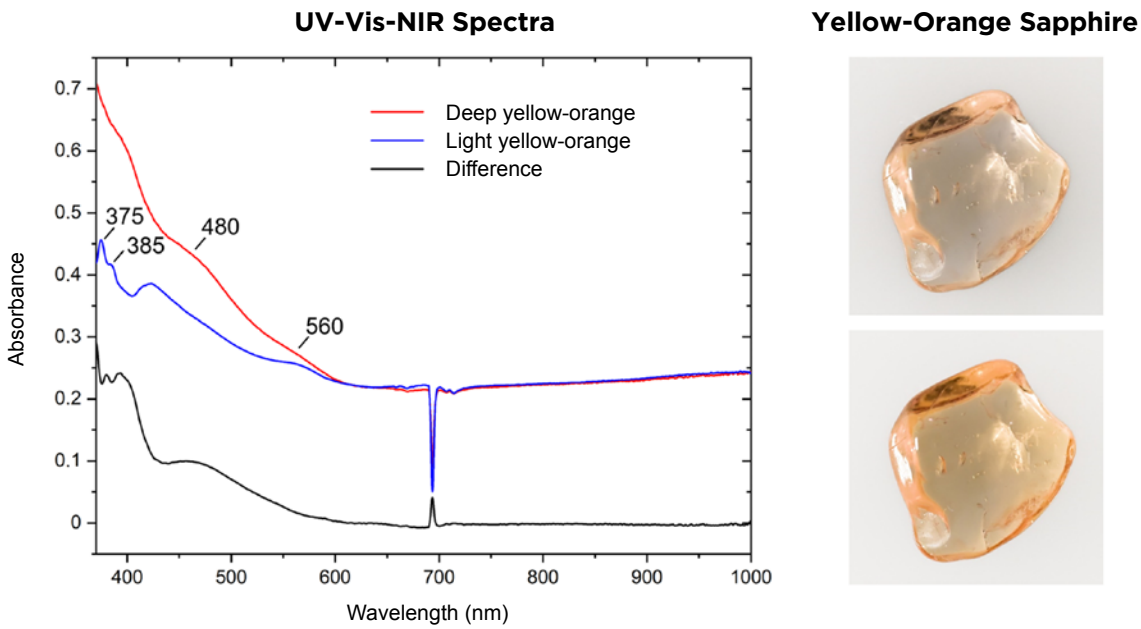

Figure 8: A 0.19 g photochromic yellow-orange sapphire (top) becomes visibly darker (bottom) following short-wave UV exposure. The corresponding spectra are consistent with those presented by Krzemnicki (2018) and Krzemnicki *et al.* (2018), who observed more intense absorption bands related to Cr^{3+} (only a weak 560 nm absorption band is visible in our spectra). (The sharp fluorescence-related emission feature due to Cr^{3+} at about 694 nm is unrelated to photochromism.) The difference spectrum shows that UV exposure increases the absorption continuum from 600 nm towards the UV region, as well as intensifies a feature at 480 nm. On the other hand, Fe^{3+}-related absorptions at 375 and 385 nm nearly disappear after UV exposure. The path length of the beam was approximately 3 mm. Photos by Philippe Deniard.

diamonds to some degree. Is it simply a matter of brown appearing and disappearing, or is it more complex? Brown is caused by an absorption continuum rising from the near-infrared towards the UV region, no matter what the material is. The continuum found in diamonds with a brown component might be related to a variety of defects: clusters of carbon vacancies, a type Ib component, H-related defects and so on (Hainschwang 2020a, b). Thus, there is no reason to believe that all photochromic changes in diamond involving a brown colour are simply due to a single defect causing the associated absorption continuum, which appears and disappears reversibly.

CORUNDUM (SAPPHIRE)

One of the oldest published descriptions of photochromic corundum is by Pough and Rogers (1947). They showed that X-ray irradiation creates a reversible change in every colour of natural sapphire. Schiffmann (1981) verified this on an orangey yellow 45 ct Sri Lankan sapphire, for which he provided before-and-after visible-range absorption spectra. He indicated that X-ray irradiation increased the absorption, thus giving a darker orangey yellow colour. This raises the question of whether a reversible colour reaction to X-ray excitation can be considered photochromism (see definition in part 1 of this article; Blumentritt & Fritsch 2021). It was later reported that the same increase of intensity of colour could be observed in some yellow sapphires using a simple short-wave UV lamp (Nassau & Valente 1987). So, it appears that a change in colouration in sapphire can be induced by X-rays as well as by UV irradiation (typically below 300 nm).

Nassau and Valente (1987) proposed a classification of yellow sapphires into seven types, one of which included those with an unstable colour. Thus, the observation of photochromism in a yellow sapphire turning more yellow-orange apparently could be a means to recognise samples that have been 'irradiated', naturally or artificially (Nassau & Valente 1987). Gem dealers have reported to us that some rare parcels of yellow sapphire darken or turn more orange after exposure to sunlight (i.e. outdoors) compared with being illuminated by mixed shop lighting (i.e. indoors; Emmanuel Piat, pers. comm. 2006–2021). This is not a colour-change effect due to observations in different lighting, because the change of colour associated with photochromism is consistent under both lighting conditions. The photogenerated component in sapphire could be a yellow to deep orange colouration (Figure 8)

Figure 9: A 0.86 ct blue sapphire (left) appears muddy green (right) after irradiation with a powerful, broad-band UV radiation source. When exposed to visible light, the colouration reverses in a few minutes to the original blue colour. Composite photo courtesy of Thomas Hainschwang.

that disappears slowly under daylight or more quickly when samples are heated (Pough & Rogers 1947; Schiffmann 1981; Fryer 1983b; Nassau & Valente 1987; Wang *et al.* 2021).

This process does not seem to be linked to the initial stable colour of a sapphire, since this effect (i.e. the addition of a yellow to orange colour component) has also been seen in blue and pink sapphires (Pough & Rogers 1947; Nassau & Valente 1987; Krzemnicki 2018; Krzemnicki *et al.* 2018): blue sapphire turns muddy green (Figure 9), and pink sapphire turns pinkish orange, after short-wave UV exposure (Figure 10). The latter stones have been described as *padparadscha-like* sapphires (Nassau & Valente 1987; Krzemnicki 2018; Krzemnicki *et al.* 2018), although the orange component of the colour is unstable.

Another example of photochromism in sapphire was published by Gaievskyi *et al.* (2014), who described a light bluish violet sapphire—containing Fe, Cr and Mg, with traces of Ti and Ga—which turned light brown upon exposure to the UV radiation of a DiamondView. The initial, stable colour returned after exposure to natural daylight for 12 hours. This is essentially consistent with the behaviour described by Pough and Rogers (1947), who concluded that since every natural sample reacts to X-ray irradiation, the phenomenon must be due to an intrinsic colour centre, structural deformation or impurity present in all sapphires. The effect is less apparent with some pure synthetic samples (again, see Pough & Rogers 1947). However, although all sapphires react to X-rays, they do not all respond to standard long- or short-wave UV radiation (Figure 11). Thus, extrapolating Pough and Roger's conclusion to UV radiation is not valid, because photochromic yellow sapphires are relatively rare (at least at the present time).

Other options have been explored to explain the photochromism observed from UV radiation in sapphire, such as the presence of an unknown colour centre, Fe impurities, both of these, or even Ni (Nassau & Valente 1987). In all these proposed explanations of photochromism, no precise mechanism is given, but the observations tend to fit fairly well with the 'classic' model of photochromism presented in figure 2 of part 1 of this article (Blumentritt & Fritsch 2021).

The difference spectrum we obtained from a photochromic yellow-orange sapphire demonstrates that the major difference between the two colour states is an increase of the continuum rising from about 600 nm towards the UV region (consistent with Schiffmann 1981), as well as the formation of a band around 480 nm (Figure 8). In our photochromic sapphire, the Fe^{3+}-related bands at about 375 and 385 nm disappeared after exposure to UV radiation. This is consistent, although not identical, with results reported by SSEF (Krzemnicki 2018; Krzemnicki *et al.* 2018).

Research on beryllium diffusion has addressed the 480 nm band in corundum, which is attributed to a hole centre compensated by a divalent cation (in this case Be^{2+}; Fritsch *et al.* 2003). This centre is not stable when produced by UV radiation and, logically, is also unstable when produced by X-ray exposure (assuming UV and X-ray radiation produce the same type of defect).

Figure 10: A 6.08 ct photochromic sapphire is shown in its stable pink state (left) and in its photogenerated orangey pink state after short-wave UV exposure (centre). It returns to its initial pink state after illumination by a daylight-equivalent halogen lamp (right). Composite photo courtesy of Michael S. Krzemnicki, © SSEF.

Figure 11: Three initially near-colourless sapphires (2.46–2.60 ct) gain (**a**) an orangey yellow colour after exposure to X-rays, (**b**) which fades dramatically after illumination for a few minutes by intense visible light from a 100 W halogen fibre-optic lamp. (**c**) All colour completely disappears after slightly heating the samples above the flame of a cigarette lighter. These three sapphires did not change colour following exposure to UV radiation. Photos by F. Blumentritt.

The difference spectrum seen for this photochromism resembles that for Be-diffused corundum. Thus, we surmise that the photochromic reaction is related to a hole centre, in agreement with the speculation by Pough and Rogers (1947) that photochromism might be related to an intrinsic defect. In the case of the sample in Figure 8, it can probably be attributed to an intrinsic defect in the corundum structure itself, most likely a hole centre or an oxygen vacancy (a missing oxygen ion in the structure). The latter is known to be a colour centre, and is even the dominant type of defect during the crystal growth of corundum, in nature as well as in the laboratory, where this remains true even if a dopant is added (Ramírez *et al*. 2007; Itou *et al*. 2009; Harutyunyan *et al*. 2015).[2] Oxygen vacancies create a negative charge deficit (–2) in the crystal. Commonly this is compensated by a +2 (divalent) ion, Mg being the most common in nature (Emmett & Douthit 1993). It is useful to note that Mg^{2+} alone, substituting for Al^{3+}, induces a hole centre (charge +1) in corundum that produces a yellow to orange colour, as observed in yellow sapphires from Montana, USA (Emmett & Douthit 1993). Thus there might be a link with the photochromism seen in natural, Mg^{2+}-containing yellow sapphires. More complex defects, such as those containing several Mg atoms and several oxygen vacancies, are also possible (Akselrod *et al*. 2003).

We propose a global explanation for the photochromism of natural yellow corundum as being linked to hole centres that are not linked to any impurity (i.e. intrinsic defects). These colour centres are not often mentioned in gemmology, but physicists have proven them quite common. Clearly, further detailed work is needed to fully understand the factors influencing colour stability in corundum.

BARYTE

Baryte ($BaSO_4$) is faceted on occasion (see, e.g., https://gemologyproject.com/wiki/index.php?title=Barite) and is considered a gem for collectors. Only a few publications report 'colour change' descriptions which could correspond to photochromism in this mineral. Unfortunately, we were not able to procure any baryte samples approaching these descriptions from either museums or mineral dealers we contacted, so we were unable to confirm whether these observations could fit the definition of photochromism. We hope to examine such material in the future.

According to the literature, the first documented reversible colour change induced by light in baryte was reported by Carlon and Winchell (1975). The colourless to greyish yellow material from Illinois, USA, turned deep blue upon exposure to bright sunlight for a few hours (Carlon & Winchell 1975; King 1987). A similar description has been made for baryte from Hartsel, Colorado, USA (Belsher & Baldwin 1980). The blue colour faded slowly when the baryte was kept in the dark or otherwise protected from direct sunlight.

Given the current state of knowledge, and that baryte is a sulphate, it is not unreasonable to consider that blue photochromism in this mineral could be related to one or more sulphur-based polyanions, such as SO_3^- (Gilinskaya & Mashkovtsev 1995) or S_3^- (Fleet & Liu 2010), both known to induce blue colour in some gems. This speculation needs further study, including detailed spectroscopic research and interpretation on photochromic samples with a good change in colour following exposure to bright sunlight or UV radiation.

[2] It should be pointed out that although photochromic synthetic corundum has been described (Mg-doped α-Al_2O_3; Tardío *et al*. 2003), it is unlikely to be encountered by gemmologists so it will not be discussed further here.

CONCLUSION

Photochromism in many gem materials remains poorly explained and, often, little documented, with the notable exception of hackmanite (reviewed by Blumentritt & Fritsch 2021) and diamond (see above). At the present time, there is no general theory to explain photochromism in gems. It is too often limited to guesswork, but a comprehensive study would require significant funding and effort (a single colour centre may require several PhDs to be fully understood). Perhaps the production of durable photochromic materials for industrial applications will provide the incentive for further research on these rare, infinitely cyclable and often beautiful gem materials.

We wish to stress the importance of testing for photochromism before colour grading, in particular for diamond and corundum. This phenomenon can lead to complications if not fully disclosed on laboratory reports and in various other circumstances (e.g. on a sales receipt or a loan document for an exhibit). As part of this disclosure, the concerned parties should be made aware of the reversibility of the phenomenon and the means by which it can be achieved (type of illumination/radiation, heating, and so on). We also feel that photochromism should be consistently included in the curriculum of gemmology courses, in the same manner as other phenomena such as asterism or colour change. This would increase awareness of this remarkable behaviour and hopefully help to avoid problems that could occur when it is not disclosed.

REFERENCES

Akselrod, M.S., Akselrod, A.E., Orlov, S.S., Sanyal, S. & Underwood, T.H. 2003. Fluorescent aluminum oxide crystals for volumetric optical data storage and imaging applications. *Journal of Fluorescence*, **13**(6), 503–511, https://doi.org/10.1023/b:Jofl.0000008061.71099.55.

Ardon, T. 2014. Lab Notes: Chameleon diamond with nickel absorption band. *Gems & Gemology*, **50**(2), 151–152.

Belsher, D.R. & Baldwin, C.E. 1980. An occurrence of barite at Hartsel, Colorado. *Mineralogical Record*, **11**(1), 23–25.

Blumentritt, F. & Fritsch, E. 2021. Photochromism and photochromic gems: A review and some new data (part 1). *Journal of Gemmology*, **37**(8), 780–800, https://doi.org/10.15506/JoG.2021.37.8.780.

Breeding, C.M., Eaton-Magaña, S. & Shigley, J.E. 2018. Natural-color green diamonds: A beautiful conundrum. *Gems & Gemology*, **54**(1), 2–27, https://doi.org/10.5741/gems.54.1.2.

Breeze, B.G., Meara, C.J., Wu, X.X., Michaels, C.P., Gupta, R., Diggle, P.L., Dale, M.W., Cann, B.L. *et al.* 2020. Doubly charged silicon vacancy center, Si-N complexes, and photochromism in N and Si co-doped diamond. *Physical Review B*, **101**(18), 184115–184125, https://doi.org/10.1103/PhysRevB.101.184115.

Butler, J.E., Post, J.E. & Wang, W. 2017. Gem News International: The Foxfire diamond, revisited. *Gems & Gemology*, **53**(4), 479–481.

Byrne, K.S., Anstie, J.D., Chapman, J.G. & Luiten, A.N. 2012. Optically reversible photochromism in natural pink diamond. *Diamond and Related Materials*, **30**, 31–36, https://doi.org/10.1016/j.diamond.2012.09.005.

Byrne, K.S., Chapman, J.G. & Luiten, A.N. 2014. Photochromic charge transfer processes in natural pink and brown diamonds. *Journal of Physics: Condensed Matter*, **26**(3), article 035501 (6 pp.), https://doi.org/10.1088/0953-8984/26/3/035501.

Byrne, K.S., Butler, J.E., Wang, W. & Post, J.E. 2018. Chameleon diamonds: Thermal processes governing luminescence and a model for the color change. *Diamond and Related Materials*, **81**, 45–53, https://doi.org/10.1016/j.diamond.2017.10.014.

Carlon, J. & Winchell, J.R. 1975. New barite find in southern Illinois. *Mineralogical Record*, **6**(5), 235–236.

Chapman, J. 2014. Chromism in pink diamonds. *Australian Gemmologist*, **25**(8), 268–271.

Chauhan, M. 2015. Gem News International: CVD synthetic diamond with unstable color centers. *Gems & Gemology*, **51**(1), 107–108.

Copeland, L.L., Liddicoat Jr., R.T., Benson Jr., L.B., Martin, J.G.M. & Crowningshield, G.R. 1960. *The Diamond Dictionary*. Gemological Institute of America, Los Angeles, California, USA, 328 pp.

Crowningshield, G.R. 1960. Developments and highlights at the Gem Trade Lab in New York: Pink diamond. *Gems & Gemology*, **10**(3), 74.

D'Haenens-Johansson, U.F.S., Edmonds, A.M., Green, B.L., Newton, M.E., Davies, G., Martineau, P.M., Khan, R.U.A. & Twitchen, D.J. 2011. Optical properties of the neutral silicon split-vacancy center in diamond. *Physical Review B*, **84**(24), article 245208 (14 pp.), https://doi.org/10.1103/PhysRevB.84.245208.

De Weerdt, F. & Van Royen, J. 2001. Defects in coloured natural diamonds. *Diamond and Related Materials*, **10**, 474–479, https://doi.org/10.1016/s0925-9635(00)00521-5.

Del Re, N. 2020. Under the microscope: Colour instability in CVD diamonds. *Jewellery Business*, **16**(1), 42–44.

Eaton-Magaña, S., Ardon, T., Smit, K.V., Breeding, C.M. & Shigley, J.E. 2018. Natural-color pink, purple, red, and brown diamonds: Band of many colors. *Gems & Gemology*, **54**(4), 352–377, https://doi.org/10.5741/gems.54.2.352.

Emmett, J.L. & Douthit, T.R. 1993. Heat treating the sapphires of Rock Creek, Montana. *Gems & Gemology*, **29**(4), 250–272, https://doi.org/10.5741/gems.29.4.250.

Figuier, L. 1867. Le diamant caméléon. *L'Année Scientifique et Industrielle (Onzième Année 1866)*, **11**, 144–148.

Fisher, D., Sibley, S.J. & Kelly, C.J. 2009. Brown colour in natural diamond and interaction between the brown related and other colour-inducing defects. *Journal of Physics: Condensed Matter*, **21**(36), article 364213 (10 pp.), https://doi.org/10.1088/0953-8984/21/36/364213.

Fleet, M.E. & Liu, X. 2010. X-ray absorption spectroscopy of ultramarine pigments: A new analytical method for the polysulfide radical anion S^{3-} chromophore. *Spectrochimica Acta Part B: Atomic Spectroscopy*, **65**(1), 75–79, https://doi.org/10.1016/j.sab.2009.11.008.

Fritsch, E. & Delaunay, A. 2018. What truly characterises a chameleon diamond? An example of an atypical 25.85 ct stone. *Journal of Gemmology*, **36**(2), 142–151, https://doi.org/10.15506/JoG.2018.36.2.142.

Fritsch, E., Shigley, J.E., Moses, T. & Rossman, G.R. 1995. Examination of the 22-carat green chameleon diamond. *In*: Content, D.J. (ed) *A Green Diamond: A Study of Chameleonism*. W.S. Maney & Son Ltd, Leeds, 15–28.

Fritsch, E., Chalain, J.-P., Hänni, H., Devouard, B., Chazot, G., Giuliani, G., Schwarz, D., Rollion-Bard, C. *et al.* 2003. Le nouveau traitement produisant des couleurs orange à jaune dans les saphirs. *Revue de Gemmologie A.F.G.*, No. 147, 11–23.

Fritsch, E., Massi, L., Rossman, G.R., Hainschwang, T., Jobic, S. & Dessapt, R. 2007. Thermochromic and photochromic behaviour of "chameleon" diamonds. *Diamond and Related Materials*, **16**(2), 401–408, https://doi.org/10.1016/j.diamond.2006.08.014.

Fryer, C. 1981. Lab Notes: "Chameleon" diamond. *Gems & Gemology*, **17**(4), 227.

Fryer, C. 1982. Lab Notes: "Chameleon" diamond. *Gems & Gemology*, **18**(4), 228.

Fryer, C. 1983a. Gem Trade Lab Notes: Pink diamonds. *Gems & Gemology*, **19**(1), 43–44.

Fryer, C. 1983b. Gem Trade Lab Notes: Sapphire, color restoration. *Gems & Gemology*, **19**(2), 117.

Gaievskyi, I., Iemelianov, I. & Belichenko, E. 2014. Gem News International: Unusual optical effect in blue sapphire. *Gems & Gemology*, **50**(2), 161–162.

Gaillou, E. & Rossman, G.R. 2014. Color in natural diamonds: The beauty of defects. *Rocks & Minerals*, **89**(1), 66–75, https://doi.org/10.1080/00357529.2014.842839.

Gilinskaya, L.G. & Mashkovtsev, R.I. 1995. Blue and green centers in natural apatites by ERS and optical spectroscopy data. *Journal of Structural Chemistry*, **36**(1), 76–86, https://doi.org/10.1007/bf02577752.

Goss, J.P., Ewels, C.P., Briddon, P.R. & Fritsch, E. 2011. Bistable N_2–H complexes: The first proposed structure of a H-related colour-causing defect in diamond. *Diamond and Related Materials*, **20**(7), 896–901, https://doi.org/10.1016/j.diamond.2011.05.004.

Hainschwang, T., Simic, D., Fritsch, E., Deljanin, B., Woodring, S. & DelRe, N. 2005. A gemological study of a collection of chameleon diamonds. *Gems & Gemology*, **41**(1), 20–34, https://doi.org/10.5741/gems.41.1.20.

Hainschwang, T., Notari, F., Fritsch, E., Massi, L., Rondeau, B., Breeding, C.M. & Vollstaedt, H. 2008. HPHT treatment of CO_2 containing and CO_2-related brown diamonds. *Diamond and Related Materials*, **17**(3), 340–351, https://doi.org/10.1016/j.diamond.2008.01.022.

Hainschwang, T., Notari, F. & Pamies, G. 2020a. A defect study and classification of brown diamonds with deformation-related color. *Minerals*, **10**(10), article 903 (38 pp.), https://doi.org/10.3390/min10100903.

Hainschwang, T., Notari, F. & Pamies, G. 2020b. A defect study and classification of brown diamonds with non-deformation-related color. *Minerals*, **10**(10), article 914 (35 pp.), https://doi.org/10.3390/min10100914.

Harutyunyan, V., Aleksanyan, E., Grigoryan, N., Baghdasaryan, V. & Yeghiazaryan, V. 2015. Radiation-induced effects in corundum single crystals. *Armenian Journal of Physics*, **8**(3), 129–139.

Hofer, S.C. 1985. Pink diamonds from Australia. *Gems & Gemology*, **21**(3), 147–155, https://doi.org/10.5741/gems.21.3.147.

Itou, M., Fujiwara, A. & Uchino, T. 2009. Reversible photoinduced interconversion of color centers in α-Al_2O_3 prepared under vacuum. *Journal of Physical Chemistry C*, **113**(49), 20949–20957, https://doi.org/10.1021/jp908417m.

Khan, R.U.A., Martineau, P.M., Cann, B.L., Newton, M.E. & Twitchen, D.J. 2009. Charge transfer effects, thermo and photochromism in single crystal CVD synthetic diamond. *Journal of Physics: Condensed Matter*, **21**(36), 364214–364223, https://doi.org/10.1088/0953-8984/21/36/364214.

Khan, R.U.A., Martineau, P.M., Cann, B.L., Newton, M.E., Dhillon, H.K. & Twitchen, D.J. 2010. Color alterations in CVD synthetic diamond with heat and UV exposure: Implications for color grading and identification. *Gems & Gemology*, **46**(1), 18–26, https://doi.org/10.5741/gems.46.1.18.

King, J.M., Shigley, J.E., Guhin, S.S., Gelb, T.H. & Hall, M. 2002. Characterization and grading of natural-color pink diamonds. *Gems & Gemology*, **38**(2), 128–147, https://doi.org/10.5741/gems.38.2.128.

King, J.M., Moe, K.S. & Wang, W. 2016. Lab Notes: Examination of the largest Canadian diamond. *Gems & Gemology*, **52**(2), 188–189.

King, R.J. 1987. Minerals explained 6: Baryte. *Geology Today*, **3**(1), 21–24, https://doi.org/10.1111/j.1365-2451.1987.tb00482.x.

Koivula, J.I. & Kammerling, R.C. 1991. Gem News: Large "chameleon" diamond. *Gems & Gemology*, **27**(2), 116.

Krzemnicki, M.S. 2018. Padparadscha-like fancy sapphires with unstable colours. *Facette*, **No. 24**, 6–7.

Krzemnicki, M.S., Klumb, A. & Braun, J. 2018. Unstable colouration of padparadscha-like sapphires. *Journal of Gemmology*, **36**(4), 346–354, https://doi.org/10.15506/JoG.2018.36.4.346.

Lang, A.R., Yelisseyev, A.P., Pokhilenko, N.P., Steeds, J.W. & Wotherspoon, A. 2004. Is dispersed nickel in natural diamonds associated with cuboid growth sectors in diamonds that exhibit a history of mixed-habit growth? *Journal of Crystal Growth*, **263**(1–4), 575–589, https://doi.org/10.1016/j.jcrysgro.2003.11.116.

Nassau, K. & Valente, G.K. 1987. The seven types of yellow sapphire and their stability to light. *Gems & Gemology*, **23**(4), 222–231, https://doi.org/10.5741/gems.23.4.222.

Noble, C.J. 2001. *Applications of magnetic resonance in materials science and solid state physics*. PhD thesis, Monash University, Melbourne, Australia, 211 pp. (see pp. 255–272).

Pough, F.H. & Rogers, T.H. 1947. Experiments in X-ray irradiation of gem stones. *American Mineralogist*, **32**(1–2), 31–43.

Raal, F.A. 1969. A study of some gold mine diamonds. *American Mineralogist*, **54**(1–2), 292–296.

Ramírez, R., Tardío, M., González, R., Chen, Y. & Kokta, M.R. 2005. Photochromism of vacancy-related defects in thermochemically reduced α-Al_2O_3 : Mg single crystals. *Applied Physics Letters*, **86**(8), article 081914 (3 pp.), https://doi.org/10.1063/1.1870130.

Ramírez, R., Tardío, M., González, R., Muñoz Santiuste, J.E. & Kokta, M.R. 2007. Optical properties of vacancies in thermochemically reduced Mg-doped sapphire single crystals. *Journal of Applied Physics*, **101**(12), article 123520 (12 pp.), https://doi.org/10.1063/1.2748729.

Schiffmann, C.A. 1981. Unstable colour in a yellow sapphire from Sri Lanka. *Journal of Gemmology*, **17**(8), 615–618, https://doi.org/10.15506/JoG.1981.17.8.615.

Tardío, M., Ramírez, R., González, R., Chen, Y. & Kokta, M.R. 2003. Photochromic effect in magnesium-doped α-Al_2O_3 single crystals. *Applied Physics Letters*, **83**(5), 881–883, https://doi.org/10.1063/1.1597963.

Verne, J. 1884. *L'Étoile du Sud*. J. Hetzel, Paris, France, 242 pp.

Wang, Y., Yang, L., Li, M., Yang, P., Shen, A. & Wang, C. 2021. Spectral characteristics and color origin of unstable yellow sapphire. *Spectroscopy and Spectral Analysis*, **41**(8), 2611–2617.

Zaitsev, A.M. 2001. *Optical Properties of Diamond*. Springer-Verlag, Berlin, Germany, xviii + 502 pp., https://doi.org/10.1007/978-3-662-04548-0.

The Authors

Dr Féodor Blumentritt*
and Dr Emmanuel Fritsch FGA
University of Nantes, CNRS,
Institut des Matériaux Jean Rouxel (IMN),
2 rue de la Houssinière BP 32229,
F-44000 Nantes, France
E-mail: emmanuel.fritsch@cnrs-imn.fr

* Currently: GGTL Laboratories Switzerland,
2bis route des Jeunes, 1227 Geneva, Switzerland

Acknowledgements

We acknowledge the University of Nantes for financial support of this project through the provision of a doctoral contract to author FB. We warmly thank all those who helped us to find or borrow samples, or even kindly donated material, to substantiate research on photochromism in gems. We are indebted to Emmanuel Piat (Daniel H Piat, Paris, France) for loaning the yellow-orange sapphires. Dr Thomas Hainschwang (GGTL Laboratories, Liechtenstein) provided many useful comments and some photographs. We also thank Alain Martaud (Alain Martaud Minéraux, France) for interesting discussions on mysterious photochromic baryte. Thanks to Dr Philippe Deniard (University of Nantes) for his help with photography. The authors are also grateful to Drs Maria Teresa Caldes and Stéphane Jobic (both of the University of Nantes) for their constructive comments.

Gem-A Notices

MESSAGE FROM GEM-A CEO ALAN HART

Welcome to this issue of *The Journal of Gemmology*—the first of 2022. I would like to take this opportunity to wish everyone a good start to the year and to thank you, our valued Members, for your continued support.

This year promises to be both an exciting and busy one for Gem-A, with plenty of new projects in the pipeline. We are now on the cusp of launching *GemIntro*, an entry-level, Ofqual-accredited course available entirely online. The aim is to provide a first step into gemmology for enthusiasts and for those beginning their journey into the gem and jewellery trade. We hope that, by introducing newcomers to the fascinating world of gemmology, we will foster the next generation of gemmologists and help them advance in their chosen careers. Keep an eye on our social media platforms—or sign up on the website mentioned below—for more information about this exciting interactive course.

For our Members, we have lined up some fantastic webinars and in-person workshops and discussions for 2022. The first one was a Gem Central event that took place on Thursday 10 March at our headquarters in London, featuring Dr Henrik Møller, Visiting Research Fellow for Global Sustainable Development at Warwick University. His talk focused on how the Chinese trade in Burmese jadeite is organised, and why jade is in such high demand in China. An accompanying half-day workshop, titled 'Investigating Jade and Its Imitations', took place on Friday 18 March. This hands-on event, led by senior Gem-A gemmologist Pat Daly, explored how to separate jade from its numerous imitations, such as bowenite, quartzite, steatite, plastic and glass. Then, on Friday 20 May, Gem-A will host a workshop on applied gemmology for jewellery designers. What's more, we will be making recorded segments of many in-person events available to our Members this year so that, even if you cannot make it to London, you can still benefit from the knowledge conveyed at these events.

I can also confirm that we are planning an in-person Gem-A Conference on Sunday 6 November 2022, followed by a graduation ceremony for our Students on Monday 7 November. You can find more information on the events page of Gem-A's website. I personally look forward to offering a warm welcome to many of our Members and associates whom we have not had the opportunity to see for some time. That said, many of you told us that you appreciated accessing sessions from last year's conference remotely, and so—as with our other events—we will be making select talks available online for Members based around the world.

I would like to extend my sincerest thanks once again for your ongoing support. I hope you enjoy this issue of *The Journal*, and I look forward to seeing many of you again in the near future.

A dealer offers Burmese jadeite at a market in Ruili, China. Photo by Dr Henrik Møller.

GEMINTRO LAUNCHING SOON

GemIntro is the first entry-level course offered by Gem-A, which is available entirely online. Candidates can go at their own pace and discover the basics of gemmology from home. This informative and interactive course is designed for those who are already working in the gems and jewellery trade and want to develop their knowledge

further, and also for gem enthusiasts who are curious about delving deeper into gemmology.

Over the course of 11 chapters and many accompanying videos, *GemIntro* will cover everything there is to know about the basics of gemmology. Each chapter tests candidates' knowledge with a mini-quiz, and this is followed by an online final assessment, where a 'pass' earns an Ofqual Level 2 accredited certificate to download, print and display.

Access the full course and online learning materials, and earn an accredited qualification, for just £220.

If you or someone you know is ready to take their first step into the gleaming world of gemstones, register your interest at **https://gem-a.com/gemintro**. By signing up, you will be first to hear when *GemIntro* goes live and becomes available to access. Gem-A will send an invite for the course, letting you know what happens next, and allow payment to be made securely online.

In the meantime, you can also take a closer look at the specifications for the *GemIntro* course at the website above. We look forward to welcoming the next generation of gemmologists soon!

OBITUARIES

Mary A. Burland FGA
1945–2022

It is with deep sadness that we announce the passing of Mary Burland FGA, a beloved Member and former employee of Gem-A. Many of you will have known Mary through her editorial work on the Association's publications, as well as through Membership, attending various events or simply through the trade.

Mary was born on 18 November 1945 and lived in Hornsey, north London, until 1970. In September 1967, she met her future husband, Alan, at his cousin's birthday party. They discovered that they had both attended the same school and had also lived opposite each other for 5 years, and yet did not know one another. Both worked in London at that time, but had not seen each other out and about. Mary and Alan married on 6 June 1970 and moved to Hoddesdon in Hertfordshire.

Mary's early training was as a Pitman shorthand secretary. She started work in the 1960s with the National Association of Goldsmiths (NAG) in Carey Lane, by Goldsmiths' Hall in central London, as a personal assistant to Gordon Andrews. He soon passed on the job of editing *The Journal of Gemmology* to Mary. She worked from her NAG office until 1974 when her daughter, Julie, was born. She then continued her work from home, editing *The Journal* together with Alan Jobbins, who took over from John Chisholm in 1987. During the period 1974–1994 Mary had a number of other jobs but still worked on *The Journal*. From the mid-1980s to 1992 she was also a director and sales representative of a jewellery business.

In 1994, Mary returned to work with the Gemmological Association at its new location on Greville Street in Hatton Garden. There she was Events and Publications Manager and also Membership Secretary whilst still working on *The Journal*. In addition, she was Managing Editor of *Gems&Jewellery* and its predecessor *Gem & Jewellery News* (published jointly with The Society of Jewellery Historians) since being launched in 1991. She also became a Gem-A Council of Management trustee during this time. Mary officially retired at the end of 2010, but carried on editing *The Journal* and *Gems&Jewellery* from home on a freelance basis until 2018, when she fully retired. In total, Mary edited and did production work on *The Journal* for five decades.

Mary was awarded a Gem-A Fellowship Diploma (FGA) in 2010 in recognition of her high level of expertise over so many years. She had avoided sitting the exam because everyone knew her, though she would probably have passed with flying colours. The award was a big

surprise to her. She was also awarded an Honorary Lifetime Membership to Gem-A in 2014.

Mary loved going to gem and jewellery industry events, and often attended one of her favourites: the Scottish Gemmological Association's conference, where she won the raffle, earning a weekend for two at a Scottish hotel each time!

Sadly, in September 2019, Mary suffered a stroke and in June 2021 moved to a care home. She passed away on 2 February 2022 after another stroke. As word spread of Mary's passing, Gem-A and Mary's husband Alan received several thoughtful messages from friends and colleagues around the world, such as:

- 'Her dedication and effortless ability to coordinate multiple roles were the backbone of the Association.'
- 'Part of my love for the Association has to do with the people that represented it when I was younger and Mary was one of them.'
- 'Mary was a fine ambassador for Gem-A throughout its development and considerable restructuring over the years. She was charming, constructive and efficient, and most diplomatic when dealing with sensitive issues. It was always a pleasure to be able to get things done with her help and advice. She was able to engender much goodwill and support for the Association.'
- 'Mary was always helping me whenever I had a question regarding Gem-A and specifically when planning to submit an article for publication in *The Journal*.'
- 'I esteemed her dedication and constant care to *The Journal* very much.'
- 'Mary was both a friend and a mentor, and I am grateful that I had the pleasure of her knowing her for so many years.'

These comments—and others—are a testament to Mary's valuable and dedicated contributions to the Association, as well as her delightful personality. As a colleague of Mary's for many years, I recall that throughout all of her editing and organisational work she could be relied upon for her excellent planning and super accuracy with a strictly no-nonsense approach—plus a humorous and wry summing-up of any 'situation'.

Mary loved to meet with her friends, enjoyed playing bridge, reading books and going on cruises, and was a devoted grandmother to her two granddaughters. Working with Mary was an honour for anyone who had the privilege to do so. She will be deeply missed by her devoted husband, daughter and granddaughters, and by all those in the gem and jewellery community who knew her.

Ian F. Mercer FGA
Gem-A Director of Education, 1990–2009

Editor's note: Mary was a true pleasure to work with since I began editing *The Journal* in 2013. I will miss Mary's friendly demeanour and genuine care for others, as well as her concern for Gem-A and its publications.

Noel Deeks FGA
1929–2021

It is difficult to remember exactly when I first met Noel, but it was in those days long ago when the former National Association of Goldsmiths—now the National Association of Jewellers or NAJ—held its annual conference. Noel and his wife Irene were regular attendees at those events, together with his colleagues from James Walker (~~an industrial machinery manufacturing company~~)—one of the UK's leading high-street jewellers—the late Jimmy Sanders, Michael Prince and Tony Metherell. However, our friendship really strengthened when he became actively involved with the Gemmological Association of Great Britain (now Gem-A).

Sooner than anticipated, I was elected Chairman of the Gemmological Association in 1981, and I asked Noel if he would be Vice Chairman, to which he agreed. Nigel Israel very ably supported us as Treasurer. Our team was together for 14 years. From mid-1993 until mid-2001 Noel served as a trustee on Gem-A's Council of Management, and from 2002 until his death he was a Vice President of Gem-A.

Noel was born on Christmas Day in 1929—hence his Christian name—and originally trained as an engineer. His father was a watchmaker, which resulted in Noel pursuing work repairing clocks and watches, and he qualified as a CMBHI of the British Horological Institute in 1953. Having joined the renowned firm of James Walker, he soon 'graduated' into the sales area of the company, and the rest is history, as the saying goes. He became joint Managing Director in 1977 alongside Michael Prince (who was also born on a Christmas Day, incidentally). His experience behind the counter fostered an interest in gemstones, and that led him to study for his FGA, which he obtained in 1969. He then went on to earn his DGA the following year. Noel was a fervent supporter of education and training—he had created a training department at James Walker which employed over 2,000 staff—and this led him to teach the diamond grading course at Sir John Cass College in London throughout the 1970s.

Noel was a highly skilled negotiator, and without his expertise and tenacity as a Trustee of the Gem Trade Laboratory pension scheme, the laboratory staff would not have the pension they enjoy today.

But what of Noel as a personality? Quietly spoken, always business-like, he was generous with his time and utterly dependable. He had a profound sense of the ridiculous, which coincided with my wife Mary's and my sense of humour. His engineering background led him to devise or improve several gemmological instruments, which are in use throughout the world of gemmology today. Noel continued to support Gem-A following his retirement, and since 2001 he sponsored the Deeks Diamond Prize, which is awarded to the best Diamond Theory candidate of the year.

I am one of the lucky people to have enjoyed Noel's friendship and unswerving loyalty as a colleague in our various voluntary roles in the trade. I treasure the memory of those days and consider myself fortunate to have known this special man. Noel endured a lengthy illness with courage and his customary tenacity, and he died on 20 December 2021, five days short of his 92nd birthday.

David J. Callaghan FGA
Vice President, Gem-A

Learning Opportunities

Note: Event dates and formats are subject to change depending on the COVID-19 situation.

CONFERENCES AND SEMINARS

MJSA Expo
20–22 March 2022
New York, New York, USA
https://www.mjsa.org/events/mjsa-expo/seminars-events
Note: Includes a seminar programme

American Gem Society Conclave
25–27 April 2022
Oklahoma City, Oklahoma, USA
https://www.americangemsociety.org/conclave-2022

Scottish Gemmological Association Conference
29 April–2 May 2022
Cumbernauld, Scotland
https://www.scottishgemmology.org/hotelandtransport

GemGenève
5–8 May 2022
Geneva, Switzerland
https://gemgeneve.com
Note: Includes a seminar programme

Halifax 2022: GAC-MAC-IAH-CNC-CSPG Joint Meeting
15–18 May 2022
Halifax, Nova Scotia, Canada
https://halifax2022.atlanticgeosciencesociety.ca
Session of interest: Cratons, Cratonic Magmatism, and Diamonds

50th Annual Society of North American Goldsmiths Conference (SNAG X Providence)
1–4 June 2022
Providence, Rhode Island, USA
www.snagmetalsmith.org/events/conferences/snagxprovidence

JCK Las Vegas
10–13 June 2022
Las Vegas, Nevada, USA
https://lasvegas.jckonline.com/en-us/events---education.html
Note: Includes a seminar programme

NAJ Summit
10–13 June 2022
Northampton, East Midlands
https://www.naj.co.uk/summit-2022

Jewellery & Gem Asia Hong Kong
16–19 June 2022
Hong Kong
https://tinyurl.com/2p8k4pek
Note: Includes a seminar programme

Goldschmidt2022
10–15 July 2022
Honolulu, Hawaii, USA (and online)
https://2022.goldschmidt.info
Session of interest: Gems and Gem Minerals as Precious Indicators of Diverse Earth Processes

23rd General Meeting of the International Mineralogical Association (IMA 2022)
18–22 July 2022
Lyon, France
https://www.ima2022.fr
Sessions of interest: (1) Haüy 200 Years On: What News in Gem Research? (2) Mineralogy and Gemology in Cultural Heritage; (3) New Insights into Diamond Mineralogy, Geochemistry and Petrology; (4) Gemstones from the Deep: A Celebration of the Career of George E. Harlow

6th Mediterranean Gemmological & Jewellery Conference
12–14 August 2022
Thessaloniki, Greece
https://gemconference.com
Note: Will include post-conference gem, mineral and mine tours to North Macedonia, Kosovo and Serbia.

NAJA 58th Annual Mid-Year Education Conference
13–14 August 2022
Online
https://tinyurl.com/yc89zjyr

23rd Federation for European Education in Gemmology (FEEG) Symposium
3 September 2022
Paris, France
http://www.feeg-education.com/symposium

32nd International Conference on Diamond and Carbon Materials
4–8 September 2022
Lisbon, Portugal
https://www.elsevier.com/events/conferences/international-conference-on-diamond-and-carbon-materials

Maine Pegmatite Workshop
7–12 September 2022
Bethel, Maine, USA
http://www.maine-pegmatite-workshop.com

Vicenzaoro
8–12 September 2022
Vicenza, Italy
https://www.vicenzaoro.com/en
Note: Includes a seminar programme

Jewellery & Gem World Hong Kong
16–20 September 2022
Hong Kong
https://jgw.exhibitions.jewellerynet.com/specialevent
Note: Includes a seminar programme

13th Annual Portland Jewelry Symposium
2–3 October 2022
Portland, Oregon, USA
https://portlandjewelrysymposium.com

Canadian Gemmological Association (CGA) Conference
21–23 October 2022
Vancouver, British Columbia, Canada
https://canadiangemmological.com

Gem-A Conference
6 November 2022
London
https://gem-a.com/event/conference-2022

OTHER EDUCATIONAL OPPORTUNITIES

Gem-A Workshops and Courses
Gem-A, London
https://gem-a.com/education

Gemstone Safari to Tanzania
6–23 July 2022
www.free-form.ch/tanzania/gemstonesafari.html

Lectures with Gem-A's Midlands Branch
Fellows Auctioneers, Augusta House, Birmingham
Email Louise Ludlam-Snook at gemamidlands@gmail.com

- Jack Ogden—The Black Prince's Ruby: Investigating the Legend
  25 March 2022
- Paul Phillips—Fractional Crystallisation
  29 April 2022

Lectures with The Society of Jewellery Historians
Society of Antiquaries of London, Burlington House
www.societyofjewelleryhistorians.ac.uk/current_lectures

- Gonçalo de Vasconcelos e Sousa—An Aspect of Portuguese Jewellery
  24 May 2022
- Karl Schmetzer—The Late 14th-Century Royal Crown of Blanche of Lancaster
  28 June 2022
- Maria Filomena Guerra—Fresh Scientific Insights in Ancient Egyptian Gold Technology
  27 September 2022
- Usha Balakrishnan—The Jewellery of the Nizam of Hyderabad
  22 November 2022

New Media

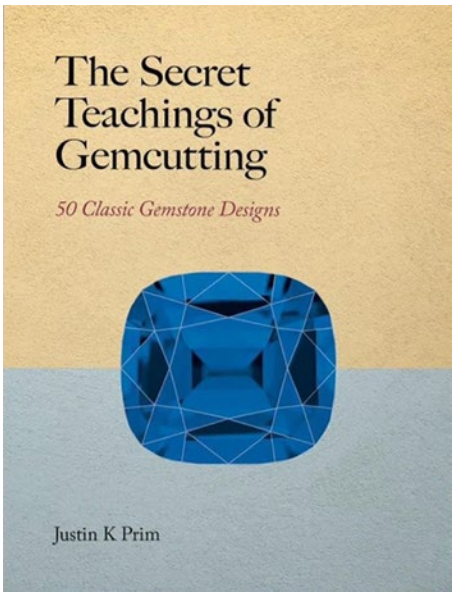

The Secret Teachings of Gemcutting: 50 Classic Gemstone Designs

By Justin K Prim, 2021. Magus Publishing, Chicago, Illinois, USA and Bangkok, Thailand, https://www.magusgems.com/product-page/the-secret-teachings-of-gemcutting, 233 pages, illus., ISBN 978-1737057802 (hardcover) or 978-0578870717 (softcover). USD100.00 hardcover or USD80.00 spiral-bound softcover.

Author Justin K Prim has divided this book into two parts. In the first part, he explains a lot about the basics of gem cutting, including the nomenclature of faceting, importance of RI, and how cutting diagrams relate to the sequence of cutting the facets themselves, as exemplified by two of the most-used gemstone designs. He explains how the colour of the rough material must be taken into account, tricks used to brighten up or intensify colour, and how pleochroism interacts with cutting. The last factor plays an especially important role when cutting gems that have a favourable colour axis, such as ruby, in order to create the most valuable stone. Prim takes the reader through the complete process of cutting a gem, from choosing a design with appropriate angles to preforming the rough and optimising the yield. This is all accompanied by interesting, less well-known information, such as the influence of RI on lustre, the correlation of tone and saturation with the design, and how to make the best use of colour-zoned rough. In addition, what I consider a highlight of this book is a section on the history of gem cutting, which is something that—at least to my knowledge—has never been part of any similar book on faceting designs. It gives a nice overview of how faceting machines were developed and, with them, the preference for certain designs throughout history.

Part two of the book gives instructions on how to cut 50 mainstream designs. Each design is accompanied by a photo of a gem (unfortunately unidentified), a short history and some instructions for cutting. This is followed by two faceting diagrams for that particular design, one for gem materials with high RI and a second one for those with low RI, each with an accompanying computer rendering. This part of the book provides a good compendium of the facet designs that are most often found on commercially cut gems, but, in my opinion, it also has some flaws.

As only two sets of different angles are given for high-RI and low-RI stones (in most cases only for the pavilion) to cover the whole range of gem varieties with large differences in RIs, it is clear that only suboptimal results will be achieved for many materials. Also, the number of facets listed in the diagrams is in many cases incorrect, which is not a big issue, but it is something that should have been checked before printing.

One of the most well-known designs described in the book is the Hearts and Arrows cut. Here it should have been mentioned that this cut was developed for diamond and that it only works for materials with a very high RI. The two Hearts and Arrows faceting diagrams presented in the book would be expected to result in some sort of 'arrows' seen face up, but in order to get the maximum light return, the angles must be adjusted for very small ranges of RIs. Regarding the 'hearts', these can only be seen when viewing the gem from the back. To create the appearance of the hearts, in my experience the material must have an RI of at least 2.2.

One point that also seems strange, at least to me, is the cutting sequence described in this book. The author suggests cutting mains before break facets, which is different from the procedure described in all books on modern faceting that I am aware of. However, this might have to do with differences pertaining to commercial cutting with handpiece machines (and rounded girdles) vs modern cutting on mast machines (and faceted girdles).

Overall, I recommend this book to anyone who wants

to learn about mainstream cuts, the how and why of gem designs, and the reasons some cuts are more popular than others. It is a great coffee-table book for jewellers, goldsmiths and anyone else in the trade, and even end consumers who would like to gain some insights into the complex process of gem cutting. But would the book be useful to someone who wants to learn faceting? I am not sure about that. If relying solely on the instructions given, you might easily run into trouble due to the cutting sequences or the inaccurate numbers of facets specified. For those who already have had some initial experience with gem cutting, the book is a great addition and a nice compendium of commercial cuts.

Dr Clemens Schwarzinger
Johannes Kepler Universität Linz, Austria

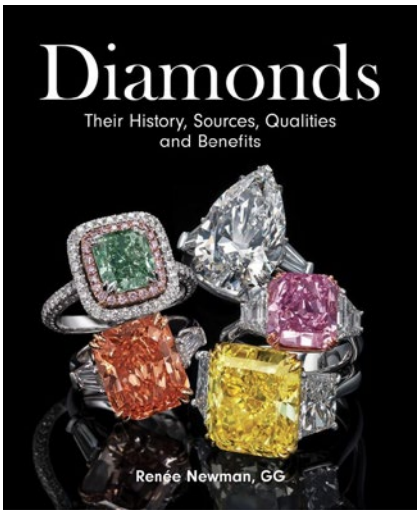

Diamonds: Their History, Sources, Qualities and Benefits

By Renée Newman, 2021. Firefly Books Ltd, Richmond Hill, Ontario, Canada, https://tinyurl.com/mpdvpymv, 272 pages, illus., ISBN 978-0228103318. CDN59.95 hardcover.

Renée Newman is well known as the author of a range of reference books and guides on gems and jewels that have been received with much acclaim. This new book on diamonds is conceived both for the general public (but not just as a 'coffee-table book') and for professionals who are looking for quick information.

The volume contains eight main chapters, each of which deals with an important topic. Chapters 1 ('What Is a Diamond?') and 2 ('Where Are Diamonds Found?') describe the mineralogy and geology of diamonds, as well as their cultural and sociological roles. Chapter 3 ('Diamond Mining and Processing') covers their production. Chapters 4 ('The Evolution of Diamond Cutting') and 5 ('The Evolution of Diamond Jewellery') are devoted to historical aspects. Finally, Chapters 6 ('How Are Diamonds Priced?'), 7 ('Laboratory-Grown Diamonds') and 8 ('Diamond's Remarkable Benefits') discuss more practical and technical subjects. All sections are well arranged so that the desired content is easy to find.

During the last decades, the world of diamonds has changed considerably. The former De Beers monopoly is no more. Some mines, such as Argyle, have been closed, while new ones, such as Diavik and Karowe, have appeared as important producers. Technical aspects, from mining to polishing, are being revolutionised by computer technology, and the trade is affected by the Internet. Diamond synthesis (by both HPHT and CVD techniques) is important for technical purposes and can pose a challenge to gemmologists. These and many other contemporary topics are discussed in clear and concise, but not too technical, language. The easy-to-read text is enhanced by many maps, diagrams and tables, as well as 380 excellent photos. Here, however, I find the only significant flaw in the book: Page 18 shows a full-page image of the Great Imperial Crown created for the coronation of Catherine the Great in 1762. However, it is not a photo of the original crown, but of a replica—and a bad one too. For example, a faceted stone represents the large polished (not faceted) red spinel on top of the original crown. This is not just annoying, it is simply not on a level with the rest of the book. The book is completed by a glossary, a bibliography, acknowledgements and an index.

All in all, this splendid volume is comprehensive, with a treasure trove of up-to-date data, and is easily readable. It will appeal to many different kinds of readers, from diamond-loving laypersons to professionals in the diamond trade to scientists. And, it is sold for a moderate price. I concur with the sentiments of another reviewer of this book (Peter Indorf): 'If you are a jeweler, gemologist, designer, appraiser, buy or sell diamonds, love or hate diamonds, buy this book, period.'

Dr Rolf Tatje
Duisburg, Germany

Other Book Titles

COLOURED STONES

Agates: Types, Mineralogy, Deposits, Host Rocks, Ages and Genesis
Ed. by Galina Palyanova, 2021. MDPI, Basel, Switzerland, 210 pages, ISBN 978-3036521831 or e-ISBN 978-3036521848, https://doi.org/10.3390/books978-3-0365-2184-8. CHF72.75 hardcover or free PDF.

Gems, Colours & Wild Stories: 175 Years of Constantin Wild
Ed. by Constantin Wild and Nina Hald, 2021. Constantin Wild GmbH & Co. KG, Idar-Oberstein, Germany, and Arnoldsche Art Publishers, Stuttgart, Germany, 304 pages, ISBN 978-3897906266. EUR124.00 hardcover with slipcase.

Jade: A Gemologist's Guide
Ed. by Richard W. Hughes, 2022. Lotus Publishing, Bangkok, Thailand, and RWH Publishing, Boulder, Colorado, USA, 536 pages, ISBN 978-0964509757. USD200.00 hardcover or USD300.00 special edition with slipcase.

Mineralogy and Geochemistry of Ruby
Ed. by Frederick Lin Sutherland and Khin Zaw, 2020. MDPI, Basel, Switzerland, 234 pages, ISBN 978-3039436156 or e-ISBN 978-3039436163, https://doi.org/10.3390/books978-3-03943-616-3. CHF72.75 hardcover or free PDF.

GENERAL REFERENCE

Geology and Mineralogy of Gemstones
By David Turner and Lee A. Groat, 2022. AGU Advanced Textbook Series, American Geophysical Union, Washington DC, USA, 288 pages, ISBN 978-1119299851 or e-ISBN 978-1119299875. USD99.95 softcover or USD80.00 eBook.

Zircon, Zirconium, Zirconia – Similar Names, Different Materials
By Bożena Arnold, 2022. Springer, Berlin, Germany, 105 pages, ISBN 978-3662642689 or e-ISBN 978-3662642696, https://doi.org/10.1007/978-3-662-64269-6. EUR76.26 softcover or EUR58.84 eBook.

JEWELLERY HISTORY

The Wyvern Collection: Medieval and Renaissance Enamels and Other Works of Art
By Paul Williamson, 2021. Thames & Hudson, New York, New York, USA, 480 pages, ISBN 978-0500024560. USD95.00 hardcover.

JEWELLERY AND *OBJETS D'ART*

Cipullo: Making Jewelry Modern
By Renato Cipullo, 2021. Assouline Publishing, New York, New York, USA, 212 pages, ISBN 978-1614289593. USD195.00 hardcover.

Cleto Munari: Jewelry Design
By Alba Cappellieri, 2021. Maretti Editore, Imola, Italy, 284 pages, ISBN 978-8893970518. EUR48.00 hardcover.

Fabergé: Romance to Revolution
Ed. by Kieran McCarthy and Hanne Faurby, 2022. V&A Publishing, London, 256 pages, ISBN 978-1838510145. GBP35.00 hardcover.

Sixième Sens par Cartier: Haute Joaillerie et Objets Précieux/High Jewelry and Precious Objects
By François Chaille, 2021. Flammarion, Paris, France, 256 pages, ISBN 978-2080256232 (French) or ISBN-9782080260338 (English). EUR95.00 hardcover.

SYNTHETICS AND SIMULANTS

Chemical Vapor Deposition (CVD): Methods and Technologies
Ed. by Levi Karlsson, 2021. Nova Publishers, Hauppauge, New York, USA, 208 pages, ISBN 978-1536199499 or e-ISBN 978-1536199901. USD160.00 hardcover or eBook.

Literature of Interest

COLOURED STONES

An attractive blue diopside from Sissone Valley, western Alps, Italy. F. Caucia, M. Scacchetti, L. Marinoni, M. Gilio, A. Langone, O. Bartoli, M. Vanotti and I. Foianini, *Minerals*, **11**(8), 2021, article 837 (23 pp.), https://doi.org/10.3390/min11080837.*

Blauer Gahnit aus Nigeria [Blue gahnite from Nigeria]. T. Stephan, U. Henn and S. Müller, *Gemmologie: Zeitschrift der Deutschen Gemmologischen Gesellschaft*, **70**(3/4), 2021, 3–18 (in German with English abstract).

Blue heaven – Tanzanite. L. Langeslag, *Gemmology Today*, December 2021, 79–83, https://tinyurl.com/2p8akuzv.*

Blue sapphires from Mogok, Myanmar: A gemological review. W. Soonthorntantikul, U. Atikarnsakul and W. Vertriest, *Gems & Gemology*, **57**(4), 2022, 292–317, https://doi.org/10.5741/gems.57.4.292.*

Characteristics of the Guatemalan feicui and its comparison to the Myammar feicui. B. Xing, G. Shi, J. Zhang, C. Long, Y. Zhang, L. He and R. Hu, *Geoscience*, **36**(6), 2021, 1769–1788, https://doi.org/10.19657/j.geoscience.1000-8527.2021.23 (in Chinese with English abstract).

Chromaticity study of emerald under Chelsea filter. Q. Zhou, H. Liu and A.H. Shen, *Journal of Gems & Gemmology*, **23**(5), 2021, 16–24, https://tinyurl.com/2przkb5y (in Chinese with English abstract).*

Colored stones from the deep. A.C. Palke and J.E. Shigley, *Gems & Gemology*, **27**(4), 2021, 390–396, https://tinyurl.com/5yp6xhte.*

Composition characteristic of turquoise from Mongolia. J. Liu, M. Yang and L. Liu, *Journal of Gems & Gemmology*, **23**(4), 2021, 12–19, https://tinyurl.com/2przkb5y (in Chinese with English abstract).*

The corundum conundrum: Constraining the compositions of fluids involved in ruby formation in metamorphic melanges of ultramafic and aluminous rocks. V. van Hinsberg, C. Yakymchuk, A.T.K. Jepsen, C.L. Kirkland and K. Szilas, *Chemical Geology*, **571**, 2021, article 120180 (19 pp.), https://doi.org/10.1016/j.chemgeo.2021.120180.

Crystal chemistry of six grossular garnet samples from different well-known localities. S.M. Antao, *Minerals*, **11**(7), 2021, article 767 (26 pp.), https://doi.org/10.3390/min11070767.*

L'euclase rose-orangé: Une nouvelle gemme découverte à Bahia, Brésil [Orange-pink euclase: A new gem discovered in Bahia, Brazil]. L. Gilles-Guéry, *Review de Gemmologie A.F.G.*, No. 214, 2021, 18–25 (in French).

Explaining colour change in pyrope-spessartine garnets. Yan Qiu and Ying Guo, *Minerals*, **11**(8), 2021, article 865 (15 pp.), https://doi.org/10.3390/min11080865.*

Gemmological characteristic of purple-brownish red garnet from Zambia. M. Qu, Y. Zhong and A.H. Shen, *Journal of Gems & Gemmology*, **23**(4), 2021, 20–28, https://tinyurl.com/4d2d7ycz (in Chinese with English abstract).*

Gemological characterization of peridot from Pyaung-Gaung in Mogok, Myanmar. M. Seneewong-Na-Ayutthaya, W. Chongraktrakul and T. Sripoonjan, *Gems & Gemology*, **57**(4), 2022, 318–337, https://doi.org/10.5741/gems.57.4.318.*

Gemological and mineralogical characteristics of diaspore jade from Linwu County, Hunan Province, China. Y. Song, L. Wang, L. Wang, L. Tao and Y. Liu, *Journal of Mineralogy and Petrology*, **41**(3), 2021, 1–8 (in Chinese with English abstract).

Gemological and spectroscopic characteristics of natural white sodalite with tenebrescence. X. Yan, S. Yue, L. Su and Z. Wang, *Spectroscopy and Spectral Analysis*, **41**(12), 2021, 3936–3941, https://tinyurl.com/ycktyfpf (in Chinese with English abstract).*

"Horsetail" inclusions in the Ural demantoids: Growth formations. A.Y. Kissin, V.V. Murzin and E.S. Karaseva, *Minerals*, **11**(8), 2021, article 825 (13 pp.), https://doi.org/10.3390/min11080825.*

Hydrophaner Opal aus dem Kosovo [Hydrophane opal from Kosovo]. H. A. Hänni, W. Engel and J. Diez, *Gemmologie: Zeitschrift der Deutschen Gemmologischen Gesellschaft*, **70**(3/4), 2021, 37–40 (in German with English abstract).

Inclusion characteristic of blue sapphire from Australia. F. Fang, J. Di and X. Yafen, *Journal of Gems & Gemmology*, **23**(5), 2021, 25–35, https://tinyurl.com/4bs7m3y3 (in Chinese with English abstract).*

Johnkoivulaite, $Cs(Be_2B)Mg_2Si_6O_{18}$, a new mineral of the beryl group from the gem deposits of Mogok, Myanmar. A.C. Palke, L.M. Henling, C. Ma, G.R. Rossman, Z. Sun, N. Renfro, A.R. Kampf, K. Thu *et al.*, *American Mineralogist*, **106**(11), 2021, 1844–1851, https://doi.org/10.2138/am-2021-7785.

Mineralogy and magnetic behavior of yellow to red Xuanhua-type agate and its indication to the forming condition. D. Zhou, G. Shi, S. Liu and B. Wu, *Minerals*, **11**(8), 2021, article 877 (12 pp.), https://doi.org/10.3390/min11080877.*

Non-invasive XRF analysis of ancient Egyptian and near Eastern turquoise: A pilot study. F. Carò, D. Schorsch, L. Smieska and B. Santarelli, *Journal of Archaeological Science: Reports*, **36**, 2021, article 102893 (14 pp.), https://doi.org/10.1016/j.jasrep.2021.102893.

The origin of trapiche-like inclusion patterns in quartz from Inner Mongolia, China. G.A. Farfan, J. Rakovan, M.R. Ackerson, B.J. Andrews and J.E. Post, *American Mineralogist*, **106**(11), 2021, 1797–1808, https://doi.org/10.2138/am-2021-7454.

Preliminary study on definition and gemological classification of jasper. S. Xu, S. Dai, X. Shi, D. Chen, W. Qu, Q. Luo and Y. Xia, *Journal of Mineralogy and Petrology*, **41**(4), 2021, 1–13 (in Chinese with English abstract).

Research on gemological and spectral characteristic of tourmaline in Altay of Xinjiang. W. Zhang, *Superhard Material Engineering*, **33**(3), 2021, 51–58 (in Chinese with English abstract).

Rhodochrosite: The power of red. A. Hart, *InColor*, No. 48, 2022, 76–78, http://www.incolormagazine.com/books/pkra/#p=76.*

Spectral characteristics and color origin of unstable yellow sapphire. Y. Wang, L. Yang, M. Li, P. Yang, A.H. Shen and C. Wang, *Spectroscopy and Spectral Analysis*, **41**(8), 2021, 2611–2617, https://tinyurl.com/bdeh67v5 (in Chinese with English abstract).*

Spectroscopy and microscopy of corundum from primary deposits found in Greece. V. Karantoni, S. Karampelas, P. Voudouris, V. Melfos, L. Papadopoulou, T. Soldatos and C. Mavrogonatos, *Minerals*, **11**(7), 2021, article 750 (16 pp.), https://doi.org/10.3390/min11070750.*

Study on difference of color genesis between yellow and brown tremolite jade. Y. Liu, Z. Zhou, X. Yang, Y. Chen, W. Ruan and L. Zhang, *Acta Petrologica et Mineralogica*, **40**(6), 2021, 1189–1196, http://www.yskw.ac.cn/yskwxzz/article/abstract/20210611 (in Chinese with English abstract).*

Study on gemological characteristics of pink-purplish red dolomite. N. Chen, C. Chen, G. Li, S. Cao, Y. Lu and H. Zhang, *Superhard Material Engineering*, **33**(2), 2021, 47–52 (in Chinese with English abstract).

A study of gemology and mineral spectroscopy characteristics of peridot from Pakistan. W. Ruan, Z. Zhou, D. Schwarz, X. Yang, Y. Chen and Y. Liu, *Acta Petrologica et Mineralogica*, **40**(3), 2021, 593–604, http://www.yskw.ac.cn/yskwxzz/article/pdf/20210312 (in Chinese with English abstract).*

Study on the mineral composition and spectral characteristics of "bumble bee stone". J. Liu, J. Luo, S. Yue and Y. Xu, *Spectroscopy and Spectral Analysis*, **41**(6), 2021, 1936–1941, https://tinyurl.com/mwnhjzzm (in Chinese with English abstract).*

Vergleichende Eigenschaften von schleifwürdigen Diasporen aus Afghanistan, Myanmar und der Türkei [Comparative characteristics of gem-quality diaspore from Afghanistan, Myanmar and Turkey]. C.C. Milisenda and M. Wild, *Gemmologie: Zeitschrift der Deutschen Gemmologischen Gesellschaft*, **70**(3/4), 2021, 41–48 (in German with English abstract).

Zoisite – A gem of many colours. L. Phillis, *Australian Gemmologist*, **27**(6), 2021, 345–347.

CULTURAL HERITAGE

A 41,500 year-old decorated ivory pendant from Stajnia Cave (Poland). S. Talamo, W. Nowaczewska, A. Picin, A. Vazzana, M. Binkowski, M.D. Bosch, S. Cercatillo, M. Diakowski *et al.*, *Scientific Reports*, **11**(1), 2021, article 22078 (11 pp.), https://doi.org/10.1038/s41598-021-01221-6.*

Comercio y contrabando de esmeraldas neogranadinas en Italia meridional: Joyería y simbología en la Edad Moderna [Trading and smuggling of new-Granadan emeralds in southern Italy: Jewellery and symbologies in the modern age]. L.L. Vargas Murcia and F. De Nicolo, *Fronteras de la Historia*, **27**(1), 2022, 328–358, https://doi.org/10.22380/20274688.1947 (in Spanish with English abstract).*

Les gemmes de deux pièces maîtresses méconnues de la collection Adèle de Rothschild au Château d'Écouen - 1). La tiare [The gems of two little-known masterpieces from the Adèle de Rothschild collection at Château d'Écouen - 1). The tiara]. G. Panczer, G. Choumil, J. Rohou and G. Riondet, *Review de Gemmologie A.F.G.*, No. 214, 2021, 6–11 (in French).

Guangzuo ivory carving: Intercultural communication on the "Maritime Silk Road" during the 17th–19th century. Z. Qiu, H. Bo, J. Yang, H. Luo and M. Wu, *Journal of Gems & Gemmology*, **23**(5), 2021, 1–15, https://tinyurl.com/yc3mamvz (in Chinese with English abstract).*

Mining and trading of ancient lapis lazuli: The exploration for a combination of twofold evidence based on historical documents and archaeology discovery. S. Lai, Z. Qiu, J. Yang, H. Luo, X. Zheng and X. Ye, *Journal of Gems & Gemmology*, **23**(4), 2021, 1–11, https://tinyurl.com/ss3484v5 (in Chinese with English abstract).*

DIAMONDS

Heavy iron in large gem diamonds traces deep subduction of serpentinized ocean floor. E.M. Smith, P. Ni, S.B. Shirey, S.H. Richardson, W. Wang and A. Shahar, *Science Advances*, **7**(14), 2021, article eabe9773 (9 pp.), https://doi.org/10.1126/sciadv.abe9773.*

Microwave spectroscopy as a potential tool for color grading diamonds. Y. Rabinowitz, A. Etinger, A. Yahalom, H. Cohen and Y. Pinhasi, *Energies*, **14**(12), 2021, article 20213507 (18 pp.), https://doi.org/10.3390/en14123507.*

Millimeter wave spectroscopy for evaluating diamond color grades. Y. Rabinowitz, A. Etinger, B. Litvak, I. Litvak, A. Yahalom, H. Cohen and Y. Pinhasi, *Diamond and Related Materials*, **116**, 2021, article 108386 (10 pp.), https://doi.org/10.1016/j.diamond.2021.108386.

Shift of CO_2-I absorption bands in diamond: A pressure or compositional effect? A FTIR mapping study. E.P. Barannik, A.A. Shiryaev and T. Hainschwang, *Diamond and Related Materials*, **113**, 2021, article 108280 (11 pp.), https://doi.org/10.1016/j.diamond.2021.108280.

Spatial distribution of defects in a plastically deformed natural brown diamond. F.H.J. Laidlaw, P.L. Diggle, B.G. Breeze, M.W. Dale, D. Fisher and R. Beanland, *Diamond and Related Materials*, **117**, 2021, article 108465 (13 pp.), https://doi.org/10.1016/j.diamond.2021.108465.

Speaking the same language – Diamonds (part four). G. Dominy, *Gemmology Today*, December 2021, 52–58, https://tinyurl.com/bdekdkj7.*

Spectroscopic features according to the color origin of yellow diamonds. S. Noh, *Wooshin Gem Lab Magazine*, **8**, 2021, 11–16, https://tinyurl.com/y4z7f8wc.*

La véritable histoire du Grand Mazarin [The true history of Grand Mazarin]. F. Farges, *Review de Gemmologie A.F.G.*, No. 214, 2021, 12–17 (in French).

FAIR TRADE

The role of artisanal mining in the sustainable development of Myanmar's jadeite industry. M. Sadan and S.L. Dan, *Environmental Science & Policy*, **126**, 2021, 189–196, https://doi.org/10.1016/j.envsci.2021.09.019.

Socio-environmental impacts of diamond mining areas in the Democratic Republic of Congo. N. Galli, D.D. Chiarelli, M. D'Angelo and M.C. Rulli, *Science of the Total Environment*, **810**, 2022, article 152037 (9 pp.), https://doi.org/10.1016/j.scitotenv.2021.152037.

GEM LOCALITIES

Age determination of oriented rutile inclusions in sapphire and of moonstone from the Mogok Metamorphic Belt, Myanmar. G. Shi, X. Zhang, Y. Wang, Q. Li, F. Wu and H. He, *American Mineralogist*, **106**(11), 2021, 1852–1859, https://doi.org/10.2138/am-2021-7487.

Australia: Colored gemstone mining and supply. D. Cody, *InColor*, No. 48, 2022, 40–41, http://www.incolormagazine.com/books/pkra/#p=40.*

Colombia: New realities in the emerald industry. G. Galvis, *InColor*, No. 48, 2022, 42–43, http://www.incolormagazine.com/books/pkra/#p=42.*

Corundum (ruby) growth during the final assembly of the Archean North Atlantic craton, southern West Greenland. C. Yakymchuk, V. van Hinsberg, C.L. Kirkland, K. Szilas, C. Kinney, J. Kendrick and J.A. Hollis, *Ore Geology Reviews*, **138**, 2021, article 104417 (18 pp.), https://doi.org/10.1016/j.oregeorev.2021.104417.*

Dominican larimar mining—Current state and future prospects. K. Broda, L. Natkaniec-Nowak, Z. Rak, J. Stasica, W. Heflik, J. Mościcki, M. Peña, R. Muñoz *et al.*, *Minerals*, **12**(2), 2022, article 181 (16 pp.), https://doi.org/10.3390/min12020181.

East Africa: Mining and rough supply. W. Vertirest, *InColor*, No. 48, 2022, 34–37, http://www.incolormagazine.com/books/pkra/#p=34.*

Fluid boiling and fluid-rock interaction as primary triggers for emerald deposition: Insights from the Dayakou emerald deposit (China). Z.-Y. Long, X.-Y. Yu, X. Jiang, B.-J. Guo, C.-Y. Ma, Y. You and Y.-Y. Zheng, *Ore Geology Reviews*, **139**, 2021, article 104454 (15 pp.), https://doi.org/10.1016/j.oregeorev.2021.104454.

Fluid inclusion and titanite U-Pb age constraints on the Yuanjiang ruby mineralization in the Ailao Shan-Red River metamorphic belt, southwest China. W. Huang, P. Ni, J. Zhou, T. Shui, J. Pan, M. Fan and Y. Yang, *Canadian Mineralogist*, **60**(1), 2022, 1–26, https://doi.org/10.3749/canmin.2100009.

Geochemical and reflectance spectroscopy data integration to characterize emerald deposits: The case of the Paraná deposit, Brazil. J.F. Araújo Neto, S.B. Barreto, T.A. Carrino, I.M.B.A. Souza and G.L. Santos, *Anais da Academia Brasileira de Ciências*, **93**(1), 2021, article 236 (23 pp.), https://doi.org/10.1590/0001-3765202120200236.*

Geoquímica y mineralogía de la mina La Pava, Muzo-Quípama: Implicaciones en la exploración de esmeraldas en Colombia [Geochemistry and mineralogy of the La Pava mine, Muzo-Quípama: Implications for emerald exploration in Colombia]. A.F. González-Durán, J. García-Toloza, G. Bonilla, C.J. Cedeño-Ochoa, L.G. Angarita-Sarmiento, A.J. Castañeda-Gómez, S.D. Parra-Bastidas, L.C. Bocanegra-Rodríguez *et al.*, *Boletín de Geología*, **43**(2), 2021, 117–142, https://doi.org/10.18273/revbol.v43n2-2021007 (in Spanish with English abstract).*

History of emerald mining in the Habachtal deposit of Austria, part I. K. Schmetzer, *Gems & Gemology*, **57**(4), 2022, 338–371, https://doi.org/10.5741/gems.57.4.338.*

History, mines and minerals of the Mogok Stone Tract, Mandalay Division, Burma. T.P. Moore, M. Mauthner and W. E. Wilson, *Mineralogical Record*, **53**(1), 2022, 13–140.

A history of tourmaline from the island of Elba. F. Pezzotta, *Mineralogical Record*, **52**(6), 2021, 669–720.

Immiscible-melt inclusions in corundum megacrysts: Microanalyses and geological implications. X.-S. Xu, X.-M. Chen, W.L. Griffin, S.Y. O'Reilly, X.-S. Zhang and L.-H. Chen, *American Mineralogist*, **106**(4), 2021, 559–569, https://doi.org/10.2138/am-2020-7347.

LA-ICP-MS U–Pb dating of Cenozoic rutile inclusions in the Yuanjiang marble-hosted ruby deposit, Ailao Shan complex, southwest China. T. Yang, X. Sun, G. Shi and Y. Liu, *Minerals*, **11**(4), 2021, article 433 (9 pp.), https://doi.org/10.3390/min11040433.*

The legend of Himalayan motherlode—Historical, cultural and economic significance of the Padder blue sapphire. J. Parihar and H. Chauhan, *Research Review: International Journal of Multidisciplinary*, **6**(12), 2021, 50–56, https://rrjournals.com/index.php/rrijm/article/view/18/7.*

Mineralogical and geochemical characteristics of green nephrite from Kutcho, northern British Columbia, Canada. B. Jiang, F. Bai and J. Zhao, *Lithos*, **388–389**, 2021, article 106030 (14 pp.), https://doi.org/10.1016/j.lithos.2021.106030.

Mozambique ruby: Red rain pours into the market. R. Hughes, *Gemmology Today*, December 2021, 44–50, https://tinyurl.com/2p88dytw.*

A new model for the formation of nephrite deposits: A case study of the Chuncheon nephrite deposit, South Korea. F. Yuhuan, H. Xuemei and J. Yuntao, *Ore Geology Reviews*, **141**, 2022, article 104655 (14 pp.), https://doi.org/10.1016/j.oregeorev.2021.104655.

North America: Digging for gems in southern California. C. Unninayar, *InColor*, No. 48, 2022, 44–45, http://www.incolormagazine.com/books/pkra/#p=44.*

North America: The ethically sourced sapphires of Rock Creek, Montana. C. Unninayar, *InColor*, No. 48, 2022, 46–47, http://www.incolormagazine.com/books/pkra/#p=46.*

Ore formation of the Dayakou emerald deposit (southwest China) constrained by chemical and boron isotopic composition of tourmaline. Z. Long, X. Yu and Y. Zheng, *Ore Geology Reviews*, **135**, 2021, article 104208 (18 pp.), https://doi.org/10.1016/j.oregeorev.2021.104208.

Overview of gemstone resources in China. X.-Y. Yu, Z.-Y. Long, Y. Zhang, L.-J. Qin, C. Zhang, Z.-R. Xie, Y.-R. Wu, Y. Yan *et al.*, *Crystals*, **11**(10), 2021, article 1189 (22 pp.), https://doi.org/10.3390/cryst11101189.*

The Poldnevskoye deposit of demantoid (Middle Urals): Geology and mineralogy. E.S. Karaseva, A.Y. Kissin and V.V. Murzin, *Lithosphere (Russia)*, **21**(5), 2021, 683–698, https://doi.org/10.24930/1681-9004-2021-21-5-683-698 (in Russian with English abstract).*

A review of garnet deposits in western and southern Iran. F. Nouri, R.J. Stern and H. Azizi, *International Geology Review*, **64**, 2021, article 1838335 (28 pp.), https://doi.org/10.1080/00206814.2020.1838335.

Sapphire-bearing magmatic rocks trace the boundary between paleo-continents: A case study of Ilmenogorsky alkaline complex, Uralian collision zone of Russia. E.S. Sorokina, R.E. Botcharnikov, Y.A. Kostitsyn, D. Rösel, T. Häger, M.A. Rassomakhin, N.N. Kononkova, A.V. Somsikova *et al.*, *Gondwana Research*, **92**, 2021, 239–252, https://doi.org/10.1016/j.gr.2021.01.001.

Sri Lanka: Holding strong. A. Sammoon, *InColor*, No. 48, 2022, 38–39, http://www.incolormagazine.com/books/pkra/#p=38.*

Trace element geochemistry and mineral inclusions constraints on the petrogenesis of a marble–hosted ruby deposit in Yunnan Province, China. W. Huang, P. Ni, T. Shui, J. Pan, M. Fan, Y. Yang, Z. Chi and J. Ding, *Canadian Mineralogist*, **59**(2), 2021, 381–408, https://doi.org/10.3749/canmin.2000054.

A visit to the Indonesian opal fields in 2019 – Opal types, mining and treatments. Part 2. T. Coldham, J. Ivey and A. Smallwood, *Australian Gemmologist*, **27**(6), 2021, 315–327.

Yogo sapphire production. O. González and J. Edington, *Gems&Jewellery*, **30**(4), 2021, 18–19.

INSTRUMENTATION AND TECHNOLOGY

Alternative selection of Raman or LIBS spectral information in hierarchical discrimination of raw sapphires according to geographical origin for accuracy improvement. C. Eum, D. Jang, S. Lee, K. Cha and H. Chung, *Talanta*, **221**, 2021, article 121555 (9 pp.), https://doi.org/10.1016/j.talanta.2020.121555.*

Measurement of gem colour using a computer vision system: A case study with jadeite-jade. S. Zhang and Y. Guo, *Minerals*, **11**(8), 2021, article 791 (11 pp.), https://doi.org/10.3390/min11080791.*

Raman and photoluminescence mapping of gem materials. S. Eaton-Magaña, C.M. Breeding, A.C. Palke, A. Homkrajae, Z. Sun and G. McElhenny, *Minerals*, **11**(2), article 2021177 (31 pp.), https://doi.org/10.3390/min11020177.*

Rapid analysis of chemical composition and physical properties of gemstones using LIBS and chemometric technique. S. Dubey, R. Kumar, A.K. Rai, J.K. Pati, J. Kiefer and A.K. Rai, *Applied Sciences*, **11**(13), 2021, article 6156 (17 pp.), https://doi.org/10.3390/app11136156.*

JEWELLERY HISTORY

Fabergé in London: Romance to revolution. Anonymous, *Gems&Jewellery*, **30**(4), 2021, 20–23.

The mirror, the magus and more: Reflections on John Dee's obsidian mirror. S. Campbell, E. Healey, Y. Kuzmin and M.D. Glascock, *Antiquity*, **95**(384), 2021, 1547–1564, https://doi.org/10.15184/aqy.2021.132.*

S. M. Tagore's *Maṇimālā* and the meanings of diamonds in late Victorian Britain and India. D. Kinsey, *Nineteenth-Century Contexts*, **43**(4), 2021, 479–501, https://doi.org/10.1080/08905495.2021.1960040.

MISCELLANEOUS

Color predictions for a bright future: The 2022 forecast color palette. K. Champion, *InColor*, No. 48, 2022, 50–51, http://www.incolormagazine.com/books/pkra/#p=50.*

From curio to design gem…rise of the trapiche. J.S. Smith, *Gems&Jewellery*, **30**(4), 2021, 26–29.

Gem painting: Where art meets nature. V. Pardieu, *InColor*, No. 48, 2022, 56–58, http://www.incolormagazine.com/books/pkra/#p=56.*

Gemstones and the artist's palette – Natural mineral colouring of paint pigments. M. Clark, *Australian Gemmologist*, **27**(6), 2021, 330–342.

Hidden gems: Using collections in museums to discover the motivations of collectors. J. Freedman, *Collections: A Journal for Museum and Archives Professionals*, **17**(4), 2021, 319–336, https://doi.org/10.1177/1550190621998330.

NEWS PRESS

Afghan gems have a future, a longtime dealer says. V. Gomelsky, *New York Times*, 22 November 2021, https://tinyurl.com/4d85bhwd.*

Archaeologists discover ancient 'hangover prevention' ring. M.C. Hills, CNN Style, 9 November 2021, https://tinyurl.com/ykmez5nt.*

Gold jewelry including a necklace, lotus flower pendant and a tiara from the era of Nefertiti is found inside two 3,000-year-old Bronze Age tombs in Cyprus. S. Liberatore, *Daily Mail*, 2 December 2021, https://tinyurl.com/5x6haw9n.*

This huge black diamond just sold for $4.3 million. No one knows where it came from. M. Wei-Haas, *National Geographic*, 9 February 2022, https://www.nationalgeographic.com/science/article/the-science-of-the-mysterious-black-diamond-sold-at-auction.*

Metal detectorist finds small gold bible near York. BBC Yorkshire, *BBC*, https://www.bbc.com/news/uk-england-york-north-yorkshire-59181714.*

'Ugly diamonds' get a makeover. M. Lazazzera, *New York Times*, 6 December 2021, https://tinyurl.com/22r4x8b6.*

ORGANIC/BIOGENIC GEMS

Amber, copal and defaunation resin. M.M. Solórzano-Kraemer, *Bursztynisko (The Amber Magazine)*, No. 45, 2021, 182–185, https://tinyurl.com/nra8fx8e (in English and Polish).*

Amber of Lebanon. D. Azar, *Bursztynisko (The Amber Magazine)*, No. 45, 2021, 186–187, https://tinyurl.com/nra8fx8e (in English and Polish).*

Are ivory antiques actually antique? J. Kufnerová, K.P. Brabcová, V. Suchý, Z.A. Ovšonková, J. Frouzová, T. Cajthaml and I. Světlík, *Crime, Law and Social Change*, **76**(3), 2021, 219–231, https://doi.org/10.1007/s10611-021-09963-0.

Conservation, preparation and imaging of diverse ambers and their inclusions. E.-M. Sadowski, A.R. Schmidt, L.J. Seyfullah, M.M. Solórzano-Kraemer, C. Neumann, V. Perrichot, C. Hamann, R. Milke *et al.*, *Earth-Science Reviews*, **220**, 2021, article 103653 (24 pp.), https://doi.org/10.1016/j.earscirev.2021.103653.*

Crystallographic characteristics of inorganic mineral in mammoth ivory and ivory. X. Sun, M. He and J. Wu, *Minerals*, **12**(2), 2022, article 117 (12 pp.), https://doi.org/10.3390/min12020117.*

From Europe to China: An overview of the history of the amber trade. M. Cwaliński, *Bursztynisko (The Amber Magazine)*, No. 45, 2021, 164–168, https://tinyurl.com/nra8fx8e (in English and Polish).*

Gemological and spectral characteristics of Mexican red blue amber. T. Zhao, Y. Wang, L. Liu and Y. Li, *Spectroscopy and Spectral Analysis*, **41**(8), 2021, 2618–2625, https://tinyurl.com/yjk27kpm (in Chinese with English abstract).*

Identification characteristics of helmeted hornbill and its imitations. Y. Zhang and C. Chan, *Superhard Material Engineering*, **33**(2), 2021, 61–65 (in Chinese with English abstract).

Mitochondrial DNA profiling to combat the illegal trade in tortoiseshell products. E.L. LaCasella, M.P. Jensen, C.A. Madden Hof, I.P. Bell, A. Frey and P.H. Dutton, *Frontiers in Marine Science*, **7**, 2021, article 595853 (10 pp.), https://doi.org/10.3389/fmars.2020.595853.*

The new amber extraction from the Goitzsche Lake near Bitterfeld and first scientific results. I. Rappsilber and A. Wendel, *Bursztynisko (The Amber Magazine)*, No. 45, 2021, 190–195, https://tinyurl.com/2p99n65z (in English and Polish).*

Oxygen content and colour change characteristic of blood amber from Myanmar. L. Dong, *Journal of Gems & Gemmology*, **23**(5), 2021, 60–64, https://tinyurl.com/2p82txr5 (in Chinese with English abstract).*

Shining NIR light on ivory: A practical enforcement tool for elephant ivory identification. A. Chaitae, R. Rittiron, I.J. Gordon, H. Marsh, J. Addison, S. Pochanagone and N. Suttanon, *Conservation Science and Practice*, **3**(9), 2021, article e486 (11 pp.), https://doi.org/10.1111/csp2.486.*

Vivianite and its oxidation products in mammoth ivory and their implications to the burial process. M. Shen, Z. Lu, Y. Xu and X. He, *ACS Omega*, **6**(34), 2021, 22284–22291, https://doi.org/10.1021/acsomega.1c02964.*

PEARLS

The effects of nacre microstructure on green and pink interference colors in *Pinctada fucata martensii* pearls. G. Muhammad, T. Fujimura and A. Komaru, *Aquaculture*, **535**, 2021, article 736424 (11 pp.), https://doi.org/10.1016/j.aquaculture.2021.736424.

Gemmological characteristic of orange–red *Tridacna*. J. Chen, Y. Luo and Y. Wang, *Journal of Gems & Gemmology*, **23**(4), 2021, 29–32, https://tinyurl.com/4xrzmw49 (in Chinese with English abstract).*

The mesoscale order of nacreous pearls. J. Gim, A. Koch, L.M. Otter, B.H. Savitzky, S. Erland, L.A. Estroff, D.E. Jacob and R. Hovden, *Proceedings of the National Academy of Sciences*, **118**(42), 2021, article e2107477118 (8 pp.), https://doi.org/10.1073/pnas.2107477118.*

Pearl grading factors and methods. A. Kim, *Wooshin Gem Lab Magazine*, **8**, 2021, 6–10, https://tinyurl.com/y4z7f8wc.*

The spectral characteristics of "Edison" pearls and nucleated pearls with dyeing treatment. L. Yu and Y. Wang, *Spectroscopy and Spectral Analysis*, **41**(8), 2021, 2626–2632, https://tinyurl.com/2h7r5p7z (in Chinese with English abstract).*

Study on the influence of porosity of the nacre layer on the luster and surface roughness of Chinese large freshwater nucleated pearl. D. Zhou, T. Lu, R. Sun and J. Zhang, *Crystals*, **12**(2), 2022, article 234 (6 pp.), https://doi.org/10.3390/cryst12020234.*

SIMULANTS

Characteristics and identification of a gemstone with trade name "Thailand cat's eye". L. Yu, *Superhard Material Engineering*, **33**(4), 2021, 46–51 (in Chinese with English abstract).

Simulated malachite with barium sulfate as the main constituent. Y. Kim, *Wooshin Gem Lab Magazine*, **8**, 2021, 2–5, https://tinyurl.com/y4z7f8wc.*

Spectroscopic identification of amber imitations: Different pressure and temperature treatments of copal resins. T. Zheng, H. Li, T. Lu, X. Chen, B. Li and Y. Liu, *Crystals*, **11**(10), 2021, article 1223 (17 pp.), https://doi.org/10.3390/cryst11101223.*

Study on gemological characteristics of a kind of turquoise imitation. H. Zhu, S. Chen, X. Zhao, Y. Cheng, C. Fan, Y. Wang and T. Li, *Journal of Mineralogy and Petrology*, **41**(3), 2021, 9–15 (in Chinese with English abstract).

Study on gemological characteristics of a sapphire imitation (sapphirine). H. Zhu, X. Zhao, T. Li, F. Yan and S. Chen, *Superhard Material Engineering*, **33**(2), 2021, 57–60 (in Chinese with English abstract).

SYNTHETICS

From ashes to diamonds: Making lab-grown afterlife. F. Calvão and L. Bell, *Tsantsa*, **26**, 2021, 122–138, https://doi.org/10.36950/tsantsa.2021.26.6916.*

A comparative analysis of energy and water consumption of mined versus synthetic diamonds. V. Zhdanov, M. Sokolova, P. Smirnov, L. Andrzejewski, J. Bondareva and S. Evlashin, *Energies*, **14**(21), 2021, article 7062 (13 pp.), https://doi.org/10.3390/en14217062.*

Diamond growth and characteristics in the metal-silicate-H_2O-C system at HPHT conditions. Z. Lu, H. Zhao, Y. Wang, S. Fang, Z. Cai, Z. Wang, H. Ma, L. Chen *et al.*, *Lithos*, **404–405**, 2021, article 106470 (11 pp.), https://doi.org/10.1016/j.lithos.2021.106470.

Identification characteristic of "recrystallized synthetic emerald". L. Lu and A.H. Shen, *Journal of Gems & Gemmology*, **23**(5), 2021, 51–59, https://tinyurl.com/5n7ccvpv (in Chinese with English abstract).*

Identification of pink-coloured CVD synthetic diamonds from Huzhou Sino-C Semiconductor Co. in China. Z. Song, H. Dai, B. Gao and W. Zhu, *Crystals*, **11**(8), 2021, article 872 (11 pp.), https://doi.org/10.3390/cryst11080872.*

Laboratory-grown diamond: A gemological laboratory perspective. S. Eaton-Magana, T. Ardon and C.M. Breeding, *Journal of Gems & Gemmology*, **23**(6), 2021, 23–59, https://doi.org/10.15964/j.cnki.027jgg.2021.06.003 (in Chinese with English abstract).*

Luminescence of brown CVD diamond: 468 nm luminescence center. A.M. Zaitsev, N.M. Kazuchits, K.S. Moe, J.E. Butler, O.V. Korolik, M.S. Rusetsky and V.N. Kazuchits, *Diamond and Related Materials*, **113**, 2021, article 108255 (7 pp.), https://doi.org/10.1016/j.diamond.2021.108255.

Man-made crystals: A review of their historic and contemporary context and use. S. Boons, *International Journal of Design in Society*, **15**(2), 2021, 63–71, https://doi.org/10.18848/2325-1328/CGP/v15i02/63-71.*

TREATMENTS

Characteristic and identification of bleached and filled aquamarine. Q. Jia, G. Li, X. Li, Y. Xiao, H. Wang and J. Luo, *Journal of Gems & Gemmology*, **23**(5), 2021, 43–50, https://tinyurl.com/2p8kwrwv (in Chinese with English abstract).*

Coloration changes in natural ruby induced by oxygen ion implants correlated with cathodoluminescence data. T. Tengchaisri, D. Bootkul, S. Intarasiri, U. Tippawan and A.Y. Kuznetsov, *Nuclear Instruments and Methods in Physics Research Section B: Beam Interactions with Materials and Atoms*, **502**, 2021, 29–36, https://doi.org/10.1016/j.nimb.2021.06.002.

An energy-saving method of organic dyeing of agates. C. Ericksson, I.A.S. de Brum and W.M. Ambrós, *Environmental Challenges*, **2**, 2021, article 100019 (5 pp.), https://doi.org/10.1016/j.envc.2020.100019.*

Experiment and research on the process of heat treatment of nephrite to change color imitating material. H. Li, X. Deng, X. Chan, Y. Ni, Y. Hu and C. Zeng, *Superhard Material Engineering*, **33**(4), 2021, 56–61 (in Chinese with English abstract).

Gamma-ray effect on natural quartz gem crystals' quality from Qazvin and Astane regions, Iran. R. Rezaee, S.A. Feghhi and F. Masoudi, *Journal of Gems & Precious Metals*, **1**(1), 2021, 49–55, https://doi.org/10.29252/GEM.2021.101026.*

The gamma ray interaction properties of India spinel. P. Limkitjaroenporn, W. Hongtong and J. Kaewkhao, *Materials Today: Proceedings*, **43**, 2021, 2563–2568, https://doi.org/10.1016/j.matpr.2020.04.617.

Gemmological characteristic and colour of zircon under heat treatment in reducing condition. X. Yan, S. Yue, S. Li and P. Wang, *Journal of Gems & Gemmology*, **23**(4), 2021, 33–38, https://tinyurl.com/yc6rtr2d (in Chinese with English abstract).*

Heat treatment of dark blue sapphire from Australia. Y. Xu and J. Di, *Journal of Gems & Gemmology*, **22**(6), 2020, 20–32, https://tinyurl.com/msjwk238 (in Chinese with English abstract).*

Identification characteristic of purple jadeite treated with bleaching, filling and dyeing. L. Yu, H. Dai, L. Li, S. Cao, F. Wang, L. Guo and Z. Yu, *Journal of Gems & Gemmology*, **23**(5), 2021, 65–74, https://tinyurl.com/mwm7ynvu (in Chinese with English abstract).*

Research process of gemstone irradiation treatment technology in recent years. X. Yan and S. Yue, *Superhard Material Engineering*, **33**(3), 2021, 41–45 (in Chinese with English abstract).

Spectroscopic characteristics and coloring mechanism of brown tourmaline under heating treatment. S. Yue, X. Yan, J. Lin, P. Wang and J. Liu, *Spectroscopy and Spectral Analysis*, **41**(8), 2021, 2524–2529, https://tinyurl.com/2zsnapph (in Chinese with English abstract).*

Study on composition and spectral characteristics of turquoise treated by "porcelain-added". L. Huang, Q. Chen, X. Gao, Y. Du and F. Xu, *Spectroscopy and Spectral Analysis*, **41**(7), 2021, 2245–2250, https://tinyurl.com/yfxr5zuw (in Chinese with English abstract).*

Study on gemological characteristics of a filled aquamarine ring stone. H. Zhu, X. Zhao, T. Li, B. Sun and S. Chen, *Superhard Material Engineering*, **33**(3), 2021, 46–50, (in Chinese with English abstract).

Thermal process of rock crystal: Cause of infrared absorption band at 3585 cm^{-1}. J. Li, Y. Zheng, X. Liu, G. Li, X. Yu, Y. Wang, H. Liu *et al.*, *Crystals*, **11**(9), 2021, article 1083 (7 pp.), https://doi.org/10.3390/cryst11091083.*

Treatment disclosure and other notes from the eastern front. R.W. Hughes, *GemGuide*, **41**(1), 2022, 4–6.

Untersuchungen an natürlichen und wärmebehandelten Demantoiden aus dem zentralen Uralgebirge in Russland [Investigations of natural and heat-treated demantoids from the central Ural Mountains in Russia]. A. Sugzdaite, T. Häger, E. Sorokina, M.P. Popov, A. Nikolaev, R. Botcharntkov and W. Hofmeister, *Gemmologie: Zeitschrift der Deutschen Gemmologischen Gesellschaft*, **70**(3/4), 2021, 19–36 (in German with English abstract).

COMPILATIONS

***G&G* Micro-World.** Apatite-CO_2 inclusions in Burmese sapphire • Chondrodite in Burmese red spinel • Black coral with polyp structure • Demantoid with horsetail inclusions • Radioactive green diamond • Rainbow graining in diamond • Monazite(?) in quartz • Spiral nacre in natural pearl • 'Windmill' zoning in tourmaline • Rutile on hematite. *Gems & Gemology*, **57**(4), 2022, 382–389, https://tinyurl.com/3x8spbzm.*

Gem News International. Biogenic carbon in pink sapphire from Greenland • Yogo (Montana, USA) sapphire update • Banded turquoise from Zhushan County, China • Blue zircon from Malawi • Historic sales of pink and blue diamonds from Australia's Argyle mine • Chalcedony-epoxy composite imitation of 'candy agate' • 'Floating flower' inclusions in aventurine quartz • GSA conference report. *Gems & Gemology*, **57**(4), 2022, 398–412, https://tinyurl.com/ynxxafew.*

Lab Notes. Color-zoned cat's-eye chrysoberyl • Diamond faceted as iconic Apple logo • Two pairs of antique Mughal spectacles with diamond and emerald lenses • Pink euclase • Vaterite on surface of freshwater cultured pearls • Star rhodochrosite • 31 ct orange sapphire • Flux-induced 'fingerprints' in synthetic sapphire • Circuit-board pattern on tourmaline. *Gems & Gemology*, **57**(4), 2022, 372–381, https://tinyurl.com/yjnk5j8m.*

CONFERENCE PROCEEDINGS

7th International Gem & Jewelry Conference—GIT 2021: Towards the Sustainable Gem Industry Beyond 2022. Chanthaburi, Thailand, 2–3 February 2022, 310 pp., https://tinyurl.com/yemett5u.*

**Article freely available for downloading or reading online, as of press time*

Coming Soon!

GemINTRO

GemIntro is a Level 2, online, entry-level course which will introduce you to the fascinating world of gemmology and the enormous variety of beautiful gems available. You can discover the basics of gemmology at your own pace - perfect for anyone looking to start or grow their career in the gems and jewellery trade, or for those completely new to gemmology and with an interest in gems.

Register your interest now at **gem-a.com/gemintro**

Gem-A
THE GEMMOLOGICAL ASSOCIATION OF GREAT BRITAIN

Gem-A, 21 Ely Place, London, EC1N 6TD, UK. T: +44 (0)20 7404 3334, W: www.gem-a.com. Registered charity no. 1109555.